Room-temperature passive terahertz imaging based on high-sensitivity field-effect transistor detectors

Dissertation
zur Erlangung des Doktorgrades
der Naturwissenschaften

vorgelegt beim Fachbereich Physik
der Johann Wolfgang Goethe -Universität
in Frankfurt am Main

von
Dovilė Čibiraitė-Lukenskienė
aus Švenčionys, Litauen

Frankfurt am Main 2021
(D 30)

vom Fachbereich Physik der
Johann Wolfgang Goethe - Universität als Dissertation angenommen.

Dekan: Prof. Dr. Harald Appelshäuser

Gutachter: Prof. Dr.-Ing. habil. Viktor Krozer
Prof. Dr. Hartmut G. Roskos

Datum der Disputation: 21.07.2021

Abstract

Terahertz (THz) technology is an emerging field that considers the radiation between microwave and far-infrared regions where the electronic and photonic technologies merge. THz generation and THz sensing technologies should fill the gap between photonics and electronics which is defined as a region where THz generation power and THz sensing capabilities are at a low technology readiness level (TRL). As one of the options for THz detection technology, field-effect transistors with integrated antennae were suggested to be used as THz detectors in the 1990s by M. Dyakonov and M. Shur from where the development of field-effect transistor-based detector began. In this work, various FET technologies are presented, such as CMOS, AlGaN/GaN, and graphene-based material systems and their further sensitivity enhancement in order to reach the performance of well-developed Schottky diode-based THz sensing technology. Here presented FET-based detectors were explored in a wide frequency range from 0.1 THz up to 5 THz in narrowband and broadband configurations.

For proper implementation of THz detectors, the well-defined characterization is of high importance. Therefore, this work overviews the characterization methods, establishes various definitions of detector parameters, and summarizes the state-of-the-art THz detectors. The electrical, optical, and cryogenic characterization techniques are also presented here, as well as the best results obtained by the development of the characterization methods, namely graphene FET stabilization, low-power THz source characterization for detector calibration, and technology development for cryogenic detection.

Following the discussion about the detector characterization, a wide range of THz applications, which were tested during the last four years of Ph.D. and conducted under the ITN CELTA project from HORIZON2020 program, are presented in this work. The studies began with spectroscopy applications and imaging and later developed towards hyperspectral imaging and even passive imaging of human body THz radiation. As various options for THz applications, single-pixel detectors as well as multi-pixel arrays are also covered in this work.

The conducted research shows that FET-based detectors can be used for spectroscopy applications or be easily adapted for the relevant frequency range. State-of-the-art detectors considered in this work reach the resonant performance below 20 pW/√Hz at 0.3 THz and 0.5 THz, as well as 404 pW/√Hz cross-sectional NEP at 4.75 THz. The broadband detectors show NEP as low as 25 pW/√Hz at around 0.6 THz for the best AlGaN/GaN design and 25 pW/√Hz around 1 THz for the best CMOS design. As one of the most promising applications, metamaterial characterization was tested using the most sensitive devices. Furthermore, one of the single-pixel devices and a multi-pixel array were tested as an engineering solution for a radio astronomy system called GREAT in a stratosphere observatory named SOFIA. The exploration of the autocorrelation technique using FET-based

devices shows the opportunity to employ such detectors for direct detection of THz pulses without an interferometric measurement setup.

This work also considers imaging applications, which include near-field and far-field visualization solutions. A considerable milestone for the theory of FET technology was achieved when scanning near-field microscopy led to the visualization of plasma (or carrier density) waves in a graphene FET channel. Whereas another important milestone for the THz technology was achieved when a 3D scan of a mobile phone was performed under the far-field imaging mode. Even though the imaging was done through the phone's plastic cover, the image displayed high accuracy and good feature recognition of the smartphone, inching the FET-based detector technology ever so close to practical security applications. In parallel, the multi-pixel array testing was carried out on 6x7 pixel arrays that have been implemented in configurable-size aperture and imaging configurations. The configurable aperture size allowed the easier detector focusing procedure and a better fit for the beam size of the incident radiation. The imaging has been tested on various THz sources and compared to the TeraSense 16x16 pixel array. The experimental results show the big advantage of the developed multi-pixel array against the used commercial technology.

Furthermore, two ultra-low-power applications have been successfully tested. The application on hyper-frequency THz imaging tested in the specially developed dual frequency comb and our detector system for 300 GHz radiation with 9 spectral lines led to outstanding imaging results on various materials. The passive imaging of human body radiation was conducted using the most sensitive broadband CMOS detector with a log-spiral antenna working in the 0.1 – 1.5 THz range and reaching the optical NEP of 42 pW/√Hz. The NETD of this device reaches 2.1 K and overcomes the performance limit of passive room-temperature imaging of the human body radiation, which was less than 10 K above the room temperature. This experiment opened a completely new field that was explored before only by the multiplier chain-based or thermal detectors.

To summarize, it was shown in this work that field-effect transistor-based THz detectors can be used as universal power detectors for various room-temperature broadband and narrow-band applications: short-pulse detection, time-domain or frequency-domain spectroscopy, active near-field but mainly far-field imaging in various optical configurations. The detectors can be easily produced as multi-pixel arrays and be cooled for sensitivity enhancement. The development of the detectors reached the sensitivity performance needed for the completely passive room-temperature THz imaging which is a higher readiness level of the FET-based THz detector technology now reaching TRL 4-5.

Kurze Zusammenfassung

Mikrowellen- und IR-technologien verschmelzen miteinander bei der Entwicklung der elektronischen und photonischen Technologien im terahertz (THz) Bereich. Die Quellen- und Sensortechnologien sollten die Lücke zwischen Photonik und Elektronik schließen, wo die Strehlungsleistung und die Empfindlichkeit von Sensoren schwach sind. Als eine der Optionen für die THz-Detektionstechnologie schlagen wir Feldeffekttransistoren vor, die mit integrierten Antennen erforscht werden sollen, um hochempfindliche Bauelemente für den THz Bereich bereitzustellen. Die Transistoren wurden theoretisch in den 1990er Jahren von M. Dyakonov und M. Shur als THz-Detektoren vorgeschlagen. In dieser Arbeit werden wir verschiedene FET-Technologien, wie CMOS, AlGaN/GaN und graphenbasierte Materialsysteme, untersuchen. Die Detektoren werden in einem breiten Frequenzbereich von 0,1 bis 5 THz in Schmalband- und Breitbandkonfigurationen erforscht.

Für die richtige Implementierung von THz-Detektoren ist die gut definierte Charakterisierung von großer Bedeutung. Deshalb werden in dieser Arbeit die Charakterisierungsmethoden und verschiedene Definitionen von Detektorparametern vorgestellt. Wir werden den Stand der Technik von THz-Detektoren und unsere neuesten Entwicklungen zusammenfassen. Von der Seite der Charakterisierung werden wir die elektrischen, optischen und kryogenen Charakterisierungstechniken verwenden und die besten Ergebnisse präsentieren. Manche neue Techniken wurden durch die Entwicklung der Charakterisierungsmethoden entwickelt, nämlich Graphen-FET-Stabilisierung, Charakterisierung von THz Quellen mit niedriger Leistung für die Detektorkalibrierung, und Technologieentwicklung für den kryogene Messungen. Diese Techniken werden hier auch präsentiert.

In dieser Arbeit wird ein breites Spektrum von THz-Anwendungen untersucht. Angefangen bei den spektroskopischen Anwendungen und der Bildgebung bis hin zur hyperspektralen Bildgebung und sogar zur passiven Bildgebung der THz-Strahlung des menschlichen Körpers. In dieser Arbeit werden sowohl Einzel-Pixel-Detektoren als auch Multi-Pixel-Arrays vorgestellt.

Die untersuchte Autokorrelationstechnik zeigt die Möglichkeit, solche Detektoren für die direkte Detektion von THz Pulsen ohne interferometrischen Messaufbau einzusetzen. Unsere hochmodernen Detektoren erreichen eine schmalbandige Sensitivität unter 20 pW/√Hz bei 0,3 THz und 0,5 THz, sowie 404 pW/√Hz Querschnitts-NEP bei 4,75 THz. Die breitbandige Detektoren zeigen ein NEP von nur 25 pW/√Hz bei etwa 0,6 THz für das beste AlGaN/GaN-HEMT Design und 25 pW/√Hz bei etwa 1 THz für das beste CMOS FET Design. Diese Detektoren können für Spektroskopie angewendet werden und einfach für den relevanten Frequenzbereich angepasst werden. Als eine der vielversprechendsten Anwendungen wurde die Charakterisierung von Metamaterialien mit den entwickelten Geräten getestet. Eines der Ein-Pixel-Geräte und ein Multi-Pixel-Array wurden als technische Lösung für ein

Radioastronomiesystem namens GREAT im Stratosphären-Observatorium namens SOFIA getestet.

Zu den vorgestellten Bildgebungsanwendungen gehören Nahfeld- und Fernfeldlösungen. Die rasternde Nahfeldmikroskopie führte zur Visualisierung von Plasmawellen in einem Graphen-FET-Kanal. Die Fernfeld-Bildgebung hingegen machte einen 3D-Scan eines Mobiltelefons durch dessen Kunststoffabdeckung hindurch und zeigte eine hohe Genauigkeit und eine gute Erkennung der Merkmale des Smartphones. Für die Multi-Pixel-Array-Tests verwendeten wir 6x7-Pixel-Arrays, die in Konfigurationen von konfigurierbarer Größe der Apertur oder Bildgebung implementiert wurden. Die konfigurierbare Größe der Apertur ermöglicht eine einfachere Detektorfokussierung und eine bessere Anpassung an die Strahlgröße der einfallenden Strahlung. Die Bildgebung wurde an verschiedenen THz-Quellen getestet und mit TeraSense 16x16 Pixel-Arrays verglichen. Die experimentellen Ergebnisse zeigen den hohen Vorteil unserer Entwicklung gegenüber der verwendeten kommerziellen Technologie.

Zwei Anwendungen unter sehr niedrigem THz Leistung wurden erfolgreich getestet. Die Anwendung auf Hyperfrequenz-THz-Bildgebung, die im speziell entwickelten Doppelfrequenzkamm getestet wurde, und unser Detektorsystem für 300 GHz-Strahlung mit 9 Spektrallinien führten zu hervorragenden Bildgebungsergebnissen auf verschiedenen Materialien. Die passive Bildgebung der Strahlung des menschlichen Körpers, die mit dem vorgestellten Breitband-CMOS-Detektor mit Log-Spiral-Antenne erreicht wurde, der im Bereich von 0,1 - 1,5 THz arbeitet und die optische NEP von 42 pW/√Hz und NETD von 2,1 K erreicht, übertrifft die Leistungsgrenze der passiven Raumtemperatur-Bildgebung der Strahlung des menschlichen Körpers, die weniger als 10 K über der Raumtemperatur lag. Dieses Experiment eröffnete ein völlig neues Feld, das zuvor nur von den elektronischen Vervielfacherketten oder thermischen Detektoren erforscht wurde.

Zusammenfassend wurde in dieser Arbeit gezeigt, dass Feldeffekt-Transistoren dienen als universelle Leistungsdetektoren im THz Bereich und können für verschiedene Breitband- und Schmalbandanwendungen Anwendungen bei Raumtemperatur eingesetzt werden, wie zum Beispiel, Kurzpulserkennung, Spektroskopie im Zeit- oder Frequenzbereich, aktive Nahfeld- und hauptsächlich Fernfeldabbildung in verschiedenen optischen Konfigurationen. Die Detektoren lassen sich leicht als Multi-Pixel-Arrays herstellen und können zur Erhöhung der Empfindlichkeit gekühlt werden.

Publication list

This thesis summarizes the author's work on TeraFET detectors. The work was funded by the ITN CELTA project of the HORIZON2020 program (see in the Appendix) and conducted with collaboration partners from Germany, France, Spain, Ireland, Sweden, Lithuania, and Poland. It is published in the following journals and conferences (indentation is used for comments and author's contribution to the publication):

Journals

1. A. Lisauskas, K. Ikamas, S. Massabeau, M. Bauer, D. Čibiraitė, J. Matukas, J. Mangeney, M. Mittendorff, S. Winnerl, V. Krozer, and H. G. Roskos, "Field-effect transistors as electrically controllable nonlinear rectifiers for the characterization of terahertz pulses," *APL Photonics*, vol. 3, no. 5, p. 051705, Mar. 2018.
    - I have conducted electrical characterization on AlGaN/GaN HEMT detector and participated in the optical measurement session using fs laser at Ecole Normale Superieure-PSL Research University, CNRS.
2. K. Ikamas, D. Čibiraitė, A. Lisauskas, M. Bauer, V. Krozer, and H. G. Roskos, "Broadband Terahertz Power Detectors Based on 90-nm Silicon CMOS Transistors With Flat Responsivity Up to 2.2 THz," *IEEE Electron Device Letters*, vol. 39, no. 9, pp. 1413–1416, Sep. 2018.
    - I have prepared and characterized the detector module, built the setup, and conducted electrical and optical experiments.
    - I also actively participated in proofreading the first draft.
    - Technical correction to this article was published in vol. 40, no. 2, pp. 354–354, Feb. 2019.
3. J. Zdanevicius, D. Cibiraite, K. Ikamas, M. Bauer, J. Matukas, A. Lisauskas, H. Richter, T. Hagelschuer, V. Krozer, H.-W. Hübers, and H.G. Roskos, "Field-Effect Transistor Based Detectors for Power Monitoring of THz Quantum Cascade Lasers," *IEEE Transactions on Terahertz Science and Technology*, vol. 8, no. 6, pp. 613–621, Nov. 2018.
    - I have conducted electrical and optical characterization of the detector and conducted noise measurement at DLR.
    - I have actively participated in preparing data analysis and graphical representation of Fig. 3b, Fig. 7, Fig. 8.
    - I have participated in proofreading and review corrections.
4. K. Ikamas, A. Lisauskas, S. Massabeau, M. Bauer, M. Burakevič, J. Vyšniauskas, D. Čibiraitė, V. Krozer, A. Rämer, S. Shevchenko, W. Heinrich, J. Tignon, S. Dhillon, J. Mangeney, and H. G. Roskos, "Sub-picosecond pulsed THz FET detector characterization in plasmonic detection regime based on autocorrelation technique," *Semicond. Sci. Technol.*, vol. 33, no. 12, p. 124013, Nov. 2018.

- I have conducted noise and optical characterization on AlGaN/GaN HEMT using fs laser at Ecole Normale Superieure-PSL Research University, CNRS.
- I have documented the experiments in very detail and proofread the draft.

5. M. Bauer, A. Rämer, S. A. Chevtchenko, K.Y. Osipov, D. Čibiraitė, S. Pralgauskaitė, K. Ikamas, A. Lisauskas, W. Heinrich, V. Krozer, and H.G. Roskos, "A High-Sensitivity AlGaN/GaN HEMT Terahertz Detector With Integrated Broadband Bow-Tie Antenna," *IEEE Transactions on Terahertz Science and Technology*, vol. 9, no. 4, pp. 430–444, Jul. 2019.
   - I have experimentally verified the published value and provided the sample for the imaging.
   - I have prepared the state-of-the-art table for this publication.
   - I have participated in proofreading and review corrections.
6. F. Meng, M.D. Thomson, B. Klug, D. Čibiraitė, Q. Ul-Islam, and H.G. Roskos, "Nonlocal collective ultrastrong interaction of plasmonic metamaterials and photons in a terahertz photonic crystal cavity," *Opt. Express, OE*, vol. 27, no. 17, pp. 24455–24468, Aug. 2019.
   - I have conducted spectroscopy experiments using the CW system and analyzed data to provide spectral information on metamaterial transmission characteristics.
7. A. Soltani, F. Kuschewski, M. Bonmann, A. Generalov, A. Vorobiev, F. Ludwig, M. M. Wiecha, D. Čibiraitė, F. Walla, S. Winnerl, L. Eng, J. Stake, and H. G. Roskos, "Direct nanoscopic observation of plasma waves in the channel of a graphene field-effect transistor", Light: Science & Applications, 2019.
   - I prepared the experimental setup for electronic and optical detection of GFET signals. I was also responsible for GFET characterization and preparation for the s-SNOM experiment. I participated in the first two sessions of s-SNOM experiments in FELBE.
   - Later, I have consulted the co-authors on DC resistance measurement of GFET and stability issues to obtain trustful resistance data for the last sessions of the experimental study on carrier density waves in the GFET channel.
8. D. Čibiraitė-Lukenskienė, K. Ikamas, T. Lisauskas, V. Krozer, H. G. Roskos, and A. Lisauskas, "Passive Detection and Imaging of Human Body Radiation Using an Uncooled Field-Effect Transistor-Based THz Detector," Sensors (Basel, Switzerland), vol. 20, no. 15, 2020.
   - I have prepared the detector module and the experimental setup, then conducted the experiments and analyzed experimental data.
   - I have actively participated in theoretical calculations on thermal detector sensitivity. As there is no suitable experiment or prediction of the human palm emissivity at the THz range, I have overviewed the literature on skin emissivity in the range of interest and predicted an expected mean value for the conducted experiment.

- I have prepared the graphical representation (Fig. 2 - 8), wrote the draft and submitted it, and implemented the corrections after the review process.

9. P. Martín-Mateos, D. Čibiraitė-Lukenskienė, R. Barreiro, C. De Dios, A. Lisauskas, V. Krozer, and P. Acedo, "Hyperspectral terahertz imaging with electro-optic dual combs and a FET-based detector," *Scientific reports*, vol. 10, no. 1, p. 14429, 2020.
    - I have organized the improvement of TeraFET and dual-comb specification in such a way, that both systems could merge into one hyper-spectral imaging system.
    - I have implemented the detector module with a build-in low-noise amplifier and conducted detector characterization with and without the amplifier. I have built the optical measurement setup and developed imaging software.
    - I have written the detector part in the paper and proofread the draft.
10. M. Ferreras Mayo, D. Cibiraite-Lukenskiene, A. Lisauskas, J. Grajal, and V. Krozer, "Broadband sensing around 1 THz via a novel biquad-antenna-coupled low-NEP detector in CMOS," *IEEE Trans. THz Sci. Technol.*, p. 1, 2020.
    - I have prepared the readout circuit for the new detector array design and built the detector module for the experiment. I have prepared the experimental setup and led the characterization experiments. I have measured the noise of the detector and characterized Toptica power.
    - I have actively participated in the draft corrections and suggestions, made review corrections from the experimental side.

Conference proceedings

1. M. Bauer, M. Andersson, A. Zak, P. Sakalas, D. Čibiraitė, A. Lisauskas, M. Schröter, J. Stake, and H. G. Roskos, "The potential for sensitivity enhancement by the thermoelectric effect in carbon-nanotube and graphene Tera-FETs," *J. Phys.: Conf. Ser.*, vol. 647, p. 012004, Oct. 2015.
    - I have conducted experiments on the physical properties of GFETs.
2. J. Vyšniauskas, A. Lisauskas, M. Bauer, D. Čibiraitė, J. Matukas, and H. G. Roskos, "Hydrodynamic modelling of terahertz rectification in AlGaN/GaN high electron mobility transistors," *J. Phys.: Conf. Ser.*, vol. 906, p. 012023, Oct. 2017.
    - I have provided experimental data on thermal effects on AlGaN/GaN HEMT devices which helped in the discussions on simulation results.
3. D. Cibiraite, M. Bauer, A. Lisauskas, V. Krozer, H. G. Roskos, A. Rämer, W. Heinrich, S. Pralgauskaite, J. Zdanevicius, J. Matukas, and M. Andersson, "Thermal noise-limited sensitivity of FET-based terahertz detectors," in *2017 International Conference on Noise and Fluctuations (ICNF)*, Vilnius, Lithuania, 2017, pp. 1–4.

- I conducted resistance and noise measurements on the presented detectors studied resistance stability and described resistance stabilization methods created for the experiment.
- I have analyzed the data and prepared the graphical representation.
- I led the writing preparing the publication draft, later extension, and necessary corrections on it.

4. K. Ikamas, A. Lisauskas, M. Bauer, A. Rämer, S. Massabeau, D. Čibiraitė, M. Burakevič, S. Chevtchenko, J. Mangeney, W. Heinrich, V. Krozer, and H. G. Roskos, "Efficient detection of short-pulse THz radiation with field effect transistors," in *2017 International Conference on Noise and Fluctuations (ICNF)*, 2017, pp. 1–4.
   - I have conducted noise experiments and participated in optical response measurements.
   - I have prepared detailed documentation of the experimental setup and experiment itself, conducted at Ecole Normale Superieure-PSL Research University, CNRS. Later, the documentation was used for the preparation of the first draft. I also proofread the draft.
5. D. Čibiraitė, M. Bauer, A. Rämer, S. Chevtchenko, A. Lisauskas, J. Matukas, V. Krozer, W. Heinrich, and H. G. Roskos, "Enhanced performance of AlGaN/GaN HEMT-Based THz detectors at room temperature and at low temperature," in *2017 42nd International Conference on Infrared, Millimeter, and Terahertz Waves (IRMMW-THz)*, 2017, pp. 1–2.
   - I have built a cryogenic measurement system and designed a cryogenic finger suitable for the temperature transfer from the cryostat to the detector. I also redesigned the detector module so that it fits the cryostat and holds the detector in the optical axis.
   - I have conducted the experiments and simulations on AlGaN/GaN HEMT and prepared the graphical representation of it.
   - I also wrote the draft and extension of this publication and hold an oral presentation during the conference.
6. K. Ikamas, J. Zdanevičius, L. Dundulis, S. Pralgauskaitė, A. Lisauskas, D. Čibiraitė, D. Voß, V. Krozer, and H. G. Roskos, "Quasi optical THz detectors in Si CMOS," in *2018 22nd International Microwave and Radar Conference (MIKON)*, 2018, pp. 719–721.
   - I have prepared the detector module for 65-mm detector technology chips and electrically characterized the detectors.
7. K. Ikamas, D. Cibiraite, M. Bauer, A. Lisauskas, V. Krozer, and H. G. Roskos, "Ultrabroadband Terahertz Detectors Based on CMOS Field-Effect Transistors with Integrated Antennas," in *2018 43rd International Conference on Infrared, Millimeter, and Terahertz Waves (IRMMW-THz)*, 2018, pp. 1–2.
   - I have prepared the optical setup for the experiment and conducted response experiments on the log-spiral antenna and Golay Cell detectors.

8. J. Zdanevicius, D. Cibiraite, K. Ikamas, M. Bauer, J. Matukas, A. Lisauskas, H. Richter, T. Hagelschuer, V. Krozer, H.-W. Hübers, and H. G. Roskos, “Field-Effect Transistor Based Detector for Measuring Power Fluctuations of 4.75-THz Quantum-Cascade Laser-Generated Radiation,” in *29th IEEE International Symposium on Space Terahertz Technology* at *NRAO database*, p. 3, 2018.
    - I have conducted noise and linearity measurements and analyzed data.
    - I have prepared the publication draft with the graphical representation of the experimental setup and measured data.
9. M. Wan, H. Yuan, D. Čibiraitė, J. J. Healy, H. G. Roskos, and J. T. Sheridan, „Terahertz Spectrum Detection Based on Interferometry“, in Proc. *Digital Holography and Three-Dimensional Imaging 2019*, 19–23 May 2019, Bordeaux, France.
    - I have designed and built in the missing parts for the experimental setup and conducted 1/3 of the experiment.
10. M. Wan, H. Yuan, D. Čibiraitė, D. Cassidy, A. Lisauskas, J. J. Healy, H. G. Roskos, V. Krozer, and J. T. Sheridan, "Terahertz quantitative metrology using 300 GHz in-line digital holography ", Proc. SPIE 11030, Holography: Advances and Modern Trends VI, 110300R (23 April 2019).
    - I have built the detector module and detection part of the experimental setup.
11. D. Cibiraite, M. Wan, A. Lisauskas, A. Rämer, S. Chevtchenko, W. Heinrich, H. G. Roskos, J. T. Sheridan, and V. Krozer, “TeraFET multi-pixel THz array for a confocal imaging system,” in *2019 44th International Conference on Infrared, Millimeter, and Terahertz Waves (IRMMW-THz)*, Paris, France, 2019, pp. 1–2.
    - I developed the multi-pixel array with a low-noise read-out circuit. I have built the electronic and automation parts of the experimental setup. I have conducted electrical and optical detector characterization and imaging experiments.
    - I have prepared the draft with the graphical representation of the experiment and measured data. I also extended the abstract and presented it at the conference.
12. A. Soltani, F. Kuschewski, M. Bonmann, A. Generalov, A. Vorobiev, F. Ludwig, M. Wiecha, D. Čibiraitė, F. Walla, S. C. Kehr, L. M. Eng, J. Stake, and H. G. Roskos, “Unveiling the plasma wave in the channel of graphene field-effect transistor,” in *2019 44th International Conference on Infrared, Millimeter, and Terahertz Waves (IRMMW-THz)*, Paris, France, 2019, pp. 1–1.
    - I prepared the experimental setup for electronic and optical detection of GFET signals. I was also responsible for GFET characterization and preparation for the s-SNOM experiment. I participated in the first two sessions of s-SNOM experiments in FELBE.
    - Later, I have consulted the co-authors on DC resistance measurement of GFET and stability issues to obtain trustful resistance data for the last sessions of the experimental study on carrier density waves in the GFET channel.

13. M. Wan, D. Čibiraitė, B. Li, H. Yuan, V. Krozer, H. Roskos, D. Wang, and J. T. Sheridan, "Polarization and sectioning characteristic of THz confocal microscopy," in *2019 44th International Conference on Infrared, Millimeter, and Terahertz Waves (IRMMW-THz)*, Paris, France, 2019, pp. 1–2.
    - I have prepared the mechanical part of the measurement setup and proofread the draft.
14. F. Meng, M. D. Thomson, B. Klug, D. Cibiraite, Q. ul-Islam, and H. G. Roskos, "Ultrastrong coupling of plasmonic metamaterials and photons in a terahertz photonic crystal cavity," in *2019 44th International Conference on Infrared, Millimeter, and Terahertz Waves (IRMMW-THz)*, Paris, France, 2019, pp. 1–2.
    - I have conducted spectroscopy experiments using the CW system and analyzed data to provide spectral information on metamaterial transmission characteristics.
15. D. Cibiraite-Lukenskiene, A. Lisauskas, K. Ikamas, P. Martín-Mateos, C. De Dios, P. Acedo, and V. Krozer, "Field-Effect Transistor-Based Detector for Hyperspectral THz Imaging," in *2020 23rd International Microwave and Radar Conference (MIKON)*, Warsaw, Poland, May. 2020 - Aug. 2020, pp. 300–304.
    - I have specified the necessary improvement for TeraFET and dual-comb systems to be able to merge them into one hyper-spectral imaging system.
    - I have implemented the detector module with a build-in low-noise amplifier and conducted detector characterization with and without the amplifier. I have built the optical measurement setup and developed imaging software.
    - I have analyzed the data, prepared the state-of-the-art table and graphical representation (except Fig. 3 (right)).
    - I have written and extended the paper and gave an oral presentation of the experiment during the conference.
16. D. Čibiraitė-Lukenskienė, K. Ikamas, T. Lisauskas, A. Rysiavets, V. Krozer, G. H. Roskos, and A. Lisauskas, "Completely Passive Room-Temperature Imaging Of Human Body Radiation Below 1 THz With Field-Effect Transistors," in *2020 45th International Conference on Infrared, Millimeter, and Terahertz Waves (IRMMW-THz)*, Buffalo, NY, the U.S., 2020, pp. 1–2.
    - I have prepared the detector module, the experimental setup, conducted the experiments and analyzed experimental data.
    - I have actively participated in theoretical calculations on thermal detector sensitivity. As there is no suitable experiment or prediction of the human palm emissivity at the THz range, I have overviewed the literature on skin emissivity in the range of interest and predicted an expected mean value for the conducted experiment.
    - I prepared the graphical representation and wrote the draft. I also extended it and gave an oral presentation.
17. M. Ferreras, D. Čibiraitė-Lukenskienė, A. Lisauskas, J. Grajal, and V. Krozer, "Substrate-illuminated THz antenna-coupled detectors in CMOS: analytical and experimental

comparison of various designs," in *2020 45th International Conference on Infrared, Millimeter, and Terahertz Waves (IRMMW-THz)*, Buffalo, NY, the U.S., 2020, pp. 1–2.

- I have prepared the readout circuit for the new detector array design and built the detector module for the experiment. I have prepared the experimental setup and led the NEP characterization experiments. I have measured the noise of the detector and characterized Toptica power.
- I have proofread the draft.

18. K. Ikamas, A. Solovjovas, D. Čibiraitė-Lukenskienė, V. Krozer, and A. Lisauskas, "Optical Performance Of Liquid Nitrogen Cooled Transistor-Based THz Detectors," in *2020 45th International Conference on Infrared, Millimeter, and Terahertz Waves (IRMMW-THz)*, Buffalo, NY, the U.S., 2020, pp. 1–2.
    - I have built a cryogenic measurement system and designed a cryogenic finger suitable for the temperature transfer from the cryostat to the detector. I also redesigned the detector module so that it fits the cryostat and holds the detector in the optical axis.

Acknowledgments

I would like to take the opportunity to thank all the people who have contributed to the success of this work conducted during the last four years:

My special thanks go to Prof. Viktor Krozer for the research and networking opportunities, which I got during the ITN CELTA project and for the unprecedented support and freedom. This situation enabled me to grow as a scientist, develop my work organization and soft skills as well as self-confidence. Thank you for the tips that helped me to overcome the main obstacles I had during the last four years. Likewise, I would like to thank my supervisor Prof. Alvydas Lisauskas, with whom I have closely worked for many years. Thank you for your scientific ideas, valuable discussions with constant energy and curiosity, which led to the fast development of my scientific skills as well as our research topic.

For the professional support and opportunities of intergroup collaboration, I thank Prof. H.G. Roskos. I would also like to thank Prof. W. Heinrich, Prof. P. Acedo, Prof. J. Sheridan, Prof. J. Matukas, Prof. H.-W. Hübers, Prof. J. Stake, Prof. J. Grajal, and J. Mangeney for the fruitful collaboration with their groups that led to a wide range of applications explored during the recent years that is unusual for a Ph.D. thesis. I would like to acknowledge the HORIZON2020 Program for the funding of the ITN CELTA project where I had the opportunity to deepen my knowledge and skills in the international environment during the Summer Schools, secondments, conferences, and other informal activities within the project network.

For the valuable discussions and experiments as well as the time together, I would like to thank my colleagues from a joint AG Rokos/Krozer group: Maris, Robert, Freddy, Hui, Daniel, David, Florian, Matthias, Marie, and all others. Big thanks go to Ms. Sanchez-Maroto and Ms. Jordan, as well as electronics and mechanics workshops, as your contribution to this work cannot be assessed.

For the friendship and the necessary support during the Ph.D., and especially its last months, I would like to thank my husband Adomas, “my German family”, my friends Toma, Irma, Anželika, Darius and Kirsten, also “brothers and sisters of the same fate” Justinas, Robert, Marie, Marta, and of course Christine, Vanessa, and Marius, who were “the Three Musketeers” for me during the Ph.D.!

Finally, my greatest thanks go to my family, especially my mother, who has given me unlimited support from my early years and provided a broad spectrum of education. She rose my love for science and world exploration. I would like to specially acknowledge my teachers from my little hometown, called Švenčionėliai, who made a major influence on my personality during high school time. Especially, my physics teachers T. Sansevičienė and M. Jusienė for showing me how challenging and interesting physics can be. The last thanks go to my Alma Mater - Vilnius University for the knowledge, personal growth, and people I met during the six years.

Contents

1. Introduction to THz detectors

1.1 Introduction to THz applications

Terahertz (THz) radiation range is between the infrared (IR) and millimeter-wave. It is the range where electronics and photonics fields merge [1]. Until now, it has not been well defined what is the exact frequency range for THz radiation. Usually, it depends on the author's preferences for the lower and upper limits [2–4]. In this work, the lower part of THz radiation range of the 0.1 – 5 THz frequency range is considered where the focus is on the frequency range – between 0.1 and 2.5 THz (later also called low THz).

This year's Nobel Prize in Physics was given for the discovery of a supermassive object at our galaxy's center [5]. A key result of the research was the image of the shadow of a black hole which was not possible to obtain without the biggest telescope array in the world – ALMA (the Atacama Large Millimeter/submillimeter Array) which works in various bands from 31 GHz up to 950 GHz frequency and assures high-fidelity imaging. However, radio astronomy applications have a long history dating from 1932 when the radiation from our galaxy was observed for the first time by Karl Jansky [6]. The development of radio astronomy was assured using Schottky diode technology described by Schottky and Spenke in 1939 [7] which extended the operating range to shorter wavelengths. Later, there were many other cooled supersensitive photon (or quantum) detectors developed [7–9] for radio astronomy applications reaching the sensitivities in the attowatt scale [9, 10]. However, this work focuses on less sensitive, but technologically more favorable room-temperature detectors.

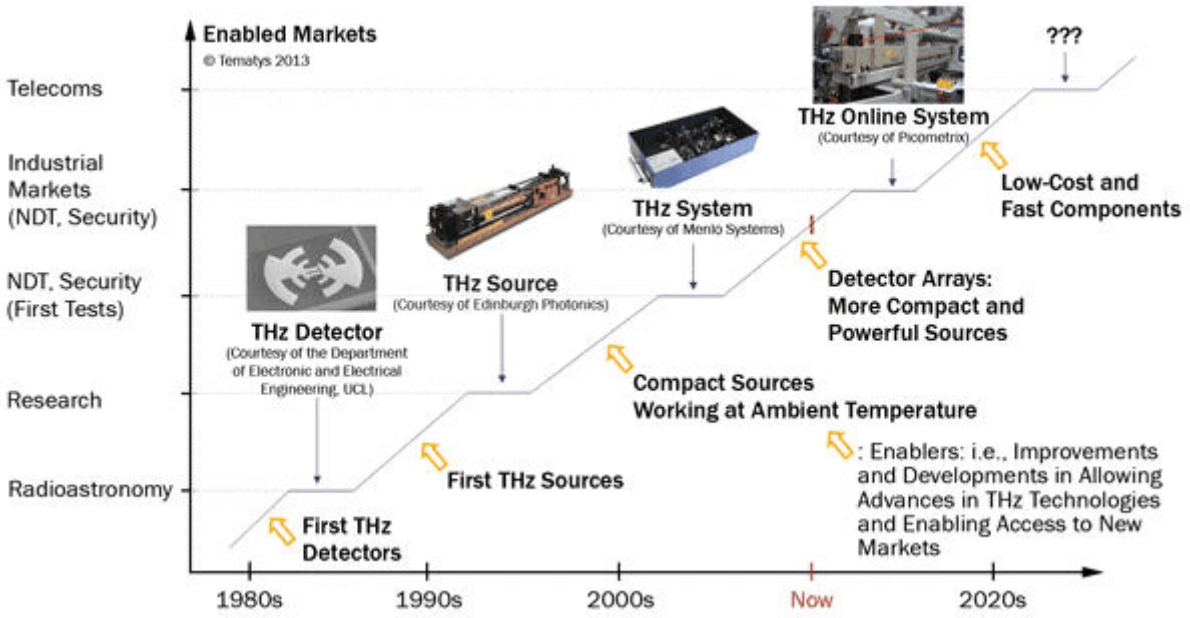

Fig. 1.1. Development of THz elements and systems. The graph was reused from [11] ©2020 Photonics Media.

From room-temperature detectors, the well-known Schottky diode technology has the longest development history as it is one of the first THz detectors developed in the 1980s as shown in Fig. 1.1. This development opened new perspectives for radio astronomy as well as other research fields. Later, photonic systems were introduced for THz detection which had also an impact on a new field of applications [4, 12] depicted in Fig. 1.2, such as research, security, or telecommunications. With the further development of THz sources and detectors, new application fields occurred, such as security screening, robotic vision, art conservation, or quality control, etc. This seems to be only the beginning of the list for the possible future applications which are defined under the exploration of future technologies [10].

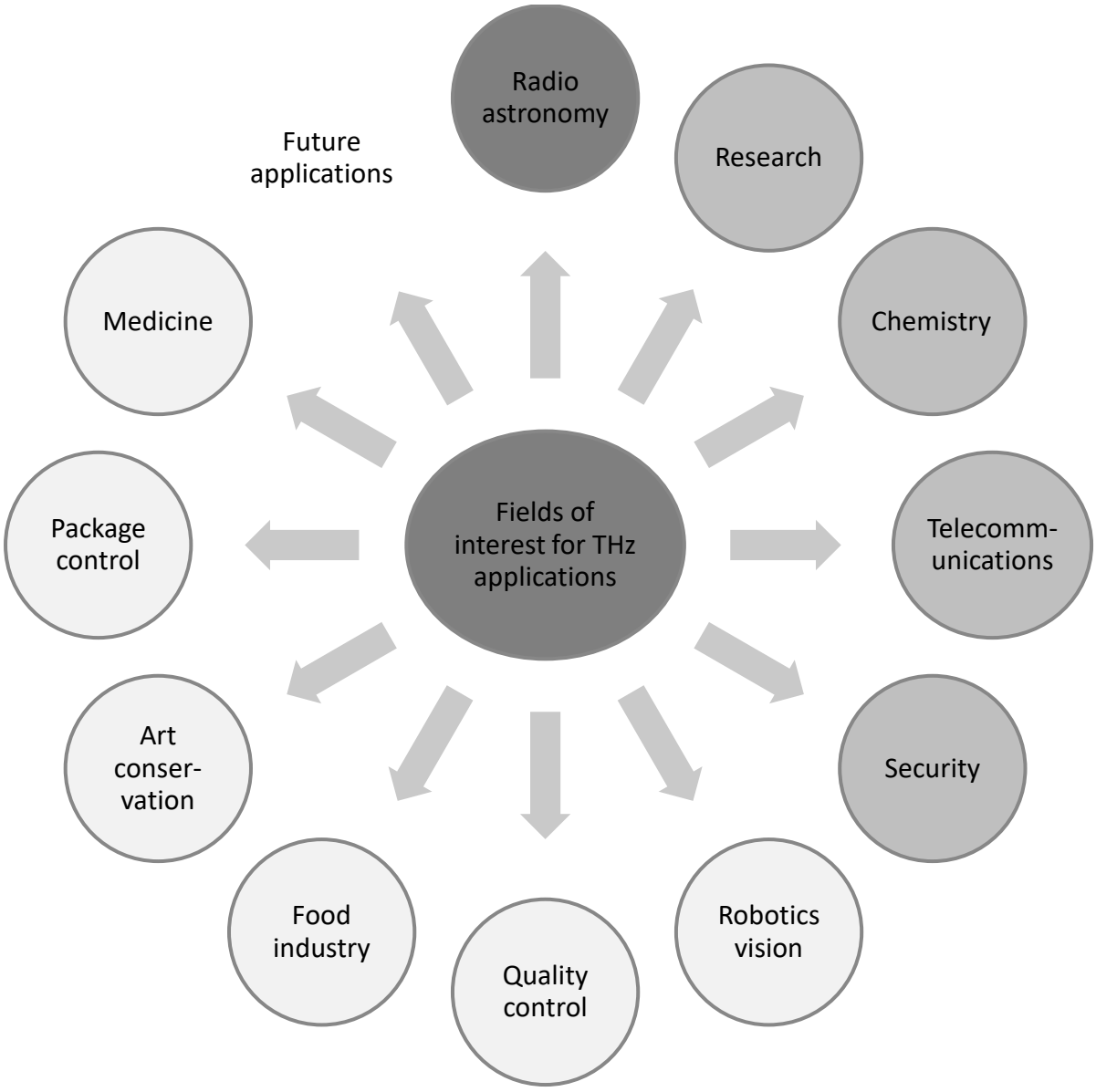

Fig. 1.2. Fields of interest for THz applications and their development in time.

For the generation of THz radiation in the aforementioned lower THz frequency range, various THz sources can be used, such as electronic [13] or optoelectronic [14] emitters, semiconductor [15] or molecular gas lasers [16], for high-power generation also gyrotrons [17] and free-electron lasers (FELs) [18]. The useful detectors for specific applications depending on the power level and frequency of the generated signal. Nowadays, a wide range of thermal [19–22], electronic [23, 24], as well as optoelectronic [14] detectors is available. However, for practical room-temperature applications, the limitation of the dynamic range close to the THz gap is still an issue. High room-temperature sensitivity, as well as short detector response time at low cost, is a desirable combination of the features for THz detectors [1, 15]. In this work, we propose field-effect transistor-based THz detectors with integrated antennae (TeraFETs) which serve as THz detectors meeting the mentioned requirements.

1.2 Present TeraFET development stage

The most common detector technology up to now in the lower THz range is the Schottky barrier diode-based solution [23, 24]. However, the performance of these detectors is limited due to the parasitic effects, high shot noise in biased operation condition, or 1/f noise [24–26]. For now, the frequencies above 1 THz are usually covered by bulky cryogenic systems used in bolometer detection [10]. For this reason, it is convenient to explore other promising room-temperature technologies for the frequencies in the less-explored THz gap region.

The TeraFET as THz detector concept is fairly new, as it was first suggested by Dyakonov and Shur in the 1990s [27]. According to Dyakonov and Shur's theory, the TeraFETs can exploit plasma-wave mixing [28] extending the available detection bandwidth above the cut-off frequency of a transistor. The actual operation frequency can be defined by the design of the integrated antenna. The cut-off frequency of the TeraFET is described as a reciprocal to a time interval which is equal to antenna resistance multiplied by parasitic capacitance. However, due to plasma (or carrier density) wave mixing, the detection bandwidth can be extended to even higher frequencies [29].

Opposite to the coherent detectors which are limited by the quantum noise, the incoherent detection is limited by the background noise [10]. However, the simplicity and possibility of the production of large-format arrays is a big advantage for room-temperature operation. Even though the TeraFETs work as rectifying detectors [28], they can also be used for real-time thermal radiation detection. This feature for the detection of human-body radiation is presented in this work for the first time. Thermal as well as rectifying state-of-the-art power detectors are presented in Table 1.1 and Fig. 1.3.

Table 1.1 presents the most sensitive detectors for the room-temperature operation which could be found to be characterized for optical NEP (see section 3.2 State-of-the-art THz detectors for other characterization methods). The table is subdivided into thermal and

electronic detectors and sorted along ascending optical NEP values. As it can be seen, the most sensitive thermal detectors are above 1 THz, whereas electronic detectors reach the highest sensitivity in the sub-THz range. The references in bold show the published author's work. All CMOS and AlGaN/GaN FET-based detectors, presented in the table, show the best sensitivity in all targeted frequency ranges reaching the performance of commercial Schottky diode-based THz detectors.

Table 1.1. State-of-the-art THz detectors up to 5 THz for room-temperature operation.

Type/Technology	Frequency [THz]	Optical NEP [pW/√Hz]	Reference
Thermal			
a-Si µBolometer	2.5	6	[30][a]
Vox µBolometer	2.54, 4.25	16.5, 14.4	[20][a]
Nb5N6 µBolometer	0.24	30.8h	[31]
Golay cell	140	100 – 1000	[22][a]
YBCO µBolometer	0.4	200 @ 0.5 mA	[32]
Pyroelectric	<20	440	[21][a]
Pyroelectric	0.1-3	1.40E+05	[19][a]
Thomas Keating	0.03 – 3+	5.00E+06	[33][a]
Electronic			
SBDs	0.1 – 1	7 – 100	[34][a]
SBDs	0.06-0.09, 0.09-0.14, 0.14-0.22, 0.22-0.33, 0.33-0.5, 0.5-0.75, 0.75-1.1, 1.1-1.7	9.5, 11, 11, 12, 7.2, 11.4, 15.2, 113.7	[23][a]
90-nm CMOS	0.3	19	**[35, 36]**[b]
AlGaN/GaN HEMT	0.5– 0.6	25–31	**[37]**[b]
65-nm CMOS	1, 0.84 – 1.29;	25, <50;	**[38]**[b]
AlGaN/GaN HEMT	0.7– 0.9	30 – 50	[39]
90-nm CMOS	0.6 – 1.5	48 – 70	**[40]**[b]
InGaAs SBD	0.25	106.6	[41]
GFET	0.4	130	[42]
GFET	0.6	515	[43]
HBD	0.6-1	850 @ 0.7 THz	[44]

[a] Commercially available
[b] This work

Fig. 1.3 visually presents detectors from Table 1.1 and their optical NEP. The least sensitive are the thermal detectors, such as Thomas Keating [33] or Golay cell [22], however, they provide the biggest aperture for radiation coupling from single-pixel devices. More sensitive solutions, with the antenna aperture comparable to the focused beam spot size, are based on quasi-optical detectors with a substrate lens that account for microbolometer [20, 30, 31], TeraFET [29, 36, 45], and Schottky-diode [23, 34] technologies. The last and the most sensitive detectors are based on Schottky-diodes coupled using waveguides. This type of radiation coupling is the most efficient, however, the bandwidth is limited by the bandwidth of the waveguide. The dash-dot line in Fig. 1.3 connects the optical NEP values provided by the manufacturer [23] at corresponding waveguide frequency ranges.

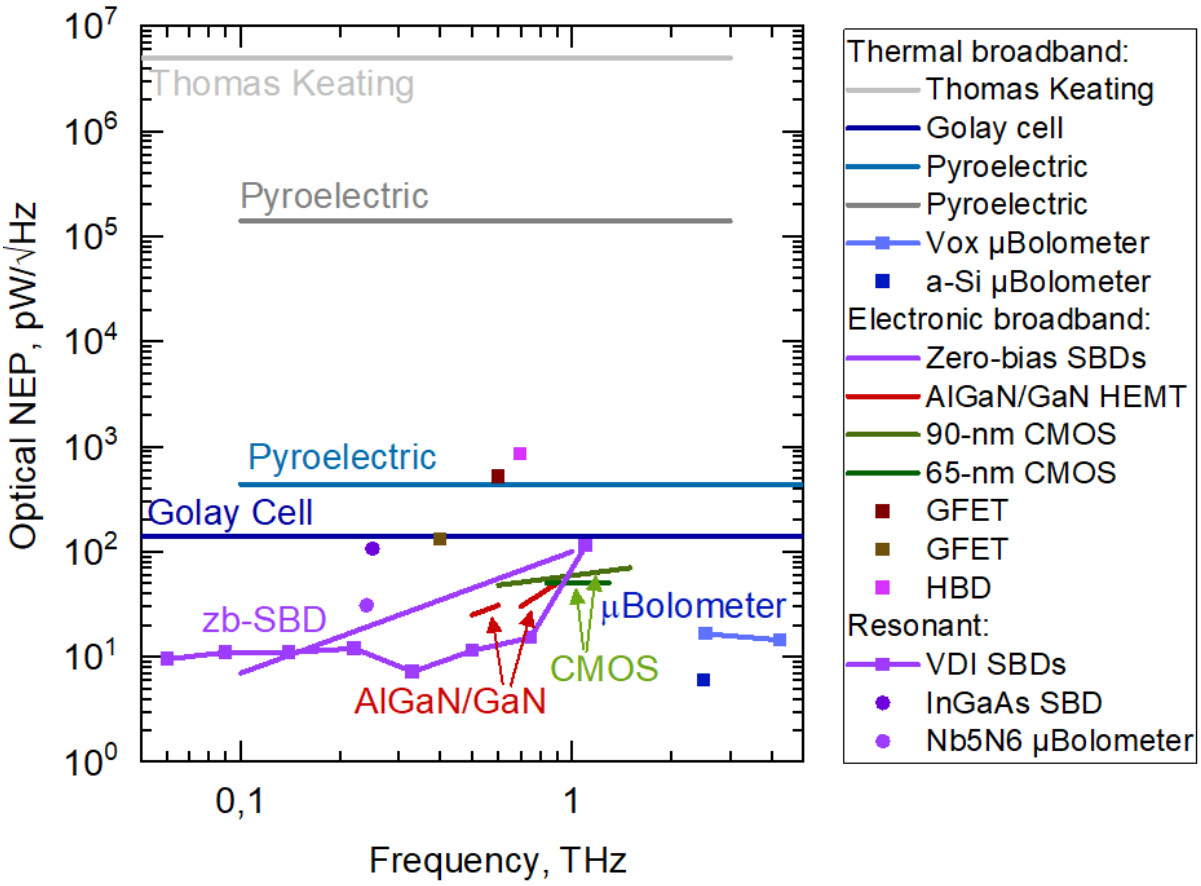

Fig. 1.3. Room-temperature state-of-the-art detectors based on thermal and rectifying technologies.

This work focuses on the quasi-optical devices with the radiation coupling using hyper-hemispherical silicon lens as this radiation coupling option is most promising to be implemented for the camera operation, whereas the waveguide coupling method is bulky and needs a better fabrication precision for higher frequencies. A few years ago, FET technology-based detectors were a few times less sensitive than the Schottky diode-based detectors which are the best quasi-optical detectors up to now [24, 26]. Therefore, this work

aimed to reach the performance of the TeraFETs comparable to Schottky diode-based THz detectors (as shown in Fig. 1.3) and explore the possible range of the TeraFET application field.

This work shows that TeraFETs can be used for various applications, such as spectroscopy [15, 35, 38, 40, 46, 47], imaging [35, 37, 48], technical vision [15, 18, 35, 37, 47] as well as research-related applications [18, 47, 49]. The intended aim of this work was to explore and present the direct detection schemes. Where the benefits on the detector performance using heterodyne detection [50] as well as cryogenic cooling [51] are open for future work.

1.3 Aim and structure of the thesis

This work is structured in such a way that it answers the main scientific questions relevant for the development of TeraFET devices:

- Is the choice of FET technology important for the TeraFET performance?
- What is the best way to define the TeraFET performance?
- Is it enough to assume the thermal noise to be the limiting aspect of the sensitivity for the practical devices?
- What are the possible TeraFET applications?

Detailed investigation of these questions leads to the proof of the hypothesis of this work:

TeraFET sensitivity can reach the room-temperature performance necessary for passive imaging of human-body radiation.

To answer the main questions and show the results on the experimental proof of the hypothesis, this work is structured in the following way. Firstly, various THz detectors and systems are overviewed. Secondly, the main work principle of a TeraFET is presented. Thirdly, device characterization procedure and challenges are discussed. Fourthly, the TeraFET applications are demonstrated, which were conducted during the last four years. Lastly, the proof of concept for the passive room-temperature imaging of the human body THz radiation using TeraFETs is shown.

The detailed theory on field-effect transistor-based THz detection has been presented in [45]. Therefore, the focus of this work is on the choice of the technology and in-depth characterization methodology which is still under development for quasi-optical devices. Therefore, an improved quasi-optical detector characterization method for trustful NEP comparison is offered in this work. And a wide range of various TeraFET applications in their early testing stage is presented.

From various applications of TeraFET detectors presented in this work, the focus is on spectroscopy and imaging applications. The spectroscopy can be conducted with various THz sources in continuous wave (CW) and time-domain (TD) modes. Therefore, femtosecond

lasers, electronic and optoelectronic CW systems, as well as free-electro laser (FEL), or a quantum-cascade laser (QCL) can be used providing a wide spectral range for future applications. The broadband detection using TD and CW systems, as well as a possibility for narrowband spectroscopy application, is shown together with the characterization technique of metamaterials which is possible to be conducted using TeraFETs.

Later, the visualization of objects and plasma wave phenomena are shown. First, the plasma wave in a FET channel is demonstrated. It provides fundamental knowledge about the plasmon-polariton interaction in the FET channel. Second, a reconfigurable array is presented which can be used for the reconfigurable aperture option in the laboratory and imaging applications and practical application of THz source imaging is shown. Third, single-pixel in-depth photography on a mobile phone is demonstrated opening the practical applications for security screening and industrial quality control.

In the last two sections of this work, the two most promising applications are detailed. The first achievement is the simultaneous hyperspectral imaging demonstrated using dual-frequency comb-based THz source and a FET-based THz detector specially developed for the used THz source. The second achievement is the passive THz imaging of human-hand radiation. To the author's knowledge, these two applications are presented for the first time for room-temperature TeraFET operation.

2. THz systems aspects

2.1 THz sources

For the mentioned imaging and spectroscopy applications, THz radiation is generated by various THz sources. For imaging applications, the most important parameter of a THz source is the output power, while spectroscopic systems need high output power as well as wide bandwidth and frequency resolution. Due to insufficient detection sensitivity, up until now, all the applications are based on the active THz sources. However, this work aims for the TeraFET imaging using black-body or even human-body radiation as a passive THz source. This idea and the active THz sources are presented in this section.

Taking into account the applications where the active THz sources are used, it is worth to mention, a time-domain system (TDS) assuring a wide frequency bandwidth with the resolution of a few GHz of a pulsed signal [52]. Photoconductive antenna concept-based systems [14], can work in both modes (pulsed and CW) reaching 1 GHz resolution, but at lower output power. Higher power CW sources are usually based on electronic solutions [53] for lower THz frequencies and QCL sources for higher THz frequencies. However, bandwidth and tunability might be of an issue to employ these THz sources for wide bandwidth spectroscopy.

2.1.1 Passive THz sources

2.1.1.1 Blackbody

Before going into the details of active THz sources, it is worth looking at the natural radiation sources. Every black body of temperature *T* radiates electromagnetic radiation in a wide spectral range with the radiation maximum at $\lambda_{max} = 2.898 \cdot 10^{-3}/T$ m. Therefore, hot black bodies radiate much higher spectral power in the IR range whereas the maximum of the radiation power of colder black bodies shifts towards the sub-THz frequency. Therefore, one of the passive imaging applications in the sub-THz and THz range is used for observation of cold universe background.

Spectral radiance $L(f,T)$ of such a black body can be defined using the Planck's law:

$$L(f,T) = \frac{2hf^3}{c^2}\frac{1}{e^{\frac{hf}{k_B T}} - 1}$$

where h is Plank's constant, c – light velocity, k_B – Boltzmann's constant. The spectral radiance for five common temperatures is depicted in Fig. 2.1 (a). It shows indoor and outdoor background compared to human palm, 400 K temperature radiator used in [54] and 773.15 K radiator used in [55], both for the detection with TeraFETs. The calculated power spectral density focused on the antenna is depicted in Fig. 2.1 (b). The power spectral density

is flat over a very wide frequency range. Therefore, the radiation can be only detected using an ultra-broadband and highly sensitive detector which must be more sensitive than the integrated power over the detector's bandwidth. If 1 THz bandwidth of an antenna coupled detector is assumed, 773.15 K black body radiates 10 nW, 400 K – 5 nW, and human palm – 3.9 nW power (see Fig. 2.1, b) into the detector. To detect this radiation, one possibility is to use a cooled background. However, this work is focused on exploration of passive room-temperature detection limits of temperature difference between two black bodies where room temperature radiates 3.77 nW in 1 THz bandwidth. This means that the detection of human palm radiation without accounting for palm emissivity is possible only with a detector reaching constant NEP of the detector over the frequency range up to 1 THz with sensitivity sufficient for detection of the 130-pW power difference.

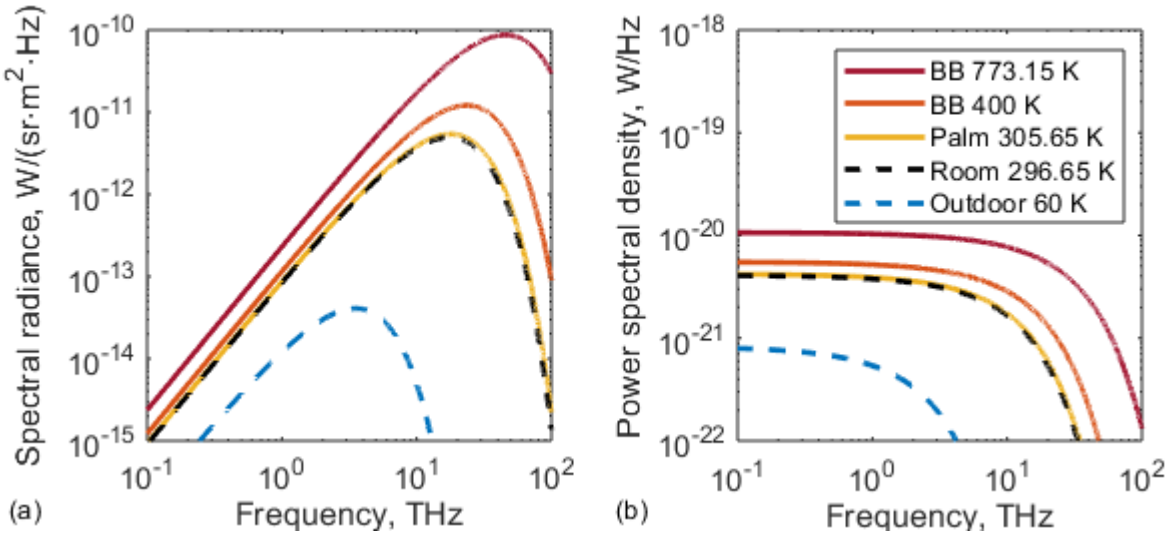

Fig. 2.1. (a) Spectral radiance of various black body radiators: 773 K [55] and 400 K [54] black bodies, 306 K temperature palm, laboratory (room of 297 K) background radiance, as well as outdoor background radiance of around 60 K [56]. (b) Power spectral density of analogous radiators. Author's work, reprinted from MDPI Sensors [48] under © CC BY 4.0.

2.1.1.2 Human body radiation

Human skin can be assumed to be a gray body, which means that the emissivity of the skin is not equal to 1. It is well known that the skin emissivity in the IR range is around 0.97 - 0.99 [57]. However, until now there is not so much research done on the emissivity of human skin, as well as palm, in the low THz range. Therefore, this section overviews the main studies on human palm emissivity up to date.

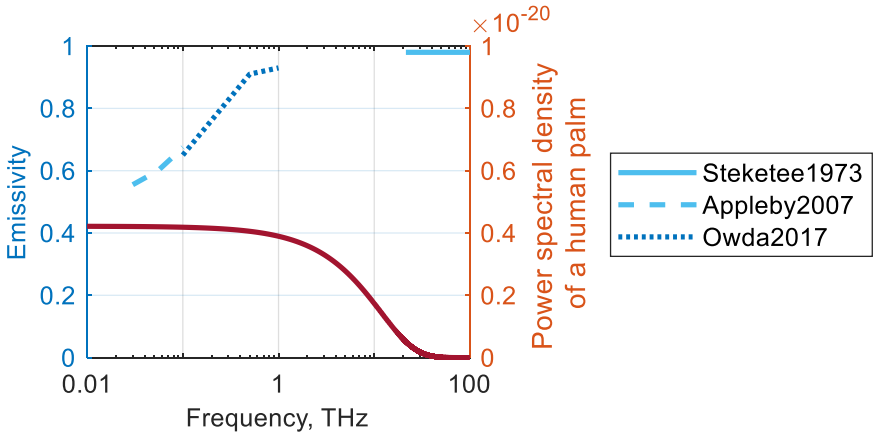

Fig. 2.2. Reported human palm/skin emissivity (various lines) and human palm power density (solid line).

At lower THz frequencies (0.3 – 300 GHz) the human skin emissivity rises from 0.4 to 0.8 [58]. This behavior was related to the fall of water dielectric permittivity. A follow-up publication describing 90 GHz human skin emissivity measured with calibrated radiometer on 60 healthy participants [59] (36 male and 24 female) shows the quantitative variations of the skin emissivity between individuals as well as gender and locations they come from, or even body mass index. The mean emissivity of the male palms was 0.451 with a standard deviation of 0.0997. Female palm emissivity was measured to be 0.430 and a standard deviation of 0.0951. According to the research, the emissivity is higher at higher body mass index and thicker skin. Another study [60] shows a higher emission of the human palm skin at around 0.5 THz under mental and physiological activity compared to the rest state. Appleby [61] reports three values for emissivity at 0.1 THz, 0.5 THz, and 1 THz. The summary of published values is depicted in Fig. 2.2. A slight mismatch between the data points of various authors may occur due to differences in human skin emissivity in various body locations [59], as well as different measurement techniques [57]. However, the emissivity studies above 1 THz are still missing.

To detect the black body or even human body radiation, one has to consider the extension of the detection bandwidth, cooling of the detector, reduction of possible noise sources, and effective implementation of the optical setup. Successful detection of human-body radiation using a TeraFET is the main goal of this work.

2.1.2 Active THz sources

2.1.2.1 Electronic CW source

Electronic sources include electronic oscillators (such as Schottky or IMPATT diodes), power amplifiers with a frequency multiplier (so-called amplifier/multiplier chain (AMC)), and transmitters. These elements deliver the oscillating frequency up to 200 GHz which must be

amplified in order to increase the radiation frequency even further. Such solutions can reach up to 1 THz frequency with 1 mW output power and around 10 % tunable bandwidth around the central frequency [13, 62]. Higher frequency solutions are already commercially available, however, with much lower power and only at discrete frequency ranges [13].

This type of THz source is comparably powerful as they provide around 200 mW output power around 0.1 THz [62] and 0.05 mW power at around 1 THz [13] in tunable operation. The output power for a fixed frequency might be even higher. However, the tunable frequency range for some spectroscopy applications might be too narrow and the users might need multiple sources for different frequency ranges.

2.1.2.2 Quantum Cascade Laser (QCL)

For high-sensitivity high-resolution spectroscopy measurements, a quantum cascade laser (QCL) can be employed [63, 64]. QCL is a sandwiched semiconductor structure with formed quantum wells inside the structure. Photon emission occurs between electron subbands.

QCLs can provide 1 – 100 mW power in the range of approx. 2 -10 THz, however, the higher output power tends to be at the higher THz frequencies [4]. They are very fast devices and can be used in gas spectroscopy due to the wide tunability and high precision of the emitted radiation frequency.

2.1.2.3 Femtosecond laser

Laser is a coherent radiation source that can be used for the generation of fs THz pulses. For example, the bandwidth of the 15-fs THz pulse excited with an interdigitated photoconductive antenna can reach 20 THz where the spectra maximum is at few THz [65]. The signal-to-noise ratio (SNR) can reach 105 [46] of such a THz source. The system can be used for simultaneous wide frequency detection, however with lower resolution than other THz sources.

In our experiments, we used a Ti:sapphire laser generating 15-47 fs IR pulses with a pulse energy of around 4 nJ. The pulse was used to generate THz radiation via interdigitated photoconductive antenna. More details about the pulsed system used in this work can be found in [46].

2.1.2.4 Dual-comb system

THz frequency comb systems are based on telecom lasers (or other CW radiation sources) and non-linear elements with an antenna [66]. A narrow-linewidth diode laser, strongly driven phase modulators, and electro-optical modulators are employed for master optical frequency comb generation, phase coherence, and exact line separation by modulation frequency of the optical comb teeth. The chosen lines are filtered out and mixed. The

difference between any two lines corresponds to the wanted THz beat frequency which is mixed in a nonlinear element and radiated into the air.

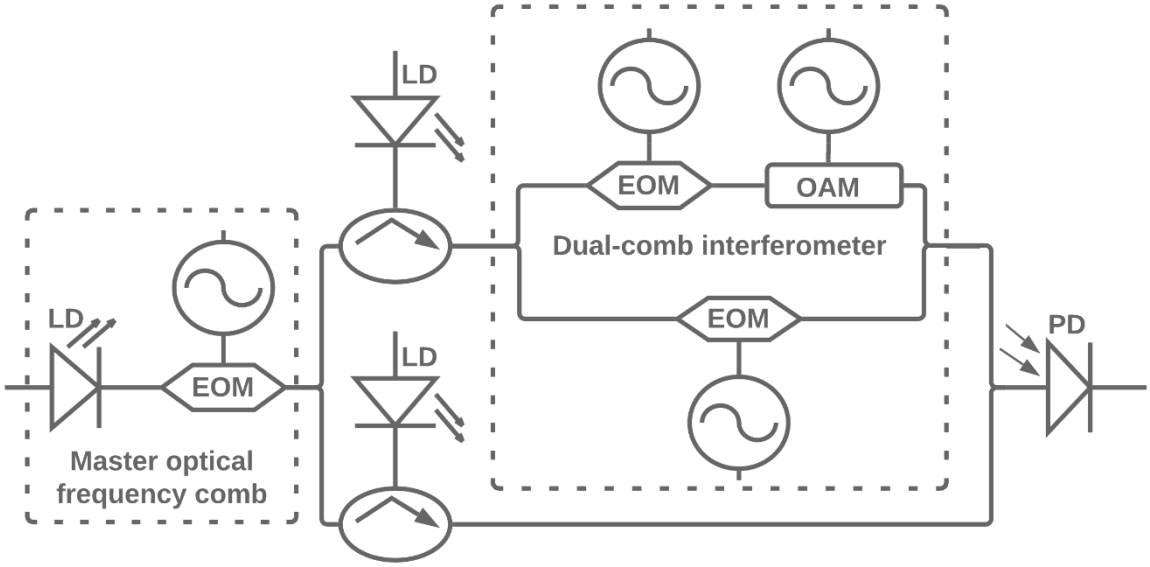

Fig. 2.3. THz frequency comb schematics.

Such systems are of very high precision due to very low phase noise and extremely high resolution reaching the separation of a few kilohertz between THz lines. The lines can be tuned shifting the laser lines. The signal power per comb tooth gets lower when more lines and/or wider spectrum are generated.

In collaboration with UC3M, a THz frequency comb system was extended up to 300 GHz. Due to the very high sensitivity and fast response of a TeraFET, hyperspectral imaging is possible. The first experiment with the THz frequency comb and a TeraFET system is presented in the last chapter of the thesis.

2.2 THz detector technologies

This chapter overviews the main IR and THz technologies used for the detection of THz radiation. The brief descriptions of the technologies give useful information for the following chapters, where more details about most of the described technologies can be found in [67].

In general, there are two direct detection methods: thermal and electronic detection. Thermal detection is involved in photoacoustic detectors, such as Golay Cell and pyroelectric detectors, as well as bolometers and microbolometers. Schottky barrier diodes, photoconductors, radiometers, and field-effect transistor-based detectors can be defined as electronic THz detectors. The differences between these technologies are overviewed in this section.

2.2.1 Thermal detectors

The development of thermal radiation detection in the THz range comes from the know-how or even the same technology of thermal detection in the IR frequency range. Thermal detectors usually have an aperture in the range of few or tens of centimeters. They respond to the power change of the incident radiation in seconds or few milliseconds. They are power detectors and should be usually optically or electrically chopped to obtain the difference between ON/OFF radiation.

2.2.1.1 Photoacoustic detectors

The two main detectors using the photoacoustic principle in IR and THz range are Thomas Keating power meter [33] and Golay Cell [22]. Both are based on a gas-filled chamber where thermal expansion of the gas under incident radiation takes place. Thomas Keating measures the expansion with a pressure sensor where the Golay Cell measures the expansion of the gas membrane with a photodiode.

Photoacoustic detectors are broadband, detecting IR-THz radiation from 0.1 THz up to 20 THz. They are suitable for power calibration or monitoring of slow power changes, as they have a comparably big aperture and wide operation range. One of the limitations for these detectors is the detectable power range which is from 100 nW to a few mW for Golay Cell. Whereas Thomas Keating needs an even higher incident radiation power.

Since photoacoustic detectors depend on the thermal processes, the THz signal should be chopped at the rate of a few tens of Hz which is a slow modulation rate in comparison with other detector technologies.

2.2.1.2 Bolometers and microbolometers

Bolometers and microbolometers detect thermal radiation due to a change of electrical resistance. They can be also called (IR) radiometers and should not be mixed up with the mm-wave radiometers which are presented later.

The bolometers are extremely sensitive detectors but they need a bulky cryogenic cooling system whereas microbolometers are less sensitive room-temperature detectors but extremely small and therefore are often used for IR cameras [9, 20, 68]. The main materials for microbolometers are amorphous Silicon and vanadium oxide.

Although microbolometers are based on a thermal process, they are much faster and more sensitive than photoacoustic power meters. However, for the microbolometer technology itself, there is a trade-off between the sensitivity and the detection speed [69]. The microbolometers are suitable for the detection of frequencies from few THz going as low as hundreds of GHz [20, 69].

2.2.1.3 Pyroelectric detector

Polar crystals (e.g., Lithium tantalate) can be used for broadband IR, MM-wave, or THz detection due to a pyroelectric effect. The crystal tries to compensate for the net polarization change caused by the applied electromagnetic field where the potential difference is induced along the crystal.

Pyroelectric detectors [21, 70, 71] can measure from 100 nW to a few mW of mean power and need a slow modulation frequency of a few Hz. The usual aperture size is from a few mm. They are suitable for the pyroelectric arrays which can be used for beam profiling down to 1 THz with a pixel pitch of 80 µm.

2.2.2 Electronic detectors

All electronic detectors can be optically coupled to the device using a lens or a waveguide. There are few types of electronic systems used for THz detection: mm-wave radiometers, photoconductors, Schottky detectors, and field-effect transistors.

2.2.2.1 Millimeter-wave (mm-wave) radiometers

A radiometer is usually an IR or UV radiant flux measuring device, therefore here the radiometers working below the classical cut-off frequency, namely mm-wave radiometers, are described. The main concept is based on the radiation coupling through the horn antenna and amplification of the THz signal before the transfer to a rectifying element. They have the best performance below 0.5 THz, where the sensitivity of the diodes and preamplifiers' gain has the best performance. However, these parameters drop drastically at higher frequencies. These devices are developed based on mm-wave technologies and reach the lower THz frequency limit.

There are two mm-wave radiometer configurations for direct detection mode: total power and Dicke radiometers. The received power over the whole receiver bandwidth is integrated and the total received power is measured with total power radiometers. The Dicke receiver switches between the incoming signal and the reference resistor, each half of the integration period. This technique makes the radiometer less sensitive to various instrumental drifts [56].

For decades, the mm-wave radiometer technology has been developed and reached an impressive sensitivity. A state-of-the-art NEP level for W-band (75 - 100 GHz) reaches 10 fW/√Hz [72] or even to 0.28 fW/√Hz [73] for a super-pixel design. The performance of the radiometer can be further improved by implementing a heterodyne detection scheme.

As well as IR radiometer, the mm-wave radiometers can detect thermal radiation but usually in W-band and have a relatively narrow bandwidth of 5-40 GHz. They are used for human body radiation imaging, security imaging, technical vision, such as cars or airplanes, remote atmosphere sensing, and radio astronomy.

2.2.2.2 Photoconductors

Photoconductor technology is based on a highly resistive direct semiconductor which is usually an III/V group material. A photon with energy larger than the energy gap of a semiconductor is coupled through an antenna into a photoconductor. The absorbed photon energy creates an electron-hole pair which makes the semiconductor conductive for a short period. The free carriers move along the semiconductor to opposite directions along the applied electric field and create a photocurrent. To avoid radiative recombination, defects should be implanted into the semiconductor as they reduce the carrier lifetime to less than 1 ps.

The photoconductive antenna can be used as a THz receiver, as well as a THz transmitter. Detection is sensitive to the amplitude and phase of the electric field and can be obtained by modulating the applied voltage between the antenna electrodes. Such a kind of detector is a coherent detector. It can be used for spectroscopy applications where the information of amplitude and phase is needed.

2.2.2.3 Schottky detectors

Schottky barrier diode work principle is based on a potential energy barrier between a metal and a semiconductor which has a parabolic shape of the band edges in junction proximity. The difference between the Fermi level and the conduction band edge for n-type semiconductor (and valence band edge for p-type) is called the Schottky barrier. A part of electrons cannot cross the barrier without an external field applied along the barrier, namely those which cannot tunnel through the barrier and do not have enough energy to cross the barrier.

The detectors are usually based on high-frequency electronics technologies, such as InP, SiGe, or GaAs, and can reach sensitivities down to 5-10 pW/√Hz [24, 26, 74] for quasi-static detectors where radiation is coupled through a high-resistivity silicon lens, or even less, if the radiation is coupled via narrower frequency band horn antenna [26]. The response time is measured to be less than 25 ps [26]. These detectors show the detection up to 5 THz or even higher frequencies [75, 76].

Schottky diodes can be employed for THz generation as well as direct and heterodyne detection, or signal mixing. They are highly sensitive and can work either at room or at cryogenic temperature providing a quick response time. However, the noise limits the performance, as Schottky diodes must be modulated with high-frequency modulation to avoid high $1/f$ (flicker) noise and have shot noise additionally to the thermal noise. Cooling these devices is, therefore, a useful method to decrease the noise level.

2.2.2.4 TeraFET

There are three operation modes for FET-based THz detection [28]: resistive mixing, distributed resistive mixing, and plasma (carrier density) wave mixing which enable TeraFET detection up to 4.3 THz and higher frequencies [28, 29]. The frequency response of the detector depends on the chosen antenna and impedance matching.

The reason for resistive mixing is the kinetic inductivity of free carriers under the applied THz field. This is due to retardation meaning that the applied field changes faster than the electrons can respond to the change. For even higher frequencies, the plasmonic mixing regime can be exploited. For this, one has to create an antenna, coupling the radiation into the transistor channel, and make the coupling conditions asymmetric, as the asymmetry creates an electric field gradient resulting in the induced current.

The main technologies used for TeraFET are based on III/V group materials such as GaN and GaAs, as well as commercially available CMOS technology or even the novel materials, such as graphene. All three groups of FET technologies are briefly discussed in this work.

The major advantage of transistor-based detectors is the possibility to use a close-to-zero current for detection with a high dynamic range. Whereas, diodes need either some voltage and/or have considerable leakage current. The low 1/f noise in FETs enables the use of TeraFETs for the THz power monitoring in real-time. Due to the wide possible detection range, they can be used for spectroscopy applications using a tunable THz source or an autocorrelation technique in time-domain spectroscopy (TDS) system, or dual-frequency comb-based THz source. As their response time is much faster than of the thermal detectors, they can be modulated at high frequency which is usually limited by the readout circuit. The noise of TeraFETs is limited mainly by the thermal noise [77], therefore, they can be also used for DC detection.

The reproducibility of TeraFETs in CMOS technology and the small pixel size makes TeraFET technology suitable for multi-pixel arrays. Therefore, the TeraFET is a comprehensive technology for the future mobile THz cameras below 2 THz at the frequency range where microbolometers are less sensitive. Uncooled TeraFETs report the broadband optical (optical losses excluded) NEP around 25 pW/√Hz [37, 40], and below [35] 20 pW/√Hz for the resonant detector design which is much better than the widely used thermal Golay Cell detector. The enhanced detection can be reached via cooling and heterodyning techniques.

2.2.3 Multi-pixel array

Described detectors are single-pixel detectors and find their applications in all the possible fields. However, imaging applications, security screening, fast scanning, or beam steering applications need a higher number of pixels, either distributed along a line or a plane. Such configurations can increase detection speed, the field of view, or be of practical use for scientific laboratory use.

Multi-pixel arrays can be based on pyroelectric, microbolometer, or TeraFET technology, even on mm-wave radiometers or Schottky diodes. However, the diode-based technologies have a higher dispersion of the electrical parameters and therefore are more difficult to implement for bigger multi-pixel arrays. Horn-antenna coupling is more effective for resonant detectors, however, less usual for big multi-pixel arrays as they are bulkier and need high-precision micromachining making them difficult to produce.

Therefore below 2 THz, the solutions based on CMOS technology are the most common as they use well-developed technology and the dispersion of the electrical parameters is comparably small. This means that one needs a good antenna scalable to high frequencies and a good detector. The easiest way to couple the radiation is through a high resistivity silicon lens. However, optical losses are much higher than the coupling through a horn antenna. On the other hand, for higher frequencies, microbolometer-based camera solutions are already well known, and therefore, commercially available solutions became very affordable [78].

While microbolometer technology has been known for a long time, the fully integrated CMOS technology-based 3×5 pixel focal-plane array (FPA) for 0.6 THz radiation has been presented for the first time only in 2019 [79]. TeraFET detectors are still under development and slowly reach their theoretical sensitivity limit. And probably will soon become commercially available and cover the lower THz detection range for commercially available camera technologies.

2.3 THz systems used in this work

2.3.1 Photomixer-based frequency domain spectroscopy system

Continuous THz wave can be generated using two InGaAs lasers and a photomixer. A photomixer is a metal-semiconductor-metal structure with a broadband antenna. Incoming optical radiation from two lasers with adjacent frequencies creates charge carriers in the semiconductor which causes the photocurrent due to applied bias voltage on the metal electrodes of the photomixer. The photocurrent oscillates at the beat frequency equal to the difference frequency of the two lasers. Generated THz power is radiated to the ambient via an antenna and a silicon lens.

The opposite mechanism works from the receiver side. The incoming THz wave generates the potential difference on the antenna. The conductivity of the photomixer is modulated by the same beat signal as on the transmitter side. The photocurrent (I_R) is induced in the photomixer which is proportional to the amplitude of the THz electric field (E_{THz}) and depends on the phase difference ($\Delta\varphi$) between these signals:

$$I_R \propto E_{THz} \cos(\Delta\varphi)$$

The detection mechanism of the Toptica system is based on a coherent detection scheme. Therefore, it shows a very high dynamic range of 80 dB (and 40 dB for the power detection). Toptica TeraScan 1550 system used in this work includes three 1550-nm lasers which have a bit different central frequency. This leads to three configurations of two lasers providing a continuous frequency range from 50 GHz to 2.7 THz with the reachable maximum power of only 10 µW. Absolute frequency accuracy in the low-frequency range (0 – 1.2 THz) is limited to a few GHz and the relative accuracy is less than 10 MHz.

2.3.2 Free-electron laser

Free-electron laser (FEL) THz source is based on relativistic electron beam which is accelerated using electron accelerators. They can radiate coherent radiation in 333 THz down to 30 GHz depending on the configuration [80]. Most of them are widely tunable. FELs can deliver pulses of various duration at various repetition rates. These are high power THz sources, where the average power is from milliwatts up to 0.5 kW for the NovoFEL1 source [80]. The peak power can reach 2 GW for the FELICE source. This type of THz source is very complex and needs big facilities with special personnel, as it operates in continuous mode with the research organized in shifts.

In this work, a FELBE laser with a pulse width of 10 ps at 2 THz at a repetition rate of 13 MHz was used. The pulse energy was equal to 3.5 nJ and peak power was 346 W. The s-SNOM operation with FEL laser is presented in [18].

2.3.3 Scattering-type Scanning Near-field Optical Microscope (s-SNOM)

Looking at the near-field of a material, one can overcome the standard wavelength resolution limit using the scattering-type Scanning Near-field Optical Microscope (s-SNOM) technique. This technique can be used for the detection of complex optical properties in a nanoscale area under a SNOM tip. The optical amplitude and phase of scattered light and some harmonics of it can be measured. Surface plasmon polaritons can be observed using this technique as well as carrier density changes change the local optical properties of the material surface. As it is based on Atomic Force Microscope (AFM) technique, simultaneously a picture of surface roughness can be measured [18]. This technique can be used for hard materials with high dielectric constants, reflectivity, or strong optical resonances.

We have used this technique for imaging of the plasma waves in a field-effect transistor channel with a high-power THz FEL laser which is presented in the last chapter.

3. FET transistor as THz detector: TeraFET

This chapter describes an unusual phenomenon of FETs. It is commonly known that FET devices have their electronic limits: the maximum operation frequency f_{max} for stable unity gain and the cut-off frequency f_t. However, some features which are not considered by the classical FET theory can enable additional functionality of FETs which is above the frequencies described by f_t and f_{max}. In this chapter, the FET function to detect THz radiation and necessary conditions are considered.

3.1 TeraFET concept and operation above cut off frequency

Here the main concept of TeraFETs as THz detectors is presented. As the name suggests, the main part of a TeraFET detector is a field-effect transistor (FET). The difference between the classical transistor and the TeraFETs is an asymmetric radiation coupling into the transistor channel [27, 28]. The classical mixing at GHz frequencies evolves to resistive and plasma (carrier density) wave mixing in the channel at higher frequencies. Carrier density wave in a two-dimensional electron gas (2DEG) channel is induced because the carriers react to the electric field change with some delay. The rectified signal depends on the radiation frequency and amplitude, the carrier density along the channel, as well as the speed of the carrier density (or plasma) wave.

The coupled radiation excites the plasma wave in the channel. Therefore, it is important to optimize the radiation coupling between the free space and the transistor. The first detection experiments were conducted coupling the radiation through the bond wires of the transistor which act as an antenna for the linear polarization. The most usual radiation coupling methods nowadays include a horn antenna [13] or a planar antenna coupling [28], whereas a more expensive solution would be using a Winston cone [15]. Another well-known solution for the optical broadband radiation coupling is monolithically integrated antennae with a hyper hemispherical Si lens coupling the incident THz radiation from the backside of the detector chip [37, 38, 40]. This arrangement assures the best power transfer from the free space for a wide frequency range and removes the Fabry-Perot interference in the detector's substrate. Therefore, this kind of power coupling configuration is used for most of our detectors.

3.1.1 Hydrodynamic model

Device modeling using a physics-based model was developed at Goethe University in collaboration with Vilnius University. It is based on the hydrodynamic model combined with the electrical and optical losses in the THz coupling path. This path contains the optical losses on the Si lens, antenna, as well as the electrical losses from the antenna contact towards the active region of the channel. Fig. 3.1 depicts the transistor channel (dashed) for AlGaN/GaN HEMT transistor where C_{MIM} is MIM capacitance formed via antenna between the source and

the gate. Here, Z_g is a gated channel impedance, whereas the R_{un} accounts for the ungated channel. Due to C_{MIM}, all the radiation is coupled via antenna impedance Z_{ant} to the drain terminal and transferred to the gated channel part responsible for the mixing of the radiation.

The calculation of either rectified current responsivity $\mathcal{R}_I$ or voltage responsivity $\mathcal{R}_V$ (both are related via Ohms law, $\mathcal{R}_V = \mathcal{R}_I \cdot R_{dc}$ with R_{dc} being a quasi-static resistance) starts with the simplified hydrodynamic transport model which omits carrier diffusion and carrier heating [27]. Furthermore, the rectification can be modeled using the concept of an equivalent current (as was described previously in [28]) or voltage source. The model considers the radiation losses on the lens, radiation coupling through the antenna into the transistors channel, its transfer to the active region, and conversion to the DC signal in the active region which was described by Dyakonov and Shur theory [27]. Here we will follow the calculation presented in [28].

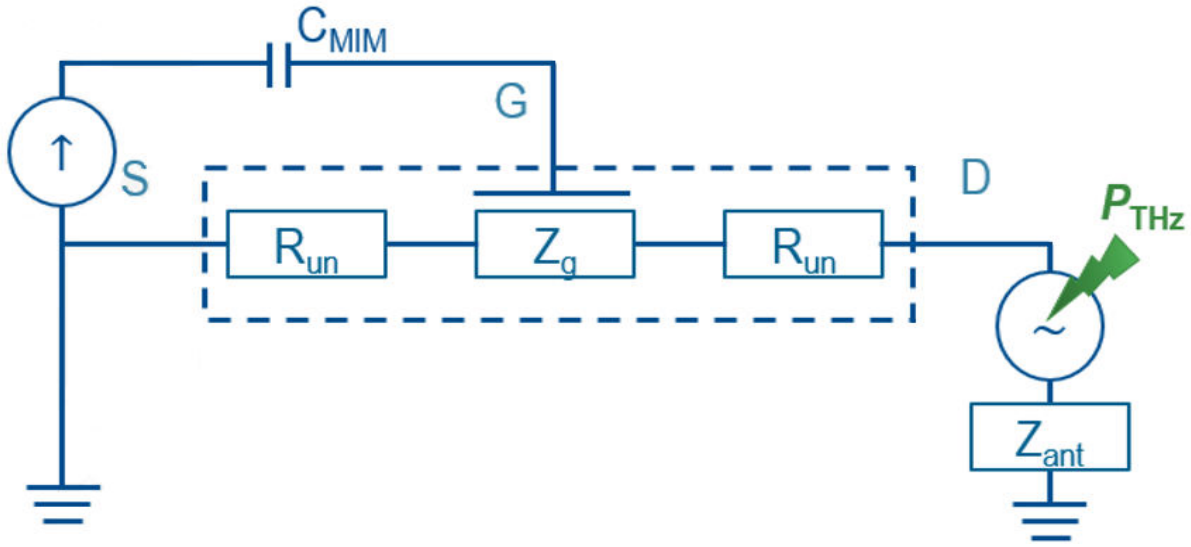

Fig. 3.1. TeraFET scheme.

Therefore, the calculated voltage responsivity can be calculated as follows:

$$\mathcal{R}_V \left[\frac{1V}{1W}\right] = \frac{V\ response\ [V]}{[1V^2]} \cdot Delivered\ power \left[\frac{1V^2}{1W}\right] \cdot \eta \qquad \text{Eq. 1}$$

Where η – efficiency factor accounting for optical coupling losses and antenna efficiency. The plasma wave velocity in the gated transistor part can be described as:

$$s = \sqrt{\frac{q}{m} \cdot n \cdot \left(\frac{\partial n}{\partial U_g}\right)^{-1}} \qquad \text{Eq. 2}$$

And the impedance of the gated part is calculated as follows:

$$Z_g = -\frac{iks^2 \tanh(kL)\tau}{\omega L} \cdot R_{ch} \qquad \text{Eq. 3}$$

where $k = \frac{\omega}{s}\sqrt{1+\frac{i}{\omega\tau}}$ and the conversion efficiency ratio between low-frequency resistive mixing and plasma wave enhanced non-resonant mixing

$$f_{non-res}(\omega,\tau) = \left[1+\frac{2\omega\tau}{\sqrt{1+\omega^2\tau^2}}\right] \quad \text{Eq. 4}$$

Here q is the elementary charge, $m = 0.2m_0$ is an effective electron mass in AlGaN/GaN ($m = 0.26m_0$ for Si), ω is THz frequency and τ carrier relaxation time. According to the mentioned relationship, the intrinsic voltage swing in the gated (or active) channel region to the unity power is:

$$\frac{V\ response}{[1V^2]} = \frac{q}{m}\frac{f_{non-res}(\omega,\tau)}{4s^2} = \frac{q}{m}\frac{1}{4s^2}\left[1+\frac{2\omega\tau}{\sqrt{1+\omega^2\tau^2}}\right] \quad \text{Eq. 5}$$

The power delivered from the antenna to the active transistor area is

$$\frac{1}{Delivered\ power}\left[\frac{1V^2}{1W}\right] = 8R_{ant}\frac{|Z_g|^2}{|Z_g+R_{un}|^2} \quad \text{Eq. 6}$$

This accounts for the relation between the generator (antenna) and the load (transistor) matching derived in [82](p. 77) as well as power delivery to the active transistor area. Therefore, the optical responsivity of the detector equals to:

$$\mathcal{R}_V\left[\frac{1V}{1W}\right] = \frac{q}{m}\frac{1}{4s^2}\left[1+\frac{2\omega\tau}{\sqrt{1+\omega^2\tau^2}}\right]\cdot 8R_{ant}\frac{|Z_g|^2}{|Z_g+R_{un}|^2}\cdot \eta \quad \text{Eq. 7}$$

Where Z_g is the complex gated channel impedance, R_{un} ungated channel resistance of one side of the gate.

Accounting for a voltage source, we can calculate the responsivity from the voltage response $q/m\cdot f(\omega,\tau)/(4s^2)$ to a unity amplitude of excitation voltage which is multiplied by a factor $8R_{ant}H^2$ corresponding to the squared voltage amplitude for a 1 W power delivered by the antenna. Considering the current responsivity $\mathcal{R}_I = \mathcal{R}_V/R_{dc}$ we get the following expression:

$$\mathcal{R}_I\left[\frac{1V}{1W}\right] = \frac{q}{m}\frac{1}{4s^2}\left[1+\frac{2\omega\tau}{\sqrt{1+\omega^2\tau^2}}\right]\cdot 8R_{ant}\frac{|Z_g|^2}{|Z_g+R_{un}|^2}\cdot\frac{\eta}{R_{dc}} \quad \text{Eq. 8}$$

The calculated optical responsivity can be expressed by the macroscopic detector parameters, momentum relaxation time, and optical coupling efficiency as follows:

$$\mathcal{R}_V = -\frac{2}{R_g}\frac{\partial R_g}{\partial V_g}\left[1+\frac{2\omega\tau}{\sqrt{1+\omega^2\tau^2}}\right]\cdot\frac{|Z_g|^2}{|Z_g+R_{un}|^2}\cdot R_{ant}\cdot\eta$$

Intrinsic Dyakonov&Shur responsivity | Power delivery from antenna | Optical coupling

Fig. 3.2. Modeling formula and explanation of the main parameters.

3.1.2 Modeling of TeraFET device

The formula presented in Fig. 3.2 can be applied for the detector measurements depicted in Fig. 3.3. The left graph shows the measured DC resistance of the AlGaN/GaN transistor with a log-spiral antenna at 130 K and room temperature. The resistance fitting routine was described in [45]. It determines external device parameters ungated-channel resistance R_{un}, gated-channel impedance Z_g, and gated-channel resistance gradient $\partial R_g/\partial V_g$, as well as internal parameters: effective electron mass m and momentum relaxation time τ. Once the device parameters are obtained, the model can be experimentally verified using the measured optical responsivity data. The Fig. 3.3 shows the modeled and measured DC resistance and optical current responsivity. The only unknown parameter for optical responsivity calculation is the antenna coupling factor η. From the practical experience, it is assumed to be around 0.025. This includes antenna efficiency ≈0.4, Gaussian beam coupling efficiency ≈0.7-0.8, transmission at the Si surface ≈0.7 [83], and scattering factor 0.5.

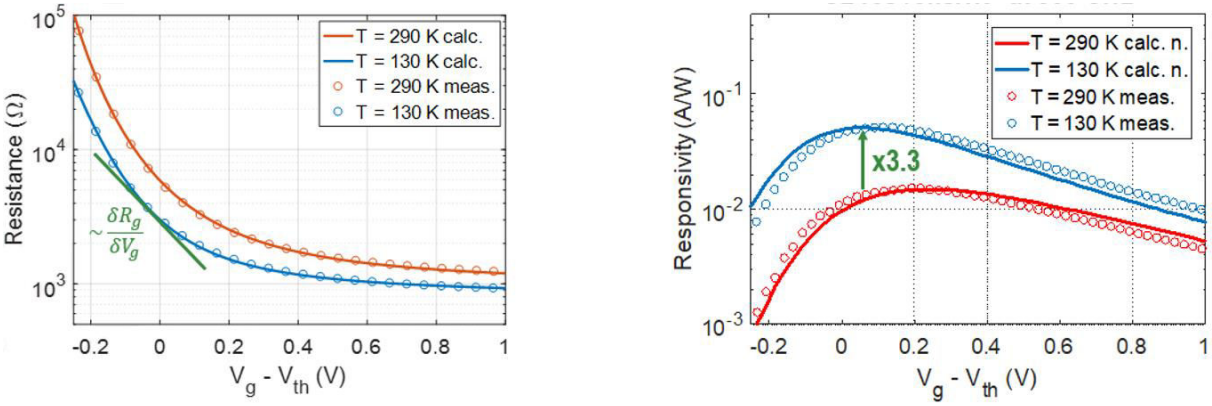

Fig. 3.3. Application of the model for two measurements.

This means that due to optical coupling and antenna matching, the total responsivity for the TeraFET under real operation conditions is almost 100 times lower than the intrinsic

responsivity of the active region of the FET channel, which is the parameter often given in the literature. The intrinsic responsivity is proportional to the power absorbed by the gated channel Z_g region [82]. This ideal intrinsic responsivity could be approached by reducing the power losses in optical and electronic parts of the quasi-optical TeraFET detector. The main radiation losses are shown in Fig. 3.4 which also shows the different definitions of the responsivity (intrinsic, electrical, optical, etc.) depending on the reference power and the previously described extrinsic loss factors included in the calculation, e.g. the optical responsivity can be calculated assuming that all incident radiation power is available for detection. However, along the way of the radiation coupling into the intrinsic device, the power is lost due to reflection and attenuation in the lens, later, on the chip substrate, antenna metals, and the mismatch between the beam and antenna pattern, where the rest power can be assumed for the calculation of the antenna de-embedded detector parameters. When all the losses are assumed, including antenna-transistor impedance mismatch and power transfer loss from the antenna terminal to the gated region of the transistor channel, then one accounts for the intrinsic detector parameters. These differences are considered in the next section.

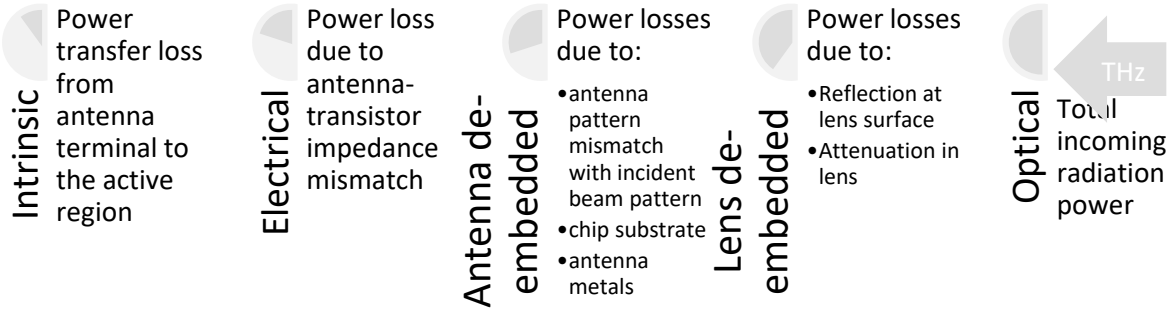

Fig. 3.4. Responsivity definitions and respective power losses along the coupling path.

In conclusion, the formula derived from the hydrodynamic model under the assumption of the power loss on the lens, antenna, and in the transistor channel, can be used for the modeling of device responsivity and extraction of the intrinsic device parameters from the measured channel resistance characteristics. However, in presence of any additional effects, such as carrier heating effects, they have to be considered additionally. The more explicit theoretical description of TeraFETs and the additional thermoelectric effect is given in [45] and its follow-up work [84].

3.2 State-of-the-art THz detectors

This chapter concentrates on various methods to describe the detector's parameters, namely responsivity $\mathcal{R}$ and noise-equivalent power (*NEP*). Depending on the used characterization technique as well as the goal of the experiment itself, the responsivity and

the NEP can be defined in various ways. This chapter is dedicated to the newcomers in the THz detection field as it intentionally summarizes various methods of responsivity and NEP measurement and calculation. It also shows state-of-the-art THz detector performance overviewed for various THz detector technologies and categorized for the types of characterization techniques.

First, to calculate the responsivity one needs to know an incoming THz power and a detected signal (current or voltage):

$$\mathcal{R} = \frac{Detected\ signal}{Radiation\ power} \qquad \text{Eq. 9}$$

Second, the NEP is the ratio between the detector's noise and its responsivity:

$$NEP = \frac{Noise\ density}{\mathcal{R}} \qquad \text{Eq. 10}$$

These parameters can be described in various ways and therefore, for the comparison of detector parameters, the differences in the description must be considered where possible [85]. Therefore, particular care should be taken for the detailed characterization description.

3.2.1 Proposed NEP definitions

To better understand the differences, let us first investigate Fig. 3.5. The right figure shows a ring antenna and various ways to describe the antenna area. Physical antenna area A_{ph} is defined by the size of the antenna and depicted with the black solid line. The effective antenna area $A_{\mathrm{eff}} = \lambda^2 D/4\pi$ (also called antenna aperture of antenna cross-section) is smaller than the physical antenna area [76, 86] and describes the area which couples the radiation the best. Here, *D* is the antenna directivity and λ corresponds to the wavelength. For the ideal antenna, the effective antenna area equals the physical antenna area $A_{\mathrm{eff}} = A_{\mathrm{ph}}$.

Usually, both the physical as well as effective antenna areas are smaller than the incoming beam size. The NEP calculation using the total beam size (or the total power) of the used system is called optical NEP. If the total power is coupled into the detector, the total NEP definition is used, mostly for the multi-pixel arrays. The total NEP and especially the optical NEP are the most upper limits of the NEP describing the performance of the complete detector device before implementation of the read-out electronics.

Optical NEP can be improved by the optimization of two aspects: the detection system as well as the detector performance. Other parameters, however, do not depend on the setup as they are normalized to the incoming radiation power on the specified antenna area. The lower limit of the device NEP performance is the intrinsic NEP which accounts only for the radiation power coupled into the active detector part (described by Dyakonov and Shur for the TeraFETs [27]). This parameter is a useful parameter for the comparison of the Dyakonov and Shur contribution between the electronic devices, however, it is less common for practical devices, as it excludes the power coupling through the antenna and optical losses which influence the optical device performance a lot. It should be considered, that some

devices can also be defined by the electrical NEP which accounts for the power coupled into the electronic element and in the ideal device it should approach the intrinsic NEP. Table 5.2 describes the summarized description methods:

Table 3.1. Summary of various definitions for NEP calculation.

Name of the characterization method	Accounted detector area	Accounted power
Intrinsic NEP	N/A	Power coupled into the active region of the rectifying element
Electrical NEP	N/A	Power coupled into transistor terminals
De-embedded NEP (here includes from optical loss de-embedding to gain de-embedding [38])	N/A	Power after accounting for optical and radiation losses For gain de-embedding: power available at transistor terminals
Cross-sectional NEP [87] (also comparable to pattern de-embedded NEP in [38])	Effective antenna area = Antenna cross-section = Antenna aperture A_{eff}	Average power or total intensity on the area
Cross-sectional NEP (ideal antenna case)	Physical antenna area A_{ph}	Average power or total intensity on the area
Optical NEP	N/A	Total power
Total NEP	Total beam size or focal spot size	Total power

The methods shown in Table 3.1 are the most usual characterization methods for the responsivity and NEP calculation of quasi-optical devices. Considering this, the total NEP is used in focal plane array (FPA) characterization, where the beam diameter is smaller than the array size and the total signal is the integral of all the pixels receiving the power. This method is optimal, as it accounts for the optical NEP with the optimal detector area. Optical NEP calculation for the single-pixel devices usually accounts for a higher radiation power than the one which is coupled into the device as the beam diameter is bigger than the diameter of the antenna (see Fig. 3.5, right).

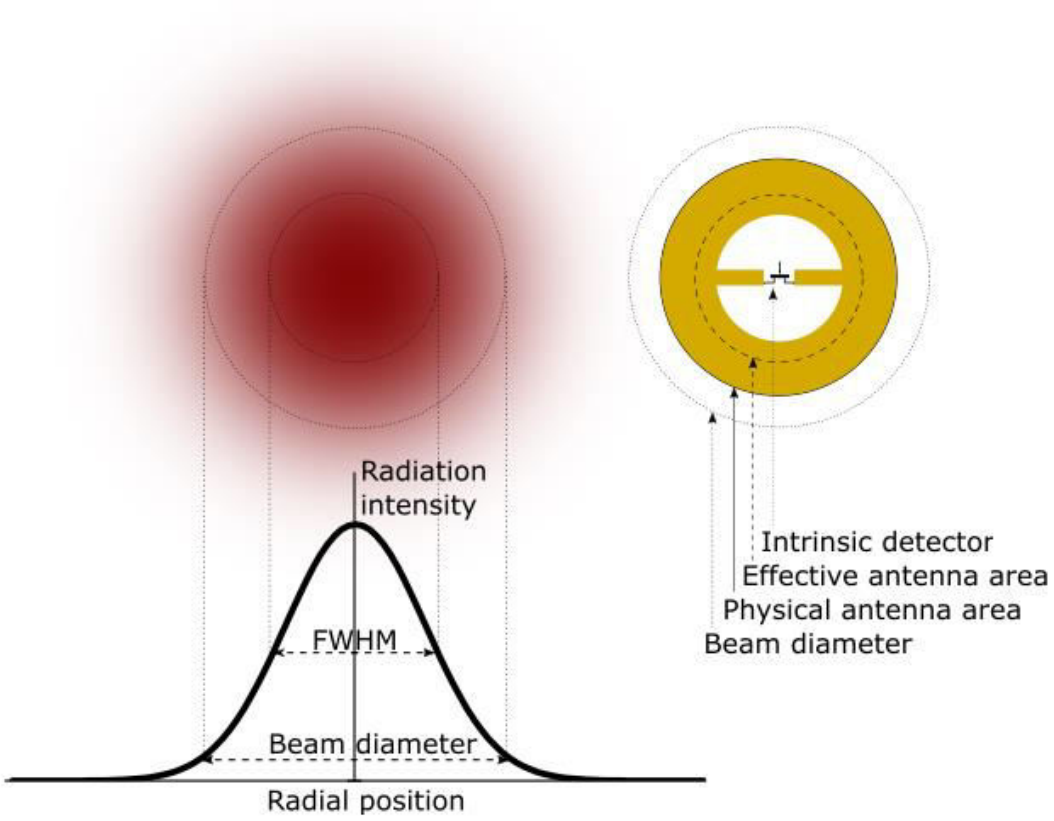

Fig. 3.5. Beam profile comparison to the antenna area.

When performing the calculation of the radiation power on the physical and effective antenna area, the precise calibration of the beam must be assured. The main Gaussian beam parameters are depicted in Fig. 3.5, left. However, depending on the measurement setup and simulation tools, various groups use either average radiation power or the integrated power on the specific detector area which also can give slightly different results. Despite this, it is still challenging to simulate the directivity of the antenna, especially for the higher THz frequencies and multi-pixel detectors cases, due to differences in the antenna pattern between a single pixel and a multi-pixel detector [88]. However, the author would assume this detector characterization method for the early research stage.

3.2.2 De-embedding procedure for detector comparison

To eliminate the issues associated with the detector performance comparison, the de-embedding procedure has been introduced [38]. This method is useful for the detector comparison, as it accounts for the various stages of the radiation coupling into the detector: incident radiation on the lens, antenna plane, and transistor terminals, etc. Up to now, there are some uncertainties due to limitations of lens simulation and antenna pattern, or challenging measurement routines, but some simulation and laboratory-experience-based de-embedding coefficients can be already considered.

Despite some uncertainties of the de-embedding procedure, the relevant development shows it as a promising tool for the easier comparison of the performance of various detectors which will be helpful for future THz detector development and decision making.

Up to now, the defined gain de-embedding procedure [38] accounts for *optical losses*, such as reflection (r_s) on the lens-air interface, described by the Fresnel losses

$$r_s = \left(\frac{n-1}{n+1}\right)^2 \approx 0.3 \qquad \text{Eq. 11}$$

as well as cross-polarization and Gaussicity of the antenna radiation pattern (assuming Gaussian beam); and *antenna radiation efficiency,* accounting for the losses on the antenna and lossy substrate. Additionally, one could account for *transistor-antenna impedance matching* to calculate the electrical NEP and *electrical losses* in the transistor which would lead to the prediction of the intrinsic NEP. A detailed example of the de-embedding procedure is described in [38].

3.2.3 State-of-the-art THz detector comparison

The mentioned device parameters are summarized in Table 3.2 and Table 3.3 which show the room-temperature state-of-the-art detectors for the comparison taken from multiple review sources [10, 15, 37, 89] as well as other scientific references and commercial web pages. The reference [90] of Table 3.2 mentions the differences in circuit level of the reported FET-based detector responsivity and NEP values in various references: biased and unbiased detector channel, active amplification as well as the video-rate camera operation. For simplicity only unbiased (or biased at very low bias/current) detectors are included, the amplification and video-rate operation are explicitly described. All the shown devices work in uncooled conditions, however, most of them (especially electronic devices) can be additionally cooled to improve the detector's sensitivity. References in bold show the author's work included in the thesis.

The following Tables Table 3.2 and

Table 3.2 summarizes all the broadband detectors which have the best sensitivity for each of the technologies, which are divided into thermal (photoacoustic, pyroelectric, and microbolometer technologies), electronic (FET-based and zero-bias Schottky diode-based technologies), and others which are less common. The classification of characterization methods shows some common use of characterization methods for particular technologies. For example, microbolometer technology provides the characterization of total optical NEP. The SBDs and FETs use all possible definitions from intrinsic to optical NEP. Pyroelectric technology shows only optical NEP, whereas other novel technologies presented in the table usually apply cross-sectional NEP calculation.

The most sensitive broadband technologies are microbolometer, field-effect transistor, and Schottky-barrier diode technologies. The presented optical NEP was 200 pW/√Hz @

0.5 mA at 0.4 THz for microbolometer detector [32], and 7−100 pW/√Hz at 0.1 – 1 THz, respectively, for zero-bias SBD technology [34]. The presented results on FET technology were 25−31 pW/√Hz at 0.5 – 0.6 THz [37], respectively, and <50 pW/√Hz at 0.84 – 1.29 THz reaching 25 pW/√Hz at 1 THz [38]. The graphical representation of state-of-the-art THz detectors based on the optical NEP characterization method is shown in Fig. 1.3.

As one can see, only the detectors based on the same characterization method can be used for comparison. However, for some definitions, such as cross-sectional NEP, the values can differ by a few times between the presented values, depending on the chosen detector area [76]. One example of the publication which can be the most useful for detector comparison is [38], showing optical, gain de-embedded, and electrical NEP of the detector.

Table 3.3 show the main THz detector technologies and the published state-of-the-art values which were obtained using various characterization methods. Table 3.2 and Table 3.3 were summarized only into a few relevant cases for comparison purposes. Both tables aim:

- to summarize state-of-the-art THz detectors,
- to classify the characterization methods of THz detectors,
- to show the most common methods for the main technologies,
- to compare the performance of detectors presented in this work with other THz detectors of the same or different detector technology,
- to compare resonant and broadband detectors in separate tables, as resonant detectors are usually more sensitive due to a better antenna matching for narrowband frequency range (discussed in Section 6.1.2),
- to raise the importance of the description of used methods leading to proper detector comparison.

Table 3.2. Broadband room-temperature THz detectors and their state-of-the-art performance.

Refe-rence	Type/ Technology	Radiation coupling	Frequency [THz]	NEP [pW/√Hz]	Responsivity [kV/W]	Characterization method	Modu-lation [Hz]
	Thermal						
	Photo-acoustic						
[33][c]	Thomas Keating	D>30 mm aperture	0.03 – 3+	5E6 (typical)	8.6E-4[d] (internal);	Ohmic heating[e]; Optical NEP	10 – 50

[c] Commercially available device

[e] Ohmic heating of an internal metal film for the calibration of internal responsivity [91].

Refe-rence	Type/ Technology	Radiation coupling	Frequency [THz]	NEP [pW/√Hz]	Responsivity [kV/W]	Characterization method	Modu-lation [Hz]
					3.7E-4[d] (optical)		
[22][c]	Golay cell	D = 6 mm aperture	0.04 – 20	100 – 1000	100	Optical NEP, incl. amplifier	10 – 20
	Pyroelectric						
[21][c]	Pyro-electric	Winston cone D = 15 mm	<20	440-1250[f]	18.3-5.6[f]	Optical NEP, G = 20-200[f]	10 – 320
[19][c]	Pyro-electric	D = 10 mm aperture	0.1 – 3	1.4E5	N/A[g]	Optical NEP, incl. amplifier	<50
	µBolo-meters						
[20][c]	Vox	HRFZ-Si window film and optical objective	2.54, 4.25	16.5, 14.4[h,i] (30 fr./s)	N/A	Total NEP of the integrated system[j]	30
[30][c]	a-Si	λ/4 cavity with crossed bow-tie antenna	2.5	6[i] (25 fr./s)	12.6	Total NEP of the integrated system[j]	25
[92]	AlGaN/GaN	Spiral antenna	2.55	5000[k]	N/A[k]	Cross-sectional NEP	1E3
[32]	YBCO	Spiral antenna + lens	0.4	200 @ 0.5 mA	0.1 @ 0.5 mA	Optical NEP	5E3 – 7E3
[93]	YBCO	Spiral antenna + lens	0.4	50 @ 1 mA	0.05 @ 1 mA	Intrinsic NEP	1E5

[d] GUF data: internal responsivity was calibrated, optical responsivity – calculated at 0.5 THz

[f] Corresponding the given modulation frequency range

[g] ≈1.5E-3 mA/W

[h] Estimated: $\mathrm{NEP} = \mathrm{MDP}/\sqrt{f_{frame}}$

i Corresponding the given THz frequency

j Pixel, ROIC, electronics, etc.

k Noise estimated at Vds = 2 mA, responsivity estimated to be 40 mA/W at Vds = 8 mA

Refe-rence	Type/ Technology	Radiation coupling	Frequency [THz]	NEP [pW/√Hz]	Responsivity [kV/W]	Characterization method	Modu-lation [Hz]
[94]	PBCO	Log-spiral + lens	0.65	N/A	1.6E-3 @ 0.5 mA	Optical responsivity	1E4
[94]	PBCO	Log-spiral + lens	0.65	152 @ 0.5 mA	0.033 @ 0.5 mA	Measured intrinsic NEP	1E4
	Electronic						
	Zero-bias SBDs						
[25]	ErAs: InAlGaAs	Log-periodic + lens + LNA	0.104	0.88; 1.4	6.8[l]	Measured intrinsic NEP; Embedded antenna loss to intrinsic NEP	N/A
[34][c]	N/A	Log-spiral antenna with amplifier + lens	0.1 – 1	7 – 100	25 – 2	Optical NEP	8E3, max. 1E6
[23][c]	N/A	0.1-0.45 THz with lens; 0.6-0.9 THz with horn	0.1 – 1	45 – 115	0.1 – 0.25	N/A	Max. 4E10
	FETs						
[37][p]	AlGaN/GaN HEMT	Bow-tie antenna + lens	0.5 – 0.6	25 – 31	790.4[l] @ 0.5 THz	Optical NEP	DC-12.2+
[39]	AlGaN/GaN HEMT	Differential dipole + lens	0.7 – 0.9	30 – 50	N/A	Optical NEP	N/A
[90]	65-nm CMOS	Differential ring antenna + lens	0.79 – 0.96	100 @ 0.86 THz	140 @ 0.86 THz	Cross-sectional NEP	1E3
[95]	65-nm CMOS	Folded dipole	0.66 – 1	66 @ 1 THz	N/A	Cross-sectional NEP	1E3
[40][p]	90-nm CMOS	Bow-tie antenna + lens	0.6 – 1.5	48 – 70	0.22 @ 0.6 THz	Optical NEP	DC – 888+

l Calculated from published data

Refe-rence	Type/ Technology	Radiation coupling	Frequency [THz]	NEP [pW/√Hz]	Responsivity [kV/W]	Characterization method	Modu-lation [Hz]
[38][p]	65-nm CMOS	Biquad antenna + lens	1, 0.85 – 1.3; 1; 1	25, <50; 9.6; 6.2	0.46, 0.76; N/A; N/A	Optical NEP; Gain de-embedded NEP; Electrical NEP	7777
[43]	GFET	Bow-tie antenna + lens	0.6	515	0.014	Optical NEP	33 – 33E3
[42]	GFET	Bow-tie antenna + lens	0.4	130	0.074	Optical NEP	333
	Others						
[96]	Thermo-couple	Full-wave dipole	0.812	130	N/A	Cross-sectional NEP	1E3
[97]	Diode in 130-nm CMOS	Patch antenna	0.823	36.2	2.56	Cross-sectional NEP	1E6
[98]	NW-based FET	Bow-tie antenna	1.63	629	0.11	Cross-sectional NEP[m,n]	N/A
[44]	HBD	Butterfly-shaped slot antenna	0.6 – 1	850 @ 0.7 THz	0.5 – 0.25[o] 0.6 @ 0.7 THz	Total optical NEP	N/A
[85]	Ballistic rectifier	Bow-tie antenna	0.1	35 (50[o])	0.4[o]	Cross-sectional NEP[o]	N/A

Table 3.2 summarizes all the broadband detectors which have the best sensitivity for each of the technologies, which are divided into thermal (photoacoustic, pyroelectric, and microbolometer technologies), electronic (FET-based and zero-bias Schottky diode-based technologies), and others which are less common. The classification of characterization methods shows some common use of characterization methods for particular technologies. For example, microbolometer technology provides the characterization of total optical NEP. The SBDs and FETs use all possible definitions from intrinsic to optical NEP. Pyroelectric

[m] Partially de-embedded NEP

[n] Small V_{ds} is applied

[o] Approximate values are taken from the presented graphs as the nominal value is doubtful due to standing wave pattern in the setup

technology shows only optical NEP, whereas other novel technologies presented in the table usually apply cross-sectional NEP calculation.

The most sensitive broadband technologies are microbolometer, field-effect transistor, and Schottky-barrier diode technologies. The presented optical NEP was 200 pW/√Hz @ 0.5 mA at 0.4 THz for microbolometer detector [32], and 7−100 pW/√Hz at 0.1 – 1 THz, respectively, for zero-bias SBD technology [34]. The presented results on FET technology were 25−31 pW/√Hz at 0.5 – 0.6 THz [37], respectively, and <50 pW/√Hz at 0.84 – 1.29 THz reaching 25 pW/√Hz at 1 THz [38]. The graphical representation of state-of-the-art THz detectors based on the optical NEP characterization method is shown in Fig. 1.3.

As one can see, only the detectors based on the same characterization method can be used for comparison. However, for some definitions, such as cross-sectional NEP, the values can differ by a few times between the presented values, depending on the chosen detector area [76]. One example of the publication which can be the most useful for detector comparison is [38], showing optical, gain de-embedded, and electrical NEP of the detector.

Table 3.3. Narrow-band room-temperature THz detectors and their state-of-the-art performance.

Refe-rence	Type/ Techno-logy	Antenna type	Frequency [THz]	NEP [pW/√Hz]	Respon-sivity [kV/W]	Characterization method	Modu-lation [Hz]
	FETs						
[35, 36][p]	90-nm CMOS	Slot with dipoles + lens	0.3; 0.3	19; 20.8	0.5; 55	Optical NEP; Optical NEP, incl. LNA G = 40.8 dB	DC – 2E5
[99]	250-nm CMOS	Slot antenna	0.3	320	2.3	Cross-sectional NEP, incl. LNA of G = 46 dB	75 – 2025
[87]	65-nm CMOS	Dipole antenna	0.63	13.6	2.8	Cross-sectional NEP	N/A
[87]	90-nm CMOS	Patch antenna	0.63	10	2.55	Cross-sectional NEP	N/A
[15][p]	90-nm CMOS	Patch antenna	4.75	404	0.075	Cross-sectional NEP	331
[100]	90-nm CMOS	Patch antenna	2.52, 3.11, 4.25	63, 85, 110	0.336, 0.308, 0.230	Cross-sectional NEP	~1E3

[p] This work

Refe-rence	Type/ Techno-logy	Antenna type	Frequency [THz]	NEP [pW/√Hz]	Respon-sivity [kV/W]	Characterization method	Modu-lation [Hz]
[86]	65-nm SOI NMOS	Folded-dipole antenna + lens	0.65	17	1.93	Cross-sectional NEP	1E3
[101]	65-nm CMOS	Ring antenna + lens	0.724	14	2.2	Power on a physical 3-mm lens area excluding the power loss on lens-air interface	200
	Bipolar transistor						
[102]	130-nm SiGe	Octagonal loop antenna	0.26	7.9 – 8.8	2.6	Cross-sectional NEP, incl. LNA of G = 37 – 55.7 dB	5E3 (up to 1E5)
[89]	130-nm SiGe	Dipole antenna + WR3.4	0.315	21.2	6.1	Measured electrical NEP	2E4
[1]	SiGe	Folded-dipole antenna	0.645	30	0.85	N/A	1E3
	HBDs[q]						
[103]	SiGe	Folded-dipole antenna + lens	0.170	2.14	~3.5	De-embedded NEP for optical losses	N/A
[104]	Sb	Folded-dipole antenna + lens	0.1	0.18	9.8	Measured electrical NEP	N/A
	SBDs						
[23][c]	N/A	Waveguide	0.06 – 0.09, 0.09 – 0.14,	9.5, 11, 11,	2.8, 2.4, 2.4,	Optical (total) NEP	N/A

[q] Heterostructure Backward Diodes

Refe-rence	Type/ Techno-logy	Antenna type	Frequency [THz]	NEP [pW/√Hz]	Respon-sivity [kV/W]	Characterization method	Modu-lation [Hz]
			0.14 – 0.22, 0.22 – 0.33, 0.33 – 0.5, 0.5 – 0.75, 0.75 – 1.1, 1.1 – 1.7	12, 7.2, 11.4, 15.2, 113.7	2.2, 1.6, 1 0.75, 0.1		
[41]	130-nm CMOS	Patch antenna	0.283, 0.86	29, 32	0.323, 0.355	Cross-sectional NEP	1E6
[76]	130-nm CMOS	Patch antenna	4.92	430 @ 10 – 20 nA; 4920 as ZBD	0.383 @ 10 – 20 nA; 0.38 as ZBD	Cross-sectional NEP	300
[105]	InGaAs	Square spiral + cylindrical lens	0.25	106.6	0.0985	Optical NEP[r]	<3E4
[75]	GaAs	Long-wire antenna	2.54	N/A	0.06	Optical NEP	1E5
	Others						
[31]	Nb_5N_6 µBolo-meter	Dipole antenna + lens	0.24	30.8[l]	320 @ 0.19 mA	Optical NEP	4E3
[106]	InP HEMT	Wires + contact pads	0.292	N/A	0.026 @ V_{ds} = 2 mV	Optical responsivity	N/A
[106]	InP HEMT	Asymmetric metal grating gate	1	15	2.2	Cross-sectional NEP	117
[107]	Thermo-couple	Dipole antenna	0.812	170	0.026	Cross-sectional NEP	40 – 12.5E3

The narrowband devices are mainly based on electronic technologies, such as SBDs, Heterostructure Backward Diodes (HBDs), FETs, and bipolar transistors. However, there are also thermal and electrical devices using rather unusual radiation coupling. All the devices

[r] Characterized at single frequency

use either a narrowband antenna or a waveguide coupling, which limits the detector bandwidth. The main characterization methods for the narrowband devices are cross-sectional and optical NEP. However, the mismatch in the frequency range between detectors can be an issue for the comparison of the detector performance, as the detector performance depends on frequency.

Comparison of the NEP performance between Table 3.2 and Table 3.3 shows that the narrowband detectors are expected to be a few times better than any broadband detector. Therefore, it is a good practice to compare broadband detectors with broadband ones, and resonant detectors with resonant ones. For comparison, this aspect will be graphically addressed in Section 6.1.2. The HBDs showed in Table 3.3 present outstanding NEP performance values, however, they cannot be compared to any other technology as both HBDs use completely different characterization methods than the most common ones.

However, for the precise comparison, one has to take it into account, that e.g. cross-sectional NEP definition here accounts for both, effective as well as physical antenna areas that are not equal [76]. The optical NEP can be comparable to the total NEP, as the total NEP is the ideal case of the setup optimization for the optical NEP characterization. The details on the characterization of the best optical NEP values for the TeraFET detectors are presented in Section 6.1.2. The comparison to other THz detector technologies using a comparable characterization method is given in Section 1.2.

4. From design to the functioning device

4.1 TeraFET technologies

The previous chapter showed many TeraFET technologies used for THz detection. This chapter summarizes the pros and cons of each TeraFET technology used in this work. It is important to point out that each technology has its usage depending on the application.

4.1.1 Novel graphene FET technology

Considering the applied technologies, a graphene monolayer transistor as a laboratory-developed FET technology was used for THz sensors (GFETs). The GFETs were fabricated at Chalmers University of Technology [43]. They are based on a single-carbon-atom-thick monolayer which theoretically provides a very high carrier velocity up to 1/300 of the speed of light. However, in practice, the carrier velocity depends on the materials supporting the monolayer and how the electronic device is designed. The technology is relatively new: the first publication on graphene exfoliation was presented in 2004 [108], the first integrated circuit solution – in 2011 [109].

However, considering the novelty of graphene flakes, it is either expensive or cannot provide a high material quality for a high rate of repeatability of electrical parameters between the fabricated electronic elements. Therefore, this technology is less useful for multi-pixel array production. It is also very sensitive to electrostatic discharge and therefore lacks robustness. However, due to the simplicity of the epitaxy and unique material properties, this technology is of use for theoretical predictions and a better understanding of physical phenomena [18, 84].

This work presents plasma (or carrier density) wave microscopy using an s-SNOM technique on graphene-based FET that was specifically designed with the plane graphene layer on top of the gate oxide [18, 110]. This design enabled us to scope the electrical features on the transistor channel (graphene layer) under incident THz radiation which is presented in the last chapter of this Thesis. Our standard approach for THz detectors based on graphene monolayers has been presented earlier in [77, 111, 112] and showed the influence of thermoelectric effects on TeraFET detection as well as various stability issues of the novel technology transistors.

4.1.2 AlGaN/GaN HEMT technology for high power electronics

AlGaN/GaN HEMTs are fabricated using a commercial III/V group semiconductor technology based on MMIC (monolithic microwave integrated circuit) process on SiC substrate, which is a well-developed technology at Ferdinand Braun Institute, Leibniz-Institut für Höchstfrequenztechnik (FBH) in Berlin [113].

This technology overcomes some technological challenges of a well-known commercial CMOS process. The AlGaN/GaN HEMT technology is III/V group semiconductor technology which has a higher carrier saturation velocity, mobility, and breakdown voltage than the CMOS technology. It is also robust in harsh environments such as space applications where ionizing radiation can break the semiconductor structure [114]. The lower sheet resistance (400 – 600 Ω/sq) allows a better impedance matching to the antenna. However, this technology does not reach the physical node limit of the CMOS technology, which could assure a better plasma wave screening by the gate electrode which influences free carriers in the channel [115]. AlGaN/GaN HEMT technology can also be used for multi-pixel array fabrication and assure a wide range of variable parameters to choose from in order to optimize the detector performance.

4.1.3 Commercial CMOS technology

CMOS – complementary metal-oxide-silicon technology is a commercially available and most usual semiconductor technology used for computer components based on various integrated circuits (ICs) and digital logic circuits as well as analog circuits, for example, communication systems, data converters, image sensors, or radio-frequency (RF) circuits.

Due to various applications and high-volume factory production, the important technological parameters are well defined and therefore the functionality of the elements can be easily modeled for standard applications. This commercial technology reaches low node numbers as the lower is the node, the faster is the functional element which is important for further computer development. This technology also provides high functional integration possibility which is important for future prototyping and mass production [21, 42]. However, due to a low breakdown voltage, it is sensitive to a high electrostatic discharge. Furthermore, the modeling in the THz domain, above the transistor cut-off frequency, is still challenging. The foundry models do not necessarily agree with some physical models specified for the frequency range of interest [40] far beyond the f_T and f_{MAX} of the transistor.

For the experiments presented in this work, mainly NMOS transistors on 65-nm and 90-nm technologies were used which were mostly fabricated by TSMC (Taiwan Semiconductor Manufacturing Company) process. Detector design was developed by colleagues at J.W. Goethe University Frankfurt in collaboration with Vilnius University and Universidad Politecnica de Madrid.

4.2 Detector chip implementation for THz detection

Once the design according to the simulation tools and modeling is fulfilled in the chosen TeraFET technology, it has to be built-in into a detector module and characterized. Therefore, this section presents the common assembling method of a single-pixel detector and its configuration for the cryogenic and multi-pixel detector design.

4.2.1 Single-pixel detector module

The produced chip with TeraFETs must be first fixed to the PCB and connected electrically. It can be done either using flip-chip technology or simply using a carrier substrate that can be glued to the PCB and carry the chip and then bonded. For the latter method, the epoxy glue from EPO-TEK® is used. The PCB contains the electrical contacts for the input and output signals which are used for electrical characterization. This set can be already used for the electrical characterization, however, for better noise characteristics an additional electrical shielding is preferred.

For the optical characterization, the lens is placed in a conical lens holder assuring the lens position to be along the optical axis of the setup. For this purpose, the lens holder is adapted to the Thorlabs 60-mm-cage or 30-mm-cage system. For detector alignment along the optical axis and precise focusing of the antenna into the beam, the detector PCB is built into the optomechanical x-y translation stage. Depending on the system requirements, various types of PCB holders were designed. In such a configuration, the detector chip can be moved along the plane of the silicon lens and therefore various detectors can be exploited on a single chip.

For the small-signal detection, the detector is enclosed in a metal case which protects the detection signal from the ambient noise sources. The complete detector module is depicted in Fig. 4.1. From right to left you can see the metallic lens holder, the lens, the PCB with electrical contacts, PCB holder, and x-y translation stage which are all fixed in the 30-mm-cage system and enclosed in a metallic box. The electrical connections can be easily installed at the back cover of the enclosure (not shown).

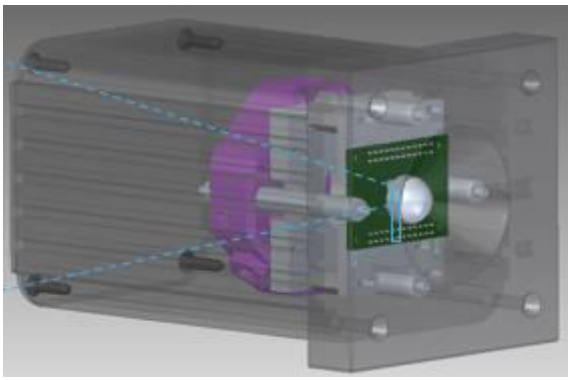

Fig. 4.1. Detector module.

Once the detector is characterized, it can be used for specific applications either as it is or after additional readout implementation. For example, a low-noise amplifier stage can be implemented to reduce the influence of the measurement system noise or increase the amplitude of the detected signal [15, 35, 46]. The characterized design can be also implemented for a multi-pixel array application by simply repeating the detector's design in

a suitable-size matrix. Both readout implementations, for single-pixel signal amplification as well for the multi-pixel array readout, are discussed in Section 6.2.2 Reconfigurable aperture multi-pixel array.

From 2016 to 2020, various implementations of the detector module were created starting with the 60-mm-cage system presented in [37], followed by the 30-mm-cage system which was suitable for the cryogenic characterization. Later, the detector module has been made even smaller so that the detectors reach the compact size suitable for applications with space constraints as well as commercialization. All the configurations have four degrees of freedom (*x*, *y*, *z* axes, and rotation in the polarization plane) which assures the optimal alignment in each optical setup.

4.2.2 Cryogenic system

Due to space limitations and the requirement of a good thermal conductivity towards the sample, a cryogenic system was built. The detector module was reconfigured to fit the cooling setup. The laboratory-built setup was based on an Oxford Instruments system which was reconfigured for the measurements of TeraFET based detector. The cooling rod of the original cryostat was cut off. Therefore, the cryogenic finger extension suitable for the experiment was designed. The outer shield was replaced by the designed parts with more space available for the detector module. The electrical wires were replaced to measure the temperature at two points of the cryogenic system and to characterize the tree-terminal device.

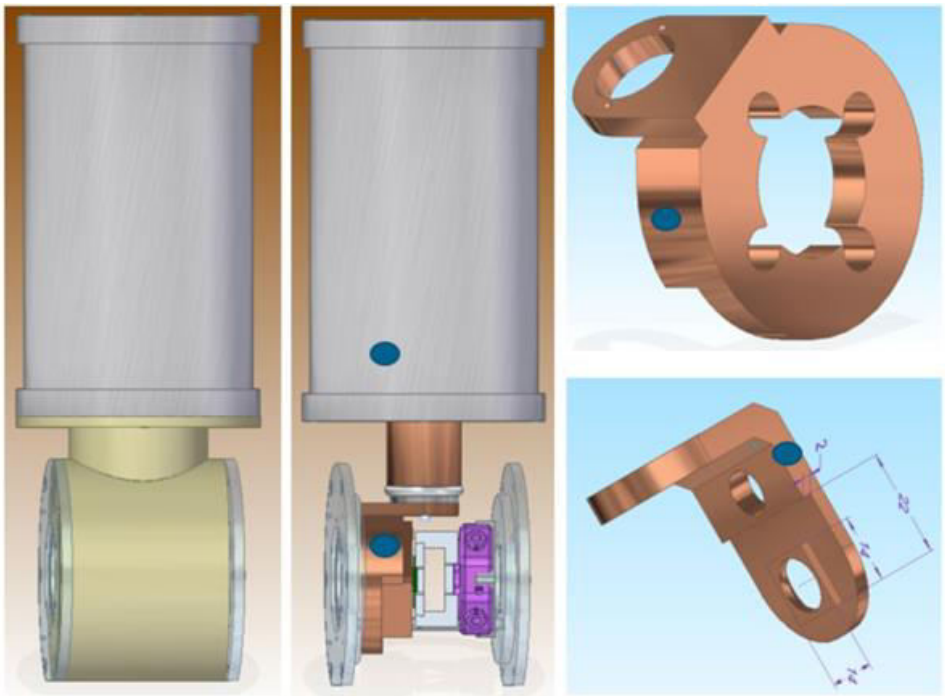

Fig. 4.2. In-house-made cryogenic system for TeraFET characterization. Left: dimensions of the system. Center: thermo-optomechanical system. Right: two designs of cryogenic finger extension. The dots show the temperature monitoring spots.

Fig. 4.2 shows the implemented cryogenic system. The optical cryostat design is shown at the left. The optomechanical system in contact with the cryogenic finger through the cryogenic finger extension is shown in the center of Fig. 4.2. The heat transfer proceeds through the designed cooper cold-finger adapter (depicted on the right top picture) goes towards the cooper lens holder (the only available thermal connection) which is designed with a special cone, repeating the lens surface curvature to assure a better thermal contact. Through the lens, heat is transferred to the Si wafer on which TeraFETs are glued. The THz beam goes through a Teflon window containing an 8-deg difference between the inner and outer planes to avoid the Fabry-Perot effect in the window. The sample holder is fixed to the front cryostat wall. Total space for the detector in the cryogenic chamber is enclosed in a space of 80 mm in diameter and 66.4 mm in length along the optical axes of a detector.

The focusing procedure is the same as in the room-temperature experiments. The sample is focused in ambient conditions and then the cryogenic system is closed to create a vacuum environment and later cool down the system to liquid nitrogen temperature (77 K).

As the detector must be cooled down, two designs of cryogenic finger extension were fabricated. Both are shown on the right of Fig. 4.2. The upper one assures perfect mechanical stability, as the lens holder moves in the plane parallel to the extension and keeps the lens in the same position assuring a good thermal contact between the lens holder and cryogenic finger extension. The lower one is made for an optimized thermal capacity and volume of the detector module. In this case, the lens must be glued to the optical axis on the detector PCB before the experiment and inserted into the cryogenic finger extension. In both cases, the optomechanical system, except for the cryogenic finger extension, is fixed to the front wall of the cryostat via thermally isolating rods to keep the detector and the lens in the optical axis during the whole experiment. The temperature is measured in real-time with PT100 thermal resistors built into the cold finger at two spots shown with the dots in the center picture of Fig. 4.2.

4.2.3 Multiple-pixel design with readout

To explore the camera applications, two reconfigurable arrays were designed and built: one on CMOS (designed by A. Lisauskas) and another one on AlGaN/GaN HEMT technology (designed by A. Rämer). CMOS detector is targeted to 4.75 THz frequency and AlGaN/GaN was designed for a broadband performance below 1 THz. The design of a multi-pixel array is rather simple: the chosen pixel design is repeated in the desired matrix and all the transistors of one column are connected in parallel and are pinched off for OFF condition. The rows share the same gate. Therefore, it is possible to turn on single pixels one by one, or a matrix of the preferred size. The use of both options is presented in section 6.2.2 Reconfigurable aperture multi-pixel array.

The implemented readout circuit is presented in Fig. 4.3. All the source contacts are connected to the ground. Gates and drains are controlled by the Arduino Nano via

Multiplexers/Demultiplexers. Two gate voltages are provided – the working point voltage and the pinch-off voltage. The induced camera output signal is amplified using a low-noise amplifier and then recorded in the computer via the LabView program.

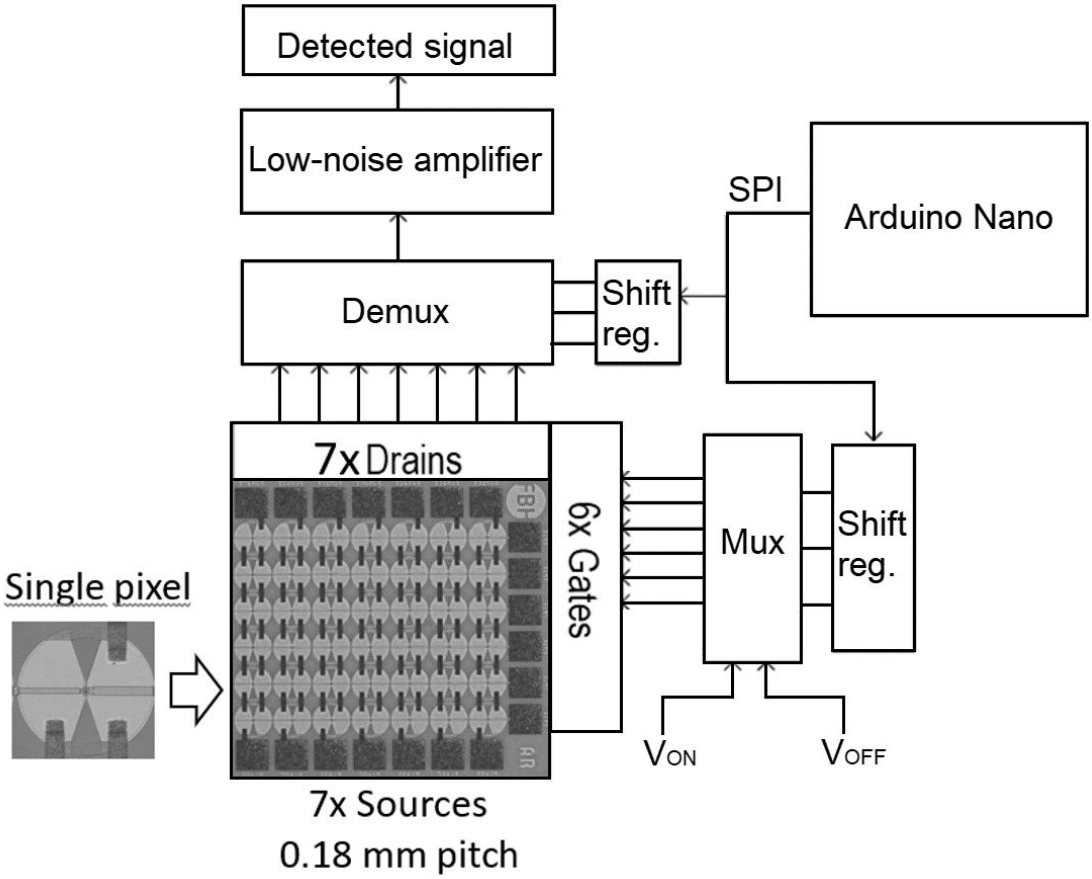

Fig. 4.3. Multi-pixel camera array read-out scheme.

To reduce the ambient noise, the chip with the readout electronics is placed in a shielding box, shown in Fig. 4.4. The customized enclosure contains a hyper-hemispherical lens holder and a USB connection for data communication. The camera can be placed in the optical axis due to the adapter ring which is designed for Thorlabs x-y translation stage and 60-mm or 30-mm cage system. This device design is optimized for simple laboratory use and due to serial-peripheral interface (SPI), it can be easily adapted for a higher number of pixels.

Fig. 4.4. Camera enclosure with a lens holder and USB connection.

The developed multi-pixel array-based THz camera has a broadband performance of up to 1 THz. The same readout circuit is also implemented for a 6x7 pixel CMOS camera designed to meet 4.25 THz frequency. The camera was used for testing purposes of a multi-pixel array design, whereas further implementation assures a higher number of pixels and a faster readout scheme.

This implementation of the camera reaches better sensitivity than a commercial TeraSense camera, however, it is still inferior to the commercial solutions in the number of pixels. Despite this, the camera can be used for THz source imaging and other applications which are shown in Section 6.2.2.

5. NEP calibration and enhancement of TeraFET detectors

This chapter is dedicated to a brief description of the techniques used to characterize the FET-based THz detectors. As usual for TeraFETs, the main characteristics of interest were the electrical transistor characterization [15, 47] and the optical device characterization [45, 46] at room and cold temperatures [51, 116]. However, this chapter additionally overviews the detector resistance stability issues for various technologies and gives a detailed study on electrical noise fluctuations in TeraFETs which was briefly presented in [77].

The optical detector calibration technique presented in [37] was recently extended for a broadband FET optical calibration over a spectral range of TeraScan 1550 transmitter which is also presented in this chapter as well as in [38]. This technique was proven using another calibration technique of passive black body detection (presented in Chapter 6.4 and in [48]).

The cryogenic optical characterization on long-term AlGaN/GaN HEMT detector development shows the NEP performance enhancement at cryogenic temperatures. It depends on various epitaxies which were implemented during the development of FET-based THz detectors.

5.1 Electrical characterization

Electrical characterization shows the quality of the production, issues with the material system, or differences between the simulated and produced electronic element and the limitation by noise sources [98]. During the development of TeraFET detectors, all these conditions were experienced showing the importance to prove the repeatability of trivial measurements, such as noise or channel resistance measurement. An overseen measurement information might lead to a wrong conclusion for the more complex measurements as well.

The most important characteristics for TeraFETs would be the channel resistance or current $I_d(V_g)$, the gate leakage current $I_g(V_g)$, and the noise. As it was discussed before, the resistance shows the expected optical responsivity behavior. It is also a measure of the thermal noise which is the main noise source limiting the best detector performance where the second might be the leak current caused shot noise. The resistance measurements show the stability of the detector behavior as the resistance might change depending on the ambient conditions. Realization of these changes can help to further develop TeraFET technologies.

The described aspects are discussed in this section for three different material systems: (a) foundry CMOS technology; (b) GaN HEMT technology for high power electronics, and (c) research-facility fabrication of graphene TeraFETs. All the presented know-how gained via electrical characterization was used in this and the following chapters, especially for the optical calibration, cooling experiments, reconfigurable array, and near field imaging of TeraFETs.

5.1.1 Resistance measurements and stability issues

During the development of this work, electrical characterization was undertaken for hundreds of transistors. This section overviews the main differences of the electrical characteristics of various transistors and some important methods for it developed during the last years.

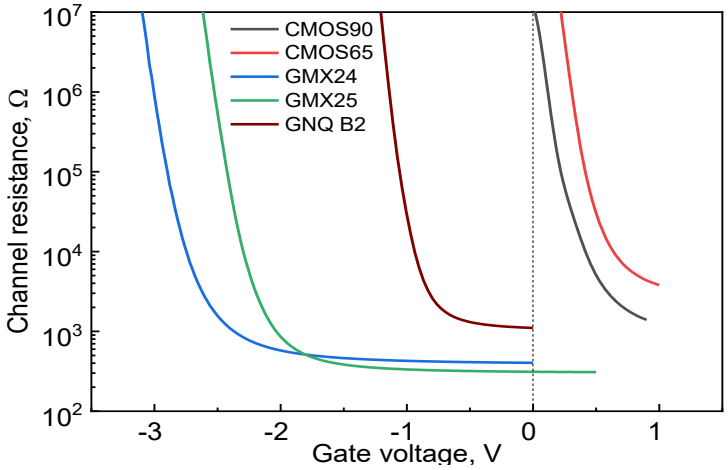

Fig. 5.1. Channel resistances of used detectors.

Fig. 5.1. shows the usual resistances of transistors in the used AlGaN/GaN and CMOS technologies. The CMOS technology is stable and therefore the resistances of the same technology are in good agreement. Therefore, this graph depicts 65-nm and 90-nm technology low-threshold-voltage transistor channel resistance. AlGaN/GaN HEMTs do differ between various technologies as well as within the same technology. The graph shows three resistances of the transistors which are presented in this work in most detail as they reach the best optical performance. GNQ transistors had lower threshold voltage whereas the GMX technology runs have the threshold voltage lower than -1.5 V. For AlGaN/GaN detectors slight variations in the resistance are expected even between the same technology transistors as shown in Fig. 5.2.

The resistance measurements presented in this work use an average of the channel current $I_d(V_g)$ measurements at V_d = ±10 mV as shown in Fig. 5.2., left. GNQ B2 device shows a good resistance agreement between the two lines expressing positive and negative channel bias conditions. In opposite, the resistance curves of the device GNQ C4 indicate unusual transistor behavior. It can be proven via gate leakage measurements $I_d(V_g)$ as shown in Fig. 5.2, right. The GNQ C4 device has three orders of magnitude higher gate leakage current than the GNQ B2 and therefore shows the need for design reconsideration. For some technologies, such as GFET or AlGaN/GaN, technological parameters are very important as they change the behavior of transistor channel resistance or gate leak current. As an example, the leakage current of GMX 23 epitaxy is depicted which shows a different dependency on gate voltage than the epitaxy called GNQ.

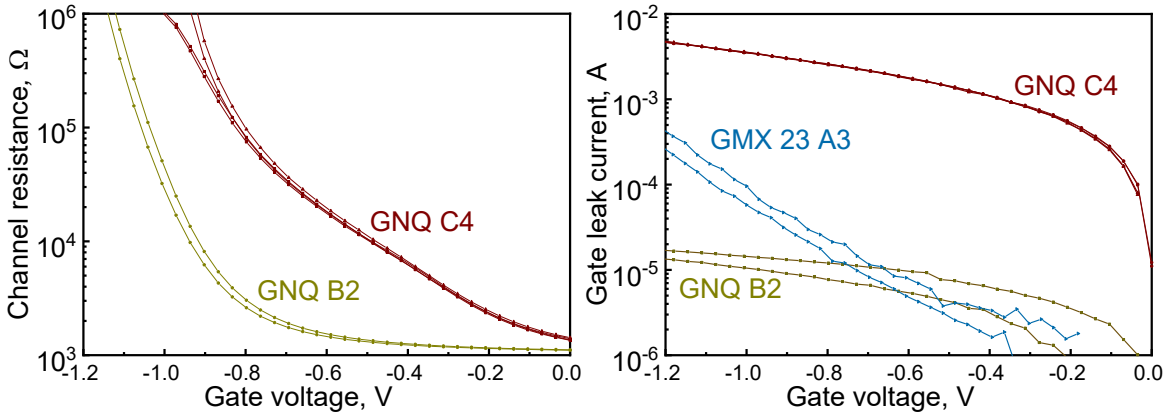

Fig. 5.2. Channel resistances (left) and gate current (right) at various technologies.

Since the resistance curve directly relates to the thermal noise and the optical responsivity of the detector, two aspects should be considered, namely, the stability of the channel resistance and the possible issues caused by resistance instability for the studied material system. Here are some important aspects presented which had to be considered before the detector performance analysis of the detectors used in this work.

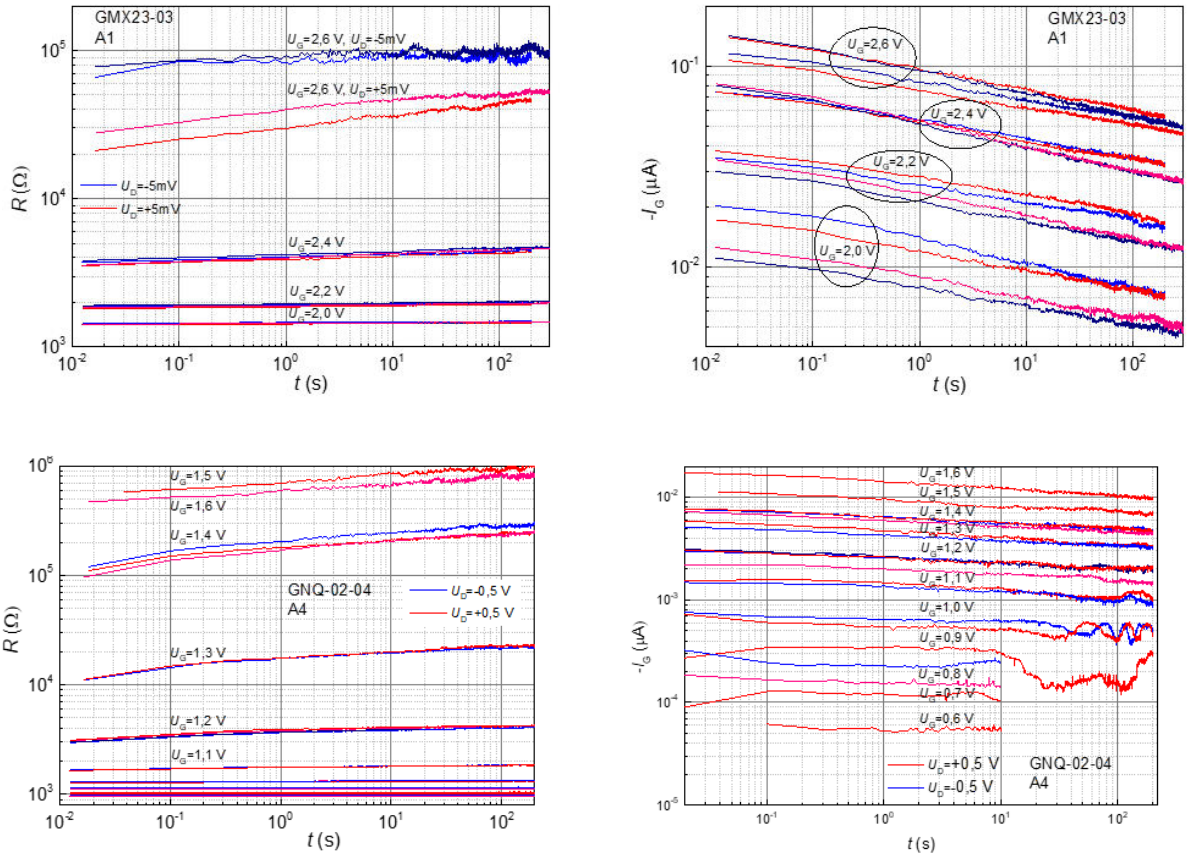

Fig. 5.3. Comparison of the carrier trapping effect in GMX23 and GNQ runs.

The first aspect is transient effects caused by charge trapping-like mechanisms which caused time-dependent resistance change in AlGaN/GaN HEMTs and graphene FETs [117, 118]. The second aspect refers to the gate leakage currents leading to some AlGaN/GaN transistor designs which led to a misleading result of the resistance measurement as well as the access noise additionally to the thermal noise [77]. The third is based on carrier generation in an indirect CMOS semiconductor at laboratory ambient illumination.

All these issues can be solved as soon as they are recognized. For example, with the changes in AlGaN/GaN HEMT epitaxy or design, e.g. the issues on gate leakage current and carrier trapping on Fe doping layer of the GaN buffer were solved. This can be done only due to the tight collaboration with Ferdinand-Braun Institute for high-frequency electronics (FBH) which has developed the AlGaN/GaN HEMT technology and can make some changes on it as well. The comparison of the difference of the trapping effect in GMX23 and GNQ runs is shown in Fig. 5.3.

The resistance instability issues found in CMOS-based detectors can be easily solved by enclosing the detector in a box which is the case for any out of the laboratory application. However, not all CMOS technologies show this issue. The latter issue on carrier absorption by the 17 nm thick Al_2O_3 gate oxide layer of graphene FETs was solved by the implementation of a vacuum chamber for current annealing and heating of a FET. The study used comparably low current and temperature up to 80 °C and was presented in [111]. The annealing procedure enables comparably good control of the resistance stability [111], however, only for the time until GFETs are again exposed to ambient conditions.

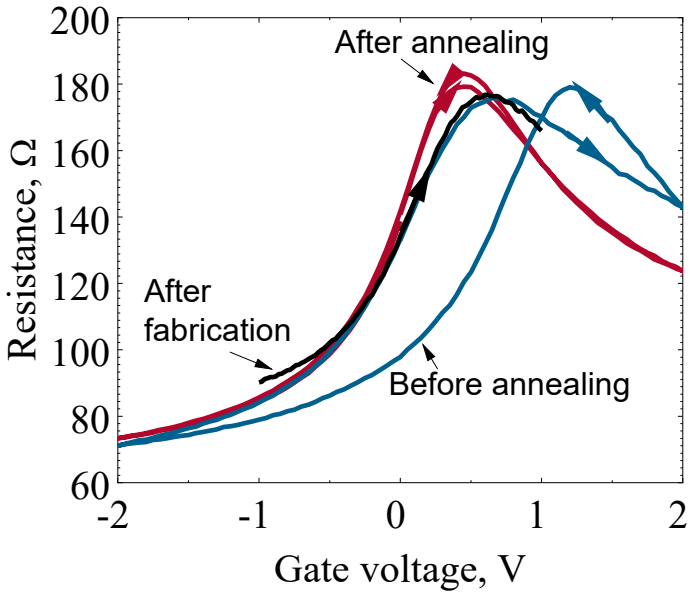

Fig. 5.4. Graphene FET resistance hysteresis stabilization by current annealing at 353 K temperature in vacuum conditions. Author's work, adapted from [77] IEEE X*plore* under © 2017, IEEE.

The GFET characterization setup is based on the vacuum chamber with a transparent high-density polyethylene (HDPE) window for optical characterization. The setup uses a standard optical characterization module [37] with two 16 W Peltier elements next to the lens holder applying the considered temperature on the detector. The experiments show good GFET resistance stability after heating up to 80 °C and current annealing with 0.3 mA current for at least 5 minutes.

The stability of the GFET plays an important role in the better understanding of the fundamental laws. Therefore, this know-how was used in the s-SNOM experiment in the FELBE facility [18], however, without the possibility to implement an annealing procedure on site.

5.1.2 Noise characterization in various material systems

In the publications on FET-based detectors, most of the time it is assumed that the unbiased transistor channel noise is limited only by the thermal noise of channel resistance. However, the noise measurements must be conducted for each new technology to make sure that the theory is valid for that material system and used technology run. To this end, the noise experiments were conducted on all three material systems. Most of the conducted experiments were presented in [77] as well as [15, 38, 46, 48, 119, 120]. This section presents the experimental noise study in more detail.

5.1.2.1 Noise measurements using noise measurement setup

To support the statements of the introduction of section 5.1.2, the noise experiments were conducted at Vilnius University in the Noise laboratory which has been built in a Faraday cage, and therefore, it is shielded from the electromagnetic radiation coming from outside the laboratory. Additionally, the noise measurement setup is shielded as well. And the measurement equipment used in the setup (especially, a self-made low-noise amplifier providing <4 nV/√Hz input voltage noise) is specifically designed for the low noise characterization of various electronics devices.

The setup for the channel noise measurements is described in Fig. 1 of [121]. The only difference in our experiment was an additional gate bias provided by an external power source for the tuning of the channel resistance as FET is a three-terminal device. All the characterized transistors were unbiased – there was no drain-source bias applied on the channel. The resistance of the channel was shifted applying gate-source voltage. Fig. 5.5 shows the spectral voltage noise density. The thermal noise is dominant over the whole frequency range. It can be seen that well above the threshold voltage, at -2.9 V and more, where the resistance of the channel is the highest, 1/f noise starts dominating. All the peaks in the spectrum correspond to 50 Hz signal harmonics from the utility power network supply.

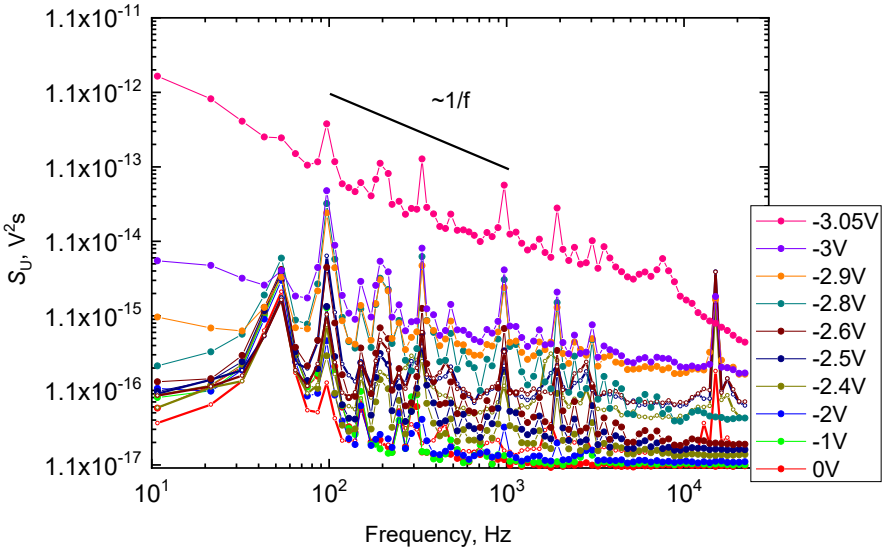

Fig. 5.5. Spectral voltage noise density of the GMX23 run of AlGaN/GaN HEMT.

To explore the difference of AlGaN/GaN HEMT epitaxy variations, noise spectral density was measured also for GNQ epitaxy. The experiment resolves that the 1/*f* noise does not show up in the whole gate voltage range for the GNQ technology run. From the measured data, the values corresponding to the thermal noise were collected, in this case, at frequencies before the roll-off. The right graph shows the measured voltage noise density at the corresponding channel resistance of the same gate-source voltage. All the values spread along the dashed line depicting the thermal noise calculation.

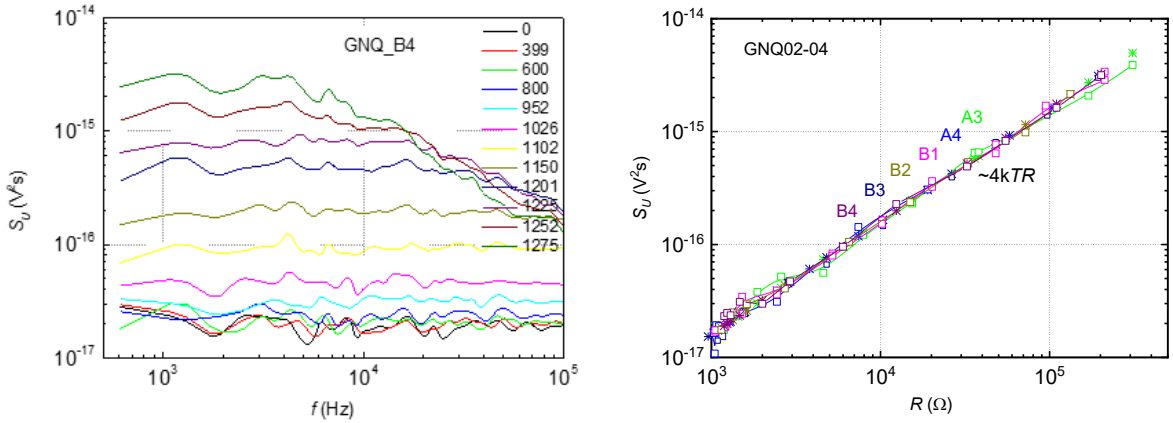

Fig. 5.6. Spectral voltage noise density of the GNQ run of AlGaN/GaN HEMT (left) and comparison with the resistance of all the detectors on the chip (right).

This experiment led to the observation of the carrier trapping effects in AlGaN/GaN HEMTs which were shown in the previous section 5.1.1 and presented in [77]. The analogous experiment has been conducted on GFETs which is presented in the same publication and

shows the need to measure the resistance hysteresis before and after the measurement which took only a couple of minutes in this case. This was enough time under applied bias voltage to shift the resistance curve (the experiment was conducted in a shielded-laboratory environment). The graph at the right shows the noise spectral density dependency on the channel resistance, which agrees well with the thermal noise approximation.

The summary of all the technologies based on the same measurement procedure is shown in the following graph. All the data points are lined up along the thermal noise approximation. The data excludes the data points which show the changes of the transistor resistance (hysteresis), as for AlGaN/GaN HEMTs [77].

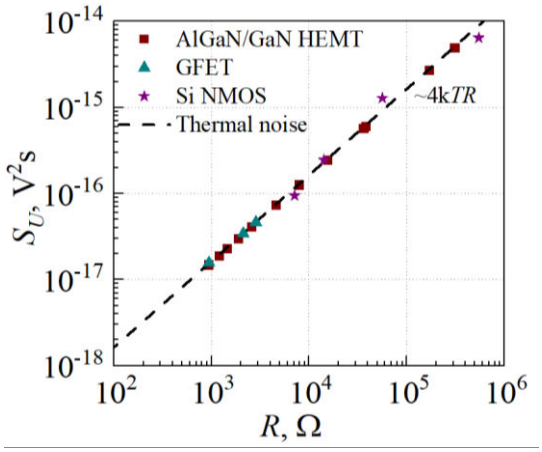

Fig. 5.7. Spectral noise density of three mentioned material systems: AlGaN/GaN HEMT, graphene FET, and silicon NMOS. The data is compared to the fundamental thermal noise (dashed line). Author's work, adapted from [77] IEEE X*plore* under © 2017, IEEE.

The conducted study on the noise of the TeraFETs opened some important aspects, such as the change of the resistance during or between a few tests of the same measurement. This observation led to the improvement of the measurement setup as some ideas on resistance measurements were implemented after finding out about the hysteresis of the resistance. Resistance stability is of high importance as it serves for the extraction of the intrinsic FET parameters and sensitivity or NEP prediction, as well for the future development of the detector design as it allows a better prediction for the impedance matching.

5.1.2.2 Noise characterization in standard laboratory conditions

The data presented in the previous chapter was measured using a noise measurement experiment conducted in a Faraday-cage environment assuring that no ambient noise influences the measurement.

In this section, various measurement techniques are discussed. The techniques were used for detector characterization in different laboratories which were not specifically built for the noise characterizations of the devices. Usually, in a standard laboratory environment,

ambient noise or even high-power equipment in other laboratories can limit the actual sensitivity range due to the increase of the noise level. Some common issues are presented here, such as lack of shielding, optical noise addition, as well as a non-trivial task to build the noise measurement setup with the equipment of the optical laboratory.

a. Noise pick-up using pulsed optical systems

During the experiments in a non-shielded environment, three types of additional noise sources were observed. Some fluctuations arose in the setup, such as 50/60 Hz frequency harmonics from the utility power network or optical noise coming from the radiation source. Other fluctuations came from the radiating equipment in the laboratory (cell phone, wireless devices, or ever a lamp). The last group of the noise sources was outside the laboratory: mobile network signals, radiofrequency towers, or even a powerful laser that was switched on two floors above. All these noises can be present during an experiment, and the known solutions to deal with the mentioned noise sources are the following: improve shielding, reduce the number of electrical loops in the setup, or simply reduce the optical noise in the setup. Although the solutions to these problems may seem trivial at a first glance, certain know-how is necessary when implementing them in an experimental setup.

The first thing starting the experiment, is to avoid the 50/60 Hz frequency signal and its higher harmonics modes as the modulation frequency for the experiment. The second thing is to avoid long cables in the setup as they have a higher capacitance than the shorter cables. The third offer before the experiment would be to check, either the measured noise equals the expected noise of the detector, e.g. TeraFET noise should be limited only by the thermal noise. Normally, the expected signal amplitude should be measured. However, during the preparation of this work, there were a few cases where this procedure did not work sufficiently well.

Two out of three cases with a strong offset of the measured noise were in the setups with laser systems. The first experiment was conducted on AlGaN/GaN HEMT-based TeraFETs in École Normale Supérieure and graphically presented in [46, 120] using an 18 fs laser pulses. The measured noise level was ≈100 times higher than the thermal noise limit. Although the detector was shielded and the possible ground loops [122, 123] were removed, the noise was still there. The issue was solved only after implementing a shunt resistance of 1 kΩ between the source and the gate.

The second experiment was conducted in DLR on the detection of QCL radiation with 90-nm CMOS TeraFETs, as presented in [15, 119] and briefly summarized in section 6.1.2 of this work. The optical noise impact (noise offset) with cryocooler-influenced signal fluctuations (narrow lines) has been seen in the TeraFET noise spectrum. The offset due to optical noise was reduced by attenuating the optical signal by 60 %. This is a useful technique to reduce the influence of the standing waves in the setup.

b. Noise measurement technique using a lock-in amplifier

Fig. 5.8. presents the noise measurement data collected with DSP7265 lock-in amplifier [124] (the same one was also used for the optical response measurements) working in noise measurement mode with current input (at the left). Considering the graph at the left of Fig. 5.8, the measured current noise is well above the expected thermal noise of the used 8.2 kΩ etalon resistor. This is due to a comparable input impedance (<2.5 kΩ at 100 Hz) of the amplifier in a low-noise mode which is the limitation of the used lock-in amplifier to measure the noise of a few kΩ resistors.

To avoid this uncertainty, one might either account for the additional resistance and back-calculate the expected noise current or use different equipment suitable for the sample load. In this case, the noise was measured using an additional SR570 transimpedance amplifier at a low-noise 10 μA/V sensitivity setting as this amplifier has a better input resistance (100 Ω) than the lock-in amplifier.

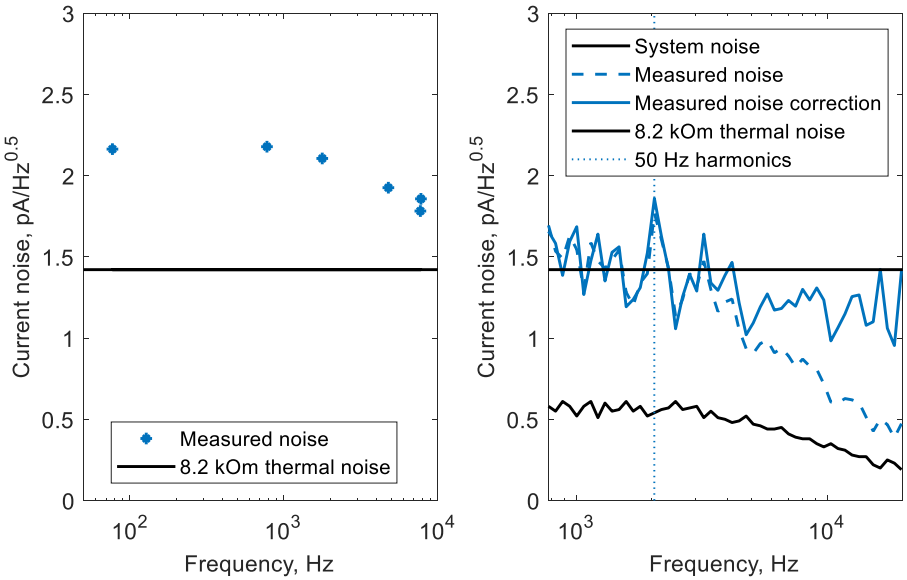

Fig. 5.8. Left: current mode noise measurement. Right: Noise measurement correction.

The performed noise measurement is presented at the right of Fig. 5.8. The measured system noise and expected thermal noise of the same resistor are depicted in black. The measured noise of the resistor is depicted in the dashed blue line with the correction of the RC limited roll-off implemented on the solid blue line. The solid line is close to the theory. This shows that sufficient noise measurement can be conducted in a laboratory environment, however, all internal parameters of the devices used in the experiment have to be analyzed in great detail first.

5.2 Responsivity calibration and measurement techniques

As presented before, the characterization of intrinsic responsivity and intrinsic NEP of THz detectors is not a very trivial task due to a wide range of unknown parameters and characteristics in the beam path. Therefore, only optical responsivity and optical NEP are characterized which are the complete-device parameters. Therefore, in this section, the calibration procedure of the optical responsivity and extraction of the optical NEP value is shown.

The responsivity $\mathcal{R}_I$ or $\mathcal{R}_V$ is calculated as a ratio between the incoming THz power P_{in} and the detected signal (current ΔI or voltage ΔV):

$$\mathcal{R}_I = \frac{\pi}{\sqrt{2}} \cdot \frac{\Delta I}{P_{in}} \quad or \quad \mathcal{R}_V = \frac{\pi}{\sqrt{2}} \cdot \frac{\Delta V}{P_{in}} \qquad \text{Eq. 12}$$

As shown in Eq. 12, it is important to take $\pi/\sqrt{2}$ constant into account. This constant accounts for the difference between the measured PP value and the expected RMS value. As it was shown in section 5.1.2, the noise of the detector is a thermal noise of the channel resistance. Optical NEP is the ratio between the detector's noise and its responsivity:

$$NEP_I = \frac{\sqrt{\frac{4k_B T}{R}}}{\mathcal{R}_I} \quad or \quad NEP_V = \frac{\sqrt{4k_B T R}}{\mathcal{R}_V} \qquad \text{Eq. 13}$$

The last optical parameter used in this work is the Signal-to-Noise Ratio (SNR) which shows how much the signal can rise above the noise level in the given optical system. The SNR is calculated as a logarithm of the ratio between the noise power P_N and detected signal power P_S:

$$SNR = 10 \log_{10} \frac{P_S}{P_N} \qquad \text{Eq. 14}$$

To measure an incoming THz power P_{in} and a detected signal, two setup configurations were uses: with a detector and with the power meter. For both configurations, the electronic RPG 500 – 750 GHz source of approx. 50 µW power level was employed.

5.2.1 Electronic tunable 600 GHz source power

To set up the detector for optical characterization, it is adjusted onto the focus of the beam, as shown in Fig. 5.9. The response signal to the incident radiation power in the focal point is measured. Then the Thomas Keating power meter is set into the THz path in an approximate position of the THz detector without moving other parts, such as parabolic mirrors and the THz source.

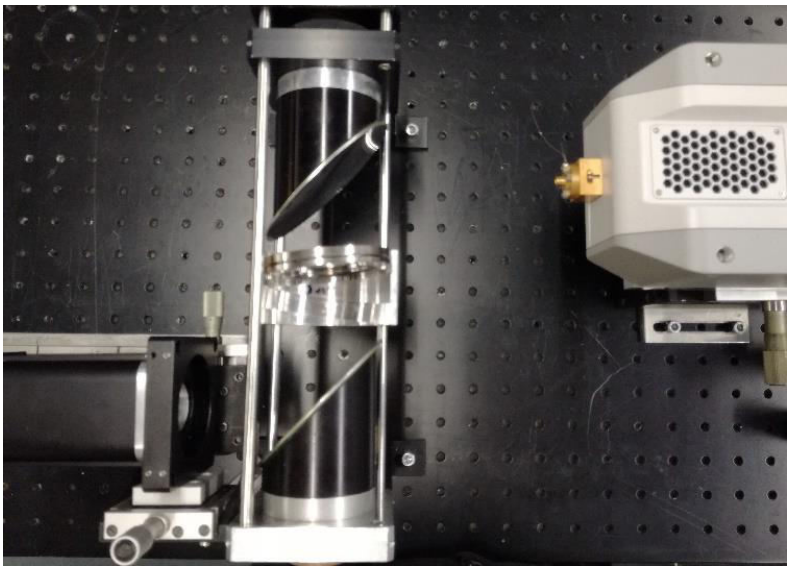

Fig. 5.9. Detector characterization setup using electronic THz source.

The incident power is measured with a Thomas Keating power meter using a lock-in technique. For the measured signal of Thomas Keating, the noise power has to be subtracted as the power meter works at its sensitivity limit under the average incoming radiation power of 50 µW. In both, power calibration and response measurements, a wide-band filter is used to reduce the back reflection from the detector which creates a standing wave pattern in the system and thus causes the uncertainty of a measured TeraFET signal. The calibration of the electronic source power using the Thomas Keating power meter is shown below.

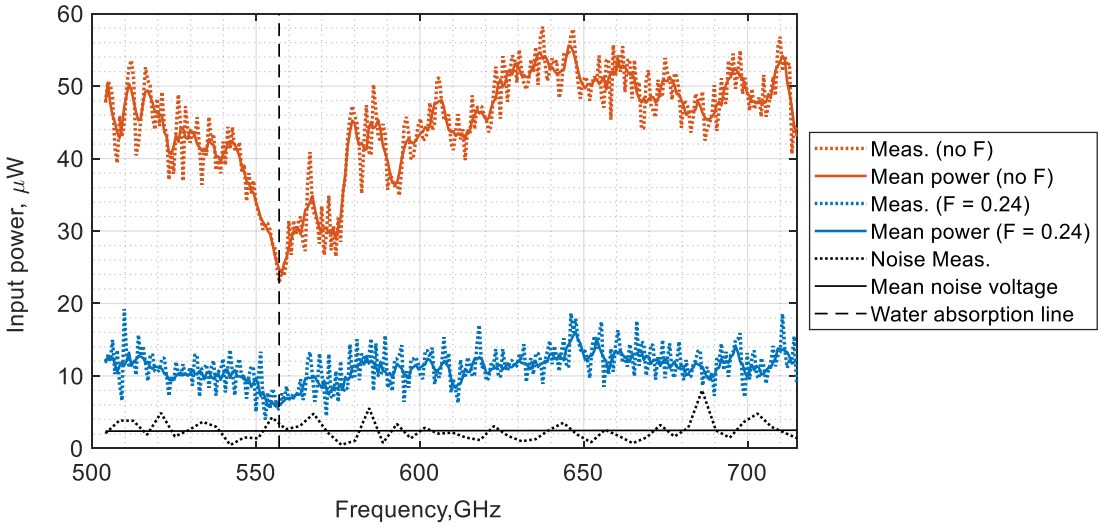

Fig. 5.10. Power calibration of the electronic THz source.

The measured data multiplied by the Thomas Keating responsivity is shown with dotted lines in Fig. 5.10. The solid lines show the mean value of each measurement: full incoming power(red), measured power with 0.24 transmission filter (blue), Thomas Keating noise measurement (black). For the power measurements close to the noise limit, the mean noise power was subtracted from the measured signal power. The dashed vertical line depicts the water absorption line of 557 GHz [125] which is present in the used frequency range.

One important aspect for the characterization of the THz detector is assuring that the optical system does not have strong standing waves such as Fabry-Perot interference, which might occur between the reflecting surfaces of the optical system or in optical elements. If the optical system has standing waves, the interference minima and maxima are expressed in the response signal. For most of the experiments, the detector is aligned for the constructive interference (maximal response signal) condition. This leads to a misleading assumption of the responsivity and NEP values, especially for a single-frequency measurement where it is difficult to assume how big is the influence of the interference as the detected signal is maximized only at a single radiation frequency. The effect can be strongly reduced attenuating the incoming radiation power for the detector alignment as well as the response measurements. The standing-wave pattern can be observed by spectral [37] or spatial scans [126].

5.2.2 Power calibration of Toptica system

This section considers the use of the commercial supplier Toptica system [127], which was implemented for broadband characterization of THz detectors. However, the coherent detection system is challenging to be used for direct detection measurements. Therefore, some important aspects of the use of the Toptica system for the characterization of THz detectors are discussed here.

5.2.2.1 Challenges of detector characterization using Toptica system

The main aspects which show up in direct detection mode using the Toptica system are multi-harmonic signals with slight shifts in the frequency and low output signal power. Fig. 5.11. shows the characterization setup using a TeraFET. As a THz source, a broadband photomixer of a Toptica 1550 system was used. The setup is depicted in Fig. 5.11. It contains four parabolic mirrors creating a middle focal point where an aperture is placed. The TeraFET couples the radiation and generates the response signal which is measured using a DSP7265 lock-in amplifier.

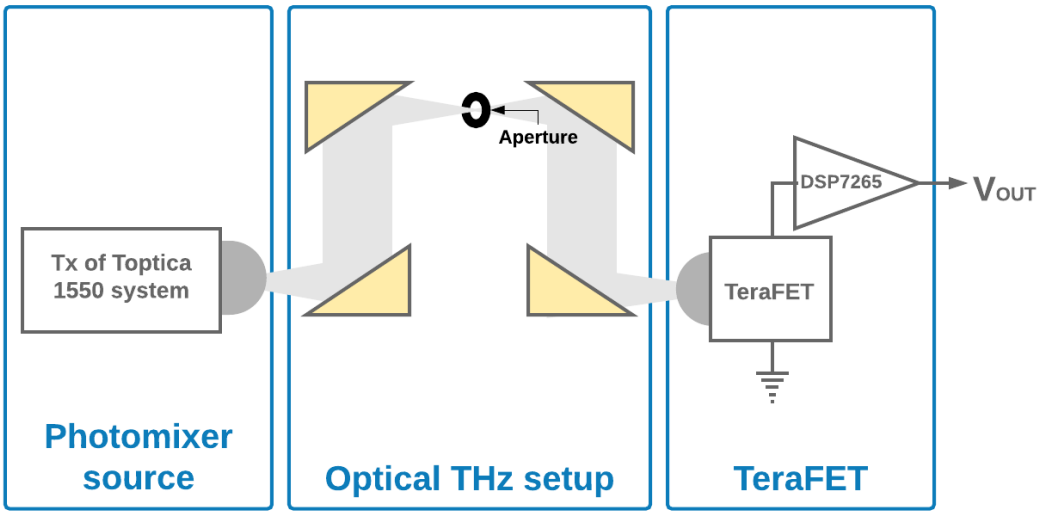

Fig. 5.11. Detector characterization setup using Toptica system.

For the coherent detection, multiple signal harmonics are not relevant, as only the mixing component corresponding to LO signal frequency is detected. However, for broadband direct detection, every generated frequency component has some contribution to the total detected signal. Therefore, measuring higher frequency components of the generated signal, an offset signal (above 1 THz) caused by the low-frequency modes can be seen as the low-frequency modes make a bigger contribution to the detected signal than actual THz frequency. This is because the TeraFETs are more sensitive at 0.1 THz than at 1 THz. This contribution is depicted in Fig. 5.12.

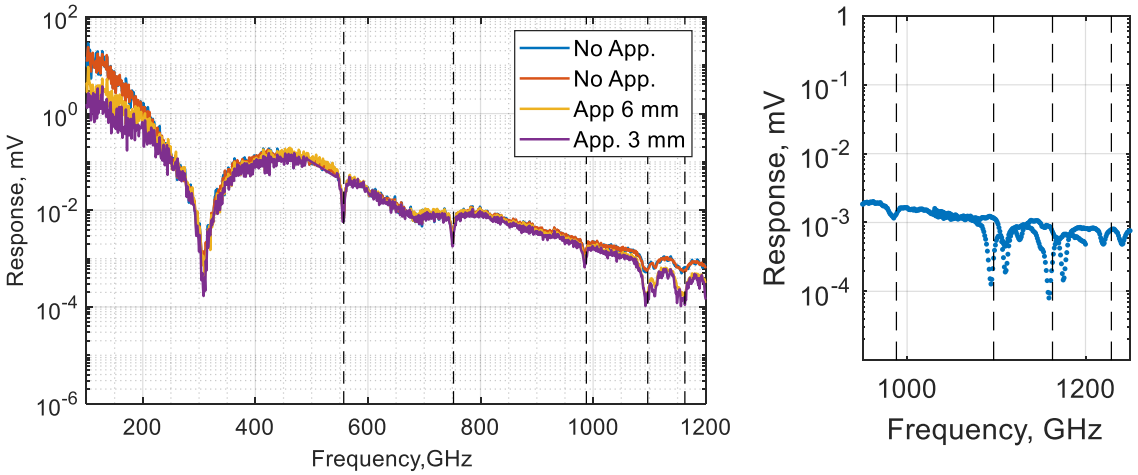

Fig. 5.12. Response signal difference with different apertures in the middle focal point (left) and frequency mismatch (right).

The signal without aperture shows an offset above 1 THz, both measurements are repeatable which is shown by plotting two measurements (blue and red). Implementing an aperture for the low frequencies blocks a part of the low-frequency component, therefore the offset is reduced. The measurement using a 3-mm aperture showed a good agreement with the expectation that the water absorption lines between 1 THz and 1.2 THz should show a 10 times lower signal. In this graph, dashed lines show the water absorption lines. The dip at 300 GHz is caused by the ring of the AlGaN/GaN HEMT-based TeraFET antenna structure.

Another aspect of the characterization, very important for spectroscopy applications, is a frequency shift by a few GHz which can be seen using two different laser configurations overlapping in frequency in the right of Fig. 5.12. This mismatch occurs due to the old calibration settings of the system. The mismatch was corrected using well-defined water absorption lines (depicted in black).

5.2.2.2 Lock-in measurement technique for the direct power detection

As the lock-in is sensitive to the fundamental frequency of the reference signal it can be used for the measurement of low-amplitude signals. It shows the RMS voltage (V_{RMS}) of the fundamental component of the input signal. For the 50 % duty cycle square wave (ON/OFF) signal, the detected voltage V_{DC} was obtained by multiplying the measured RMS value by the factor pi/sqrt(2) ≈ 2.2 corresponding to the peak-to-peak voltage of the original input square wave signal.

In case, the input signal is not close to the 50 % duty cycle square wave (ON/OFF) signal, then the correction factor can be measured to obtain the correct V_{DC} of the detector to V_{RMS} measured by the lock-in amplifier. Therefore, a measurement with the reference input signal of the Toptica system was conducted. After this experiment, it was possible to compare the calibration measurements (sensitive to the square wave) to the lock-in measurements (sensitive to the fundamental harmonic of the reference).

The measurement depicted in Fig. 5.13 shows the reference signal, and the square-wave signal generated by the Toptica system. The RMS value of the whole cycle is 25 % lower than the expected one from the theoretical estimation. Here the blue line (Ch. 2) is the modulation function of the square wave THz output of the Toptica system. The yellow line (Ch. 1) is the detected signal by TeraFET which is linearly proportional to the radiation power. Therefore, it is clear that the THz radiation pattern does not completely correspond to the 50 % duty cycle square wave (ON/OFF) signal. The ratio between theoretical and measured Cycle RMS value equals 1.9 mV/2.45 mV = 0.775.

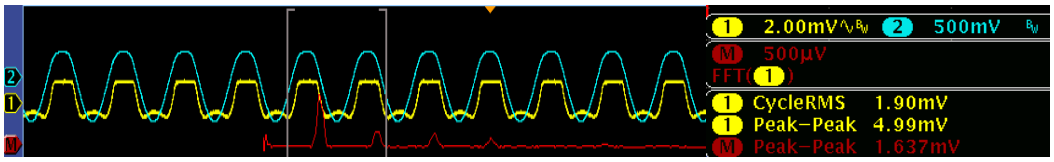

Fig. 5.13. Modulation signal comparison with THz signal.

Channel M (red) is the FFT spectra of the detected signal. The first harmonics of this signal equals the measured Lock-in signal. The first harmonic of the signal should be 0.63 times less than the Peak-to-Peak amplitude of the square wave signal. The corresponding coefficient between the induced V_{DC} voltage in the detector equal to $V_{1,PP}$ = 4.99 V and $V_{Lock\text{-}in}$ equal to $V_{M,PP}$ = 1.64 V would lead to the ratio of 3 times.

To summarize, for the calibration with the pyroelectric detector and Golay cell, the square wave modulation for THz radiation was used in the Toptica system. The same modulation should be used for the measured detector signal. The measured lock-in RMS voltage is a factor of pi/sqrt(2) ≈ 2.2 smaller than the detected signal. The measured distortion of the square wave of the Toptica system reaches 25 % in this case. As the measurement shows, this leads to an even lower measured signal than the expected V_{DC} voltage in the transistors channel leading to a better characterization of detector performance.

5.2.2.3 Power calibration algorithm

Power calibration is a not straightforward task for Toptica TeraScan 1550 system due to low THz source power and low sensitivity of calibrated devices up to 2 THz. Therefore, multiple detectors were used for the power calibration procedure, namely, pyroelectric detector, Golay cell, and TeraScan 1550 system receiver. Later, a complex power prediction algorithm was implemented for the assumption of power dependency up to 2 THz frequency. The predicted power level is used for the optical NEP calculation of TeraFETs.

The power prediction is based on three measurements in the low (LFR) and middle (MFR) frequency range of the used Toptica 1550 system:

- Pyroelectric power calibration measurement at LFR,
- Golay cell power calibration in LFR and MFR,
- Reference data of the Toptica 1550 system itself in LFR and MFR.

This data was analyzed to predict the actual system power. The following steps were included in the data analysis:

1. The analysis procedure starts with the pyroelectric power calibration. The measured data have been multiplied by 3 (Toptica system square signal distortion factor) and divided by calibrated sensitivity of the pyroelectric detector of 42.3 V/W. The power measured with a Pyroelectric detector is shown with a dark blue line (Fig. 5.14).

At 140 GHz the detected power has a peak value as the beam spot size equal to the aperture in the setup has been reached and the whole power coming from the source reaches the detector. Then the power decreases with the exponential law. Somewhere around 850 GHz, the measured data becomes very noisy as the signal power approaches the sensitivity limit of the pyroelectric detector. Therefore, the pyroelectric data is not so trustful at higher than 0.85 THz.

2. To extend the frequency range, a broadband Golay Cell for LFR and MFR of the Toptica system was used. As it is a power detector, it has the same signal dependency on the radiation power as the pyroelectric detector. Therefore, the measured Golay Cell data was normalized using a calculated ratio from the matching frequency range (0.6 – 1 THz). In this case, the normalization factor was 1.75e+03. Corresponding data is shown with light blue.

Golay cell has a very well-expressed standing wave pattern in the whole frequency range. This is due to resonances in the Golay cell. At lower than 400 GHz frequencies, the power drops due to the aperture of the Golay cell. At higher than 1.6 THz frequencies, the used Golay Cell has resonances due to water absorption as the device had lost its isolation from water vapor during the time. However, it measures power well up to 1.9 THz, where it starts being noisy and measures unexpected offset.

3. To find out the last power dependency, the complete Toptica system with transmitter and receiver was used. The measured response and noise signals were used for the power SNR calculation:

$$SNR_P = \frac{Toptica\ Response\ Signal^2}{Toptica\ Current\ Noise^2}$$

The power SNR has been normalized to the Golay Cell spectra at a frequency range from 1.443 THz to 1.588 THz where both are in good agreement and express no water absorption lines. The spectra at MFR between Toptica and Golay Cell measurements agree from 1 THz up to 1.9 THz. As the dependency of the power SNR of the Toptica system corresponds to the measured power dependence of the Golay Cell, the power curve was extrapolated up to 2.2 THz using Toptica measurement. The low-frequency range of Toptica measurement shows higher SNR than expected. The reason for it is still unknown.

4. To predict the THz radiation power in the whole range, the power points were interpolated through the whole frequency range. The interpolation allows us to exclude water absorption lines from the power spectra. We tend to avoid the overestimation of

the detector performance. Therefore, it is better to predict higher power than it could be which might lead to the wrong detector performance estimation.

The power data follows the pyroelectric measurement up to 0.89 THz. From 1 THz, the Toptica system envelope was used which follows the Golay Cell measurement up to 1.9 THz. From 0.9 THz to 1 THz the data was interpolated and checked that it is not lower than any of the measurements.

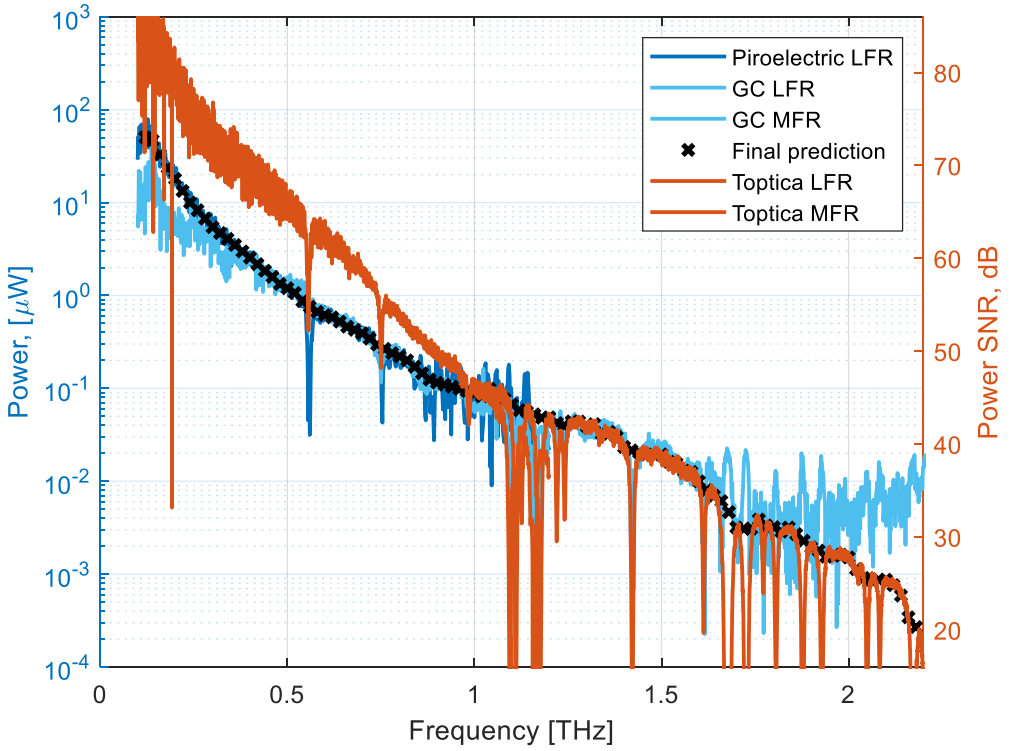

Fig. 5.14. Power calibration curves for Toptica photomixer source.

This data analysis led to the power calibration curve of the low-power Toptica 1550 system power source based on a photoconductive antenna. This calibrated curve is used for the NEP and responsivity calculation of state-of-the-art TeraFETs in Section 6.1.2 Broadband THz detectors for spectroscopy applications.

5.3 Cryogenic measurements

To explore the sensitivity enhancement and epitaxy influence on the performance of AlGaN/GaN detectors at cold temperatures, the cryogenic characterization was performed down to 77 K. The conducted work is important for the theoretical implementation of device modeling and the development of the TeraFET fabrication process in case of a need for higher sensitivity or temperature stability for future applications. It is shown in this section, that depending on the epitaxy process, completely different resistance dependency on the

temperature could be expected. The experimental results of three different AlGaN/GaN samples produced by FBH are also presented here. The result of the cooling experiments with CMOS detectors will be presented elsewhere.

5.3.1 Cryogenic experiment setup

Cryogenic measurements were conducted in collaboration with the Vilnius university team [128] using the cryogenic system presented in section 4.2.2. The optical setup with implemented cryogenic characterization module is depicted in Fig. 5.15. The system is analogous to the one described before, only the modulated signal is detected via dynamic signal analyzer instead of a lock-in amplifier and the electronic RPG source is replaced by the VDI source for the same frequency range.

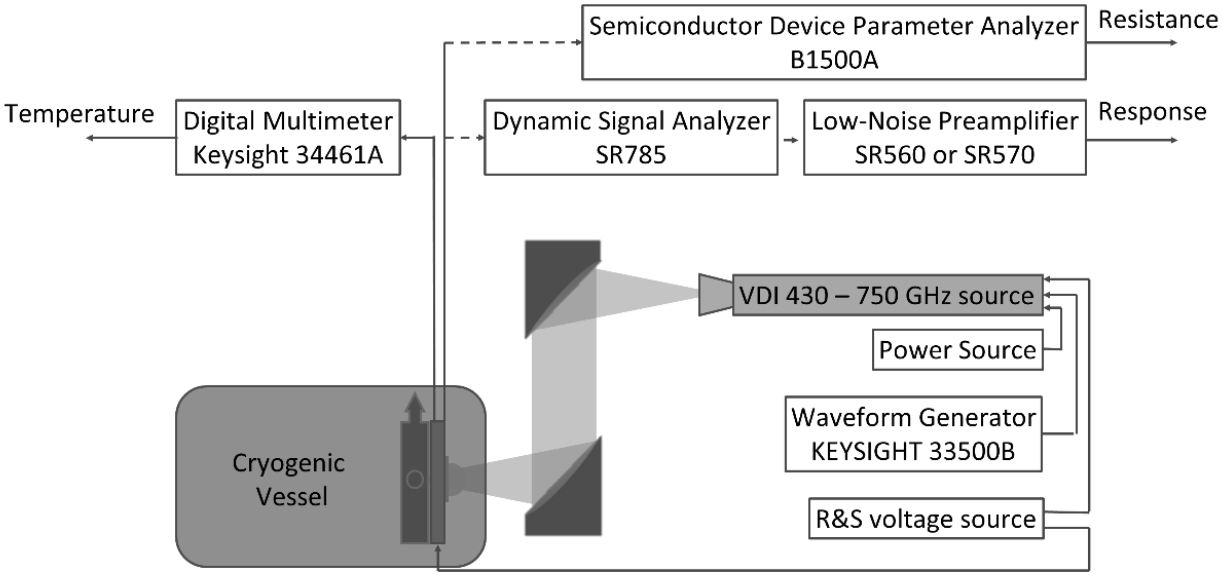

Fig. 5.15. Detector characterization setup with detector cooling. The inset shows the measured power of the VDI source.

The experiments were conducted on AlGaN/GaN samples designed and produced at FBH with different epitaxy. Table 5.1 represents the main design parameters of the samples.

Table 5.1. Investigated AlGaN/GaN detectors and main design parameters.

Name	Gate length	Gated channel width	Gate-to-channel separation	Antenna
GNQ B2	200 nm	3000 nm	12 nm	Bow-tie antenna
GMX24 TT2	200 nm	3000 nm	23 nm	Bow-tie antenna
GMX25 TT2	200 nm	3000 nm	14 nm	Bow-tie antenna

All the measured samples were designed with the same gate length, gated channel width, and the same type of antenna, where only the gate-to-channel separation was different. The detector GNQ B2 from the detector GNQ B4 presented in [37] differs only by the gate length which is only half of the length in B4 compared to B2, therefore the detector B4 has better sensitivity. However, for the prediction of the sensitivity enhancement ratio at cold temperature, the assumption is made that the detector performance enhancement is similar for both detectors as they are based on the same technology run.

5.3.2 Intrinsic detector parameter extraction

To explore the sensitivity limit of the presented room-temperature detector [37], a cooling experiment was conducted on an analogous sample with two times longer transistor channel. The experimental data were analyzed using a resistance fitting procedure presented in [45] which enables the extraction of the intrinsic technology-dependent transistor parameters. Fig. 5.16 shows the resistance dependence on the temperature at various gate voltages, the threshold voltage was set as 0 V. The right graph shows the extracted temperature dependence on the carrier mobility.

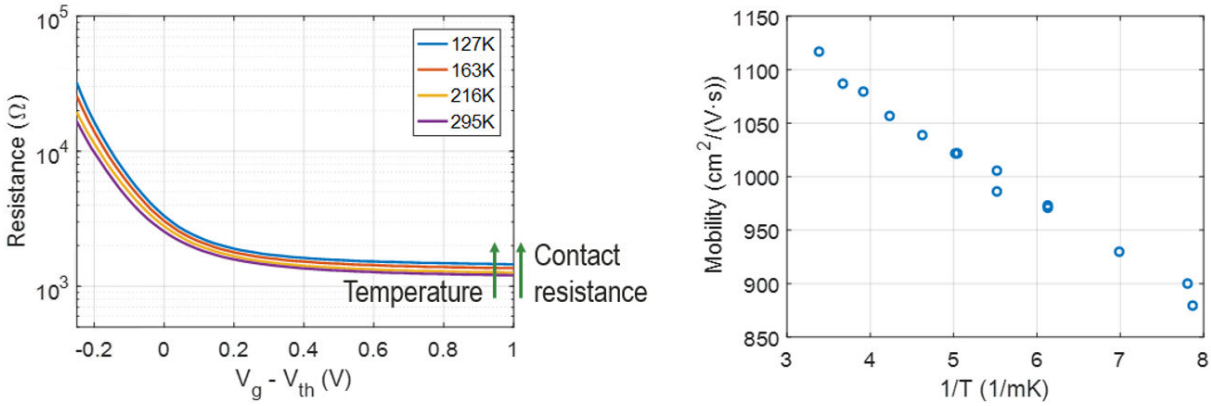

Fig. 5.16. Measured temperature dependency of GNQ B2 sample (left) and extracted carrier mobility (right).

The sample expressed irregular behavior - that the carrier mobility increases at lower temperatures. This could be explained as a complex behavior of the tens of used epitaxial layers which were designed for the best performance at room temperature. Therefore, the parasitic resistance, as well as the carrier mobility, are the best at room temperature. Despite the unusual behavior, the sensitivity limit of this epitaxy was explored, in order to know the possible sensitivity limit of the detector presented in [37]. Therefore, the optical response and the thermal noise voltage were measured at different temperatures, then optical responsivity and optical NEP were calculated. The measured and analyzed data is shown in Fig. 5.17.

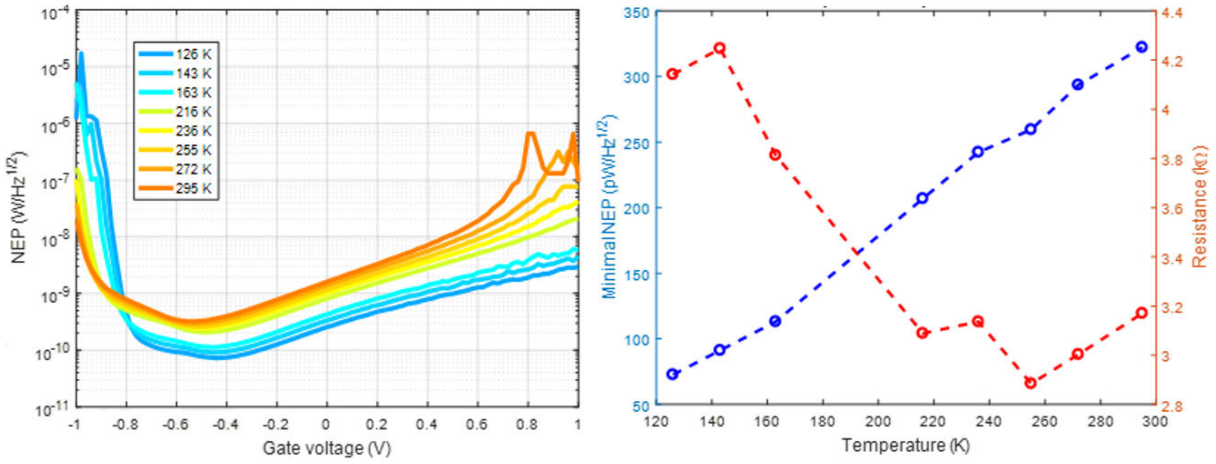

Fig. 5.17. Cooling optical experiment on GNQ B2 and temperature dependency of the measured parameters.

At the left of Fig. 5.17, the optical NEP dependency on gate voltage at different temperatures at 630 GHz is shown where each curve has an offset along the gate voltage axis so that the threshold voltage is centered. One curve is missing due to an error during the measurement at 190 K temperature. The graph shows an improvement in the temperature as well as the phase change of the detected signal at positive gate voltages which is due to carrier heating effects described in [45]. The extracted temperature dependences of the resistance and minimal NEP are depicted at the right. Despite increasing resistance at lower temperatures, the minimal NEP decreases. This dependency has a linear behavior in the measured temperature range from 295 K to 126 K where the optical NEP decreases from 80 pW/√Hz to 18 pW/√Hz.

Therefore, the detector improvement from 25.4 pW/√Hz to ≈4-5 pW/√Hz for analogous TeraFET presented in [37] at 77 K even without optimization of the epitaxial structure is expected. However, the unexpected behavior of the transistor technology demands a detailed investigation of the difference between various changes in epitaxial layers which can make the detectors more suitable for low-temperature operation or a constant NEP at various temperatures.

5.3.3 Technology development for cryogenic experiments

The following figures Fig. 5.18, Fig. 5.19, and Fig. 5.20 show the cooling experiment for the three samples described in Table 5.1 on GNQ, GMX24, GMX25 technologies, respectively. Interestingly, the parasitic resistance in all three cases has a different performance. The newer GMX24 version shows a stable resistance at various temperatures. And the newest GMX25 technology shows the expected resistance performance on the temperature, where

the resistance slope at higher than the threshold voltage gets higher and the parasitic resistance gets lower at lower temperatures.

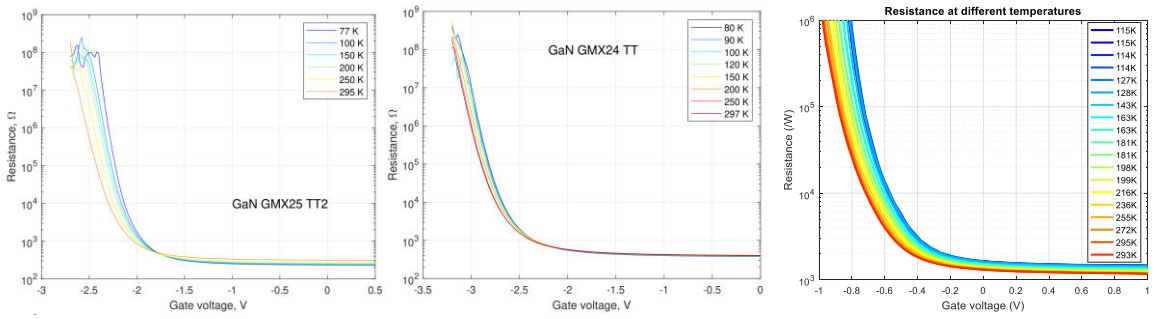

Fig. 5.18. Channel resistance at various temperatures.

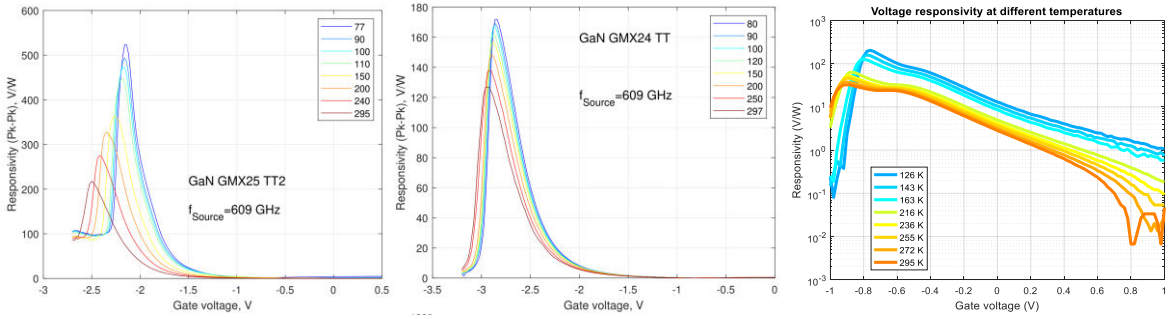

Fig. 5.19. Optical responsivity at various temperatures.

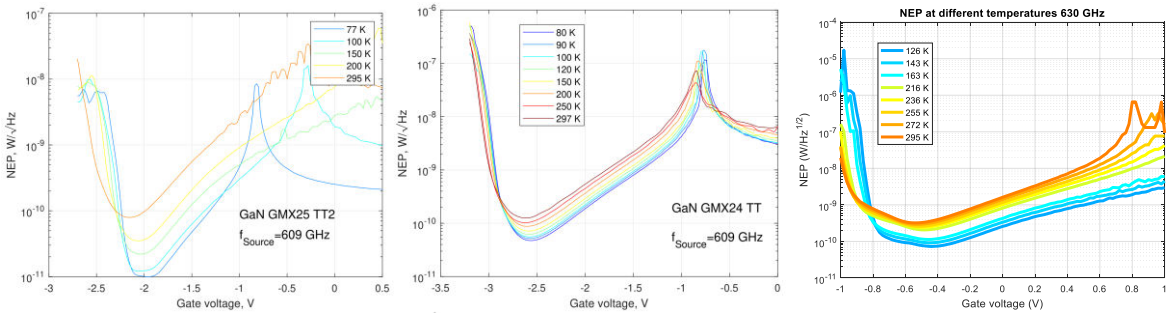

Fig. 5.20. Optical NEP at various temperatures.

The optical NEP as well as the optical responsivity of the GMX24 device shows stable behavior compared to the other two technologies. It can be therefore considered for applications in an unstable temperature environment. This feature of optical parameter stability has been presented in [129]. The improved GMX25 design shows a sensitivity enhancement by 8 times at liquid nitrogen temperature compared to room temperature which means that the epitaxial structure of this technology is far better for cold temperatures than the ones of the

previous technology runs, such as GNQ [37]. Therefore, it could be used for the sensitivity enhancement of the specific designs for applications where sensitivity is especially important.

Table 5.2. Summary of optical NEP improvement at a lower temperature.

Name	Lowest temperature	Min NEP at room temperature	Min NEP cooled	NEP ratio
GNQ B2	126 K	80	18	4.4
GMX24 TT2	77 K	47.0 (37[s])	12.6	3.7
GMX25 TT2	77 K	79.1 (45[s])	9.9	8.0

The results of cooling experiments show the sensitivity improvement at low temperatures summarized in Table 5.2. It can be concluded that the improvement at low temperatures depends on the epitaxy of the AlGaN/GaN HEMT structure. The sensitivity improvement from room to liquid-nitrogen temperature is found to be from 4 to 8 times better, similar as in [130]. As it is shown in the reference, the best enhancement of the detector response is expected at even lower temperatures.

[s] The best measured optical NEP for this detector design and epitaxy

6. Applications of TeraFETs and THz systems

This chapter presents the TeraFET applications from two sides:

- THz imaging,
- THz spectroscopy.

All presented work was conducted with different research groups what brought this work the broader view on the possible TeraFET applications.

6.1 TeraFET applications for spectroscopy systems

Spectroscopy applications in THz field play an important role as it can be useful in various fields: radio astronomy [131], chemistry [12, 132], medicine [133], security [12, 52], various industries [12], etc. Depending on the purpose, various detectors can be used, as some applications demand a broadband detection range, whereas others focus on a very narrow bandwidth around a well-known absorption or transmission line. Most of the systems use a homodyne or heterodyne detection scheme which has a very high dynamic range and can deliver the amplitude and the phase information of the electric field. Some applications, however, do not demand such information or dynamic range, but rather have space constraints. Therefore, the TeraFET can be used for such applications which is one of the most compact solutions working at room temperature for THz detection. If necessary, it can be also implemented for the homodyne or heterodyne detection to gain the previously mentioned benefits.

6.1.1 Detection of Short-Pulse THz Radiation

TeraFETs are versatile detectors as they can be used in various environmental conditions for different THz sources. In this section, the study on TeraFET applications for spectroscopy system is based on TDS system [65] of 20 THz bandwidth of 15-fs laser pulse with up to 27.5 nJ energy per pulse reaching peak power of sub-milliwatts presented in [46, 47]. The study mainly considered various detection regimes and an autocorrelation technique for the detection of the processes in the picosecond scale. The follow-up study on comparison of the detection regimes between the TeraFET and zero-bias Schottky barrier diode was conducted by researchers from Vilnius and presented in [134].

TeraFETs have a linear and a super-linear response regime to THz radiation which can be controlled via gate bias. Fig. 6.1 shows the experimental results of the AlGaN/GaN detector previously presented in [37, 46, 47]. The experiment has been conducted using a TDS system with photoconductive GaAs antenna generating 20-fs laser pulses which were modulated at 13 kHz frequency. The left graph shows the voltage response dependency on gate voltage at different THz radiation power (proportional to the square of the applied voltage amplitude of the photoconductive antenna). The right graph depicts the response voltage dependency

on the applied voltage on the photoconductive antenna in the linear and super-linear detection regimes.

Depending on the gate voltage, there are two detection regimes shown here: (i) in a linear detection regime below V_{th}, the detected voltage depends linearly; (ii) in a super-linear detection regime, to the square of the applied THz power at a gate voltage of -1.2 V. The THz response signal linearly depends on THz power in the linear detection regime depicted in the left graph of Fig. 6.1 to the right of the transistor threshold voltage equal -0.98 V. To the left of the threshold voltage, however, the response voltage has a more complex dependency on the applied THz radiation power. At low THz power the dependency is linear, whereas at higher THz power, just before the saturation, THz detector response voltage dependency has a different power of the exponent. In the presented graph it is close to the power of 2. These regimes can be manipulated by applying the considered gate voltage. It should be noted, that if the THz power is too high (not shown here), the detector gets saturated [47, 135, 136] and therefore, any of these regimes cannot be considered. These detection regimes have been observed also in CMOS-based TeraFET [47] as well as zero-bias Schottky diode [134, 137]. As it was shown [46, 135], this phenomenon can be explained by the modeling of the carrier density dependency on the gate voltage in the transistor channel.

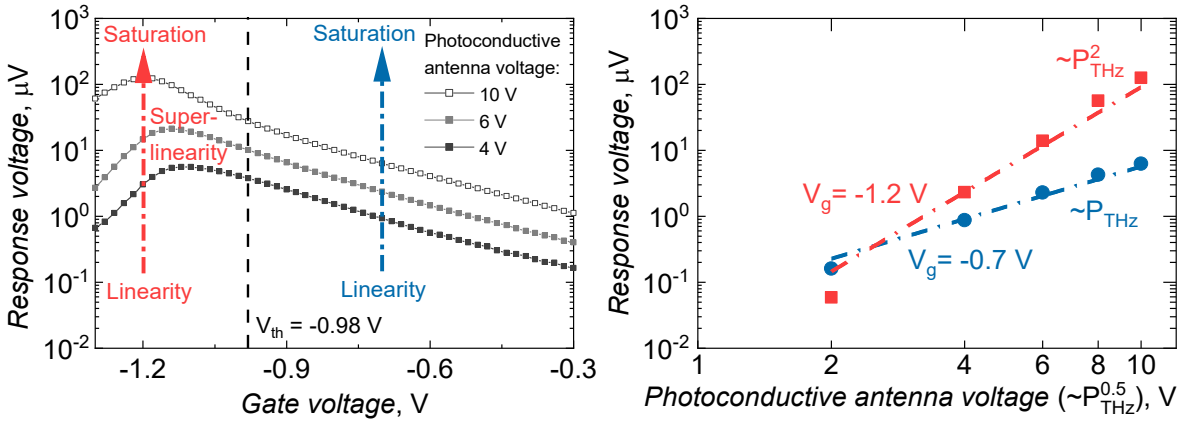

Fig. 6.1. Voltage response dependency on the gate voltage and incoming THz power. Author's work, adapted from APL Photonics [47] under © CC BY 4.0.

For the investigation of the spectral response of this detector, an interferometric autocorrelation technique [136] was used to obtain the spectral information of the detector responsivity. In [46] the responsivity was given in arbitrary units, however, after the calibration of the Toptica source power, it was possible to obtain the total responsivity of the detector after the normalization of the data into the calibration data using the electronic RPG source which is shown in Fig. 6.2.

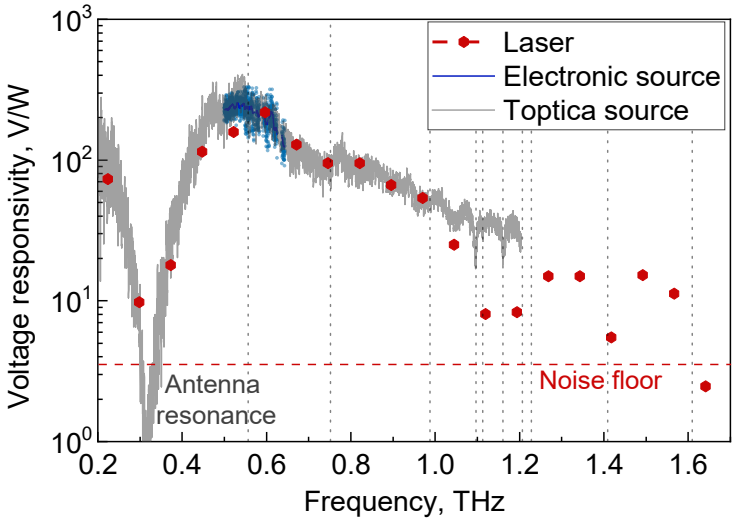

Fig. 6.2. Optical detector responsivity measured with different techniques: calibrated with electronic RPG source, pre-calibrated with Toptica source (calculated from the response data presented in [37]), and TDS measurement data (presented in [46]).

The calibration procedure was conducted in the same way as it was described in the 5.2.1 section. Some data points had to be removed as the source was not able to provide any power at some radiation frequencies. The measured data is depicted in Fig. 6.2 with blue dots whereas the thin blue line represents the averaged responsivity curve in the 0.5 – 0.65 THz range. The data at 0.5 THz can be compared to the one in [37] the obtained NEP value was 33 pW/√Hz, and optical responsivity reached 238 V/W or 68 mA/W at -1.02 V gate voltage. Slightly better optical parameters, as described in [37], might be due to a better radiation coupling in the optical system. The gate voltage for each of the experiments as well as the channel resistance and corresponding noise are given in Table 6.1.

Table 6.1. Measurement parameters.

Optical system	**TDS**	**Toptica**	**RPG**
Gate bias	-0.98 V	-1.09 V	-1.02 V
Resistance	2900 Ω	7600 Ω	3550 Ω
Noise limit	6.8 nV/√Hz	11.1 5 nV/√Hz	7.6 nV/√Hz

Another calibration (depicted in grey) was made using Toptica as THz source, where the data presented in [37] has been used with the new power calibration data excluding the power oscillations due to Golay Cell optical resonances. The calibrated power was measured in a better-aligned setup after implementing the new power calibration technique and the work point was at different gate voltage. This led to the responsivity measured with the Toptica system which was two times lower than the one calibrated with RPG electronic source. This mismatch was corrected by normalizing the whole curve to the responsivity of

238 V/W at 0.5 THz as the shape of the responsivity spectrum does not change much for the neighboring work points. The dip in the spectrum at 0.3 THz is caused by the resonance of the antenna ring and therefore, no radiation can be detected around 0.3 THz. The shape of the responsivity curve is a bit higher above 1 THz as this curve was measured without aperture and therefore, it has an offset above 1 THz caused by a low-frequency component. It was discussed in more detail before in the 5.2.2 section.

Lastly, the spectrum obtained from TDS characterization using the autocorrelation technique is presented with red dots in the graph. As the power of the signal is unknown, the data points were normalized to the previously characterized curves where some main features can be recognized. The antenna resonance and water absorption (depicted with dotted lines) can be observed in the graph. Although the spectral resolution was not high, the experiment shows that the broadband characterization of TeraFETs using this technique is possible. The depicted graph shows that this detector design is sensitive even at 1.5 THz. The dashed line shows the measured noise level normalized correspondingly to conserve the same dynamic range value.

The detector has the dynamic range of 24 dB at 1 THz and 36 dB at 0.6 THz in the direct detection regime which is comparable to the electro-optical detectors if employed in the coherent detection mode [50]. However, the direct detection regime using the autocorrelation technique is enough for the broadband characterization of the TeraFET.

Another application of autocorrelation measurement using AlGaN/GaN HEMTs could be the measurement of temporal characteristics. Autocorrelation technique using TeraFETs suits for the determination of the pulse duration of the THz source, especially in the super-linear regime where the modulation depth is much higher than in the saturation regime [47, 136]. The monitoring of the laser pulses can be led under room temperature conditions which is an improvement compared to the cryogenic cooling of the quantum-engineered devices which are used for such purposes [138, 139]. This technique enables the detection of the intrinsic rectification signal build-up time reaching tens of picoseconds and dependent on the gate voltage which is not possible to detect otherwise due to limitations of the read-out circuit [46, 47, 140].

Therefore, the TeraFETs can be employed for direct detection of THz pulses without interferometric measurement setup, if the TeraFET response time of more than ten picoseconds is enough [141, 142]. The detector is suitable for THz spectroscopy applications in both, direct as well as coherent detection schemes. The autocorrelation technique is a useful technique for the characterization of the detector's bandwidth and intrinsic detector parameters.

6.1.2 Broadband THz detectors for spectroscopy applications

For the broadband detector characterization and observation of spectroscopic features of various materials, a direct detection scheme with an intermediate focal point (depicted in

Fig. 6.3) was implemented. The system is based on the THz transmitter of the Toptica TeraScan 1550 system and a TeraFET receiver using a DSP7265 lock-in amplifier for the small-signal readout.

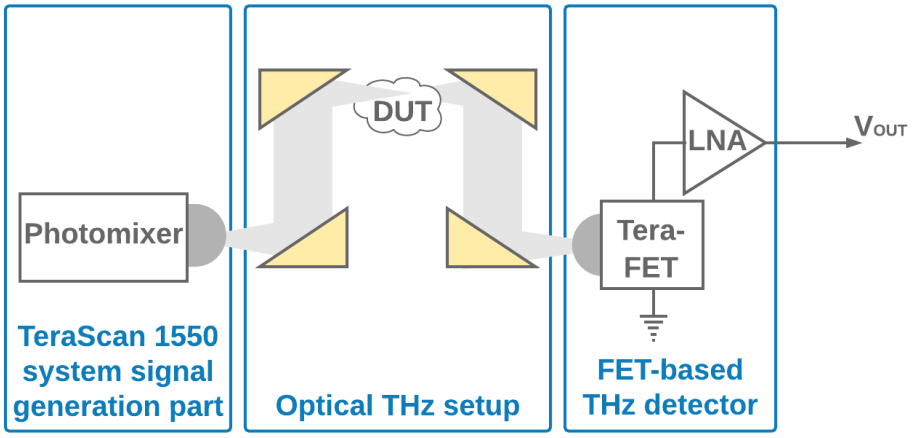

Fig. 6.3. Implemented broadband spectroscopic characterization system.

As discussed earlier, an aperture was used to measure the signal above 1 THz without an unwanted low-frequency THz signal. The reference signal to THz radiation from the Toptica system up to 2.2 THz is depicted in Fig. 6.4. The spectrum shows the spectroscopic absorption of the laboratory air which was measured using a 90-nm technology-based ultra-broadband CMOS detector with a bow-tie antenna [40]. The antenna resonance is at 0.15 THz and all the other spikes in the spectra represent absorption lines by water molecules in the air. They are depicted with black dashed lines up to 1.8 THz frequency [125]. In the given setup, the detector itself is sensitive up to 2.4 THz. The depth of the water absorption lines corresponds to the expected spectra which shows that the measurement was without the additional low-frequency offset mentioned in Fig. 5.12. Above 2 THz, where the radiation power of the Toptica source is only 1 nW or less, the detector still shows a dynamic range of 10 dB before reaching the noise level depicted by the dashed line.

Fig. 6.5 shows the comparison of AlGaN/GaN and CMOS technologies-based detectors, both with implemented bow-tie antenna. Both detectors show a broadband detection range of at least up to 1.5 THz. Detection at higher frequencies is limited by the low power of the THz source. Both antennae have a resonance absorption which can be seen in the spectrum. Due to low radiation coupling into the antenna, AlGaN/GaN detector cannot deliver the power into the transistor channel at 0.3 THz, and the CMOS detector, at 0.15 THz. CMOS detector shows a 10 dB dynamic range at 2 THz even at a very low THz source power of approx. 2 nW. AlGaN/GaN spectrum expresses a roll-off above 1.75 THz which might be present either due to a challenging optical focusing at low THz power, or due to weaker plasmon screening by the gate electrode which is placed 23 nm above the transistor channel. Despite these small differences, both technologies are equally suitable for TeraFET

development. The main limitation remains the optical and electrical coupling solution in the specific design implementation.

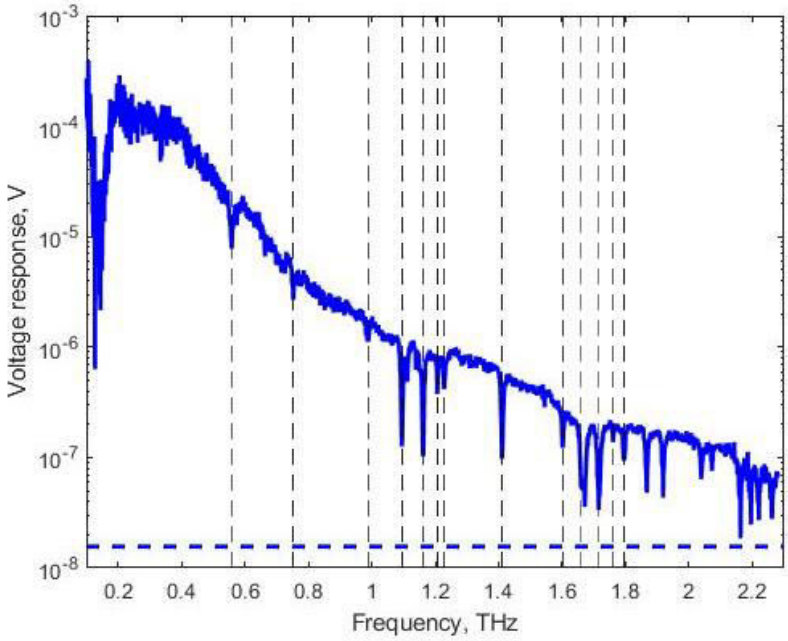

Fig. 6.4. Reference spectrum of Toptica transmitter using CMOS detector.

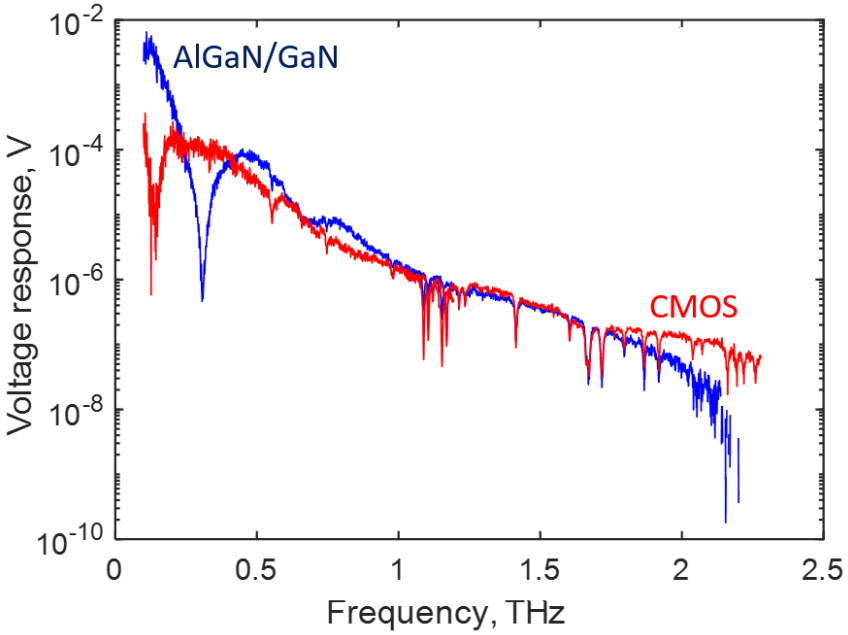

Fig. 6.5. Comparison of the measured signal between broadband detectors based on CMOS and AlGaN/GaN TeraFET technologies.

From 2016 to 2020, hundreds of detectors were electrically characterized and tens of them were characterized optically. All of them were based on AlGaN/GaN, CMOS, and GFET

technologies with various antennae. Table 6.2 shows the best-characterized detectors and the main technology description as well as the best measured NEP at specified frequencies. As one can see in Table 6.2, some of the scientifically significant detectors were published whereas others were not published at all due to their rather incremental improvement. The resonant detectors are the best at a resonant frequency, as they have a better impedance matching at the chosen frequency. The wideband detectors express the best NEP on the designs with implemented bow-tie antenna.

Table 6.2. Investigated TeraFETs and main design and operation parameters.

Name	Antenna	Antenna type	Min optical NEP, pW/√Hz	Frequency, THz	Gate-to-channel separation/ Technology	Published
GNQ B4	Bow tie	Wideband	25; 33	0.5; 0.6	12 nm	[37]
GNQ B2	Bow tie	Wideband	81 (after gluing)	0.63	12 nm	N/A
GMX24	Bow tie	Wideband	37	0.5	23 nm @ -2.6 V	N/A
GMX25	Bow tie	Wideband	45	0.5	14 nm @ -2 V	N/A
GaN 6x7	Slot bow tie	Wideband	44; 100	0.28; 0.48	N/A	[143]
300 GHz	Slot + dipole	Resonant	19	0.3	90-nm CMOS	[35, 36]
600 GHz	Dipole	Resonant	17	0.49	90-nm CMOS	[40]
Proxi3 BT	Bow tie	Wideband	48; 70	0.6; 1.5	90-nm CMOS	[40][t]
CELTA D53	Biquad	Wideband	25	0.84 – 1.29	65-nm CMOS	[38]
CMOS 4.75 patch	Patch (no lens)	Resonant	404[u]	4.75	90-nm CMOS	[15]
GFET C2_7_5	Bow tie	Wideband	662[v] 515 (published)	0.3 @ 0 V	17-nm Al2O3	[43][w]

The optical NEP of the measured detectors is depicted in Fig. 6.6. Two resonant detectors for 0.3 THz and 0.5 THz (designed for 0.6 THz) are depicted in green. They reach the NEP of

[t] Also compared to the design with a log-spiral antenna
[u] Cross-sectional NEP
[v] Measured personally, cross-sectional NEP
[w] Published measurement was made with a better focusing condition

19 pW/√Hz and 17 pW/√Hz, respectively. The detectors for the wider frequency range usually are less sensitive. However, the presented detectors reach state-of-the-art quasi-optical detector performance using a lens coupling. The best of all are GNQB4 [37] and CMOS BT [40] detectors. All wideband AlGaN/GaN detectors (depicted in shades of blue and magenta) experience the sensitivity drop at 0.3 THz due to the designed ring structure discussed in [37]. However, the slot bow-tie antenna design used in the 6x7 pixel array design has a sensitivity enhancement at 0.28 THz frequency but is less sensitive at higher frequencies where the bow-tie antenna implementation is more promising.

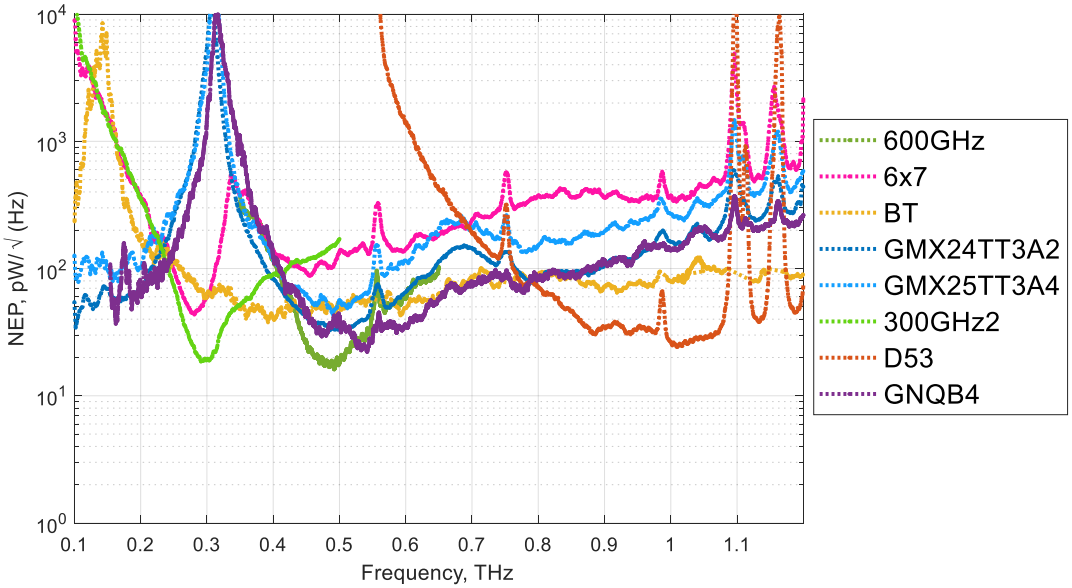

Fig. 6.6. Summary of the optical NEP of measured detectors in AlGaN/GaN and CMOS technologies. Data on these detectors were published in following papers: 600 GHz detector [144], 6x7 array [143], bow-tie CMOS detector (BT) [40, 144], 300 GHz detector [35, 36], bi-quad antenna design in CMOS (D53) [38], GNQ B4 on AlGaN/GaN technology and bow-tie antenna [37].

The presented CMOS detectors are presented in shades of orange. BT detector [40] has a nearly flat frequency response up to 2.2 THz with the optical NEP of 48pW/√Hz and 70 pW/√Hz at 0.6 THz and 1.5 THz, respectively. The optical responsivity of this detector reaches 45 mA/W or 0.22 kV/W. The D53 detector [38] designed for the best sensitivity around 1 THz is below 25 pW/√Hz in the frequency range of 0.84 — 1.29 THz. This result is only 2 times worse than the best narrowband detector presented in the literature.

TeraFETs can be compared to commercially available thermal detectors. Fig. 6.7 shows the SNR normalized for 1 Hz ENBW of the presented CMOS TeraFET with bow-tie antenna, and two commercial detectors from our laboratory: Golay Cell and Thomas Keating power meter. All the measurements were conducted in the same system with Toptica transmitter as THz source. As one can see, the Thomas Keating power meter cannot be used for the calibration

of the Toptica system as the power is too low (0.04 mW at 0.1 THz) to be measured above 0.2 THz. Therefore, a Golay Cell was used to get the preliminary calibration of the THz power. However, some additional minima and maxima along the whole frequency range can be seen which is induced by the constructive and destructive interference in the cell. This pattern introduces uncertainty of the calibrated data.

The performance of the CMOS TeraFET exceeds the dynamic range of the used Golay Cell by more than 5 dB and is only limited by the antenna resonance around 0.15 THz. The TeraFET is also much faster than the Golay Cell. For this TeraFET detector, the response signal to THz radiation was measured in the complete Toptica frequency range. This performance shows the outstanding broadband sensitivity reachable using a TeraFET. Despite an outstanding room-temperature SNR performance, the direct detection is always limited at least by the thermal noise of the detector, which compared to the sensitivity of a Toptica photomixer working in the coherent detection scheme is around 30 dB higher [37]. Similar sensitivity could be achieved also with the TeraFETs working in the coherent detection scheme [50], however, such setup implementation would be bigger and more complex.

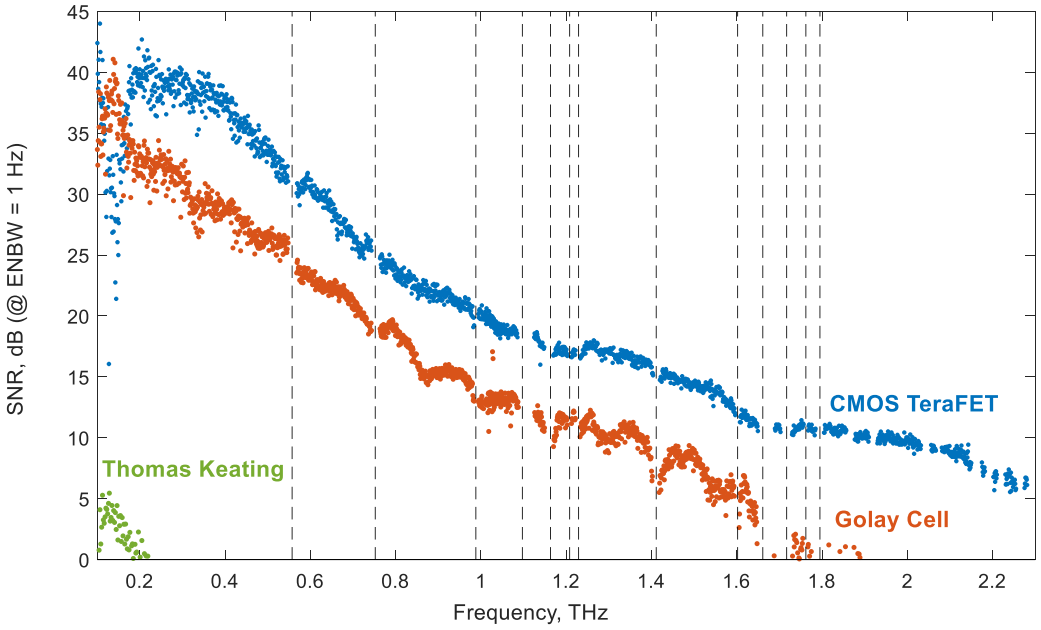

Fig. 6.7. TeraFET comparison with commercial technologies.

To sum up, broadband sensitivity can be used for spectroscopy applications where the transmission or reflection of the signal is in the given dynamic range at similar or higher THz power. For this reason, the next chapter presents spectroscopic room-temperature metamaterial and THz filter characterization.

6.1.3 Broadband spectral characterization of THz filters and metamaterials

A strong light-matter interaction in resonant cavities has a strong research interest in quantum electrodynamics as it is promising for quantum computing and quantum information processing [145–147]. The strong coupling in cavity quantum electrodynamics has been demonstrated in various systems, such as atoms, quantum wells [148, 149] and dots [150], 2D electron gases [151, 152], etc. This section presents a new approach of dielectric photonic crystal cavity for the research on strong coupling between photons and localized surface plasmons. This study was published in [49].

In this section, the dielectric photonic crystal cavity approach is presented as a new way to exploit the strong light-matter interaction. Despite the low density of quasi-particles and relatively broad resonances of the metamaterials, the results show a strong coupling regime with a high Q-factor. Hence this research is of interest for fundamental research as well as applications of voltage-controlled modulators and frequency filters, ultra-low-threshold THz polariton lasing, or ultra-sensitive biological and chemical sensing.

Here, the split-ring resonator (SRR) study is summarized which was also presented in more detail together with Swiss ring metamaterial experiments in [49]. The research on SRRs has been conducted using a continuous-wave Toptica system which has a few times better resolution than the TDS system used for Swiss ring MM experiments. TDS system resolution of 5 GHz is limited by the time-domain scanning range of 200 ps. Therefore, the resolution of the Toptica system can reach ~1 GHz resolution which depends on the SNR of the system and measured signal analysis algorithm. The resolution can be improved even further by replacing the receiver of the Toptica system with a TeraFET, as it is a power detector and therefore can measure each frequency point in the sub-GHz step.

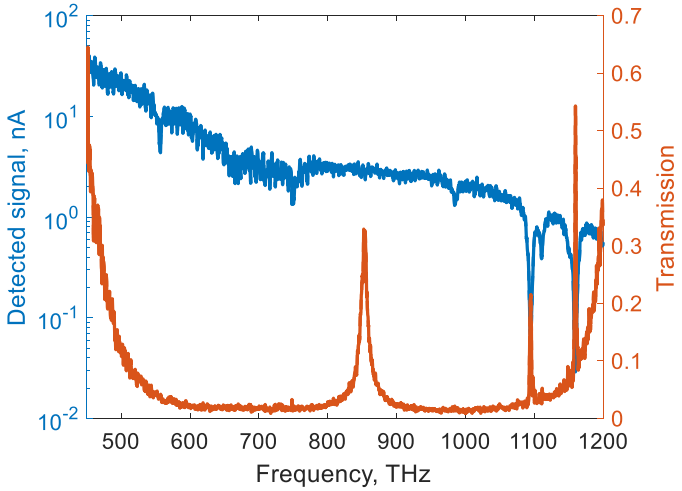

Fig. 6.8. Detected Toptica TeraScan 1550 signal as a reference for all the transmission measurements (blue). Cavity mode with the resonance peak at 854 GHz is shown in red.

The reference signal of the Toptica system is shown in Fig. 6.8. It has the highest power at lower frequencies and the clear presence of water absorption. This curve has been used as a reference signal for all the following transmission measurements. The example of the transmission spectra is shown in red. It shows the transmission of a photonic crystal cavity mode.

The main parameters of a cavity quantum electrodynamic system for characterization of the interaction between the cavity photons and the material are the following: population decay rate of the cavity photons κ, population decay rate of the photo-excited material state γ, and the coupling strength g, where $2g$ is the Rabi splitting. These parameters can be used to estimate the coupling regime, where $2g < (\gamma + \kappa)/2$ shows the weak coupling, and $2g > (\gamma + \kappa)/2$ corresponds to strong coupling. If the coupling is even stronger and reaches $g/\omega_C > 0.1$, then the regime is defined as ultra-strong coupling regime and the $g/\omega_C \approx 1$ is a deep strong coupling regime [153].

6.1.3.1 Split ring resonator in a 1D THz photonic crystal cavity

The structure of the used typical 1D THz photonic crystal cavity is shown on the left of Fig. 6.9. A single resonator (yellow) represents a layer of a periodic structure of multiple resonators of the same shape. Five polished silicon (ρ > 5 kΩ·cm) slabs (shown in gray) were separated using metal ring spacers. The layer carrying the resonant metamaterial structure is called the defect layer. The central defect layer is 50-µm thick and two outer pairs of slabs are 23 µm thick and form Bragg mirrors from both sides. Each layer is separated by 96-µm air gaps (white) formed with 6 mm and 13 mm inner and outer diameter metal spacers, respectively.

The electric field distribution (relative to the incoming light amplitude E_0) within the bare photonic cristal cavity was calculated using the transfer matrix method and is depicted at the right. Gray intervals represent Si dielectric layers where the white ones show the air gaps. The structure containing five silicon layers with a high refractive index ratio between the air and silicon interfaces creates a high Q-factor cavity mode.

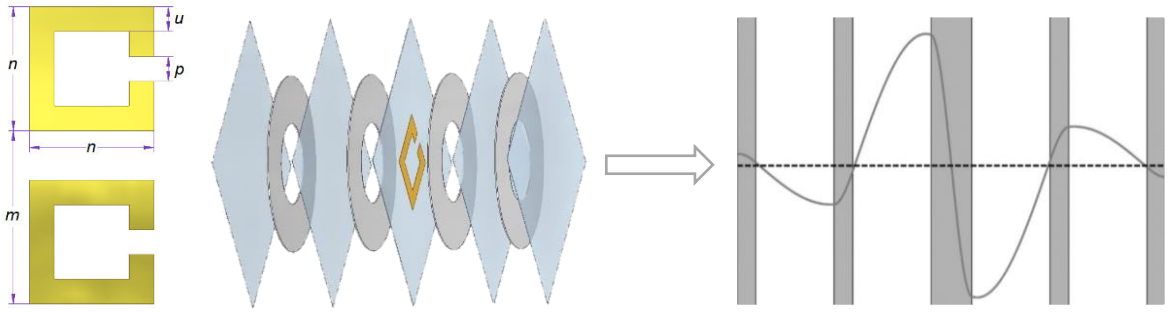

Fig. 6.9. Dimensions of the split-ring resonator (SRR). The stack of photonic crystal cavity with SRR and corresponding electric field distribution (the latter adapted from [49] under © CC BY 4.0., simulation by Dr. F. Meng).

Calculation using the transfer matrix method shows that on the opposite sides of the defect layer the electric field has two amplitude maxima of the opposite polarities. Therefore, strong electric coupling is expected for the elements placed on any surface of the defect layer. The defect layer locks the cavity mode at $f_C = 0.86\ \mathrm{THz}$ with the full width at half maximum (FWHM) of 10 GHz which corresponds to a Q-factor of 86.

The strong coupling of the metamaterials with cavity photons was the focus of the research. The SRR metamaterial has been chosen for the experiment [37]. The resonance frequency (f_m) of the SRR metamaterial has been varied using different structural parameters depicted in Fig. 6.9. The size parameters *u* and *p* were fixed both to 6 µm, where *n* has been chosen to be from 30 µm to 22 µm and period *m* from 75 µm to 55 µm for the respective resonant frequencies f_m of 0.64 THz to 0.99 THz. All the designed structures have been created by depositing gold on the defect layer surface and assembling the complete stack of photonic crystal cavity. The conducted experiment with these structures is shown in Fig. 6.10 and Fig. 6.11.

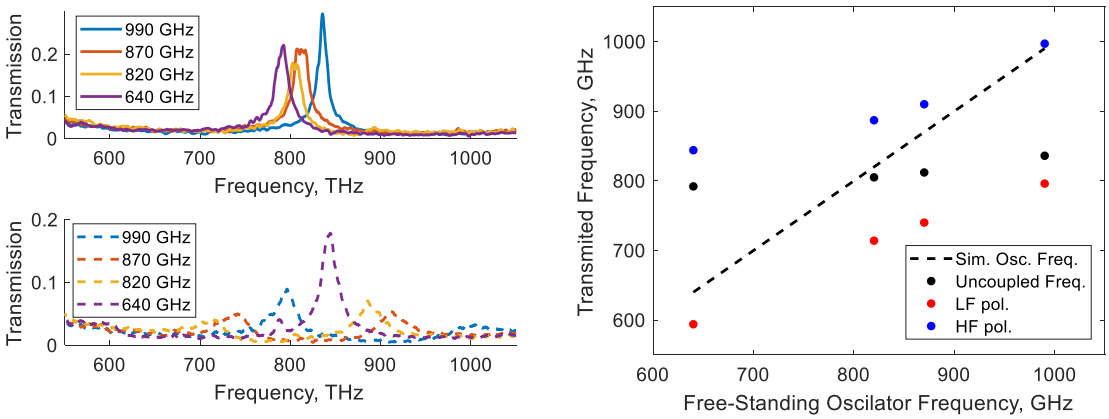

Fig. 6.10. Left: The transmission of SRRs in the cavity (left) at 90° and 0° polarization. The legend indicates the resonance frequency of the SRR metamaterial on the Si wafer. Right: The oscillation frequency of the coupled SRR with the photonic crystal cavity mode is depicted in the right figure. This data was also presented in [49], Fig. 3c-d.

The transmission of SRRs in the cavity (left) where the bottom picture shows the induced polariton modes and the top picture shows the modes excided by 90° polarization. The legend in both pictures indicated the corresponding calculated resonance frequency of SRR metamaterial on the Si wafer. It can be seen that the resonance frequency of the cavity mode is equal to 0.86 THz and the resonance frequency of the metamaterial is coupled together and therefore there is a mode splitting into two polariton modes. The oscillation frequency of the coupled SRR with the photonic crystal cavity mode is depicted in the right figure. The *x*-axis (as well as the dashed line) shows the calculated SRR on Si wafer frequency, and the *y*-axis depicts the induced frequency mode. Blue and red dots correspond to the polariton

modes whereas black dots show the case of a 90° rotated sample for the case where polariton modes cannot be induced. The behavior of the polariton modes can be explained by coupled harmonic oscillator model.

Similar to the previous experiment with different resonator parameters, an experiment on different resonator unit-area densities was conducted which shows how the SRR cells collectively interact with cavity photons. This time the resonator parameters have been kept the same for all the samples and only the period between unit cells *m* has been varied, namely, 40, 44, 52, 62, 82, and 94 µm, giving the SRR density from 6200 m^{-2} to 1100 m^{-2}. The frequency difference (Rabi splitting) between the polariton resonances of the conducted experiment is shown in Fig. 6.11. It corresponds to the square-root dependence or the resonant frequency separation which depends on the unit cell density. The Rabi splitting is bigger at a higher unit cell density.

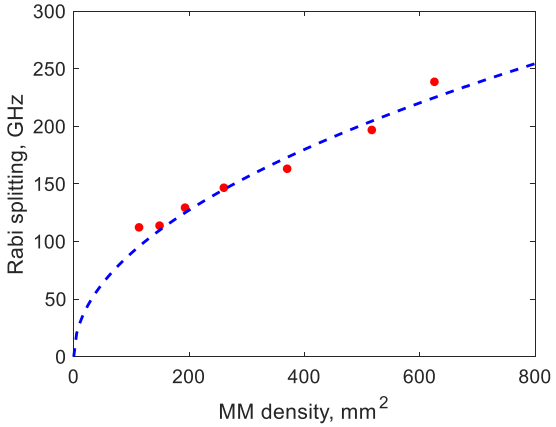

Fig. 6.11. Polariton mode splitting dependency on the density of the unit cells of the SRR extracted from the measured data. The blue curve depicts square root dependency.

These experiments show a good identification of the interaction of the photonic crystal cavity with the metamaterial unit cells. This interaction can be calculated from the polariton frequency splitting. The experiments are relevant for future applications, such as spectroscopy as they explain the main principle of the cavity and metamaterial interaction and can be used for frequency tunability, switching, polarization, and other effects.

6.1.3.2 TeraFET in a spectroscopic system for metamaterial and THz filter characterization

The same experiment was performed but on a slightly different metamaterial photonic cavity using a broadband TeraFET with a bow-tie antenna as a THz detector. The experimental data is depicted in Fig. 6.12. The top figure shows the measured reference signal under the total incoming power condition (blue) and the reference signal power transmitted through the metamaterial sample (red). The calculated transmission coefficient is depicted in the bottom figure (black). The data is compared to the TDS experiment on the same

metamaterial. Here, all the water lines have been removed from these experiments for clarity.

The strong coupling of the metamaterial sample with resonance at 0.88 THz splits the cavity mode (0.86 THz) into two polariton modes at 0.70 THz and 1.02 THz. This can be seen in the TDS experiment. However, the measurement with TeraFET does not show the 1.02 THz mode as the power of the Toptica system is too low and only the signal of more than 5 % transmission could be distinguished from the noise level at 1 THz. The blue area in the graph shows the frequency range which cannot provide a sufficient dynamic range for metamaterial characterization with a transmission coefficient above 5 %. However, the detection at 1 THz could be improved using the TeraFET designed for higher frequencies [38] which is 4 times more sensitive than the presented device at 1 THz.

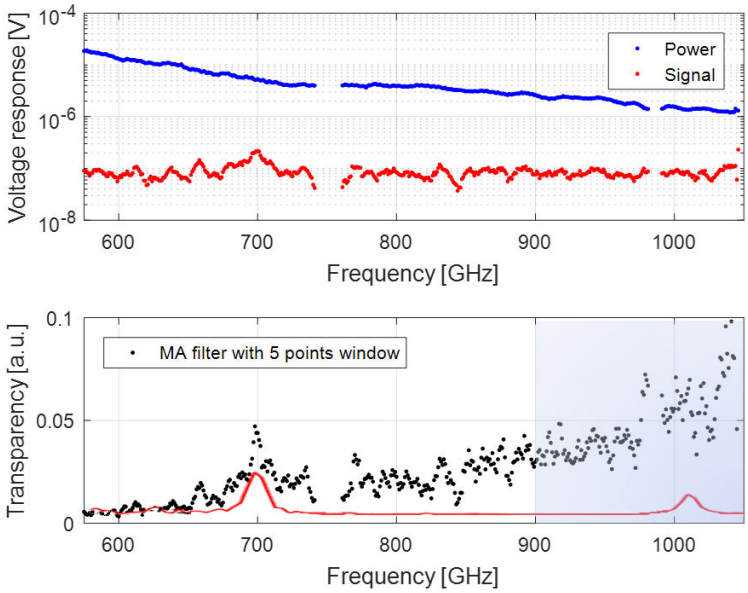

Fig. 6.12 Metamaterial photonic cavity characterization in Toptica and TDS systems. TDS experiment made by Dr. F. Meng.

Metamaterial characterization was one part of the experiment, which was intended to explore the sensitivity limit of the detector. Another experiment on multilayer THz filters has been conducted using the Toptica system with the TeraFET detector. The experiments on two filters are shown in Fig. 6.13 without the water absorption lines marked with black dashed lines for clarity. The red line corresponds to the detected signal under total radiation power where the black line shows the noise level at 1 Hz bandwidth. The blue dots depict the signal of the sample in the top figures and the transmission of the sample in the bottom figures. The black line in the left bottom figure is the predicted transmission factor using the transfer matrix method made by Dr. F. Meng.

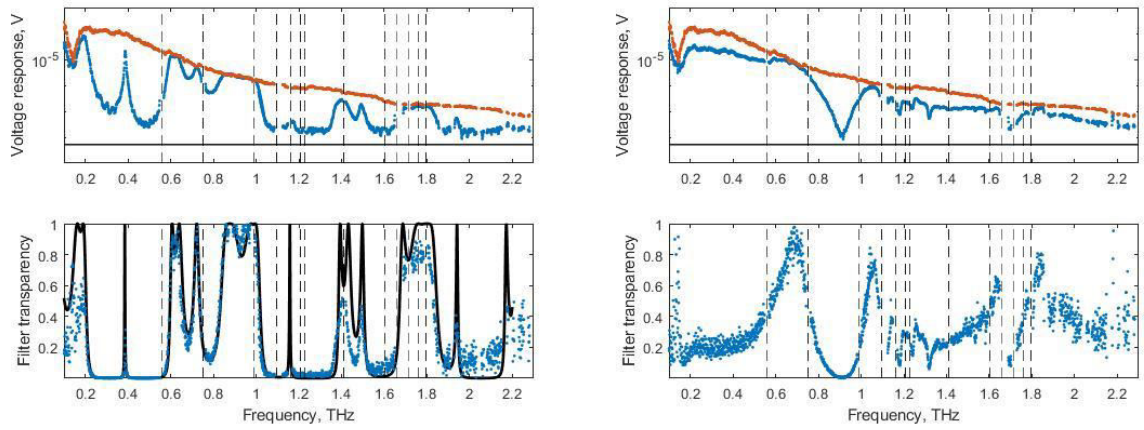

Fig. 6.13 Multilayer THz filter characterization spectra (blue). The measured signals are in red and modeled filter transmission is shown in black (left bottom figure).

In the whole frequency range, the modeling data agree well, except for the frequencies below 0.2 THz where the aperture of the sample holder blocks the radiation power and higher frequencies than 1.4 THz. This is due to the low THz source power.

Toptica system enables spectroscopic characterization in the frequency range of 0.1 THz – 2.4 THz (possibly 2.7 THz). Combined Toptica THz source with TeraFET detector system can be easily applicable for different applications. However, the standing waves in the setup and low transparency coefficient (or low THz source power) of the metamaterial spectrum are still relevant issues.

6.1.4 TeraFET for measuring power fluctuations of 4.75 THz QCL radiation

In this section, the TeraFET application in GREAT (German REceiver for Astronomy at Terahertz frequencies) spectrometer of the Stratospheric Observatory for Infrared Astronomy (SOFIA) is considered. As the observation laboratory is a modified Boeing 747SP jetliner equipped with scientific equipment and flying in the Earth's atmosphere, the vibrations and size of the used equipment become of importance.

One of the systems implemented in this laboratory is a spectrometer for the observation of the THz frequencies between 1.2 THz and 5 THz which cannot be seen from the earth due to atmospheric absorption. Here, the focus is on the improvement of 4.75 THz frequency line detection as it is important for the detection of the neutral atomic oxygen (4.7448 THz) which should help to understand the formation of massive young stars [154].

Although the GREAT spectrometer is equipped with a Ge:Ga photomixer for the THz power detection, the THz power fluctuations due to mechanical vibrations have to be additionally followed by a compact and independent power detector. Commercial room-temperature devices, such as pyroelectric or Golay Cell, cannot be easily implemented as they need additional chopping and do not fulfill space constraints. More compact GaAs Schottky diodes

designed for the high frequencies [75, 155] show a high 1/*f* noise and therefore, are not suitable for real-time power monitoring of the QCL power. Therefore, here we introduce an application of a compact TeraFET for CW monitoring of the QCL power fluctuations.

It has been shown that the TeraFETs can work at the desired frequency [156] and they do not need chopping taking additional space in the optical setup. Therefore, the practical application of compact field-effect transistor-based THz detector (TeraFET) was explored for the continuous power monitoring of the 4.7 THz frequency QCL line in the GREAT spectrometer. The work was conducted in collaboration with DLR on the equivalent spectroscopy system like the one in SOFIA.

The measurement setup is based on QCL mounted in the Stirling cryocooler and cooled to a constant 49 K temperature in a vacuum to avoid the condensation of water molecules. The second stage of the cryocooler has been modified to reduce the mechanical vibrations. The radiation is then distributed to two detectors – room-temperature TeraFET and Ga:Ga mixer cooled to liquid He temperature. We have produced beam splitters (BS) with various transmission factors equal to 10 %, 25 %, 40 %, 100 % by applying different thicknesses of Cr on top of 4-µm-thick polypropylene foil. The vibrations caused by the cryocooler were followed by acceleration sensors (AS). Detected signals from the detectors, as well as the QCL voltage and signal from the acceleration sensors (AS), were recorded.

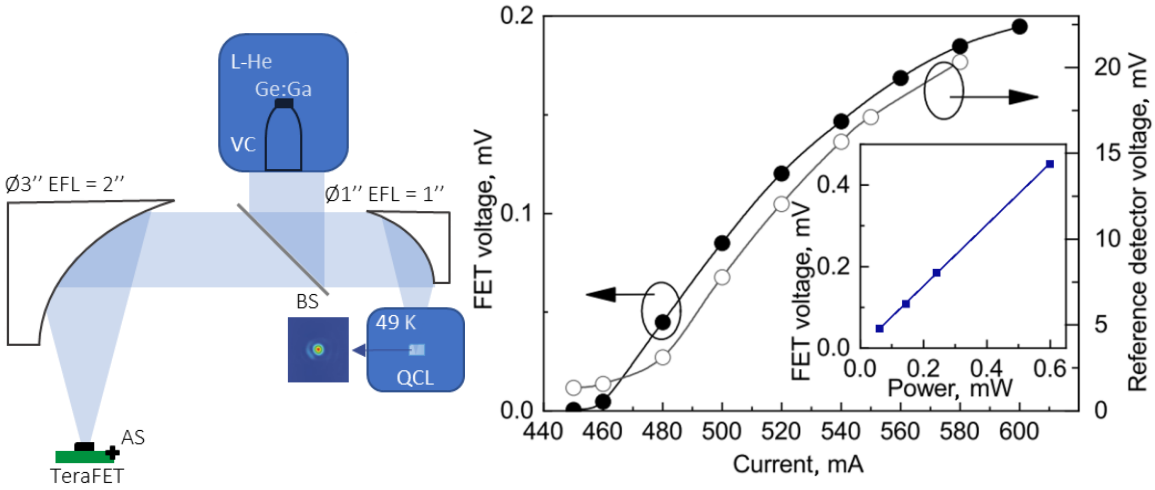

Fig. 6.14. Left: Optical measurement setup of a GREAT spectrometer with TeraFET. Right (adapted from IEEE *Xplore* [15] under © CC BY 4.0.): TeraFET and Ge:Ga sensor response dependency on QCL current.

The used TeraFETs were designed in 90-nm CMOS technology with a patch antenna and free-space radiation coupling. The detector's channel length is 100 nm and the channel width equals 400 nm. The detector area is 13 × 13 µm^2 and the distance to the ground plane is 2.2 µm. The responsivity measurements were made in DC mode using a lock-in amplifier and the modulation of the QCL current served as a reference. The right graph of Fig. 6.14 shows the

response of both detectors at different currents applied on the QCL. Both curves are in good agreement except for the low bias currents which despite the superior sensitivity of the Ge:Ga photomixer were influenced by a DC output component (≈1.6 V) change of Ge:Ga detector over a sufficiently long measurement time. The inset in the left figure shows the linear response of the TeraFET at the different attenuation levels of the THz power coming from the QCL biased at 600 mA.

6.1.4.1 Electrical characteristics

Electrical characterization of the THz signal was conducted measuring the output voltage fluctuations of the QCL THz source, as well as the TeraFET detector. The ripple of the recorded voltage fluctuation is depicted in Fig. 6.15. The blue line depicts the QCL voltage fluctuation, whereas the black line shows the corresponding detected signal by the TeraFET measured separately. Both signals show multifrequency fluctuations which are smaller than 0.03 % around the DC signal and up to 4 % for the detected signal. The Fourier spectrum of these fluctuations is depicted at the right. The top graph shows the fluctuations of the QCL output voltage which might be caused by the vibrations of the cryocooler transferred via cables which show up in Ge:Ga detector as well. The TeraFET fluctuations (dashed lines at the bottom) express the same peak behavior as in the QCL spectrum. The rise in the noise spectrum reduces to the thermal noise if the THz signal is attenuated [15], therefore it is expected, that the rise in fluctuations is due to the back reflections induced in the setup, long coaxial cables as well as the use of the external amplifier (has a long coaxial line before the first amplification stage). Additional experiments show that the replacement of a 2-inch parabolic mirror via a Winston cone, as well as the integration of an amplifier stage close to the TeraFET or a broadband THz attenuator, reduce the distortions of this type.

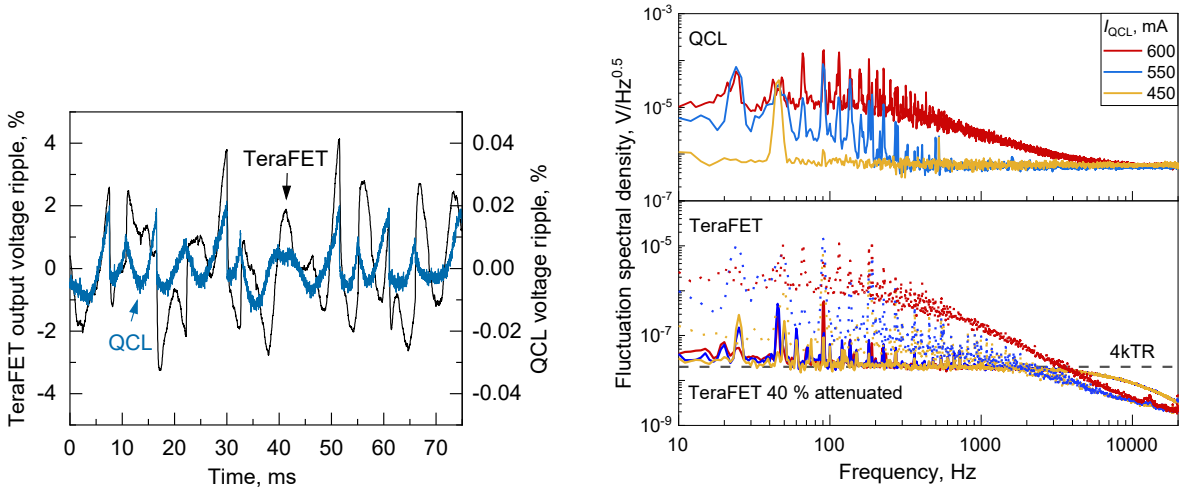

Fig. 6.15. Electrical output voltage signals of the QCL and the TeraFET with subtracted offset (left). The noise characteristics of the QCL and the TeraFET at different QCL current levels (right), data also presented in [119].

The measured electrical characteristics show that the absence of $1/f$ noise in the transistor's channel allows the real-time monitoring of the QCL power which is not the case for most commercial thermal detectors. The TeraFET detector exhibits the thermal noise of 18 nV/√Hz and has a 40-dB dynamic range for an effective measurement bandwidth of 1 Hz which allows the power monitoring even at a small fraction of the QCL power. The 45 Hz component and its harmonics induced by the vibrations of the cryocooler which transfer through the optical table to the electrical cables can be reduced by integrating a low-noise amplifier with the amplifier input noise reaching 4 nV/√Hz and the $1/f$ corner frequency of 30 Hz. The back reflections from the TeraFET can be reduced by attenuation of the THz beam or the use of Winston cone instead of the parabolic mirror. If those fluctuations are suppressed, then the TeraFET noise is limited only by the thermal noise.

6.1.4.2 Optical characterization

For the optical characterization of the THz beam, several experiments were conducted. The beam profile was measured using a microbolometer camera. The beam profile was depicted in Fig. 6.16. The estimated horizontal FWHM (full-width half-maximum) equals 1.3 mm and the vertical FWHM is 0.8 mm. Assuming Gaussian beam profile, the estimated power delivered to the detector is 0.25 mW.

The effective area $A_{eff} = D\lambda^2/4\pi = 1750\ \mu m^2$ of the antenna was estimated by using the modeled antenna directivity of D = 5.5 and the wavelength λ corresponding to 4.75 THz frequency. It should be noted that the effective antenna area for this detector at 4.75 THz is 1.7 times larger than the physical area of the implemented metal cup.

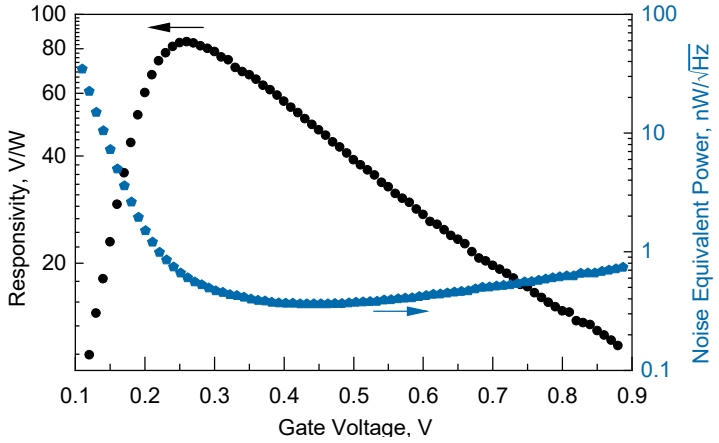

Fig. 6.16. Cross-sectional NEP and responsivity at 4.75 THz frequency (data also presented in [15]).

At 4.75 THz, the modeled radiation efficiency is 76 %. Therefore, the area-normalized NEP equals 0.4 nW/√Hz and the maximum responsivity is 75 V/W. In comparison, the state-of-the-art SBD detector in 130-nm CMOS technology exhibits cross-sectional NEP, normalized

to the simulated effective antenna area, of 4.95 nW/√Hz and 383 V/W at 300 Hz modulation frequency and radiation frequency of 4.92 THz [76]. These are the closes values for comparison which were found in the literature.

However, the authors in [76] point out the difference in the cross-sectional responsivity. The responsivity normalized to the simulated effective antenna area and Gaussian beam distribution was 4 times lower than the cross-sectional responsivity calculated for the average power of the beam on the physical antenna area. This emphasizes the uncertainty due to various optical characterization methods as discussed in Section 3.2 State-of-the-art THz detectors.

6.2 Imaging applications

THz imaging can be used in various applications as it penetrates through dust, fog, and some other materials which are not transparent in the visible light, for example, cloth, plastics, packaging materials. Therefore, THz applications are important for astronomy [157], security [37], biomedical [137], or technical vision [158, 159]. Various active and passive imaging schemes can be used for the imaging of mm-wave and THz radiation [160, 161]. Most of the applications use active imaging schemes which employ TDS or CW THz sources. However, the systems exploring the natural THz radiation of an object have to be based on passive imaging solutions (without additional radiation source).

Passive imaging does not need an additional THz source, as it detects the radiation power coming from the measured sample. However, the thermal radiation power from a sample in the THz range is very small [48]. Therefore, it is easier to use an active imaging technique that can be made either in transmission or reflection mode, where radiation from a THz source penetrates through a sample or reflects from it, respectively. The most sensitive and complex implementation is homodyne or heterodyne detection which needs a THz source with a local oscillator (LO). This imaging technique improves the signal dynamic range by a few orders of magnitude [160].

Using single-pixel detectors, the limiting aspect of a THz imaging system is the image acquisition time. For raster-scanned images, it is mainly limited by the time constant of mechanical translation. For less sensitive detectors or weaker power sources, the signal integration time is a limiting factor. However, it could depend on the technology as well where high $1/f$ noise or slow thermal processes can limit the signal readout frequency to a couple of times per second.

For the systems where the main limiting factor is the mechanical translation part or the systems which require a very high imaging speed (conveyer line), the main solution could be a multi-pixel array. Multiple pixels can detect a bigger imaging area and therefore the imaging technique becomes faster and more reliable. If the system is limited by the detector aperture, the imaging performance can be improved with a multi-pixel array as it can see a bigger imaging area and therefore, couple more energy into the array. For thermal noise-limited

systems, simultaneous signal detection through multiple pixels can reduce the noise level and therefore increase the sensitivity.

All the above-mentioned applications are based on far-field imaging. However, the first section shows a near-field application of THz microscopy which was used for plasma wave visualization in a channel of a TeraFET.

6.2.1 Near-field imaging of TeraFETs

One of the unexpected applications for the TeraFET was to use it for THz detection and simultaneously to take the AFM and s-SNOM images of it. In other words, the aim was to see the plasma waves using the scattered light near-field microscopy (s-SNOM) technique under THz radiation applied on a TeraFET. The experiment was conducted at the FELBE facility with s-SNOM from Technical University Dresden. The know-how on experimental TeraFET characterization and s-SNOM was from J.W. Goethe University Frankfurt. The devices were fabricated at the Chalmers University of Technology.

As mentioned in Section 3.1, the TeraFETs work above the cut-off frequency of the transistor due to the carrier density waves occurring in the transistor channel. The s-SNOM technique can detect such waves in near-field approximation. To realize this idea, the TeraFET transistor with a 2D graphene channel [43] has been configured for a less sensitive bottom-gate configuration. This configuration assures that the field-effect transistor channel, based only on the single-layer graphene, is on top of the whole structure and therefore the carriers of the channel are exposed for near-field microscopy.

The detector was fabricated as in [112] but the gate contact has been buried under the channel, so that the gate electrode, gate oxide, and graphene layer are placed on top of each other. Gate dielectric Al_2O_3 is 25 nm thick. Sloped gate sidewalls were implemented, in order to place graphene without suspension on the gate edges and therefore possibly breaking the graphene layer. The image of the multiple detector chip with implemented antenna contacts is shown in Fig. 6.17.

The experiment was conducted under the 2 THz radiation from the free-electro laser of the FELBE facility. The laser pulse width was 10 ps at a repetition rate of 13 MHz. The radiation was directed with a 55° angle to the surface, polarization was perpendicular to the symmetry axis of the antenna (parallel to the cantilever (p-polarized) as shown in Fig. 6.17). Radiation scattered by the probe tip had been filtered with an s-polarization filter to reduce the influence of the background radiation as the s-SNOM operated in power detection mode [162]. Higher harmonics of cantilever oscillation were recorded which correspond to the near-field signal [163, 164].

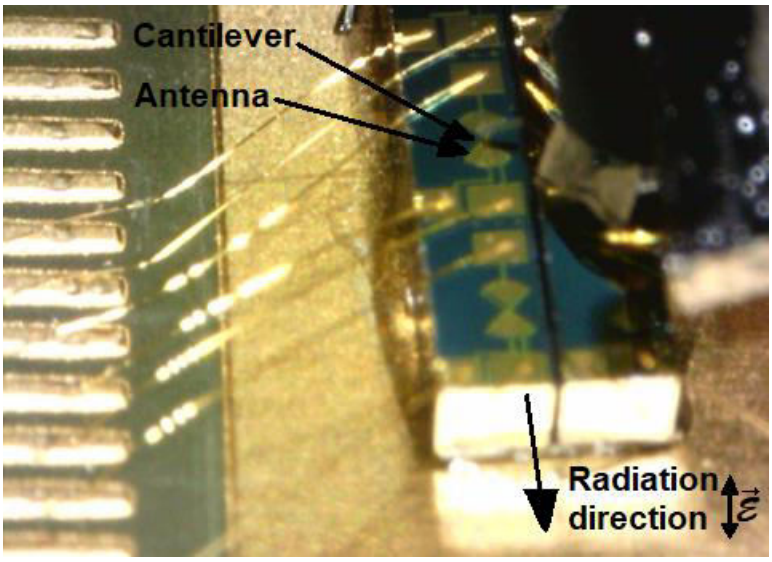

Fig. 6.17. Microscope image of the measured chip with a cantilever close to the chosen transistor's channel.

The recorded near-field images of the graphene field-effect transistor's channel, as the first to third frequency harmonics of the cantilever under 2 THz radiation, is depicted in Fig. 6.18. Channel dimensions are as follows: gate length 1.8 µm, channel length 2.7 µm, channel width 2 µm. The AFM image (top left) shows the measured height of the structure. The detected signals of the first three harmonics of the cantilever's oscillation frequency f_{OSC}. The letters in the image of the second harmonic signal $2f_{OSC}$ show source (S), gate (G), and drain (D) terminals. All images have been made simultaneously with the gate voltage set to 0.4 V ($V_{Dirac} \approx 0.55$ V) and the radiation coming from the left to the right with a 55° angle and 150 ms lock-in integration time under 19 mW THz power.

The lightest color in the images shows the strongest local electric field. The average signal amplitude on the gate and drain antenna metals is similar due to the capacitive coupling between the antenna leaves. The smaller field amplitude at the source side (darker area) shows the asymmetric antenna radiation coupling into the transistor channel. The highest amplitude of the picture is in the channel, close to the source contact where the radiation is coupled, and the electric-field amplitude drops along the channel. This shows a similar behavior as it is expected in TeraFETs.

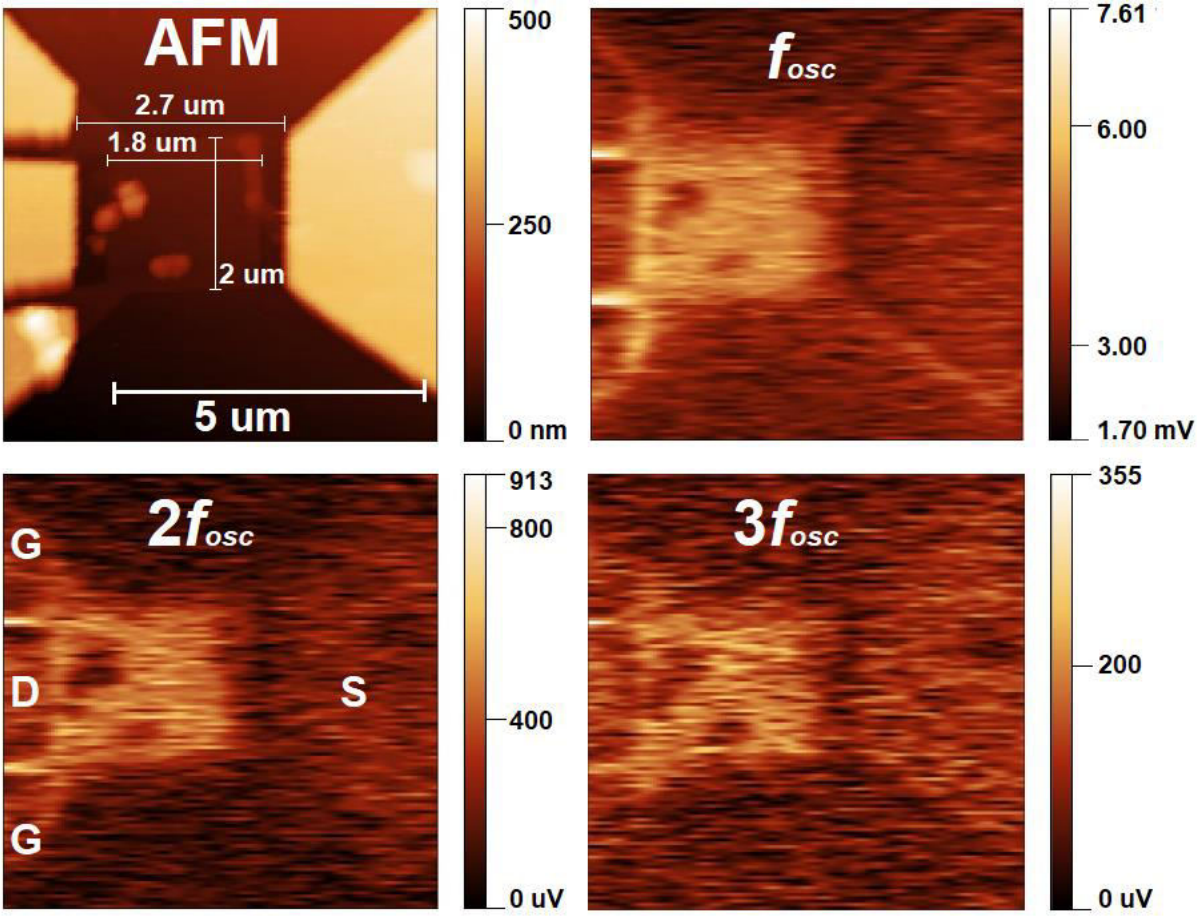

Fig. 6.18. Atomic force microscope (AFM) image of the GFET channel region (left top) and s-SNOM measurements of the 1st, 2nd, and 3rd harmonics.

The presented data are from the first experiment which was useful for further implementations, such as, sloped walls of the buried gate electrodes to assure less mechanical strain on the graphene layer, another radiation direction perpendicular to the antenna symmetry axis has been tested. And the most important for the transparent data analysis, the resistance and THz detection response have been measured between the s-SNOM scans.

To record the electrical and optical characteristics of the GFET, the know-how from [111] and Section 5.1.1 had been implemented. As the graphene is directly exposed to the air and high electromagnetic fields, it is necessary to follow the changes of impurities on the transistor channel. Therefore, the electrical properties of the channel were carefully measured between the experiments in order to know about any additional electrical charges which might become attached to the channel and therefore make an influence on the carrier density in the channel. The measurement direction, duration, and gate voltage step for the electrical measurements were kept the same for all the experiments as it is of high importance for comparison reasons between multiple experiments.

The work led to the successful imaging of carrier density (plasma) waves on the bottom-gated graphene field-effect transistor. The results and analysis method are presented in [165]. The obtained values of the analysis give the extracted plasma wave velocity and the damping time of the plasma wave which are in good agreement with the values given in the literature.

6.2.2 Reconfigurable aperture multi-pixel array

Invisible THz radiation in THz systems with low source output power close to NEP of the detectors causes difficulties in the alignment procedure of THz setup and therefore takes a lot of time. For this purpose, a 6x7 multi-pixel array was implemented which has two operating conditions. One operation is pixel-by-pixel raster scan, the second – reconfigurable aperture for single-pixel detection. This solution was considered for laboratory applications as it saves time focusing the beam and gets information about the beam power around a single pixel.

6.2.2.1 Aperture reconfiguration

The multi-pixel array can be configured for the biggest possible aperture detection of the size of the multi-pixel array. In this way, it is easier to catch the misaligned THz beam as the aperture is bigger. After the THz signal is met by the detector aperture, the beam can be focused on the optical axis. Then, the aperture can be reduced to the size of the expected beam to capture most of the beam power.

The array was designed using a slot bow-tie antenna with a pitch size of 180 µm between the pixels. All source contacts of the transistors were connected to the ground terminal. There are 6 rows of the common gate and 7 columns of common drain contact. All gate rows and all drain columns are connected in parallel and controlled with MUX/DEMUX via Arduino Nano microcontroller programmed with LabView algorithm. The readout was presented in Section 4.2.3 (Fig. 4.3).

The aperture size can be chosen as an integer number of adjacent rows and columns. The intersection size of the gates and drains in ON state is the size of the actual aperture measuring the incoming THz radiation. For example, three possible configurations are shown in Fig. 6.19.

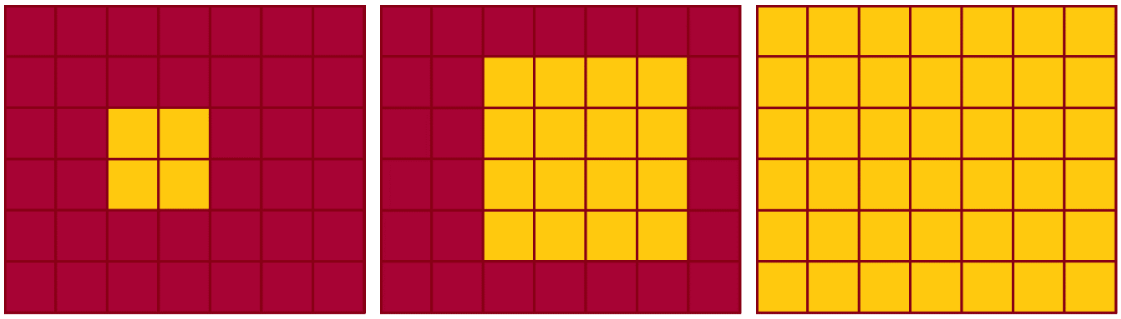

Fig. 6.19. Various aperture configurations for THz detection with a 6x7-pixel array.

Such configuration allows one to choose the optimal aperture size depending on the beam spot size and, as it was shown in [166], it reduces the NEP for bigger aperture size, as the thermal noise of the transistors connected in parallel is lower.

It has been shown that the chosen multi-pixel array design assures optimized detector aperture for beam focusing, enables the user to check the single-pixel environment, and increases the sensitivity limit for low power radiation of big spot size. Therefore, it is useful for a faster optical THz system alignment as well as single-pixel imaging applications.

6.2.2.2 THz source imaging

The imaging configuration of the multi-pixel array scans pixels one by one and acquires an image of the incident radiation power focused into the array. This configuration was used to image various THz sources using the *f-f* setup shown below.

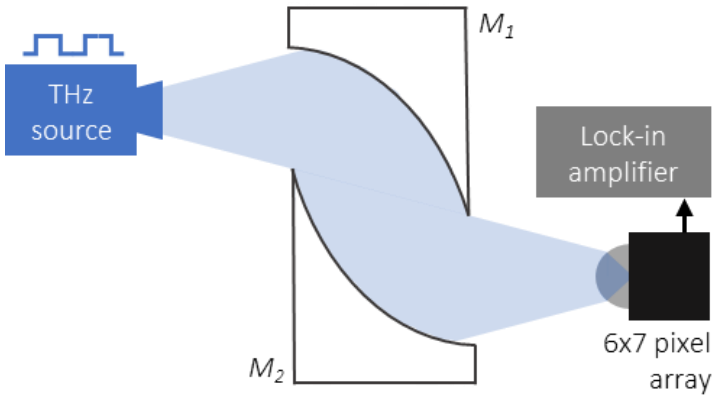

Fig. 6.20. Optical setup for THz source imaging with 6x7 multi-pixel array.

In the beginning, the single-pixel performance was characterized using an electronic 300 GHz source. Fig. 6.21 shows the distribution of AlGaN/GaN HEMT pixel resistances and the corresponding responsivity dispersion for the same pixels. The average minimal NEP for all the transistors is at around -1.7 V. The optical responsivity is around 100 V/W and the corresponding optical NEP is 44 pW/√Hz. The average responsivity curve and 2σ bars are

depicted in black. The presented advanced FET technologies, such as CMOS and AlGaN/GaN HEMT, have comparably low resistance dispersion between the transistors. This feature assures a simple FPA use in THz detection applications as all the pixels show a similar responsivity.

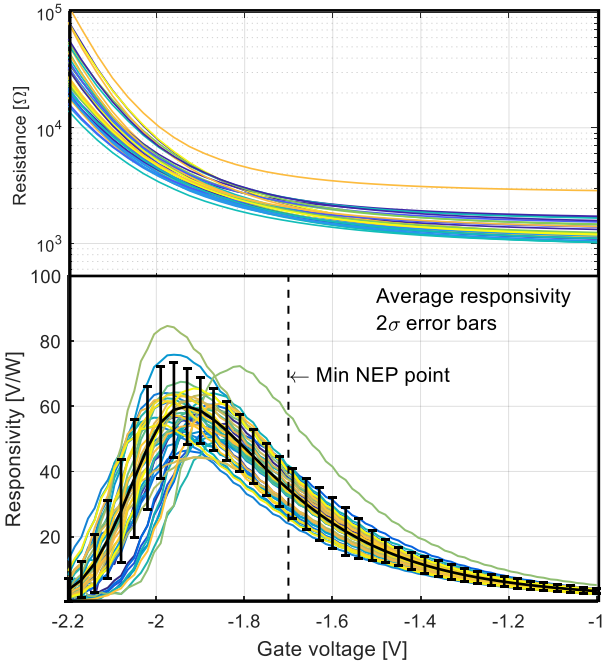

Fig. 6.21. Resistance (top) and responsivity (bottom) graphs of a 42-pixel array.

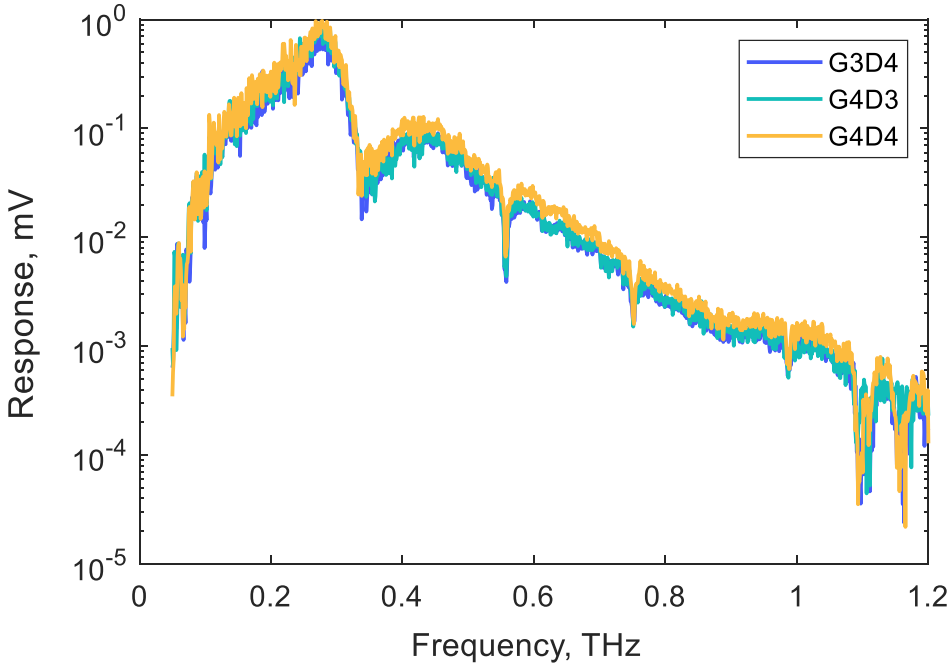

Fig. 6.22. Multiple pixel spectral characteristics.

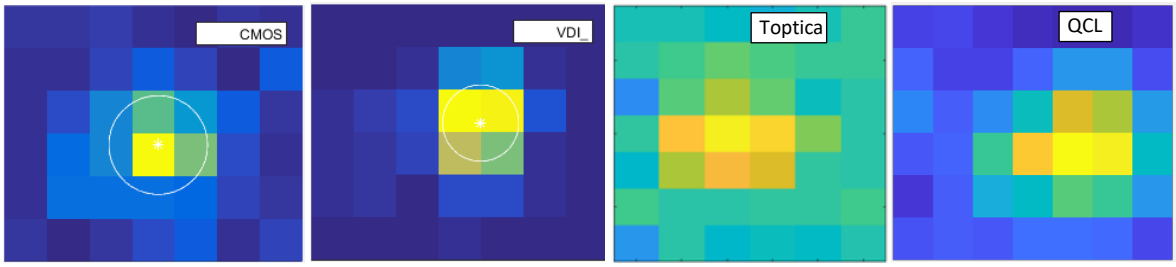

Fig. 6.23. Comparison of three different THz sources at 200 GHz imaged with AlGaN/GaN multi-pixel array: CMOS technology-based source, commercial multiplier chain-based VDI source, and commercial Toptica photomixer from left to right. The last picture was made of a QCL source at 4.75 THz using a CMOS-based multi-pixel array.

Using AlGaN/GaN HEMT-based multi-pixel array, the imaging of three different THz sources was made: wideband Toptica TeraScan1550 system, electronic VDI source, and a CMOS technology-based source designed at GUF and Vilnius University for 250 GHz frequency. Additionally, the image of a QCL source at 4.25 THz was acquired using a CMOS multi-pixel array designed for QCL power detection.

The comparison of all the images on the mentioned THz sources is shown in Fig. 6.23. The designed CMOS TeraFET-based THz source delivers power mainly into one pixel different from the commercial VDI and Toptica sources working at 200 GHz frequency. The beam has been focused into one of the pixels and then one image has been taken for each THz source. VDI source shows the highest signal of a focused light when two pixels in one row are lightened up equally. The SNR of the two pixels then equals 46 dB at THz power of 4 mW which was attenuated by 10 dB to avoid the influence of a standing wave in the optical system.

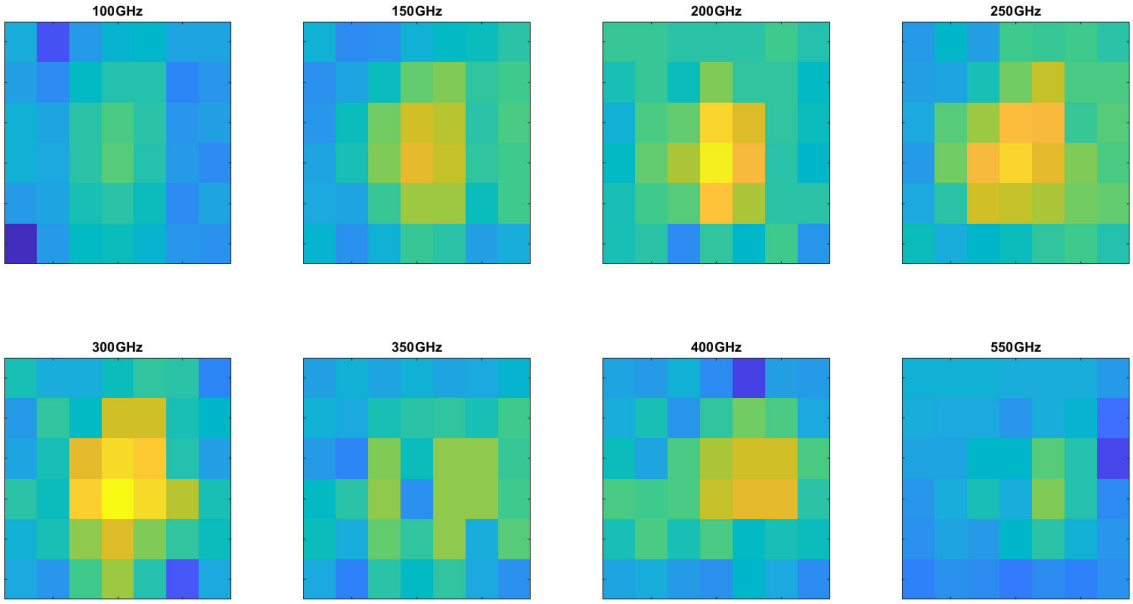

Fig. 6.24. Images of Toptica transmitter power at different frequencies.

The beam profile images at various frequencies of the Toptica system are presented in Fig. 6.24. The brightness of the detected signal in the images corresponds to the response signal at corresponding frequencies as shown in Fig. 6.22.

One can see that in all the experiments the total radiation power is dissipated over many pixels. Therefore, in the case of the use of a single-pixel device, all the information around the pixel would be lost. This also shows the difference between the characterization of total and optical device parameters, as total power accounts for the optimal detector area (pixel number) absorbing the incident radiation, whereas the single-pixel device absorbs only the part of the radiation, and part of the radiation is always lost. The radiation loss due to limited detector aperture is not considered in the calculation of the optical detector responsivity and NEP.

6.2.2.3 6x7 array comparison with a commercial TeraSense camera

256-pixel TeraSense camera has been used for the sensitivity comparison with our 42-pixel TeraFET-based focal plane array. For this purpose, a „Matlab" algorithm was implemented for the half-power bandwidth approximation of a Gaussian beam along the *x* and *y* directions from the brightest pixel of a camera. It was assumed that the beam is close to the Gaussian beam and for this experiment, the fact that our array has a substrate lens was ignored.

The algorithm searches for the brightest pixel and takes it as the focal point of the optical system. Then, it takes the corresponding row and column data points containing the pixel and fits a Gaussian function for both data sets. From the fitted data, it takes the Half Power Bandwidth calculated in both directions ($HPBW_X$ and $HPBW_Y$) and calculates the approximate half-power bandwidth $HPBW = \sqrt{HPBW_X{}^2 + HPBW_Y{}^2}$ for of the incident beam which is shown in Fig. 6.25 as a white circle around the *x* marked center of the beam data taken from the same approximation.

To test the algorithm, an experiment was conducted where a 300 GHz TeraSense source was horizontally translated out of focus. The TeraSense camera has a pixel pitch size of 1.5 mm. The position of a horn antenna at the focused beam was 14 mm. The measured data is shown in Fig. 6.25.

The presented algorithm was implemented for the shown data set. The column and the row of the brightest pixel were taken and fitted with the Gaussian function. They are shown in Fig. 6.26. The measured data shows a high saturation level although the shortest exposure time provided by the commercial supplier was used. The approximated half-power beam profile for each measurement together with the path of the beam center with calculated $HPBW_X$ and $HPBW_Y$ depicted with error bars are shown at the right of Fig. 6.26. The beam path can be seen using this algorithm which proves the functionality of this basic algorithm for the comparison of the two systems.

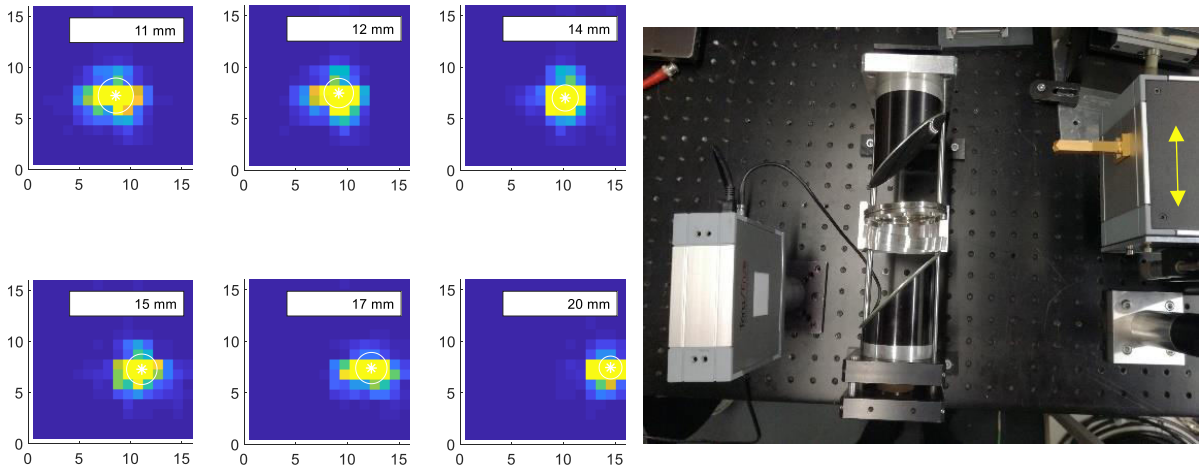

Fig. 6.25. Images of a spatial beam shift (left) and the optical setup with TeraSense source and multi-pixel array (right).

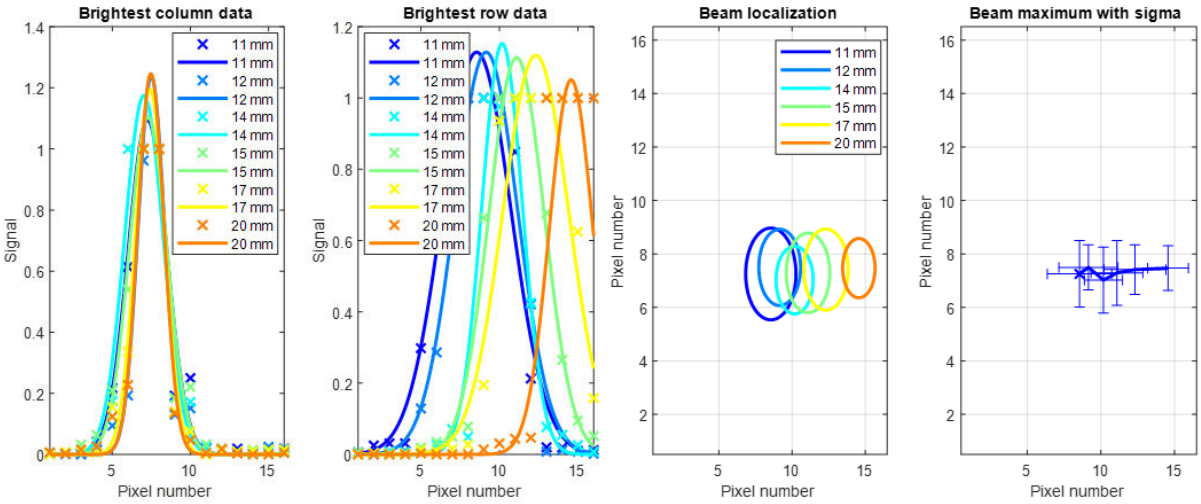

Fig. 6.26. Analysis of the beam movement assuming Gaussian beam form.

The comparison experiment has been made at different incoming radiation power levels. The incoming radiation power has been attenuated by filters of 100 %, 10 %, 1.6 %, 0.2 %, and 0.05 % transmission coefficient, named *F[transmission coefficient]* in Fig. 6.27. Our array has no implemented amplifier, therefore the lock-in technique has been used to detect the signal. Therefore, the image acquisition time was 4 s. The TeraSense camera as a commercial product has a computer interface and various tuning options to optimize the read-out electronics conditions. The main parameter which can be chosen is the exposure time, named *E[integer number]* in Fig. 6.27, which was optimized during this experiment. The recorded images are shown below.

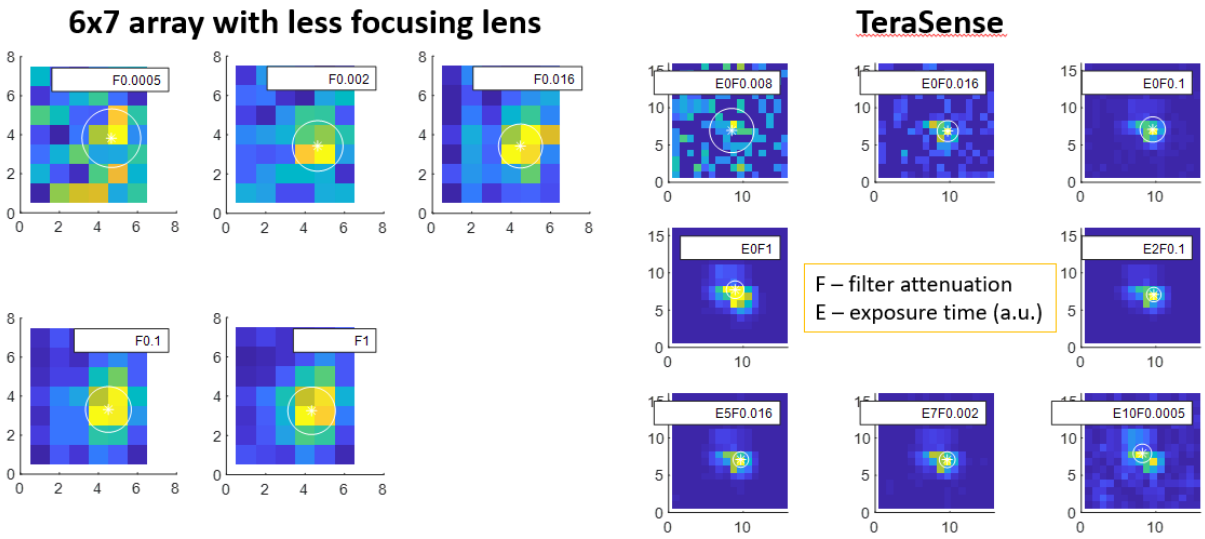

Fig. 6.27. Images for sensitivity comparison of the unamplified TeraFET based system and commercial TeraSense camera for the power transmission configurations from 1 to 0.0005.

Fig. 6.28 shows the images at various THz power attenuation levels for the AlGaN/GaN HEMT-based 6x7-pixel array and commercial TeraSense 16x16-pixel camera. The analyzed data from this set of images using the described algorithm for detection of the beam position is depicted in Fig. 6.29. As the THz source has not been moved during the experiment and the beam profile should not be changed, the approximate HPBW should be the same for all the experiments.

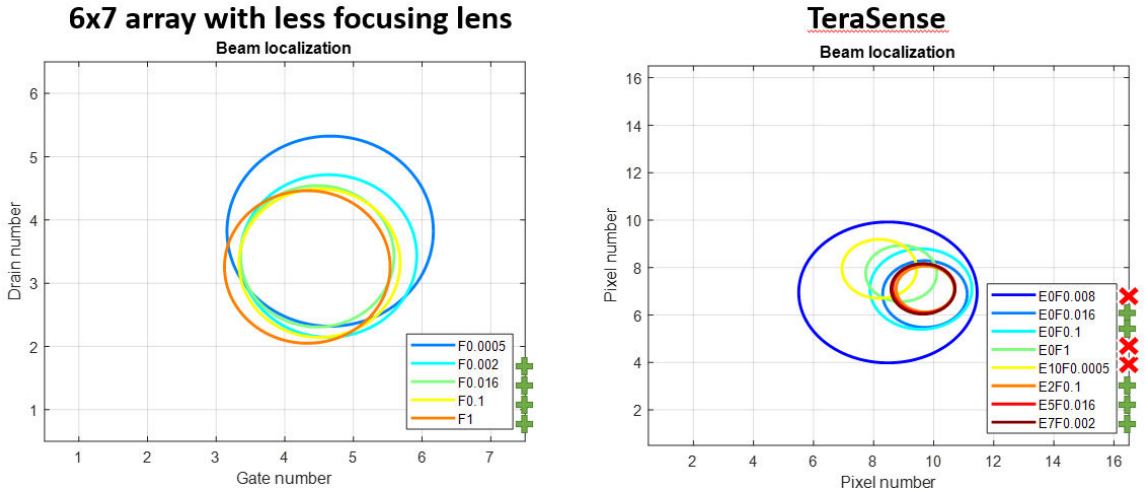

For **all** filter options the beam possition can be predicted

For **some** filter options the beam possition can be predicted **using different exposure time**

Fig. 6.29. Sensitivity comparison. Red X shows the configurations of the TeraSense camera which could not be recognized with the used algorithm.

The 6x7 array shows a good performance for all the attenuation conditions, also close to the noise level at 0.05 % attenuation, whereas the TeraSense camera obtained the beam image well at 10 % and 0.16 % attenuation for the shortest exposure time and 0.2 % with an exposure option named E7. Lower power levels could not be obtained even with the longer exposure time provided by the device. Moreover, the maximum power of the TeraSense source could not be analyzed since the central pixels were in saturation as described previously. The experiment shows a much lower dynamic range of the TeraSense system. However, our detector still needs faster readout electronics and implemented amplifiers to reach the integration level of TeraSense for portable out-of-the-lab use.

6.2.3 3D mobile phone imaging

For the test of a 3D imaging of the mobile phone as a security imaging application, a Schwarzschild telescope objective was used which is well known for its large numerical aperture and was fabricated out of aluminum. The schematic of the imaging setup is shown in Fig. 6.30. It is based on two curved mirrors where one is a convex mirror in the optical axis reflecting with a big angle so that the radiation, reflected from the concave mirror can be focused into the object behind the convex one. The effective focal length (EFL) of the telescope equals 50 mm and the numerical aperture NA = 0.67. This objective assures low (or any) chromatic and spherical aberrations [167] and therefore is also good for multispectral imaging.

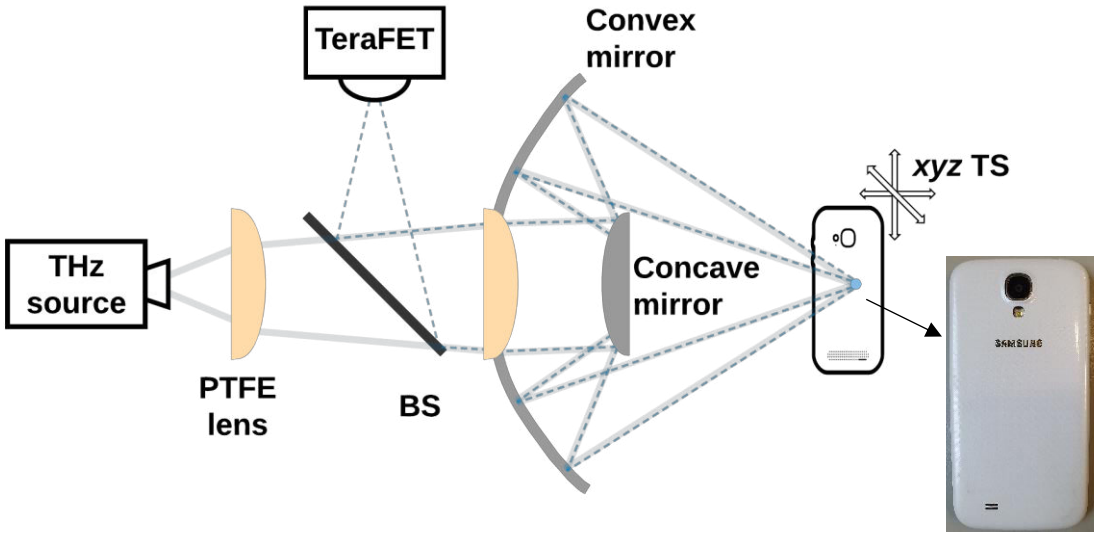

Fig. 6.30. Experimental 3D setup in a reflection configuration.

504 GHz radiation is collimated through two PTFE lenses and reflected from the concave mirror into the convex one which focuses the beam tightly into the sample. The reflected radiation from the sample returns and reflects from the silicon beam splitter then it is focused into the AlGaN/GaN TeraFET. Two PTFE lenses and a beam splitter were used for the radiation

coupling on the TeraFET. A generic mobile phone as a test sample was used and 504 GHz radiation frequency from electronic CW THz source was used to reach sub-mm resolution and sufficiently high dynamic range. During the experiment, the backside of the phone with the cover was raster scanned in three dimensions using mechanical translation stages.

The measured reflection images are shown in Fig. 6.31. Each picture shows the reflection images at different phone positions compared to the focal plane where 0 mm corresponds to the cover of the mobile phone placed in the focal plane. The last image shows the mean value over each pixel. Such a simple addition of the detected intensities shows a better contrast of single elements where each picture depicts single plane features better. For example, the letters on the plastic cover can be seen in the 0 mm position, however, they interfere destructively at the 2 mm position. The loop antenna of the mobile phone shows up the best at 1.5 mm, however, the total intensity image depicts it as well, as the summation removes the interference effect caused by a slightly shifted phone plane.

As the THz radiation penetrates through the plastic cover, the internal components from the reflected light image can be recorded. The reflection images were made in *x* and *y* directions with the step size of 0.4 mm and with the scan speed of 15 mm/s along the *x*-axis. As the Schwarzschild objective with large NA focuses radiation tightly, the depth information along the *z*-axis can be recorded. The sliced images were made in 0.25 mm steps in the *z*-direction and the sharpest images are shown in Fig. 6.31. The lock-in integration time for each image point was 20 ms and the total image acquisition time was 40 min.

The total reflection intensity of all the imaging planes is shown in Fig. 6.32. Two different color scales were used: the logarithmic scale depicts the plastic body features better, whereas the linear scale has a better contrast between the metallic and plastic features. The arrows show the main parts of the mobile phone which can be seen in the THz image. The picture at the left shows the actual sample image with a plastic cover at the side.

As in most of the THz setups, this imaging setup also exhibits standing wave interference. The interference shows up if a flat surface is tilted with respect to the focal plane and when the height of the object elements varies. Most likely, the interference pattern on the battery is the result of the standing waves. This could be solved by summing up few images with the tuned radiation frequency.

Due to a high numerical aperture, the Schwarzschild optics was chosen to reach tight focus on the imaged object. The object had been recorded in 3D at 504 GHz frequency. The features behind the plastic cover can be easily recognized. The imaging time was around 40 min which is rather a long time for possible applications. The image acquisition time can be reduced by implementing a THz camera [90, 100]. A real-time camera would reduce image acquisition time significantly. Therefore, such a type of camera would be more applicable for security and industrial applications even better than the ones offered commercially by now.

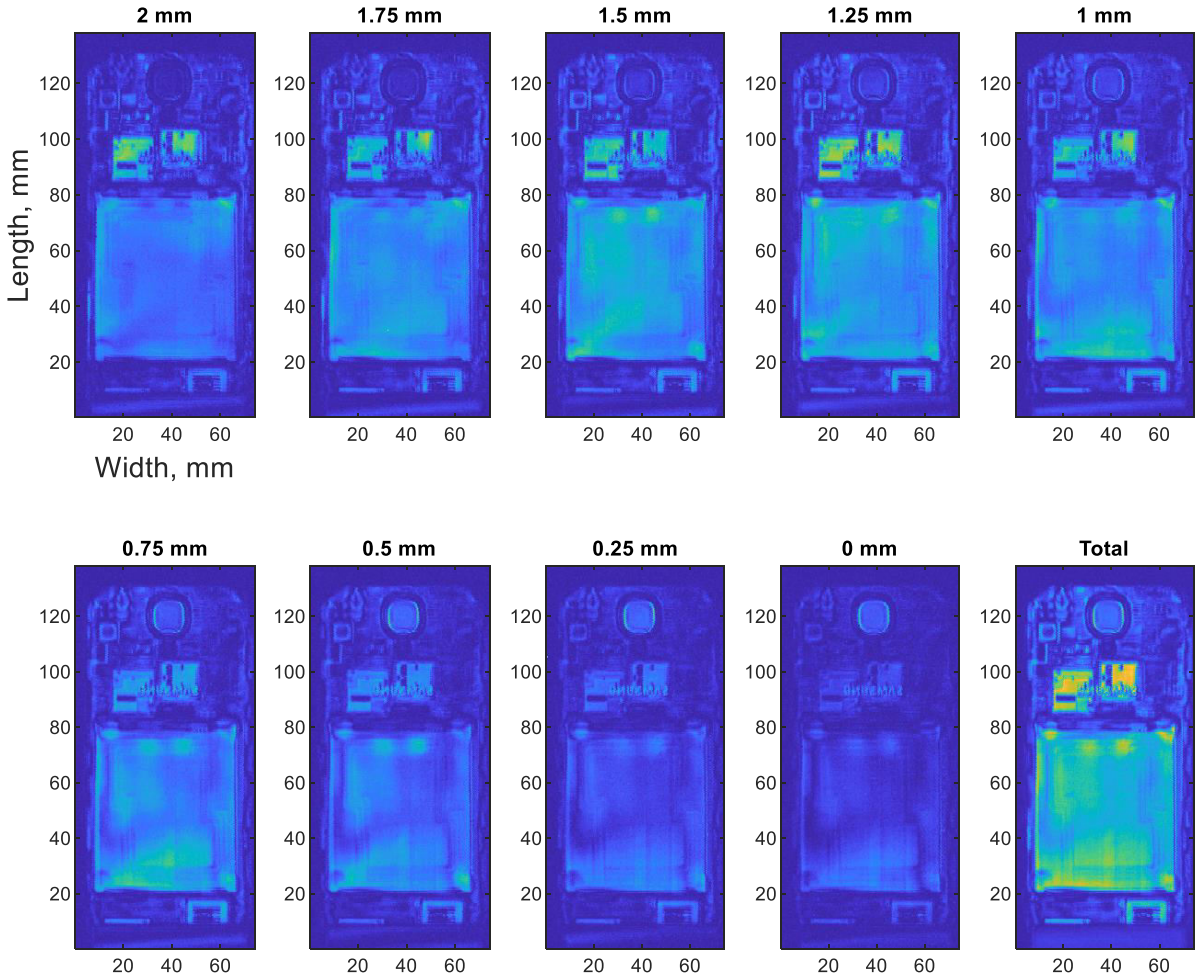

Fig. 6.31. Sliced images of a mobile phone depicted in linear scale and same color bar values.

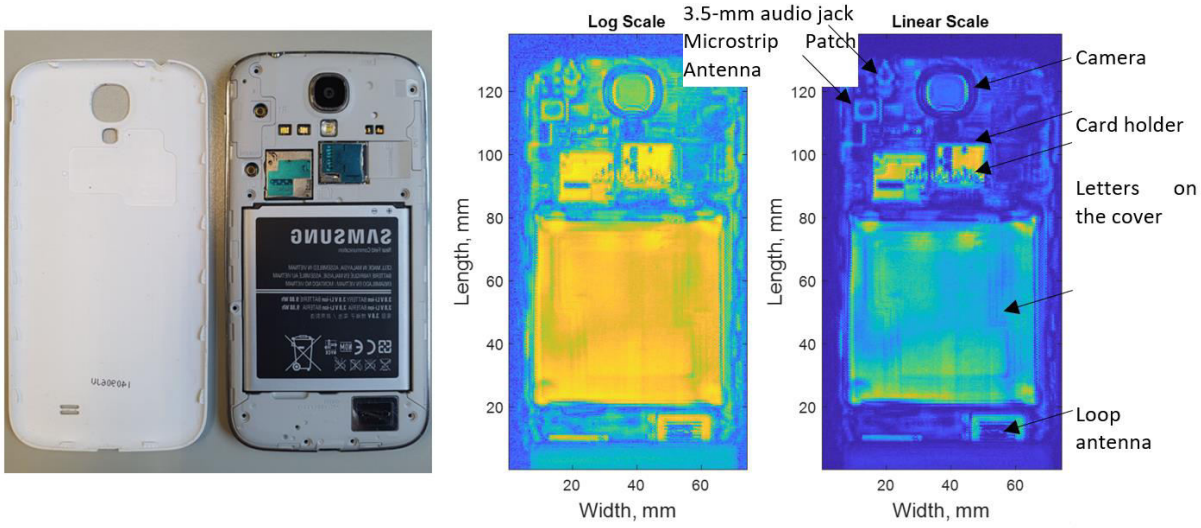

Fig. 6.32. The sample (at the left) and the 0.5 THz images of the total intensity imaged through the plastic cover (on the right).

6.3 Hyperspectral imaging

One of the unique experiments which were developed within the ITN CELTA network was based on high sensitivity TeraFET with a high precision electro-optic dual-comb source [66, 100]. The experimental setup was implemented during the secondment in Madrid Carlos III university. The idea of combining these two systems arose as the dual-comb system is of absolute frequency accuracy and high resolution of spectral lines. However, the photodiode output power is limited to few microwatts at this frequency. Therefore, the solution for this low-power THz source is can be a high sensitivity TeraFET with a broadband response. Such a system is useful for imaging applications where the absorption lines are rather narrow and therefore cannot be detected by the spectroscopy system as the 2 GHz-width oxygen line at 118.75 GHz frequency which was shown in [7], Fig 3.

Both systems were optimized for the best performance. First, the dual-frequency comb setup was extended to THz frequencies and explored in a raster-scan imaging system. Later, a suitable TeraFET design with implemented LNA for a higher repetition rate was developed. In this section, the proof of concept is presented of a multifrequency imaging scheme with a TeraFET. The work is also published in [35, 36].

6.3.1 Hyperspectral imaging system

The imaging system is shown in Fig. 6.33. A dual comb-based THz source radiates CW single- or multifrequency THz beam which is focused into the sample using two off-axis parabolic mirrors. The transmitted beam is then focused into a TeraFET detector, amplified, and digitalized for further computational processing. During the measurement, the sample was moved along the focal plane and a raster scan has been kept. The measurement has been made using a single-line (heterodyne) frequency at 266 GHz. It took around 3 hours for a 2x2.5 cm^2 image to be scanned with a 0.25 mm step in both directions.

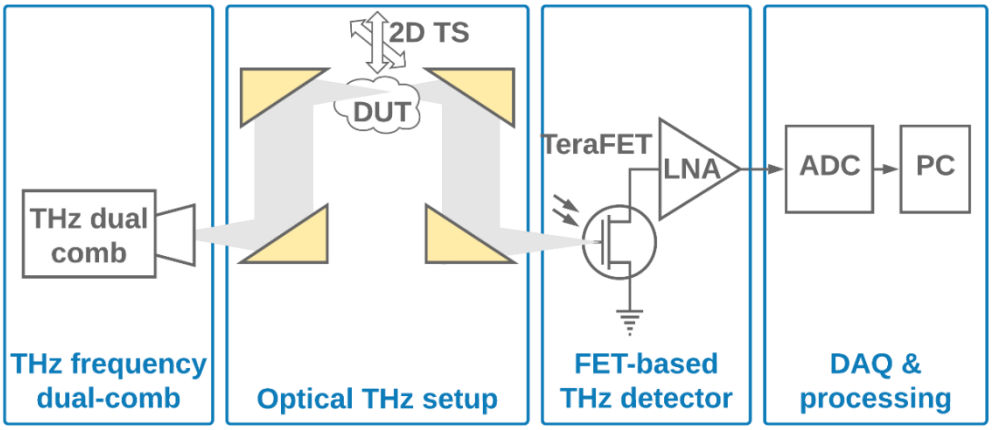

Fig. 6.33. Multifrequency imaging block diagram with an electro-optic THz dual comb, 4f optical system with a sample in the intermediate focal plane, TeraFET connected to a digital read-out circuit.

The optical part of the measurement system is shown in Fig. 6.34, where the THz output is radiated from UTC photodiode-based THz dual-comb system, focused on the sample and directed to the TeraFET. As a THz sample, a microfluidic container half-filled with water (see Fig. 6.35 left) was used where the other half part was still with some air left. For the first imaging experiment, a TeraFET detector which was not optimized for the new THz source frequency range was used, therefore, the dynamic range of the image was comparably low, only 34 dB. The signal was measured using a ZI Lock-in amplifier. Despite a limited dynamic range of the image, it was enough to make a recognizable image of a microfluidic container shown in Fig. 6.35.

The THz image is shown on the right of Fig. 6.35. One can see the THz transmission in the air above the sample and the features of the sample, such as the shape of the container, the difference between water and air in it, as well as half transmitted light in plastic parts of the container. The plastic closing pins of the container cannot be seen in the picture, as they dim the light too much, and the signal transmitted signal reached the noise level of this detector. The sharper edges of all features can be reached with a better focusing of the beam and higher radiation frequency.

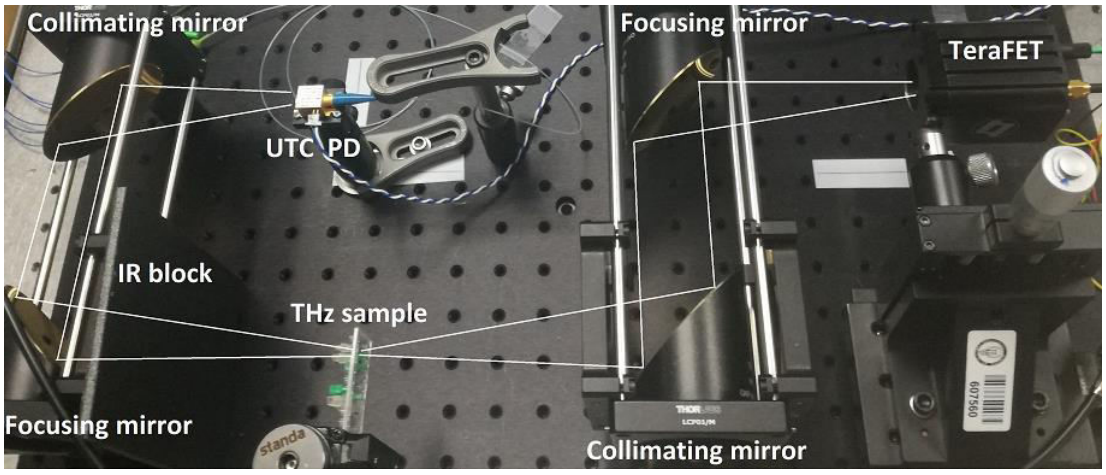

Fig. 6.34. Optical multifrequency imaging setup with a THz sample in the intermediate focus.

One important difference between the imaged sample in the left and the THz image is the position of the largest air gap and missing small air bubbles. The reason for this is that the air bubbles moved slowly during the experiment to the position shown in the right image. The blue picture in the center shows the THz raster scan of the shown sample where light blue corresponds to complete transmission above the sample and dark blue shows areas of the weakest transmission of thick plastic and water.

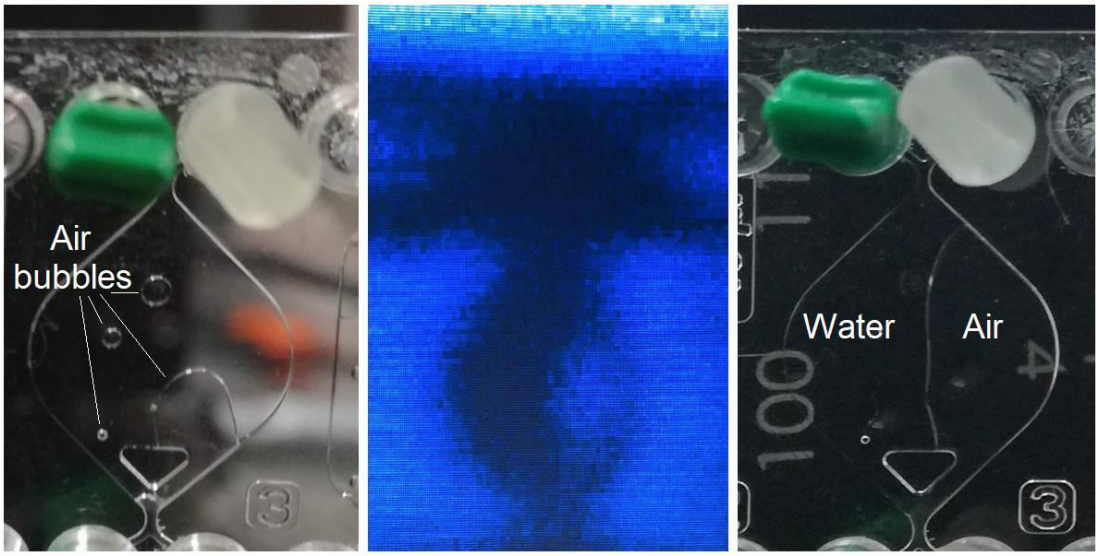

Fig. 6.35. Microfluid container with water and air bubbles. The sample before the measurement is shown on the left, after the measurement on the right. In the center – THz transmission image, the author's work presented at MIKON 2020 conference [36][x].

For the best SNR performance of such an imaging system it is important to match the following parameters:

- Electro-optical dual-comb:
  - the highest available power and central frequency
  - comb size (number of teeth)
  - the frequency difference between the teeth, and therefore the bandwidth
- Optical THz setup:
  - the smallest possible beam waist
  - step size in *x*-*y* directions ≈ beam waist
- TeraFET:
  - the lowest optical NEP and central frequency
  - the lowest amplifier input noise
  - the bandwidth of the amplifier
  - amplifier gain
- Data acquisition and processing system:
  - noise limit ≤ noise limit of the TeraFET
  - sampling speed > $2f_{MAX,RF}$

As the dual-frequency comb system was already optimized, the bottleneck was the TeraFET design in this development stage.

[x] © 2020 by Warsaw University of Technology. All rights reserved.

6.3.2 TeraFET implementation

To assure the highest dynamic range of the dual-comb system for the targeted central frequency of 330 GHz, a TeraFET was designed with an additionally implemented low-noise amplifier which reached the gain of 40.8 dB and the 3-dB bandwidth of 200 kHz. The detector was fabricated on 90-nm CMOS technology. It is based on a double-gate transistor integrated with a slot antenna. The impedance of the antenna was matched using an additional dipole configuration. The characterization was conducted on TeraFET as well as TeraFET with LNA configuration.

The measured data is shown in Fig. 6.36. The graph at the left shows the measured signal at various frequencies of the TeraFET signal as well as the signal after amplification as a response to the Toptica THz source. The dashed line shows the TeraFET noise level which is an equivalent of 5.1 kΩ channel resistance. The dips in the spectrum correspond to the water absorption lines.

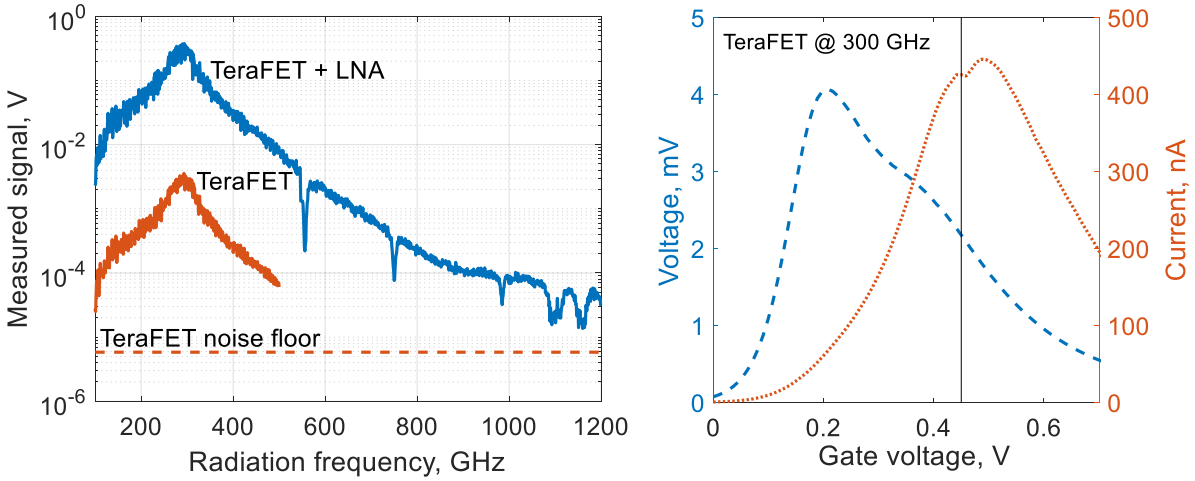

Fig. 6.36. Measured spectra with Toptica system (left) and gate voltage dependency on detected voltage and current signals (right).

The graph at the right of Fig. 6.36 represents the gate-voltage dependency of the detected signal at 300 GHz without LNA. The dashed line corresponds to the voltage and the dotted line represents the detected current. The solid line shows the best NEP point equal to the gate voltage of 0.45 V.

Fig. 6.37 shows the calculated optical responsivity and optical NEP values for this detector which is shown in the inset. Optical responsivity has its maximum at 296 GHz and FWHM bandwidth of 20 % or 42 GHz. At measured total Toptica power of 5.1 µW at 296 GHz, the optical voltage responsivity reaches approx. 0.5 kV/W and 60 kV/W for the best NEP point without and with the integrated LNA, respectively. The NEP dependency on frequency is depicted at the right. The dots show the measured data and the solid line represents the

averaged data for clarity. The best optical NEP without LNA was lower than 19 pW/√Hz whereas with amplifier it reached 20.8 pW/√Hz.

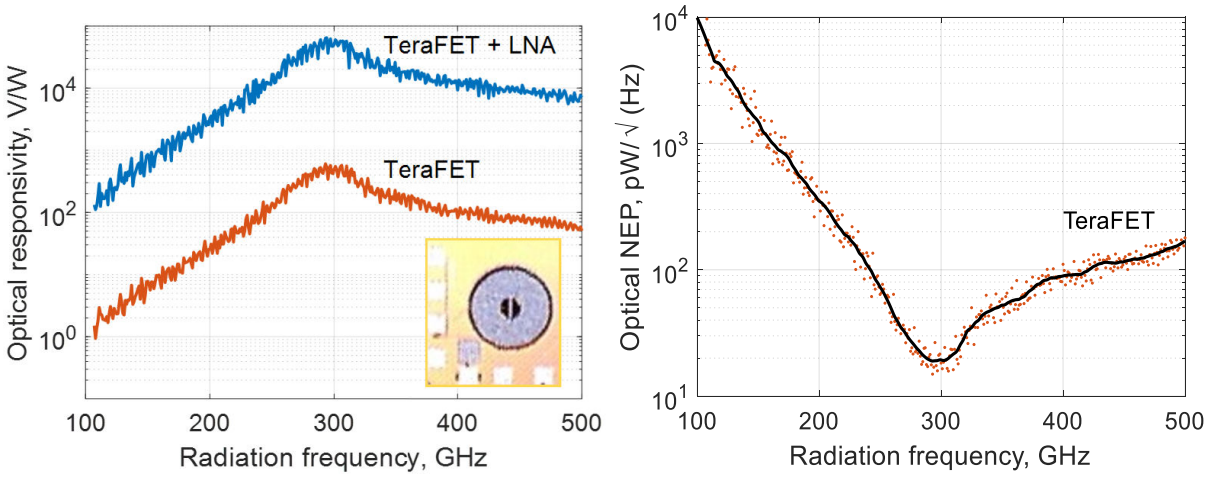

Fig. 6.37. Optical responsivity and optical NEP of the detector. Author's work presented in MIKON 2020 conference [36][y].

The LNA integration as close to the detector as possible is important for the detector protection from additional noise sources from the environment which can be inducted via cables or insufficient detector shielding. The choice of the operational amplifier for the LNA is of importance as it adds to the noise from the detector reducing the total dynamic range of the detector. Therefore, the OPA827 was chosen which has input noise of only 4 nV/√Hz above 100 Hz, a low offset voltage of 150 µV, and a gain-bandwidth product (GBW) of 22 MHz. Lastly, the gain of the amplifier should be enough so that the detected signal is not limited by the noise of the acquisition board.

With this achieved, the optimized system is now ready for hyperspectral imaging. However, it should be considered that the SNR of each frequency teeth becomes smaller with each additional frequency. Taking this into account, the hyperspectral imaging experiment with the presented TeraFET was conducted on 9 frequency teeth in various materials. The results are presented in [35].

6.3.3 Hyperspectral imaging results

The hyperspectral image was acquired after both systems were optimized for the same frequency range. The area of 32 mm by 32 mm was raster scanned in 1 mm steps. The result is depicted in Fig. 6.38. The multilayer soft plastic sample with a Velcro hook was taken to

prove the possibility of such a system to be applied for industrial applications. The sample contained few layers including a Velcro hook. Nine images were taken simultaneously during raster scanning at frequencies from 0.26 – 0.34 THz in the 20 GHz step. The differences can be seen in between the radiation intensity which was detected after transmission through the sample.

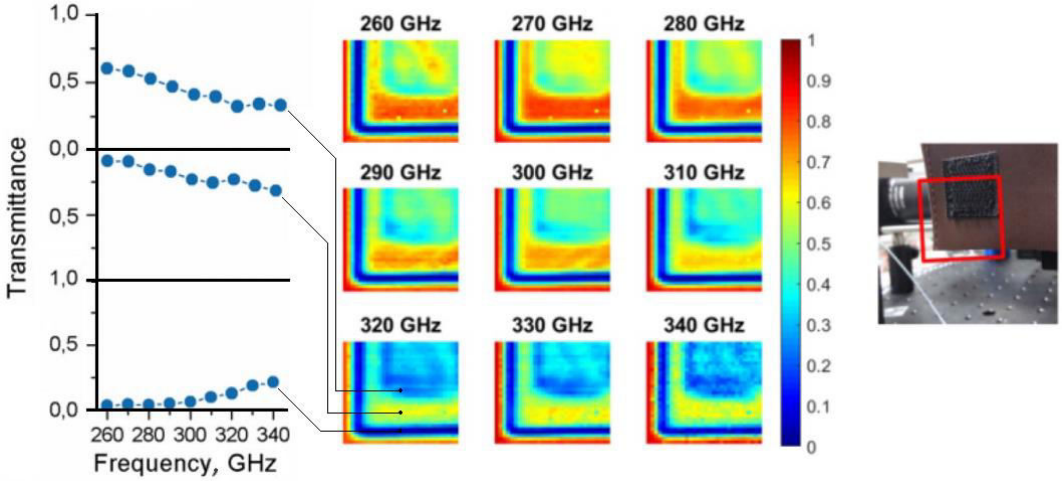

Fig. 6.38. Hyperspectral images and spectra of a sample that includes various materials. Figures 3-4 from Scientific Reports [35] merged under © CC BY 4.0.

The image acquisition time was around 1 hour in the system which was not optimized for the fast scanning as well as a fast readout. Despite this, the system shows the spectral differences of the sample layers. Both layers transmit the radiation better at lower frequencies, however, the radiation penetrates much better through the single layer. It can be seen that the Velcro hook attenuates the radiation more than the main layer. The diffraction from the edge of the sample creates a zero-transmission point which becomes more transparent at higher frequencies.

The presented experiment shows that hyperspectral imaging is possible using TeraFET detectors even with a low power source. The precision, tunability, and high-frequency resolution of the dual-frequency THz comb system assures precise spectroscopy at a considered frequency range even beyond 1 THz, where TeraFET detectors are proven to have a high sensitivity. The presented imaging system provides hyperspectral imaging at frequency resolution between THz lines down to few kilohertz. Whereas the imaging speed can be optimized by developing a multi-pixel array for hyperspectral imaging.

6.4 Passive human-body radiation imaging

This section is dedicated to the passive imaging experiment of human-hand radiation using a broadband TeraFET. This is the first experiment made using TeraFET detection on human-body radiation under complete room temperature conditions (no additional illumination or

cooling). The proof-of-concept experiment opens the new possibilities of broadband passive imaging in the sub-THz range, which can be applied in medical and security applications.

6.4.1 Black body radiation coupling

The theoretical explanation of black body radiation was discussed in Section 2.1.1 Passive THz sources. It was shown that the spectral radiance (spectral power density over a unity solid angle) of the black body at room temperature is below pW/sr·m^2·Hz. Therefore, it is a challenge to couple enough radiation into a THz detector. One of the important characteristics of black body radiation coupling into an antenna, which is derived in this section, is that the spectral power density is constant over a wide frequency range up to a few THz depending on the temperature of the black body source. Therefore, for the recent technology development, the widest possible THz detector bandwidth and the lowest NEP [50] are necessary at the optimal optical coupling conditions.

The optical system is depicted in Fig. 6.39. The system contains a black body radiator with the emissivity of ε_{BB}, two parabolic mirrors or lenses with focal lengths F_1 and F_2, and aperture diameters d_1 and d_2, and a detector with effective antenna area A_{eff} and hyper-hemispherical lens focusing the radiation into the antenna. The brown dashed lines explain the symmetry of the optical axis for the wavefront radiated by the black body. The vertical dashed line shows the symmetry axis of the system for the wavefront radiated from the left curved dashed line towards the right dashed line at the focusing detector lens surface. This means that the emitted power from the black body in the beam path at the surface of the dashed line at the left is mirrored as the incoming radiation into the detector lens.

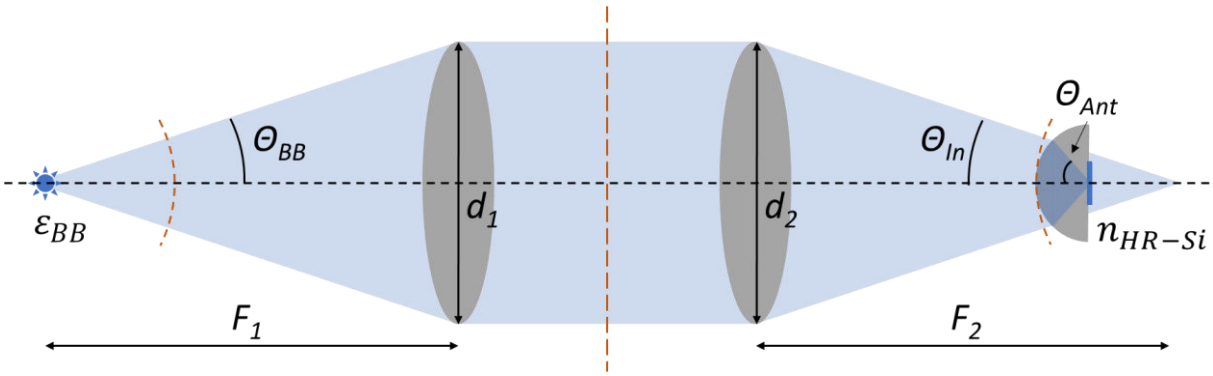

Fig. 6.39. Schematics of the optical *f-f* system for black-body radiation coupling into a TeraFET detector.

If the optical system parameters are optimized, then the radiation power $P(f, T_{BB})$ of T_{BB} temperature black body radiator of $\varepsilon_{BB}(f)$ is coupled to the TeraFET with D directivity antenna over the effective antenna area $A_{eff} = \frac{c^2}{4\pi f^2} \cdot D$ and the solid angle $\Omega_{Ant} = \frac{4\pi}{D}$ equals:

$$P(f,\, T_{BB}) = \int_{f_1}^{f_2} \varepsilon_{BB}(f) \cdot \frac{2hf^3}{c^2} \cdot \frac{\Omega_{Ant} \cdot A_{eff}(f)}{e^{\frac{hf}{k_B\, T_{BB}}} - 1}\, df \qquad \text{Eq. 15}$$

This form can be simplified using the Taylor series of the exponential function results in the following 1st order polynomial function:

$$e^{\frac{hf}{k_B\, T_{BB}}} = \sum_{n=0}^{\infty} \frac{(hf/k_B\, T_{BB})^n}{n!} = 1 + \frac{hf}{k_B\, T_{BB}} + \cdots, \qquad -\infty < x < \infty \qquad \text{Eq. 16}$$

The result leads to the Rayleigh-Jeans law [168] which is valid only when the thermal source energy $k_B T$ is much higher than the photon energy hf. For room temperature ambient this is in good agreement up to 5 THz. Therefore, for low THz frequencies radiated spectral power for both polarizations can be calculated as

$$P(f,\, T_{BB}) = 2k_B\, T_{BB} \int_{f_1}^{f_2} \varepsilon_{BB}(f)\; df \qquad \text{Eq. 17}$$

This equation shows the constant spectral power density over a wide frequency range. The graphical presentation of this equation for various temperatures of black body source as depicted in Section 2.1.1 Passive THz sources at the right of Fig. 2.1. Accounting for the antenna polarization, only half of the black body radiation induces the output signal in the detector:

$$V = \Omega_{Ant} \cdot \int_{f_2}^{f_1} \frac{P(f,\, T_{BB})}{2} \cdot \mathcal{R}_V(f) \cdot A_{eff}(f)\, df = k_B\, T_{BB} \int_{f_1}^{f_2} \varepsilon_{BB}(f) \cdot \mathcal{R}_V(f)\, df \qquad \text{Eq. 18}$$

NETD can be calculated as the thermal noise in *BW* bandwidth of the R_{ch} detector channel resistance at room temperature *T* over the signal change due to black body temperature change:

$$NETD \;=\; \frac{\sqrt{4k_B T R_{\mathrm{ch}} BW}}{\frac{\Delta V}{\Delta T_{BB}}} = \frac{\sqrt{4k_B T R_{\mathrm{ch}} BW}}{k_B \int_{f_1}^{f_2} \varepsilon_{BB}(f) \cdot \mathcal{R}_V(f)\, df} = \frac{NEP \cdot \sqrt{ENBW}}{k_B \Delta f \int_{f_1}^{f_2} \varepsilon_{BB}(f)\, df} \qquad \text{Eq. 19}$$

When the black body emissivity equals 1 and NEP is constant in THz frequency range defined by Δf the NETD of a TeraFET using the lock-in measurement technique with a particular equivalent-noise bandwidth (ENBW) setting, can be calculated as

$$NETD \;=\; \frac{NEP \cdot \sqrt{ENBW}}{k_B \Delta f} \qquad \text{Eq. 20}$$

The equations Eq. 19 and Eq. 20 are valid only for the low THz range and optimal optical setup conditions when the solid angle of the incoming radiation is close to the antenna radiation pattern. If the incoming radiation is focused differently than the optimal angle θ_{in}, the induced signal in the detector channel is less than the described ΔV and the minimal temperature difference is not detected. For the detector with log-spiral antenna used for this experiment (briefly presented in [40] as a comparison to the bow-tie antenna design), the constant NEP in 0.1 – 1.5 THz range reaches 42 pW/√Hz, therefore, the calculated NETD equals 2.17 K for 1 Hz bandwidth.

6.4.2 Thermal detection experiments

As the radiation of any black body in the THz range is very small in comparison with the IR range (see Chapter 2), the incoming power of the radiation is extremely low (was calculated in Section 2.1.1.1 Blackbody). Since now, the radiation of a black body has been detected using broadband TeraFETs which were at least an order of magnitude higher [54, 55] than the NETD needed for the detection of human body radiation and room temperature background. The temperature difference is usually around 10 K.

The thermal detection system was based on a hot ceramic. According to the specification, it can be heated up to 600 °C applying supply voltage. However, defining the temperature of the thermal source output was a complicated task. Using an IR thermometer, the measured temperature was only 140 °C despite the manufacturer's defined temperature of 600 °C. However, a red visible light emitted from the ceramic indicates the ceramic temperature to be like the specified one. The huge difference between the specified and measured values can be explained by the large integration area of the IR thermometer or/and the emissivity of the thermal source which might be far away from~1.

For the optical setup shown in Fig. 6.40. Thermal radiation passes two off-axis parabolic mirrors and is chopped at 77 Hz and focused via hyper-hemispherical lens into a CMOS-based TeraFET with a log-spiral antenna. The TeraFET with LNA of 40 dB gain and a lock-in amplifier has been used to measure mechanically chopped thermal signal.

Various parabolic mirror configurations were tested before the experiment to find the best coupling angle. The optical chopping was used for the detection of the response signal with a lock-in amplifier. The detected signal amplitude at the corresponding mirror focal length is shown in Table 6.3.

Table 6.3. Measurement parameters.

Diameter, inch	Focal length, inch	Solid angle, sr	Detected signal, µV
2	2 and 2	0.79	51
2	3 and 3	0.35	48
2	4 and 4	0.20	42

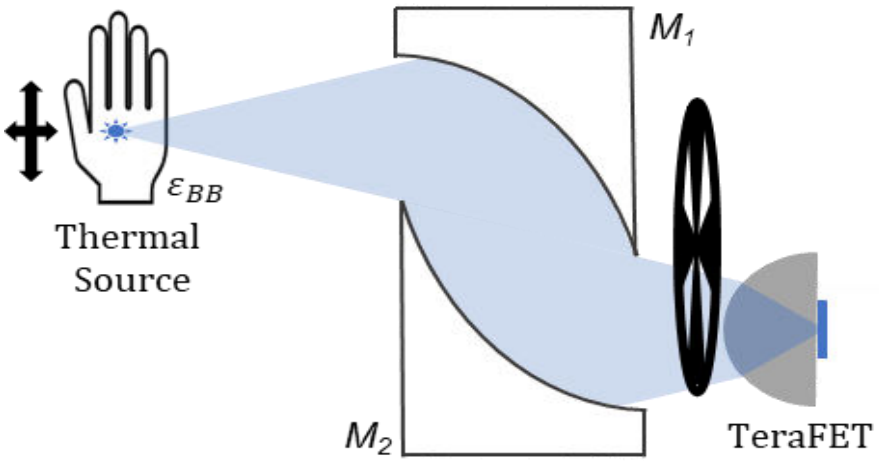

Fig. 6.40. Passive imaging setup. Used thermal sources were a hot ceramic and a human palm.

For $d < F$, the solid angles Ω in steradians (sr) corresponding to the half-angle θ can be expressed through the relation of the numerical aperture of the lens and its focal length:

$$\Omega_{BB} \approx 4\pi \frac{\frac{\pi}{4} {d_1}^2}{4\pi {F_1}^2} = \frac{\pi}{4}\left(\frac{d_1}{F_1}\right)^2 \qquad \text{Eq. 21}$$

According to this relation, the following solid angle values are shown in the third column of the table.

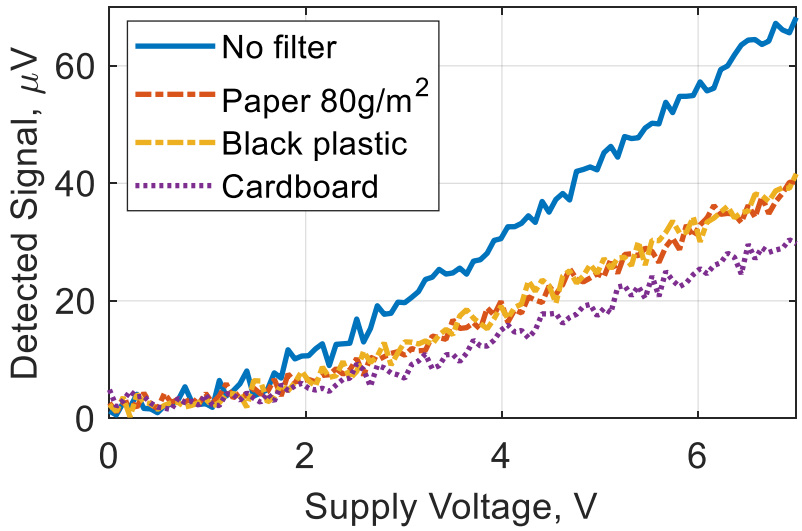

Fig. 6.41. Detected signal dependency at various thermal source supply voltages under paper, black plastic, cardboard attenuation condition.

As one can see, the optimal configuration is when the focal length of the mirrors equals 3 inches, as for the shorter focal length the incoming radiation angle is bigger than the angle of the antenna radiation pattern and some radiation cannot be coupled to the detector.

As the right configuration of the mirrors was chosen, the IR test of this thermal source was conducted using a sheet of paper reducing the thermal signal by 10 times at around 1 THz. The paper blocks the IR part of the radiation and therefore, we can see that the detected signal is due to low-frequency THz radiation. The detected signal over the thermal source supply voltage with different attenuators is depicted in Fig. 6.41. The detected signal under the attenuation is almost half of the signal without attenuation. This means that almost half of the radiation was blocked mostly above 1 THz frequency. More about paper attenuation can be found in [169].

Once the measurement setup was ready, the thermal sensitivity of the TeraFET was measured. The first experiment was made on a hot ceramic-based thermal source, which was blocked with a metal block to create ON/OFF modulation and be able to see the signal-to-noise ratio. Each measurement has been taken every second with a 200 ms time constant. The result is depicted in Fig. 6.42. The signal-to-noise ratio equals 54 times at the noise level of 1.38 µV/√Hz and lock-in time constant of 200 ms with a 12 dB/oct filter. The distribution of the detected signal is depicted in the same figure (bottom).

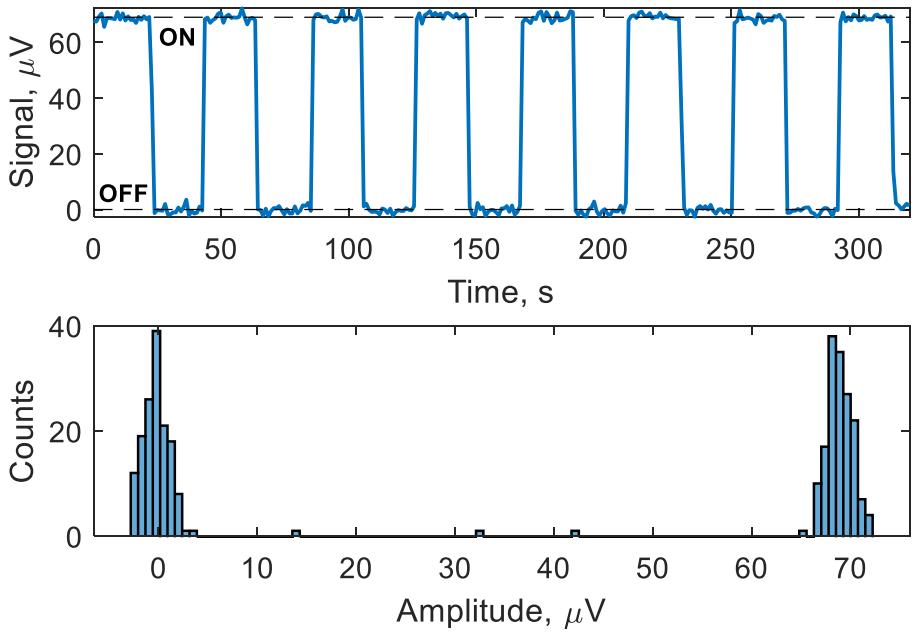

Fig. 6.42. Thermal source modulation (top) and value distribution (bottom).

As the sensitivity of the detector was high enough, the same experiment was conducted on the radiation of a human palm which is only around 10 K above the room temperature. This allows the exploration of the sensitivity limit of the TeraFET-based detector. The experiment was conducted with 5 different people (2 female and 3 male) of different ages. The hand was moved in and out of the setup focusing the palm radiation into the focal point

of the optical system. In Fig. 6.43, the modulation of palm radiation is shown at two different periods of 32 s and 40 s and the Fourier transformation for the first harmonic signal is depicted below. The signal of the experimenter called DC is the best, as it was an experienced experimenter and the hand movements in and out of the optical setup were more precise as of the other people. However, all the signals have a clear modulation at the expected frequencies.

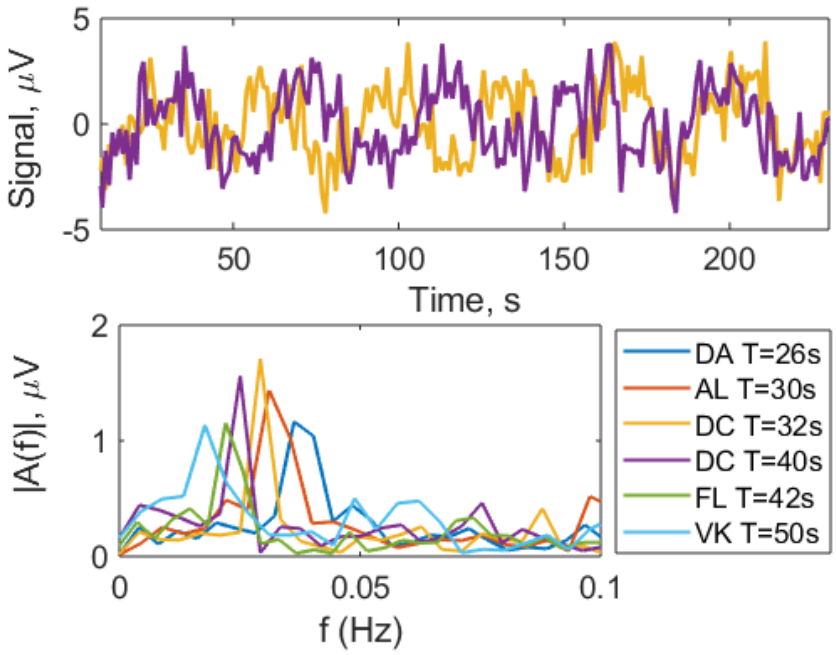

Fig. 6.43. Modulated palm radiation detected signal at 32 and 40 s period (top) and the Fourier transform spectrum of the signals of 5 people of different age and gender.

In Fig. 6.44, the closest emissivity values for our experiment of human skin from the literature are shown which were in detail presented in Fig. 2.2. To obtain the emissivity values for various bandwidths of a detector, linear interpolation was applied. The graph shows the blue data points and the calculated mean emissivity value for the bandwidth $BW = f - 30$ GHz, where f is the variable of the X-axis. The mean emissivity of 0.9 can be taken for a broadband detection up to 1 THz or higher. However, for the lower frequency bands, the radiation is not emitted so efficiently. For example, in the 30 - 100 GHz range, the mean emissivity is only 0.6. That means, by reducing the total bandwidth by 10 times, only 10 percent of the radiated power is detected which is additionally 30 % weaker due to lower emissivity of the skin at lower frequencies. For broadband detectors, the calculated emissivity equals 0.81 up to 0.5 THz, 0.9 up to 1 THz, and 0.92 up to 2 THz.

As mentioned before, the log-spiral antenna with constant NEP in 0.1 – 1.5 THz range of 42 pW/√Hz has NETD equal to 2.17 K for the ideal conditions of black body radiation at 1 Hz bandwidth. However, for the following presented experiment, the expected NETD is $\pi/\sqrt{2}$ times higher due to the detection of the chopped signal with a lock-in amplifier, therefore

for the given bandwidth one would expect NETD of 4.82 K. For the ENBW of 0.833 Hz and calculated mean skin emissivity of 0.915 up to 1.5 THz, the awaited NETD equals 4.8 K.

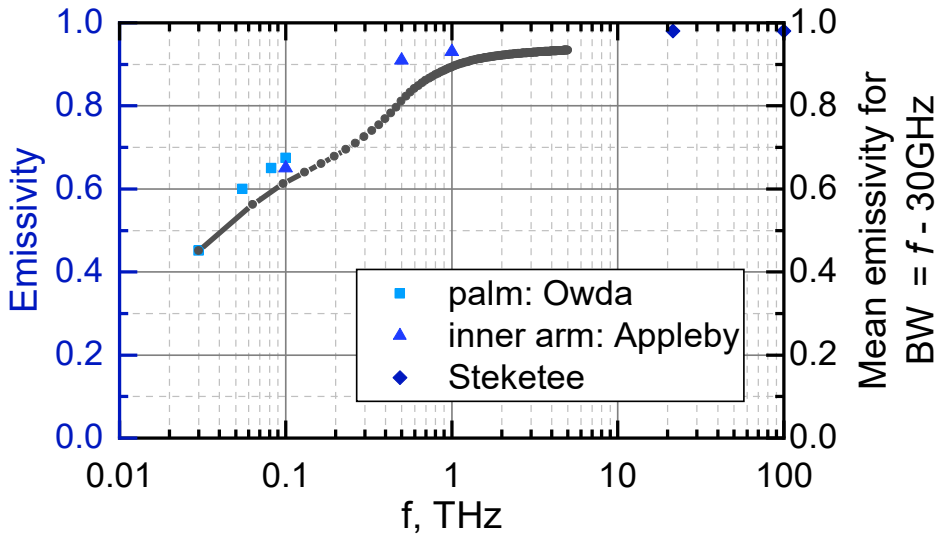

Fig. 6.44. Interpolation of the mean emissivity over the bandwidth BW = f-30 GHz using the values given in the literature. Author's work, reprinted from MDPI Sensors [48] under © CC BY 4.0.

As the experimental SNR of the palm signal (shown in Fig. 6.43.) is 1.97 and the difference between the palm and the ambient temperature was 8.7 K, the NETD for 1 Hz equals 4.4 K, and therefore, the measured NETD at 0.883 Hz bandwidth equals 4.8 K. Although both, theoretical and experimental, values are identical, this shows only a good agreement of the theory and the experiment, as the exact bandwidth of the detector was not characterized (only the part up to 1.5 THz) which would reduce the NETD if the bandwidth is wider. It is also very likely that some part of the radiation was not coupled into the detector due to discrete practical values of the angular beam for the radiation focusing into the detector as shown in Table 6.3. A less focused beam leads to a higher experimental NETD.

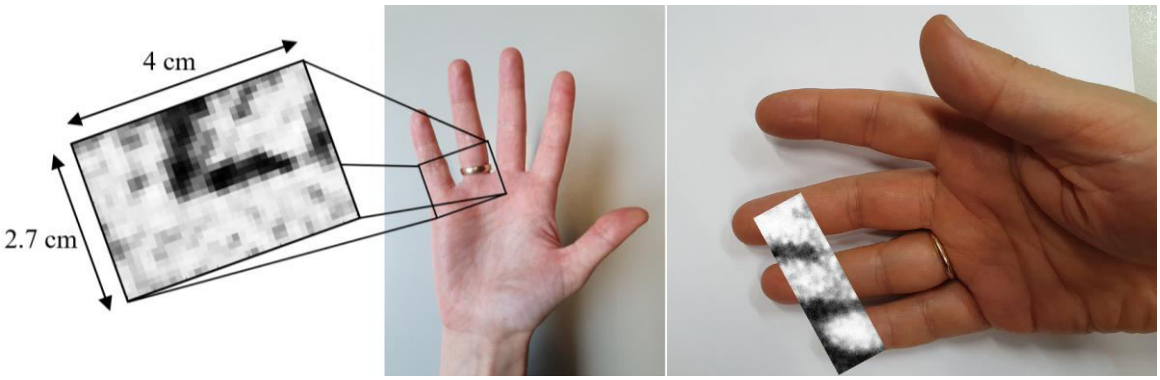

Fig. 6.45. Passive images of human body radiation of female and male hands compared to their photographs. Data from the left was published in [77]. At the right is the author's work, reprinted from MDPI Sensors [35] under © CC BY 4.0.

The presented results are the first of this type showing the TeraFET applicability for passive imaging of human body radiation. This opens a completely new field of applications for FET-based detectors. The multi-pixel implementation of this type of pixel will lead to much faster imaging of black body sources. For the applications which need more sensitivity, a multi-pixel camera can be cooled, and therefore, the NETD can be increased 4 times at 77 K [128].

7. Summary and outlook

This work focused on the field-effect transistor-based THz detectors. This work aimed to enhance the device sensitivity and explore the application field of such detectors. For that, the characterization and calibration challenges were addressed, and technical know-how was presented. The exploration of the applications was considered beyond the usual spectroscopy and active imaging applications. To this end, hyperspectral and passive imaging have been explored as new and challenging types of TeraFET applications. The proof-of-concept experiments conducted within this study for TeraFET technology were crucial for further THz system development. This showed the performance of TeraFETs to be comparable to commercial Schottky-diode technology and opened new possibilities for TeraFET applications.

Calibration challenges and optical performance definitions

This work also presented the calibration challenges of THz detectors and the means to address them. From one side, it is challenging to conduct a suitable characterization procedure for TeraFETs. On the other side, calibrated detectors cannot be easily compared to similar devices due to differences in calibration and analysis procedures between the scientific groups. To address the latter issue, the electrical model of a TeraFET was described in order to differentiate between the Dyakonov and Shur defined intrinsic detector responsivity and the losses in the radiation coupling path of the real device. This model should be helpful to explore various definitions of THz detectors presented in this work, which is important when comparing the differences between the optical, cross-sectional, electrical responsivity, or NEP.

It is expected that a better explanation of possible definitions of responsivity and NEP leads to a better quantitative comparison between future devices that should speed up the development of THz detector technologies. The more competition and technology variations there are, the better are the chances that more real-life THz applications will be seen in the near future improving the quality of life and further technology development.

TeraFET characterization

The characterization was performed with the construction of the detector module and cryogenic system which enabled the electrical, optical, and cryogenic characterization. The stability in time, as well as the device's noise limitation by the thermal noise, were proven for each new technology involved in the research and development, because of its high importance for the proper device characterization. As there are still many challenges for the device calibration, two separate techniques were used for responsivity and NEP characterization: optical and thermal characterization. Once detectors were well

characterized, they were then compared with other devices which were presented in this work.

Using Toptica transmitter, the sensitivity limits of narrowband and wideband TeraFETs based on CMOS, AlGaN/GaN, and GFET technologies were explored and compared. The state-of-the-art detectors reach the resonant performance below 20 pW/√Hz at 0.3 THz and 0.5 THz, as well as 404 pW/√Hz cross-sectional NEP at 4.75 THz. The broadband detectors show NEP as low as 25 pW/√Hz at around 0.6 THz for the best AlGaN/GaN design and 25 pW/√Hz around 1 THz for the best CMOS design.

Considering the conducted electrical and optical experiments on FET technologies, the studies illustrated that no TeraFET technology was far superior to others and the choice for the TeraFET technology depends mostly on application. The need for robustness, expected production levels, possible influence on variations in the technological run, or novelty of the technology, such as presented plasmon visualization in TeraFET channel, dictate the optimal TeraFET technology choice. Considering THz detection, it was concluded that the sensitivity of the detector depends on the efficient radiation coupling, but not on a specific technology. The most important parameters defining the TeraFET performance are impedance matching and optical coupling techniques which are defined during the design stage. However, the epitaxy differences in the same technology might cause changes in the TeraFET performance as well as device stability over time and temperature change, as presented in this work.

The main characterization results of this work were the following. (a) The calibration of the low power of the Toptica system, which was conducted using a pyroelectric power meter, Golay cell, and Toptica receiver. This result led to a broadband characterization of the optical NEP of multiple TeraFETs. (b) The in-depth electrical and noise characterization led to the improved resistance characterization techniques and opened a broader perspective into detector resistance stability, which also led to the implementation of the resistance stabilization methodology for GFET characterization. (c) Cryogenic experiments were used for the thermoelectric effect characterization and testing of the procedure developed for the extraction of intrinsic detector parameters, as well as technology implementation for sensitivity enhancement at lower temperatures.

Explored TeraFET applications and results

Spectroscopy applications

Spectroscopy, imaging, hyperspectral imaging, and passive imaging applications were explored at room temperature conditions. The spectroscopy applications were explored in TDC and CW (Toptica and QCL sources) systems. The explored autocorrelation technique using the TDS system showed the possibility to employ TeraFETs for direct detection of THz pulses without interferometric measurement setup if the TeraFET response time of more than ten picoseconds is enough. The dynamic range of 24 dB at 1 THz and 36 dB at 0.6 THz in the direct detection regime was reached which is comparable to the electro-optical detectors

if employed in the coherent detection mode. Also, linear and super-linear regimes were explored.

As one of the most promising applications, metamaterial characterization was tested using TeraFET devices and a Toptica transmitter. The limitation on the full-range metamaterial transmission characterization above 1.4 THz occurred due to the design specification and application range mismatch which can be easily improved in new designs like the one presented as D53 in 65-nm CMOS technology showing the sensitivity of more than 25 pW/√Hz in 0.84 – 1.29 THz range. Lastly, one of the single-pixel devices and a multi-pixel array were tested to be an engineering solution for a radio astronomy system called GREAT in SOFIA observatory contributing to the detection of aircraft vibration-caused noise cancelation.

Imaging applications

The presented imaging applications included near-field and far-field solutions. Scanning near-field microscopy led to the visualization of plasma waves in a GFET channel. Whereas the far-field imaging made a 3D scan of a mobile phone through its plastic cover showed high accuracy and good feature recognition of the smartphone. For the multi-pixel array testing, we used 6x7 pixel arrays which have been implemented in configurable-size aperture and imaging configurations. The configurable aperture size allows the easier detector focusing procedure and a better fit to the beam size of the incoming radiation. The imaging has been tested on various THz sources and compared to the TeraSense 16x16 pixel array. The TeraFET array could recognize the THz beam even at 33 dB attenuation of electronic 300 GHz TeraSense source, whereas the TeraSense camera was already at its noise limit. The first TeraFET application on hyper frequency THz imaging tested in the specially developed dual frequency comb and TeraFET for 300 GHz radiation with 9 spectral lines led to outstanding imaging results on various materials.

One of the biggest milestones in this work was the passive imaging of human body radiation which was reached with the presented broadband CMOS detector with log-spiral antenna working in the 0.1 – 1.5 THz (and probably higher) range. This detector reaches the optical NEP of 42 pW/√Hz and NETD of 2.1 K and overcomes the performance limit of passive room-temperature imaging of the human body radiation, which was only 10 K above the room temperature. This experiment opened a completely new field which was only possible using the multiplier chain-based or thermal detectors.

Outlook

TeraFET technology in practical applications

It was shown that TeraFETs can be used as universal power detectors for various room-temperature broadband and narrow-band applications: short-pulse detection, time-domain or frequency-domain spectroscopy, active near-field microscopy, and far-field imaging in

various optical configurations. There is a potential for TeraFETs to be implemented for autocorrelation technique in TDS systems where the response time of more than ten picoseconds is enough. The TeraFETs are comprehensive detectors in narrowband and broadband spectroscopy systems as well in imaging applications, as it was shown in 3D phone screening. This proved that the TeraFET use in practical THz systems can be foreseen.

This work mainly explored room-temperature TeraFET detector technology. However, it was shown that TeraFETs can be easily produced as multi-pixel arrays and be cooled for sensitivity enhancement, for the applications demanding a faster imaging speed or a higher detector sensitivity, respectively. Implementation of TeraFETs as THz receivers would lead to an even higher dynamic range and would be comparable to nowadays CW spectroscopic systems. Hence, this work shows that the commercialization of TeraFET-based detectors can be a potential alternative for commercial Schottky diode-based THz detectors.

Future development of hyperspectral and passive imaging systems

The proof-of-concept experiments on hyper-spectral imaging and passive human-body radiation imaging were conducted for the first time and opened new perspectives for TeraFET applications.

One of the most promising novel applications could be hyperspectral THz imaging cameras for multispectral image recognition of industrial samples, gases or drugs, as well as security imaging at various sub-THz and few THz frequencies. Such systems need very high sensitivity, wide bandwidth, as well as fast detector response, giving the low cost, small size, and easy use which were all shown to be possible using a THz camera. Up to now, only a single pixel solution was tested in a hyperspectral imaging setup. The implementation of a multi-pixel solution and the suitable read-out implementation at a video rate is demanding for real-time hyperspectral imaging applications.

Another implementation of TeraFETs can be directed to medical applications using passive imaging. Namely, human face skin imaging for diabetes detection in various frequency ranges, including IR, visible light, and sub-THz radiation. For this application, the further development of TeraFET detectors extending their sensitivity and bandwidth are necessary, as well as the spectral characterization of the thermal spectroscopy system.

The implication of this work was an effective extension of the THz technology field which was demonstrated by the experimental evidence of the possible TeraFET applications.

Zusammenfassung

Mikrowellen- und IR-technologien verschmelzen miteinander bei der Entwicklung der elektronischen und photonischen Technologien im terahertz (THz) Bereich. Die Quellen- und Sensortechnologien sollten die Lücke zwischen Photonik und Elektronik schließen, wo die Strahlungsleistung und die Empfindlichkeit von Sensoren schwach sind. Als eine der Optionen für die THz-Detektionstechnologie schlagen wir Feldeffekttransistoren vor, die mit integrierten Antennen erforscht werden sollen, um hochempfindliche Bauelemente für den THz Bereich bereitzustellen. Die Transistoren wurden theoretisch in den 1990er Jahren von M. Dyakonov und M. Shur als THz-Detektoren vorgeschlagen.

Das Ziel dieser Arbeit war es, die Empfindlichkeit des Bauelements zu erhöhen und das Anwendungsgebiet solcher Detektoren zu erforschen. Dazu mussten die Herausforderungen bei der Charakterisierung und Kalibrierung überwunden werden. Die Erforschung der Anwendungen war nicht durch die üblichen Anwendungen der Spektroskopie und der aktiven Bildgebung begrenzt, sondern es wurden hyperspektrale und passive Bildgebung als die herausfordernden Arten von Anwendungen der Feldeffekttransistoren im THz Bereich untersucht. Die Machbarkeitsnachweis-Experimente dieser Technologie sind aus historischen Gründen für die weitere Systementwicklung von entscheidender Bedeutung, da bekannte Detektoren auf der Basis von Schottky Dioden in ähnlichen Anwendungen eingesetzt werden können und aufgrund einer besseren Erfahrung in der Regel als die bevorzugte Technologie für zukünftige Anwendungen gewählt werden. Mit dem experimentellen Nachweis der möglichen Anwendung von Feldeffekttransistoren wird es hoffentlich eine größere Vielfalt an auswählbaren Technologien geben, die das Feld der möglichen THz Anwendungen erweitern können. Deswegen werden wir in dieser Arbeit verschiedene Feldeffekttransistoren-basierte Technologien, wie CMOS, AlGaN/GaN und Graphen-basierte Materialsysteme, untersuchen. Die Detektoren werden in einem breiten Frequenzbereich von 0,1 bis 5 THz in Schmalband- und Breitbandkonfigurationen erforscht.

Diese Arbeit konzentriert sich auch auf den Kalibrierungsaspekt von THz-Detektoren. Auf einer Seite ist es eine Herausforderung, ein geeignetes Charakterisierungsverfahren für Feldeffekttransistoren durchzuführen. Auf der anderen Seite können kalibrierte Detektoren aufgrund der unterschiedlichen Kalibrier- und Analyseverfahren der wissenschaftlichen Gruppen nicht ohne weiteres mit ähnlichen Detektoren verglichen werden. Um dem späteren Problem zu entsprechen, wurde das elektrische Modell eines Feldeffekttransistors mit integrierter Antenne beschrieben, um zwischen der von Dyakonov und Shur definierten intrinsischen Detektorempfindlichkeit und den Verlusten im Strahlungskopplungspfad des realen Geräts zu unterscheiden. Dieses Modell sollte hilfreich sein, um verschiedene Definitionen der vorgestellten THz Detektoren zu untersuchen, da es für den späteren Vergleich wichtig ist, den Unterschied zwischen der optischen, Querschnitts-, elektrischen Empfindlichkeit oder NEP zu sehen.

Für die richtige Implementierung von THz-Detektoren ist die gut definierte Charakterisierung von großer Bedeutung. Die Charakterisierung beginnt mit der Konstruktion des Detektormoduls, das die elektrische, optische und kryogenische Charakterisierung ermöglicht. Die zeitliche Stabilität sowie die Begrenzung des Rauschens durch das thermische Rauschen muss für jede neue Technologie, die in die Forschung und Entwicklung einbezogen wird, nachgewiesen werden, da sie für die korrekte Bauelementcharakterisierung von großer Bedeutung ist. Dazu wurden gleichzeitig manche neue Charakterisierungsmethoden entwickelt, nämlich die Stabilisierung der Graphen Feldeffekttransistoren, Charakterisierung von THz Quellen mit einer niedrigen Leistung, die danach für die Detektorkalibrierung verwendet werden, und Technologieentwicklung für den kryogenische Messungen, die in dieser Arbeit ausführlich vorgestellt wurden.

Die Kalibrierung der niedrigen Leistung des Toptica Systems wurde mit Hilfe eines pyroelektrischen Leistungsmessers, einer Golay Zelle und eines Toptica Empfängers durchgeführt. Dieses Ergebnis führte zu einer breitbandigen Charakterisierung der optischen NEP von mehreren Detektoren. Die tiefgehende elektrische und Rausch-Charakterisierung führte zu verbesserten Widerstandscharakterisierungstechniken und eröffnete eine breitere Perspektive in Bezug auf die Widerstandsstabilität der Detektoren, was auch die Widerstandsstabilisierung für die Charakterisierung von Graphen-basierten Feldeffekttransistoren ermöglichte. Kryogenische Experimente wurden für die Charakterisierung des thermoelektrischen Effekts, die Prüfung des Extraktionsverfahrens der intrinsischen Detektorparameter, sowie die Implementierung der Technologie zur Empfindlichkeitssteigerung bei niedrigeren Temperaturen verwendet.

Da es immer noch viele Herausforderungen für die Bauelementkalibrierung gibt, ist der beste Weg, die tatsächlichen optischen Parameter, wie Empfindlichkeit und NEP, zu definieren, die Verwendung von zwei getrennten Techniken: optische und thermische Charakterisierung. Diese Techniken werden hier auch präsentiert. Die gut charakterisierten Parameter eignen sich zum Vergleich mit anderen Bauelementen und zur Entscheidungsfindung über die richtige Wahl des geeigneten Detektors für die geplanten Anwendungen.

Während der durchgeführten Experimente sahen wir keine dominante Feldeffekttransistor Technologie, die über bessere Eigenschaften als die anderen verfügen würde. Die Wahl der Technologie bei bestimmten Anwendungen hängt davon ab, wie robust die Feldeffekttransistor Technologie ist, welche Produktionsmenge von TeraFETs ist zu erwarten, wie beeinflusset ist diese Technologie auf Variationen im technologischen Ablauf, oder der Neuartigkeit der Technologie, die spezifische Anwendungen ermöglicht, wie z.B. die Visualisierung von präsentierten Plasmonen im Kanal des Feldeffekttransistors. Die Empfindlichkeit des Detektors hängt eher von der effizienten Strahlungskopplung, nicht aber von einer bestimmten Technologie ab. Die wichtigsten Parameter, die die Sensitivität des Feldeffekttransistors als THz Detektors definieren, sind die Impedanzanpassung und die Techniken für die optische Kopplung, die während der Entwurfsphase festgelegt werden. Die

Unterschiede in der Epitaxie von derselben Feldeffekttransistortechnologie können jedoch zu Änderungen der Sensitivität des Detektors sowie der Stabilität des Bauelements über die Zeit und Temperaturänderungen führen.

Alle Anwendungen wurden bei Raumtemperatur durchgeführt. Die spektroskopische Anwendungen wurden in TDC- und CW-Systemen (Toptica- und QCL-Quellen) untersucht. Wir erforschten die Autokorrelationstechnik mit dem TDS-System. Das zeigte die Möglichkeit, die Feldeffekttransistoren zum direkten Nachweis von THz Pulsen, ohne interferometrischen Messaufbau einzusetzen, wenn die Ansprechzeit von dem Feldeffekttransistor von mehr als zehn Pikosekunden ausreicht. Der dynamische Bereich von 24 dB bei 1 THz und 36 dB bei 0,6 THz im direkten Detektionsmodus wurde erreicht, was mit den elektrooptischen Detektoren vergleichbar ist, wenn sie im kohärenten Detektionsmodus eingesetzt werden. Auch lineare und superlineare Regime wurden untersucht.

Unter Verwendung der Toptica Quelle untersuchten wir die Empfindlichkeitsgrenzen von schmal Bändigen und breitbandigen Feldeffekttransistoren auf der Basis von CMOS-, AlGaN/GaN- und GFET-Technologien, die in einem Diagramm mit der Zusammenfassung der veröffentlichten Daten verglichen wurden. Die hochmodernen Detektoren erreichen die Leistung Resonanzleistung unter 20 pW/√Hz bei 0,3 THz und 0,5 THz, sowie 404 pW/√Hz Querschnitts-NEP bei 4,75 THz. Die breitbandige Detektoren zeigen einen NEP von nur 25 pW/√Hz bei etwa 0,6 THz für das beste AlGaN/GaN Design und 25 pW/√Hz bei etwa 1 THz für das beste CMOS Design. Als eine der vielversprechendsten Anwendungen wurde die Charakterisierung von Metamaterialien mit unseren Detektoren getestet. Die Einschränkung ergab sich aus der Fehlanpassung der Designspezifikation und des Anwendungsbereichs, die bei neuen Designs leicht verbessert werden kann, wie das als D53 in 65-nm-CMOS-Technologie vorgestellte Design mit einer Empfindlichkeit von mehr als 25 pW/√Hz im Bereich von 0,84 - 1,29 THz. Eines der Ein-Pixel-Geräte und ein Multi-Pixel-Array wurden als technische Lösung für ein System der Radioastronomie namens GREAT im SOFIA-Observatorium getestet.

Zu den vorgestellten Bildgebungsanwendungen gehören Nahfeld- und Fernfeldlösungen. Die rasternde Nahfeldmikroskopie (s-SNOM) führte zur Visualisierung von Plasmawellen in einem Kanal der Graphen-basierten Feldeffekttransistor. Während die Fernfeld-Bildgebung einen 3D-Scan eines Mobiltelefons durch seine Kunststoffabdeckung hindurch machte, zeigte sich eine hohe Genauigkeit und eine gute Merkmalserkennung des Smartphones. Für die Multi-Pixel-Array-Tests verwendeten wir 6x7-Pixel Arrays, die in konfigurierbaren Größen für die Darstellung und Abbildung implementiert wurden. Die konfigurierbare Größe der Aperturen ermöglicht eine einfachere Detektorfokussierung und eine bessere Anpassung an die Strahlgröße der einfallenden Strahlung. Die Bildgebung wurde an verschiedenen THz-Quellen getestet und mit TeraSense 16x16-Pixel Arrays verglichen. Das Feldeffekttransistoren-basierte Array konnte den THz Strahl selbst bei 33 dB Dämpfung der elektronischen 300-GHz TeraSense Quelle erkennen, während die TeraSense Kamera bereits an ihrer Rauschgrenze war. Die erste Anwendung von Feldeffekttransistoren auf

Hyperfrequenz THz Bildgebung, die in dem speziell entwickelten Doppelfrequenzkamm und Feldeffekttransistoren für 300 GHz Strahlung mit 9 Spektrallinien getestet wurde, führte zu hervorragenden Bildgebungsergebnissen auf verschiedenen Materialien.

Zusammenfassend konnte in dieser Arbeit gezeigt werden, dass Feldeffekttransistoren mit integrierte Antena als universelle Leistungsdetektoren für verschiedene breitbandige und schmalbändige Anwendungen bei Raumtemperatur eingesetzt werden können: Kurzpulserkennung, Spektroskopie im Zeit- oder Frequenzbereich, aktive Nahfeld- und hauptsächlich Fernfeldabbildung in verschiedenen optischen Konfigurationen. Bei CMOS und AlGaN/GaN Technologien lassen sich solche Detektoren leicht als Multi-Pixel Arrays herstellen und können noch zur weiteren Erhöhung der Empfindlichkeit gekühlt werden. Das beste Ergebnis dieser Arbeit ist jedoch die passive Bildgebung der Strahlung des menschlichen Körpers, die mit dem vorgestellten breitbandigen CMOS Detektor mit Log-Spiral-Antenne erreicht wurde, der im Bereich von 0,1 - 1,5 THz (und wahrscheinlich höher) detektieren kann. Die optische NEP in dem Bereich ist 42 - 100 pW/√Hz. Damit wurde die NETD von 2,1 K erreicht, was die Leistungsgrenze der passiven Raumtemperatur-Bildgebung der Strahlung des menschlichen Körpers, die nur 10 K über der Raumtemperatur lag, überwunden hat. Dieses Experiment eröffnete ein völlig neues Feld, das zuvor nur von einer elektronischen Kette von Frequenz-Vervielfacher oder thermischen Detektoren erforscht wurde.

Verschiedene THz Anwendungen von Feldeffekttransistor als THz Detektors wurden untersucht. Angefangen bei den spektroskopischen Anwendungen und der Bildgebung bis hin zur hyperspektralen Bildgebung und sogar zur passiven Bildgebung der THz-Strahlung des menschlichen Körpers. In dieser Arbeit werden sowohl Einzel-Pixel Detektoren als auch Multi-Pixel Arrays vorgestellt. Es wurde gezeigt, dass Feldeffekttransistoren dienen als universelle Leistungsdetektoren im THz Bereich und können für verschiedene Breitband- und Schmalbandanwendungen bei Raumtemperatur eingesetzt werden, wie zum Beispiel, Kurzpulserkennung, Spektroskopie im Zeit- oder Frequenzbereich, aktive Nahfeld- und hauptsächlich Fernfeldabbildung in verschiedenen optischen Konfigurationen. Die Detektoren lassen sich leicht als Multi-Pixel Arrays herstellen und können zur Erhöhung der Empfindlichkeit gekühlt werden.

Da in dieser Arbeit viele vielversprechende Anwendungen aufgezeigt wurden, erwartet der Autor der Arbeit die Kommerzialisierung von Feldeffekttransistor-basierten Detektoren als Alternative für Schottky-Dioden-basierte THz Detektoren. Es besteht die Möglichkeit, die Feldeffekttransistoren für die Autokorrelationstechnik in TDS-Systemen zu implementieren, bei denen die Ansprechzeit von mehr als zehn Pikosekunden ausreicht. Die TeraFETs sind umfassende Detektoren in den Systemen der Schmalband- und Breitband-Spektroskopie und können auch als technische Lösung in solchen Systemen verwendet werden. Die Implementierung von Feldeffekttransistoren als homo- oder heterodyne THz Empfänger würde zu einem noch höheren dynamischen Bereich führen und wäre mit den heutigen CW-Spektroskopiesystemen vergleichbar.

Einzelpixellösungen lassen sich leicht in komplexe Bildgebungssysteme implementieren, jedoch könnten die vorsichtige Ausleseimplementierung und die Videoraten-Bildabtastung der Arrays dazu führen, dass die hochempfindlichen THz Kameras unter 1,5 THz viel besser als die heutigen kommerziellen Angebote werden könnten. Eine der vielversprechendsten Anwendungen könnten Hyperspektralbildgebungskameras sein, die eine sehr geringe Empfindlichkeit, eine große Bandbreite sowie eine schnelle Detektorreaktion benötigen, was die niedrigen Kosten, die geringe Größe und die einfache Verwendung einer solchen THz Kamera ermöglicht.

Nicht zuletzt wird es um die Implementierung von Feldeffekttransistoren für passive Bildgebungsanwendungen führen, die die mögliche Entwicklung von passiven medizinischen Bildgebungssystemen ermöglichen könnten. Die weitere Entwicklung auf diesem Gebiet ist abhängig von der Weiterentwicklung der Feldeffekttransistoren als THz Detektoren und deren Charakterisierung. Es bleibt zu hoffen, dass die bessere Erklärung der Definition der Empfindlichkeit und der NEP einen zusätzlichen Schub in Richtung empfindlicherer und besser vergleichbarer THz Detektortechnologien geben wird, da der bessere Vergleich einen besseren Wettbewerb schafft, was zu einer schnellere Entwicklung jeder Technologie führt. Je mehr Variationen in der Technologie wir in die Zukunft haben werden, desto besser sind die Chancen, dass wir in mehr reale THz Anwendungen sehen werden, die unsere Lebensqualität verbessern.

References

[1] U. R. Pfeiffer, E. Ojefors, A. Lisauskas, and H. G. Roskos, “Opportunities for silicon at mmWave and Terahertz frequencies,” in *IEEE Bipolar/BiCMOS Circuits and Technology Meeting, 2008: 13-15 Oct. 2008, Monterey, California*, Monterey, CA, 2008, pp. 149–156.

[2] N. Pala *et al.,* “Terahertz Technology for Nano Applications,” in *Springer reference, Encyclopedia of nanotechnology*, B. Bhushan, Ed., Dordrecht, London: Springer, 2012, pp. 2653–2667.

[3] S. S. Dhillon *et al.,* “The 2017 terahertz science and technology roadmap,” *J. Phys. D: Appl. Phys.*, vol. 50, no. 4, p. 43001, 2017, doi: 10.1088/1361-6463/50/4/043001.

[4] M. Tonouchi, “Cutting-edge terahertz technology,” *Nature Photon*, vol. 1, no. 2, pp. 97–105, 2007, doi: 10.1038/nphoton.2007.3.

[5] Nobel Media AB 2020, *Press release: The Nobel Prize in Physics 2020: Black holes and the Milky Way’s darkest secret.* [Online]. Available: https://www.nobelprize.org/prizes/physics/2020/popular-information/ (accessed: 1 Nov, 2020).

[6] K. G. Jansky, “Directional Studies of Atmospherics at High Frequencies,” *Proc. Inst. Radio Eng.*, vol. 20, no. 12, pp. 1920–1932, 1932, doi: 10.1109/JRPROC.1932.227477.

[7] A. A. Penzias and C. A. Burrus, “Millimeter-Wavelength Radio-Astronomy Techniques,” *Annu. Rev. Astron. Astrophys.*, vol. 11, no. 1, pp. 51–72, 1973, doi: 10.1146/annurev.aa.11.090173.000411.

[8] S. Withington, “Terahertz astronomical telescopes and instrumentation,” *Philosophical transactions. Series A, Mathematical, physical, and engineering sciences*, vol. 362, no. 1815, 395-401; discussion 401-2, 2004, doi: 10.1098/rsta.2003.1322.

[9] Y. Takeuchi, *Development of STJ with FD-SOI cryogenic amplifier as a far-infrared single photon detector for COBAND experiment: 17th International Workshop on Low Temperature Detectors.* [Online]. Available: https://slideplayer.com/slide/12739684/ (accessed: 8 Nov, 2020).

[10] F. Sizov, “Terahertz radiation detectors: the state-of-the-art,” *Semicond. Sci. Technol.*, vol. 33, no. 12, p. 123001, 2018, doi: 10.1088/1361-6641/aae473.

[11] R. Thierry and B. Clémentine, *THz Technologies Offer Varied Options for Industry.* [Online]. Available: https://www.photonics.com/Article.aspx?AID=56089 (accessed: 3 Nov, 2020).

[12] P. U. Jepsen, D. G. Cooke, and M. Koch, “Terahertz spectroscopy and imaging - Modern techniques and applications,” *Laser & Photon. Rev.*, vol. 5, no. 1, pp. 124–166, 2011, doi: 10.1002/lpor.201000011.

[13] VDI, *Custom Transmitters.* [Online]. Available: https://www.vadiodes.com/en/products/custom-transmitters

[14] Toptica Photonics, *Toptica Systems: Optoelectronic Terahertz-Generation.* [Online]. Available: https://www.toptica.com/products/terahertz-systems/

[15] J. Zdanevicius *et al.,* “Field-Effect Transistor Based Detectors for Power Monitoring of THz Quantum Cascade Lasers,” *IEEE Trans. THz Sci. Technol.*, vol. 8, no. 6, pp. 613–621, 2018, doi: 10.1109/TTHZ.2018.2871360.

[16] F. C. Cruz *et al.,* “Continuous and Pulsed THz generation with molecular gas lasers and photoconductive antennas gated by femtosecond pulses,” in *AIP Conference Proceedings*, Campinas, São Paulo (Brazil), Oct. 2007, pp. 383–385.

[17] J. Jin, M. Thumm, B. Piosczyk, S. Kern, G. Li, and T. Rzesnicki, “Highly efficient quasi-optical mode converter for coaxial ITER gyrotron at FZK,” in *2009 34th International Conference on Infrared, Millimeter, and Terahertz Waves*, Busan, South Korea, 2009, pp. 1–2.

[18] A. Soltani *et al.,* “Direct nanoscopic observation of plasma waves in the channel of a graphene field-effect transistor,” *Light, science & applications*, vol. 9, p. 97, 2020, doi: 10.1038/s41377-020-0321-0.

[19] SLT Sensor- und Lasertechnik GmbH, *THz detectors + accessoires: THz series high sensitive.* [Online]. Available: https://www.pyrosensor.de/High-Sensitive-924646.html

[20] M. Bolduc *et al.,* “Noise-equivalent power characterization of an uncooled microbolometer-based THz imaging camera,” in *Terahertz Physics, Devices, and Systems V: Advance Applications in Industry and Defense*, Orlando, Florida, United States, 2011, 80230C.

[21] QMC Instruments Ltd, *Terahertz pyroelectric detectors.* [Online]. Available: http://www.terahertz.co.uk/qmc-instruments-ltd/thz-detector-systems/pyroelectric-detectors

[22] Tydex, *Golay Detectors.* [Online]. Available: http://www.tydexoptics.com/products/thz_devices/golay_cell/#GC-1P

[23] Virginia Diodes, Inc., *Detectors: Zero bias detector.* [Online]. Available: https://www.vadiodes.com/en/products/detectors

[24] A. Semenov *et al., Eds., Schottky Diode Detectors for Monitoring Coherent THz Synchrotron Radiation Pulses*. JACoW, Geneva, Switzerland, 2014.

[25] E. R. Brown, A. C. Young, J. Zimmerman, H. Kazerni, and A. C. Gossard, “Advances in schottky rectifier performance,” *IEEE Microwave*, vol. 8, no. 3, pp. 54–59, 2007, doi: 10.1109/MMW.2007.365059.

[26] O. Cojocari *et al.,* “Quasi optical Schottky diode detectors for fast ultra-wideband detection,” in *9th International Conference on Microwave and Millimeter Wave Technology (ICMMT2016): Proceedings: June 5-8, 2016, Beijing International Convention Center (BICC), Beijing, China*, Beijing, China, 2016, pp. 52–53.

[27] M. Dyakonov and M. Shur, “Detection, mixing, and frequency multiplication of terahertz radiation by two-dimensional electronic fluid,” *IEEE Trans. Electron Devices*, vol. 43, no. 3, pp. 380–387, 1996, doi: 10.1109/16.485650.

[28] S. Boppel *et al.,* “CMOS Integrated Antenna-Coupled Field-Effect Transistors for the Detection of Radiation From 0.2 to 4.3 THz,” *IEEE Trans. Microwave Theory Techn.*, vol. 60, no. 12, pp. 3834–3843, 2012, doi: 10.1109/TMTT.2012.2221732.

[29] A. Lisauskas *et al.,* “Terahertz detection and coherent imaging from 0.2 to 4.3 THz with silicon CMOS field-effect transistors,” in *2012 IEEE/MTT-S International Microwave Symposium*, Montreal, QC, Canada, 2012, pp. 1–3.

[30] F. Simoens and J. Meilhan, “Terahertz real-time imaging uncooled array based on antenna- and cavity-coupled bolometers,” *Philosophical transactions. Series A, Mathematical, physical, and engineering sciences*, vol. 372, no. 2012, p. 20130111, 2014, doi: 10.1098/rsta.2013.0111.

[31] X.-C. Tu *et al.,* “Nb 5 N 6 microbolometer arrays for terahertz detection,” *Chinese Phys. B*, vol. 22, no. 4, p. 40701, 2013, doi: 10.1088/1674-1056/22/4/040701.

[32] S. Bevilacqua and S. Cherednichenko, “Fast room temperature THz bolometers,” in *38th International Conference on Infrared, Millimeter, and Terahertz Waves (IRMMW-THz), 2013: 1-6 Sept. 2013, Mainz on the Rhine*, Mainz, Germany, 2013, pp. 1–2.

[33] Richard Wylde, *Absolute THz Power-Energy Meters.* [Online]. Available: http://www.terahertz.co.uk/tk-instruments/products/absolute-thz-power-energy-meters

[34] M. Yahyapour, N. Vieweg, A. Roggenbuck, F. Rettich, O. Cojocari, and A. Deninger, “A Flexible Phase-Insensitive System for Broadband CW-Terahertz Spectroscopy and Imaging,” *IEEE Trans. THz Sci. Technol.*, vol. 6, no. 5, pp. 670–673, 2016, doi: 10.1109/TTHZ.2016.2589540.

[35] P. Martín-Mateos *et al.,* “Hyperspectral terahertz imaging with electro-optic dual combs and a FET-based detector,” *Scientific reports*, vol. 10, no. 1, p. 14429, 2020, doi: 10.1038/s41598-020-71258-6.

[36] D. Cibiraite-Lukenskiene *et al.,* “Field-Effect Transistor-Based Detector for Hyperspectral THz Imaging,” in *2020 23rd International Microwave and Radar Conference (MIKON)*, Warsaw, Poland, May. 2020 - Aug. 2020, pp. 300–304.

[37] M. Bauer *et al.,* “A High-Sensitivity AlGaN/GaN HEMT Terahertz Detector With Integrated Broadband Bow-Tie Antenna,” *IEEE Trans. THz Sci. Technol.*, vol. 9, no. 4, pp. 430–444, 2019, doi: 10.1109/TTHZ.2019.2917782.

[38] M. Ferreras Mayo, D. Cibiraite-Lukenskiene, A. Lisauskas, J. Grajal, and V. Krozer, “Broadband sensing around 1 THz via a novel biquad-antenna-coupled low-NEP detector in CMOS,” *IEEE Trans. THz Sci. Technol.*, p. 1, 2020, doi: 10.1109/TTHZ.2020.3031483.

[39] H. Qin *et al.,* “Detection of incoherent terahertz light using antenna-coupled high-electron-mobility field-effect transistors,” *Appl. Phys. Lett.*, vol. 110, no. 17, p. 171109, 2017, doi: 10.1063/1.4982604.

[40] K. Ikamas, D. Cibiraite, A. Lisauskas, M. Bauer, V. Krozer, and H. G. Roskos, “Broadband Terahertz Power Detectors Based on 90-nm Silicon CMOS Transistors With Flat Responsivity Up to 2.2 THz,” *IEEE Electron Device Lett.*, vol. 39, no. 9, pp. 1413–1416, 2018, doi: 10.1109/LED.2018.2859300.

[41] R. Han *et al.,* “280GHz and 860GHz image sensors using Schottky-barrier diodes in 0.13µm digital CMOS,” in *IEEE International Solid-State Circuits Conference digest of technical papers (ISSCC), 2012: 19-23 Feb. 2012, San Francisco, CA, USA ; volume 55*, San Francisco, CA, USA, 2012, pp. 254–256.

[42] A. A. Generalov, M. A. Andersson, X. Yang, A. Vorobiev, and J. Stake, “A 400-GHz Graphene FET Detector,” *IEEE Trans. THz Sci. Technol.*, vol. 7, no. 5, pp. 614–616, 2017, doi: 10.1109/TTHZ.2017.2722360.

[43] A. Zak *et al.,* “Antenna-integrated 0.6 THz FET direct detectors based on CVD graphene,” *Nano letters*, vol. 14, no. 10, pp. 5834–5838, 2014, doi: 10.1021/nl5027309.

[44] G. C. Trichopoulos, H. L. Mosbacker, D. Burdette, and K. Sertel, “A Broadband Focal Plane Array Camera for Real-time THz Imaging Applications,” *IEEE Trans. Antennas Propagat.*, vol. 61, no. 4, pp. 1733–1740, 2013, doi: 10.1109/TAP.2013.2242829.

[45] M. Bauer, *Hydrodynamic modeling and experimental characterization of the plasmonic and thermoelectric terahertz response of field-effect transistors with integrated broadband antennas in AlGaN/GaN HEMTs and CVD-grown graphene*. Frankfurt am Main: Universitätsbibliothek Johann Christian Senckenberg, 2018.

[46] K. Ikamas *et al.,* “Sub-picosecond pulsed THz FET detector characterization in plasmonic detection regime based on autocorrelation technique,” *Semicond. Sci. Technol.*, vol. 33, no. 12, p. 124013, 2018, doi: 10.1088/1361-6641/aae905.

[47] A. Lisauskas *et al.,* “Field-effect transistors as electrically controllable nonlinear rectifiers for the characterization of terahertz pulses,” *APL Photonics*, vol. 3, no. 5, p. 51705, 2018, doi: 10.1063/1.5011392.

[48] D. Čibiraitė-Lukenskienė, K. Ikamas, T. Lisauskas, V. Krozer, H. G. Roskos, and A. Lisauskas, "Passive Detection and Imaging of Human Body Radiation Using an Uncooled Field-Effect Transistor-Based THz Detector," *Sensors (Basel, Switzerland)*, vol. 20, no. 15, 2020, doi: 10.3390/s20154087.

[49] F. Meng, M. D. Thomson, B. Klug, D. Čibiraitė, Q. Ul-Islam, and H. G. Roskos, "Nonlocal collective ultrastrong interaction of plasmonic metamaterials and photons in a terahertz photonic crystal cavity," *Optics express*, vol. 27, no. 17, pp. 24455–24468, 2019, doi: 10.1364/OE.27.024455.

[50] P. Hillger, J. Grzyb, R. Jain, and U. R. Pfeiffer, "Terahertz Imaging and Sensing Applications With Silicon-Based Technologies," *IEEE Trans. THz Sci. Technol.*, vol. 9, no. 1, pp. 1–19, 2019, doi: 10.1109/TTHZ.2018.2884852.

[51] D. Cibiraite *et al.,* "Enhanced performance of AlGaN/GaN HEMT-Based THz detectors at room temperature and at low temperature," in *2017 42nd International Conference on Infrared, Millimeter, and Terahertz Waves (IRMMW-THz)*, Cancun, Mexico, 2017, pp. 1–2.

[52] N. Palka *et al.,* "THz spectroscopy and imaging in security applications," in *2012 19th International Conference on Microwaves, Radar and Wireless Communications*, Warsaw, Poland, 2012, pp. 265–270.

[53] N. Q. Vinh, "Probe conformational dynamics of proteins in aqueous solutions by terahertz spectroscopy," in *Terahertz Emitters, Receivers, and Applications VII*, San Diego, California, United States, 2016, 99340R.

[54] S. Malz, R. Jain, and U. R. Pfeiffer, "Towards passive imaging with CMOS THz cameras," in *2016 41st International Conference on Infrared, Millimeter, and Terahertz waves (IRMMW-THz)*, Copenhagen, Denmark, Sep. 2016 - Sep. 2016, pp. 1–2.

[55] J. Sun *et al.,* "Passive terahertz imaging detectors based on antenna-coupled high-electron-mobility transistors," *Optics express*, vol. 28, no. 4, pp. 4911–4920, 2020, doi: 10.1364/OE.385042.

[56] L. Yujiri, M. Shoucri, and P. Moffa, "Passive millimeter-wave imaging," *IEEE Microwave*, vol. 4, no. 3, pp. 39–50, 2003, doi: 10.1109/MMW.2003.1237476.

[57] J. Steketee, "Spectral emissivity of skin and pericardium," *Physics in medicine and biology*, vol. 18, no. 5, pp. 686–694, 1973, doi: 10.1088/0031-9155/18/5/307.

[58] A. Y. Owda *et al.,* "Millimeter-wave emissivity as a metric for the non-contact diagnosis of human skin conditions," *Bioelectromagnetics*, vol. 38, no. 7, pp. 559–569, 2017, doi: 10.1002/bem.22074.

[59] A. Y. Owda, N. Salmon, and N. D. Rezgui, "ELECTROMAGNETIC SIGNATURES OF HUMAN SKIN IN THE MILLIMETER WAVE BAND 80-100 GHZ," *PIER B*, vol. 80, pp. 79–99, 2018, doi: 10.2528/PIERB17120403.

[60] K. A. Baksheeva *et al.,* "Do humans "shine" in the sub THz?," in *2019 44th International Conference on Infrared, Millimeter, and Terahertz Waves (IRMMW-THz)*, Paris, France, Sep. 2019 - Sep. 2019, pp. 1–2.

[61] R. Appleby and H. B. Wallace, "Standoff Detection of Weapons and Contraband in the 100 GHz to 1 THz Region," *IEEE Trans. Antennas Propagat.*, vol. 55, no. 11, pp. 2944–2956, 2007, doi: 10.1109/TAP.2007.908543.

[62] ACST, *AMC/Transmitters: Overview.* [Online]. Available: https://acst.de/products/thz-custom-products/amc-transmitters/

[63] H. Richter *et al.,* "A compact, continuous-wave terahertz source based on a quantum-cascade laser and a miniature cryocooler," *Optics express*, vol. 18, no. 10, pp. 10177–10187, 2010, doi: 10.1364/OE.18.010177.

[64] F. K. TITTEL, Y. BAKHIRKIN, A. A. KOSTEREV, and G. WYSOCKI, “Recent Advances in Trace Gas Detection Using Quantum and Interband Cascade Lasers,” *rle*, vol. 34, no. 4, pp. 275–282, 2006, doi: 10.2184/lsj.34.275.

[65] P. J. Hale *et al.,* “20 THz broadband generation using semi-insulating GaAs interdigitated photoconductive antennas,” *Optics express*, vol. 22, no. 21, pp. 26358–26364, 2014, doi: 10.1364/OE.22.026358.

[66] B. Jerez, F. Walla, A. Betancur, P. Martín-Mateos, C. de Dios, and P. Acedo, “Electro-optic THz dual-comb architecture for high-resolution, absolute spectroscopy,” *Opt. Lett., OL*, vol. 44, no. 2, pp. 415–418, 2019, doi: 10.1364/OL.44.000415.

[67] B. Nabet, *Photodetectors: Materials, devices and applications / Bahram Nabet*. Oxford: Woodhead Publishing, 2015.

[68] F. Simoens *et al.,* “Uncooled Terahertz real-time imaging 2D arrays developed at LETI: present status and perspectives,” in *Micro- and Nanotechnology Sensors, Systems, and Applications IX*, Anaheim, California, United States, 2017, 101942N.

[69] B. Brandl, *Detection of Light: XI. Bolometers - Principle; XII. Bolometers - Response.* [Online]. Available: https://home.strw.leidenuniv.nl/~brandl/DOL/DTL_06_Bolometers.pdf (accessed: Oct. 22 2020).

[70] Gentec-EO, *TERAHERTZ POWER MEASUREMENT: Browse all Gentec-EO's terahertz power measurement products.* [Online]. Available: https://www.gentec-eo.com/products?type=thz (accessed: 7 Nov, 2020).

[71] Ophir Optronics Solutions Ltd, *RM9-THz with Chopper.* [Online]. Available: https://www.ophiropt.com/laser--measurement/laser-power-energy-meters/products/Laser-Thermal-Power-Sensors/High-Sensitivity-Thermal-Laser-Sensors/RM9-THz-with-chopper (accessed: 7 Nov, 2020).

[72] S. Malotaux, M. Babaie, and M. Spirito, “A Total-Power Radiometer Front End in a 0.25-um BiCMOS Technology With Low $1/{f}$ -Corner,” *IEEE J. Solid-State Circuits*, vol. 52, no. 9, pp. 2256–2266, 2017, doi: 10.1109/JSSC.2017.2705659.

[73] F. Caster, L. Gilreath, S. Pan, Z. Wang, F. Capolino, and P. Heydari, “Design and Analysis of a W-band 9-Element Imaging Array Receiver Using Spatial-Overlapping Super-Pixels in Silicon,” *IEEE J. Solid-State Circuits*, vol. 49, no. 6, pp. 1317–1332, 2014, doi: 10.1109/JSSC.2014.2310744.

[74] L. Liu, J. L. Hesler, H. Xu, A. W. Lichtenberger, and R. M. Weikle, “A Broadband Quasi-Optical Terahertz Detector Utilizing a Zero Bias Schottky Diode,” *IEEE Microw. Wireless Compon. Lett.*, vol. 20, no. 9, pp. 504–506, 2010, doi: 10.1109/LMWC.2010.2055553.

[75] V. G. Bozhkov, “Semiconductor Detectors, Mixers, and Frequency Multipliers for the Terahertz Band,” *Radiophysics and Quantum Electronics*, vol. 46, 8/9, pp. 631–656, 2003, doi: 10.1023/B:RAQE.0000024993.40125.2b.

[76] Z. Ahmad, A. Lisauskas, H. G. Roskos, and K. K. O, “9.74-THz electronic Far-Infrared detection using Schottky barrier diodes in CMOS,” in *2014 IEEE International Electron Devices Meeting (IEDM 2014): San Francisco, California, USA, 15-17 December 2014*, San Francisco, CA, USA, 2014, 4.4.1-4.4.4.

[77] D. Cibiraite *et al.,* “Thermal noise-limited sensitivity of FET-based terahertz detectors,” in *2017 International Conference on Noise and Fluctuations (ICNF)*, Vilnius, Jun. 2017, pp. 1–4.

[78] Swiss Terahertz, *RIGI Camera.* [Online]. Available: https://www.swissterahertz.com/rigicamera (accessed: 8 Nov, 2020).

[79] A. Lisauskas, U. Pfeiffer, E. Öjefors, P. H. Bolìvar, D. Glaab, and H. G. Roskos, “Rational design of high-responsivity detectors of terahertz radiation based on distributed self-mixing in silicon field-effect transistors,” *Journal of Applied Physics*, vol. 105, no. 11, p. 114511, 2009, doi: 10.1063/1.3140611.

[80] M. Helm, *Free-Electron Lasers at the ELBE - Center for High-Power Radiation Sources at the HZDR in Dresden-Rossendorf.* [Online]. Available: https://www.hzdr.de/db/Cms?pNid=471 (accessed: 16. Nov, 2020).

[81] D.-H. Kim and J. A. del Alamo, “30-nm InAs PHEMTs With $f_{T} = \hbox{644}\ \hbox{GHz}$ and $f_{\max} = \hbox{681}\ \hbox{GHz}$,” *IEEE Electron Device Lett.*, vol. 31, no. 8, pp. 806–808, 2010, doi: 10.1109/LED.2010.2051133.

[82] D. M. Pozar, *Microwave engineering,* 4th ed. Hoboken, NJ: Wiley, 2012.

[83] S. Bevilacqua and S. Cherednichenko, “Low Noise Nanometer Scale Room-Temperature YBa_2Cu_3O_{7−x} Bolometers for THz Direct Detection,” *IEEE Trans. THz Sci. Technol.*, vol. 4, no. 6, pp. 653–660, 2014, doi: 10.1109/TTHZ.2014.2344435.

[84] F. Ludwig, “Hydrodynamic modeling of charge and energy transport in graphene and fabrication of thermoelectric graphene THz detectors,” Master Thesis, Physikalisches Institut, J. W. Goethe University Frankfurt, Frankfurt am Main, 2018.

[85] G. Auton *et al.,* “Terahertz Detection and Imaging Using Graphene Ballistic Rectifiers,” *Nano letters*, vol. 17, no. 11, pp. 7015–7020, 2017, doi: 10.1021/acs.nanolett.7b03625.

[86] H. Sherry *et al.,* “Lens-integrated THz imaging arrays in 65nm CMOS technologies,” in *2011 IEEE Radio Frequency Integrated Circuits Symposium*, Baltimore, MD, USA, 2011, pp. 1–4.

[87] M. Bauer *et al.,* “Optimization of the Design of Terahertz Detectors Based on Si CMOS and AlGaN/GaN Field-Effect Transistors,” *Int. J. Hi. Spe. Ele. Syst.*, vol. 25, 03n04, p. 1640013, 2016, doi: 10.1142/S0129156416400139.

[88] D. B. But, E. Javadi, W. Knap, K. Ikamas, and A. Lisauskas, “Silicon based resonant power detector for 620 GHz,” in *2020 23rd International Microwave and Radar Conference (MIKON)*, Warsaw, Poland, May. 2020 - Aug. 2020, pp. 305–308.

[89] D. Yoon, J. Kim, J. Yun, M. Kaynak, B. Tillack, and J.-S. Rieh, “300-GHz Direct and Heterodyne Active Imagers Based on 0.13-µm SiGe HBT Technology,” *IEEE Trans. THz Sci. Technol.*, vol. 7, no. 5, pp. 536–545, 2017, doi: 10.1109/TTHZ.2017.2715419.

[90] R. Al Hadi *et al.,* “A 1 k-Pixel Video Camera for 0.7–1.1 Terahertz Imaging Applications in 65-nm CMOS,” *IEEE J. Solid-State Circuits*, vol. 47, no. 12, pp. 2999–3012, 2012, doi: 10.1109/JSSC.2012.2217851.

[91] Thomas Keating Instruments, *THz Absolute Power & Energy Meter System: Installation and Operation Instructions.* [Online]. Available: http://www.terahertz.co.uk/images/tki/PMETER/TKPOWERMETERMANUAL3p2p2.pdf

[92] J. K. Choi *et al.,* “THz Hot-Electron Micro-Bolometer Based on Low-Mobility 2-DEG in GaN Heterostructure,” *IEEE Sensors J.*, vol. 13, no. 1, pp. 80–88, 2013, doi: 10.1109/JSEN.2012.2224334.

[93] S. Bevilacqua and S. Cherednichenko, “High sensitivity terahertz bolometers as room temperature detectors,” in *39th International Conference on Infrared, Millimeter, and Terahertz Waves (IRMMW-THz), 2014: 14-19 Sept. 2014, The University of Arizona, Tucson, Arizona, USA*, Tucson, AZ, USA, 2014, pp. 1–2.

[94] A. Scheuring *et al.,* "Thin Pr–Ba–Cu–O Film Antenna-Coupled THz Bolometers for Room Temperature Operation," *IEEE Trans. THz Sci. Technol.*, vol. 3, no. 1, pp. 103–109, 2013, doi: 10.1109/TTHZ.2012.2226880.

[95] R. Al Hadi *et al.,* "A broadband 0.6 to 1 THz CMOS imaging detector with an integrated lens," in *2011 IEEE MTT-S International Microwave Symposium*, Baltimore, MD, USA, Jun. 2011 - Jun. 2011, pp. 1–4.

[96] A. K. Huhn, G. Spickermann, A. Ihring, U. Schinkel, H.-G. Meyer, and P. Haring Bolivar, "Fast antenna-coupled terahertz detectors based on uncooled thermoelements," in *2012 37th International Conference on Infrared, Millimeter, and Terahertz Waves*, Wollongong, NSW, Australia, Sep. 2012 - Sep. 2012, pp. 1–3.

[97] D. Y. Kim, S. Park, R. Han, and K. O. Kenneth, "Design and Demonstration of 820-GHz Array Using Diode-Connected NMOS Transistors in 130-nm CMOS for Active Imaging," *IEEE Trans. THz Sci. Technol.*, vol. 6, no. 2, pp. 306–317, 2016, doi: 10.1109/TTHZ.2015.2513061.

[98] X. Deng, M. Simanullang, and Y. Kawano, "Ge-Core/a-Si-Shell Nanowire-Based Field-Effect Transistor for Sensitive Terahertz Detection," *Photonics*, vol. 5, no. 2, p. 13, 2018, doi: 10.3390/photonics5020013.

[99] A. Pleteršek and J. Trontelj, "A Self-Mixing NMOS Channel-Detector Optimized for mm-Wave and THZ Signals," *J Infrared Milli Terahz Waves*, vol. 33, no. 6, pp. 615–626, 2012, doi: 10.1007/s10762-012-9901-2.

[100] A. Lisauskas *et al.,* "Exploration of Terahertz Imaging with Silicon MOSFETs," *J Infrared Milli Terahz Waves*, vol. 35, no. 1, pp. 63–80, 2014, doi: 10.1007/s10762-013-0047-7.

[101] U. R. Pfeiffer, J. Grzyb, H. Sherry, A. Cathelin, and A. Kaiser, "Toward low-NEP room-temperature THz MOSFET direct detectors in CMOS technology," in *38th International Conference on Infrared, Millimeter, and Terahertz Waves (IRMMW-THz), 2013: 1-6 Sept. 2013, Mainz on the Rhine*, Mainz, Germany, 2013, pp. 1–2.

[102] K. Sengupta, D. Seo, L. Yang, and A. Hajimiri, "Silicon Integrated 280 GHz Imaging Chipset With 4x4 SiGe Receiver Array and CMOS Source," *IEEE Trans. THz Sci. Technol.*, vol. 5, no. 3, pp. 427–437, 2015, doi: 10.1109/TTHZ.2015.2414826.

[103] S. M. Rahman, Z. Jiang, M. I. B. Shams, P. Fay, and L. Liu, "A G-Band Monolithically Integrated Quasi-Optical Zero-Bias Detector Based on Heterostructure Backward Diodes Using Submicrometer Airbridges," *IEEE Trans. Microwave Theory Techn.*, vol. 66, no. 4, pp. 2010–2017, 2018, doi: 10.1109/TMTT.2017.2779133.

[104] Z. Zhang, R. Rajavel, P. Deelman, and P. Fay, "Sub-Micron Area Heterojunction Backward Diode Millimeter-Wave Detectors With 0.18 ${\rm pW/Hz}^{1/2}$ Noise Equivalent Power," *IEEE Microw. Wireless Compon. Lett.*, vol. 21, no. 5, pp. 267–269, 2011, doi: 10.1109/LMWC.2011.2123878.

[105] S.-P. Han *et al.,* "InGaAs Schottky barrier diode array detector for a real-time compact terahertz line scanner," *Optics express*, vol. 21, no. 22, pp. 25874–25882, 2013, doi: 10.1364/OE.21.025874.

[106] T. Watanabe *et al.,* "InP- and GaAs-Based Plasmonic High-Electron-Mobility Transistors for Room-Temperature Ultrahigh-Sensitive Terahertz Sensing and Imaging," *IEEE Sensors J.*, vol. 13, no. 1, pp. 89–99, 2013, doi: 10.1109/JSEN.2012.2225831.

[107] A. K. Huhn, G. Spickermann, A. Ihring, U. Schinkel, H.-G. Meyer, and P. Haring Bolívar, "Uncooled antenna-coupled terahertz detectors with 22 µ s response time based on BiSb/Sb thermocouples," *Appl. Phys. Lett.*, vol. 102, no. 12, p. 121102, 2013, doi: 10.1063/1.4798369.

[108] K. S. Novoselov *et al.,* “Electric field effect in atomically thin carbon films,” *Science (New York, N.Y.)*, vol. 306, no. 5696, pp. 666–669, 2004, doi: 10.1126/science.1102896.

[109] Y.-M. Lin *et al.,* “Wafer-scale graphene integrated circuit,” *Science (New York, N.Y.)*, vol. 332, no. 6035, pp. 1294–1297, 2011, doi: 10.1126/science.1204428.

[110] A. Soltani *et al.,* “Unveiling the plasma wave in the channel of graphene field-effect transistor,” in *2019 44th International Conference on Infrared, Millimeter, and Terahertz Waves (IRMMW-THz)*, Paris, France, Sep. 2019 - Sep. 2019, p. 1.

[111] D. Čibiraitė, *Terahercų detekcijos grafeno lauko tranzistoriais tyrimas: magistro darbas: INVESTIGATION OF TERAHERTZ DETECTION BY GRAPHENE FIELD-EFFECT TRANSISTORS.* [Online]. Available: https://talpykla.elaba.lt/elaba-fedora/objects/elaba:20217065/datastreams/MAIN/content (accessed: 2 Nov, 2020).

[112] M. Bauer *et al.,* “The potential for sensitivity enhancement by the thermoelectric effect in carbon-nanotube and graphene Tera-FETs,” *J. Phys.: Conf. Ser.*, vol. 647, p. 12004, 2015, doi: 10.1088/1742-6596/647/1/012004.

[113] P. Kurpas, I. Selvanathan, M. Schulz, H. Sahin, P. Ivo, M. Matalla, J. Splettstoesser, A. Barnes, J. Würfl, Ed., *Stable and reproducible AlGaN/GaN-HFET processing highly tolerant for epitaxial quality variations*. Portland, USA: CSMantech, 2010.

[114] M. Shur, “Plasma wave terahertz electronics,” *Electron. Lett.*, vol. 46, no. 26, S18, 2010, doi: 10.1049/el.2010.8457.

[115] C. D. Ager, R. J. Wilkinson, and H. P. Hughes, “Periodic grating-gate screening of plasmons in heterojunction structures,” *Journal of Applied Physics*, vol. 71, no. 3, pp. 1322–1326, 1992, doi: 10.1063/1.351250.

[116] W. Knap *et al.,* “Nonresonant detection of terahertz radiation in field effect transistors,” *Journal of Applied Physics*, vol. 91, no. 11, pp. 9346–9353, 2002, doi: 10.1063/1.1468257.

[117] S. Mase, A. Wakejima, and T. Egawa, “Analysis of carrier trapping and emission in AlGaN/GaN HEMT with bias-controllable field plate,” *Phys. Status Solidi A*, vol. 214, no. 8, p. 1600840, 2017, doi: 10.1002/pssa.201600840.

[118] S. B. Cho, S. Lee, and Y.-C. Chung, “Water Trapping at the Graphene/Al 2 O 3 Interface,” *Jpn. J. Appl. Phys.*, vol. 52, 6S, 06GD09, 2013, doi: 10.7567/JJAP.52.06GD09.

[119] J. Zdanevičius, D. Čibiraitė, K. Ikamas, M. Bauer, J. Matukas, A. Lisauskas, H. Richter, V. Krozer, H.-W. Hübers, H.G. Roskos, *Field-Effect Transistor Based Detector for Measuring Power Fluctuations of 4.75-THz Quantum-Cascade Laser-Generated Radiation.* [Online]. Available: https://www.nrao.edu/meetings/isstt/papers/2018/2018132134.pdf

[120] K. Ikamas *et al.,* “Efficient detection of short-pulse THz radiation with field effect transistors,” in *2017 International Conference on Noise and Fluctuations (ICNF)*, Vilnius, Jun. 2017, pp. 1–4.

[121] J. Glemža, V. Palenskis, S. Pralgauskaitė, J. Vyšniauskas, and J. Matukas, “Properties of the surface generation-recombination noise in 1.94 µm GaSb-based laser diodes,” *Infrared Physics & Technology*, vol. 91, pp. 101–106, 2018, doi: 10.1016/j.infrared.2018.04.002.

[122] P. Horowitz and W. Hill, *The art of electronics*. New York, NY: Cambridge University Press, 2015.

[123] G. Vijayaraghavan, M. Brown, and M. Barnes, *Practical grounding, bonding, shielding and surge protection*. Amsterdam, London: Newnes, 2004.

[124] Albrecht Preusser, *Model 7265 DSP Lock-in Amplifier: Instruction Manual* (accessed: May 24 2020).

[125] D. M. Slocum, E. J. Slingerland, R. H. Giles, and T. M. Goyette, “Atmospheric absorption of terahertz radiation and water vapor continuum effects,” *Journal of Quantitative Spectroscopy and Radiative Transfer*, vol. 127, pp. 49–63, 2013, doi: 10.1016/j.jqsrt.2013.04.022.

[126] M. Wan *et al.,* “Polarization and sectioning characteristic of THz confocal microscopy,” in *2019 44th International Conference on Infrared, Millimeter, and Terahertz Waves (IRMMW-THz)*, Paris, France, Sep. 2019 - Sep. 2019, pp. 1–2.

[127] John Wallace, *TOPTICA’s TeraScan frequency-domain terahertz platform helps characterize next-generation terahertz detectors.* [Online]. Available: https://www.laserfocusworld.com/lasers-sources/article/14175457/topticas-terascan-frequencydomain-terahertz-platform-helps-characterize-nextgeneration-terahertz-detectors (accessed: 7 Nov, 2020).

[128] K. Ikamas, A. Solovjovas, D. Čibiraitė-Lukenskienė, V. Krozer, A. Lisauskas, H.G. Roskos, “Optical Performance of Liquid Nitrogen Cooled Transistor-Based THz Detectors,” in *2020 45th International Conference 08/11/2020 - 13/11/2020*, pp. 1–4. [Online]. Available: https://live-irmmwthz.pantheonsite.io/irmmw-thz-2020-technical-program-schedule

[129] K. Ikamas, Solovjovas A., D. Čibiraitė-Lukenskienė, V. Krozer, A. Lisauskas, and H. G. Roskos, “Optical Performance Of Liquid Nitrogen Cooled Transistor-Based THz Detectors,” in *2020 45th International Conference 08/11/2020 - 13/11/2020*, pp. 1–4. [Online]. Available: https://live-irmmwthz.pantheonsite.io/irmmw-thz-2020-technical-program-schedule

[130] O. A. Klimenko *et al.,* “Temperature enhancement of terahertz responsivity of plasma field effect transistors,” *Journal of Applied Physics*, vol. 112, no. 1, p. 14506, 2012, doi: 10.1063/1.4733465.

[131] A. Clegg, *Above 275 GHz.* [Online]. Available: https://sites.nationalacacledemies.org/cs/groups/bpasite/documents/webpage/bpa_049324.pdf (accessed: Oct. 21 2020).

[132] A. I. McIntosh, B. Yang, S. M. Goldup, M. Watkinson, and R. S. Donnan, “Terahertz spectroscopy: a powerful new tool for the chemical sciences?,” *Chemical Society reviews*, vol. 41, no. 6, pp. 2072–2082, 2012, doi: 10.1039/c1cs15277g.

[133] L. Yu *et al.,* “The medical application of terahertz technology in non-invasive detection of cells and tissues: opportunities and challenges,” 2019, doi: 10.1039/C8RA10605C.

[134] K. Ikamas, I. Nevinskas, A. Krotkus, and A. Lisauskas, “Silicon Field Effect Transistor as the Nonlinear Detector for Terahertz Autocorellators,” *Sensors (Basel, Switzerland)*, vol. 18, no. 11, 2018, doi: 10.3390/s18113735.

[135] N. Dyakonova *et al.,* “Saturation of photoresponse to intense THz radiation in AlGaN/GaN HEMT detector,” *Journal of Applied Physics*, vol. 120, no. 16, p. 164507, 2016, doi: 10.1063/1.4966575.

[136] S. Preu, M. Mittendorff, S. Winnerl, O. Cojocari, and A. Penirschke, “THz Autocorrelators for ps Pulse Characterization Based on Schottky Diodes and Rectifying Field-Effect Transistors,” *IEEE Trans. THz Sci. Technol.*, vol. 5, no. 6, pp. 922–929, 2015, doi: 10.1109/TTHZ.2015.2482943.

[137] E. R. Brown, S. Sung, W. S. Grundfest, and Z. D. Taylor, “THz impulse radar for biomedical sensing: nonlinear system behavior,” in *Optical Interactions with Tissue and Cells XXV; and Terahertz for Biomedical Applications*, San Francisco, California, United States, 2014, 89411E.

[138] S. Komiyama, “Single-Photon Detectors in the Terahertz Range,” *IEEE J. Select. Topics Quantum Electron.*, vol. 17, no. 1, pp. 54–66, 2011, doi: 10.1109/JSTQE.2010.2048893.

[139] H. Schneider, O. Drachenko, S. Winnerl, M. Helm, T. Maier, and M. Walther, “Autocorrelation measurements of free-electron laser radiation using a two-photon QWIP,” *Infrared Physics & Technology*, vol. 50, 2-3, pp. 95–99, 2007, doi: 10.1016/j.infrared.2006.10.028.

[140] S. Regensburger, M. Mittendorff, S. Winnerl, H. Lu, A. C. Gossard, and S. Preu, “Broadband THz detection from 0.1 to 22 THz with large area field-effect transistors,” *Optics express*, vol. 23, no. 16, pp. 20732–20742, 2015, doi: 10.1364/OE.23.020732.

[141] D. Voß *et al.,* “Imaging and Spectroscopic Sensing with Low-Repetition-Rate Terahertz Pulses and GaN TeraFET Detectors,” *J Infrared Milli Terahz Waves*, vol. 39, no. 3, pp. 262–272, 2018, doi: 10.1007/s10762-017-0447-1.

[142] K. Ikamas, A. Lisauskas, S. Boppel, Q. Hu, and H. G. Roskos, “Efficient Detection of 3 THz Radiation from Quantum Cascade Laser Using Silicon CMOS Detectors,” *J Infrared Milli Terahz Waves*, vol. 38, no. 10, pp. 1183–1188, 2017, doi: 10.1007/s10762-017-0407-9.

[143] D. Cibiraite *et al.,* “TeraFET multi-pixel THz array for a confocal imaging system,” in *2019 44th International Conference on Infrared, Millimeter, and Terahertz Waves (IRMMW-THz)*, Paris, France, Sep. 2019 - Sep. 2019, pp. 1–2.

[144] K. Ikamas, D. Cibiraite, M. Bauer, A. Lisauskas, V. Krozer, and H. G. Roskos, “Ultrabroadband Terahertz Detectors Based on CMOS Field-Effect Transistors with Integrated Antennas,” in *IRMMW-THz 2018: 2018 43rd International Conference on Infrared, Millimeter, and Terahertz Waves : 9-14 September 2018, Nagoya Congress Center, Nagoya, Japan*, Nagoya, 2018, pp. 1–2.

[145] C. C. Gerry, *Introductory quantum optics*. Cambridge: Cambridge University Press, 2005.

[146] H. Walther, B. T. H. Varcoe, B.-G. Englert, and T. Becker, “Cavity quantum electrodynamics,” *Rep. Prog. Phys.*, vol. 69, no. 5, pp. 1325–1382, 2006, doi: 10.1088/0034-4885/69/5/R02.

[147] S. Haroche, “Nobel Lecture: Controlling photons in a box and exploring the quantum to classical boundary,” *Rev. Mod. Phys.*, vol. 85, no. 3, pp. 1083–1102, 2013, doi: 10.1103/RevModPhys.85.1083.

[148] D. Dini, R. Köhler, A. Tredicucci, G. Biasiol, and L. Sorba, “Microcavity polariton splitting of intersubband transitions,” *Physical review letters*, vol. 90, no. 11, p. 116401, 2003, doi: 10.1103/PhysRevLett.90.116401.

[149] Weisbuch, Nishioka, Ishikawa, and Arakawa, “Observation of the coupled exciton-photon mode splitting in a semiconductor quantum microcavity,” *Physical review letters*, vol. 69, no. 23, pp. 3314–3317, 1992, doi: 10.1103/PhysRevLett.69.3314.

[150] J. P. Reithmaier *et al.,* “Strong coupling in a single quantum dot-semiconductor microcavity system,” *Nature*, vol. 432, no. 7014, pp. 197–200, 2004, doi: 10.1038/nature02969.

[151] G. Scalari *et al.,* “Ultrastrong coupling of the cyclotron transition of a 2D electron gas to a THz metamaterial,” *Science (New York, N.Y.)*, vol. 335, no. 6074, pp. 1323–1326, 2012, doi: 10.1126/science.1216022.

[152] Q. Zhang *et al.,* “Collective non-perturbative coupling of 2D electrons with high-quality-factor terahertz cavity photons,” *Nature Phys*, vol. 12, no. 11, pp. 1005–1011, 2016, doi: 10.1038/nphys3850.

[153] J. Casanova, G. Romero, I. Lizuain, J. J. García-Ripoll, and E. Solano, “Deep strong coupling regime of the Jaynes-Cummings model,” *Physical review letters*, vol. 105, no. 26, p. 263603, 2010, doi: 10.1103/PhysRevLett.105.263603.

[154] R. T. Boreiko and A. L. Betz, “Heterodyne Spectroscopy of the 63 μm O I Line in M42,” *The Astrophysical Journal*, vol. 464, no. 1, L83-L86, 1996, doi: 10.1086/310094.

[155] T. Yasui, A. Nishimura, T. Suzuki, K. Nakayama, and S. Okajima, “Detection system operating at up to 7THz using quasioptics and Schottky barrier diodes,” *Review of Scientific Instruments*, vol. 77, no. 6, p. 66102, 2006, doi: 10.1063/1.2206770.

[156] M. Bauer *et al.,* “Antenna-coupled field-effect transistors for multi-spectral terahertz imaging up to 4.25 THz,” *Optics express*, vol. 22, no. 16, pp. 19235–19241, 2014, doi: 10.1364/OE.22.019235.

[157] H. Dole *et al.,* “The cosmic infrared background resolved by Spitzer,” *A&A*, vol. 451, no. 2, pp. 417–429, 2006, doi: 10.1051/0004-6361:20054446.

[158] R. Appleby, “Passive millimetre-wave imaging and how it differs from terahertz imaging,” *Philosophical transactions. Series A, Mathematical, physical, and engineering sciences*, vol. 362, no. 1815, 379-92; discussion 392-4, 2004, doi: 10.1098/rsta.2003.1323.

[159] R. Appleby and H. B. Wallace, “Standoff Detection of Weapons and Contraband in the 100 GHz to 1 THz Region,” *IEEE Trans. Antennas Propagat.*, vol. 55, no. 11, pp. 2944–2956, 2007, doi: 10.1109/TAP.2007.908543.

[160] D. T. Petkie *et al.,* “Active and passive imaging in the THz spectral region: phenomenology, dynamic range, modes, and illumination,” *J. Opt. Soc. Am. B*, vol. 25, no. 9, p. 1523, 2008, doi: 10.1364/JOSAB.25.001523.

[161] M. Wan *et al.,* “Terahertz quantitative metrology using 300 GHz in-line digital holography,” in *Holography: Advances and Modern Trends VI: 1-4 April 2019, Prague, Czech Republic*, Prague, Czech Republic, 2019, p. 27. [Online]. Available: https://www.spiedigitallibrary.org/conference-proceedings-of-spie/11030/2520787/Terahertz-quantitative-metrology-using-300-GHz-in-line-digital-holography/10.1117/12.2520787.full

[162] B. Pollard, F. C. B. Maia, M. B. Raschke, and R. O. Freitas, “Infrared Vibrational Nanospectroscopy by Self-Referenced Interferometry,” *Nano letters*, vol. 16, no. 1, pp. 55–61, 2016, doi: 10.1021/acs.nanolett.5b02730.

[163] G. Wurtz, R. Bachelot, and P. Royer, “A reflection-mode apertureless scanning near-field optical microscope developed from a commercial scanning probe microscope,” *Review of Scientific Instruments*, vol. 69, no. 4, pp. 1735–1743, 1998, doi: 10.1063/1.1148834.

[164] B. Knoll and F. Keilmann, “Enhanced dielectric contrast in scattering-type scanning near-field optical microscopy,” *Optics Communications*, vol. 182, 4-6, pp. 321–328, 2000, doi: 10.1016/S0030-4018(00)00826-9.

[165] F. Walla *et al.,* “Near-Field Observation of Guided-Mode Resonances on a Metasurface via Dielectric Nanosphere Excitation,” *ACS Photonics*, vol. 5, no. 11, pp. 4238–4243, 2018, doi: 10.1021/acsphotonics.8b00900.

[166] M. Razgūnas, “KONFIGŪRUOJAMOS THZ MATRICOS ELEKTRONIKOS KŪRIMAS,” Bachelor Thesis, Applied electrodynamics and telecommunications, Vilnius University, Vilnius, 2019.

[167] W. H. Steel, “The Design of Reflecting Microscope Objectives,” *Australian Journal of Scientific Research, Series A: Physical Sciences*, vol. 4, pp. 1–11, 1950.

[168] M. L. Kutner, *Astronomy: A physical perspective,* 2nd ed. Cambridge: University press, 2003.

[169] T. Hattori, H. Kumon, and H. Tamazumi, “Terahertz spectroscopic characterization of paper,” in *35th International Conference on Infrared, Millimeter and Terahertz Waves (IRMMW-THz), 2010: 5-10 Sept. 2010, Angelicum, Rome, Italy*, Rome, Italy, 2010, pp. 1–2.

Appendix

ITN CELTA project has received funding from the HORIZON 2020 Research and Innovation Programme, grant agreement No. 675683. An International Training Network for the research in the converging field of electronics and photonics technologies was created which had the main goal to enable THz applications. Each early stage researcher working on this project had to work on THz technologies resulting with the doctoral degree, to gain experience on the collaboration with other academic or industry partners during the secondments which took at least 6 months in total, as well as to work on a group work towards one of the project demonstrators and present their work each year attending the International Travelling Summer School on Microwaves and Lightwaves (ITSS).

It was a unique experience to work with international research teams in Europe. During the secondment at University College Dublin in Ireland the THz camera, as well as single-pixel TeraFET, were tested and showed good results in an optical THz setup made for confocal imaging. The secondment at Universidad Carlos III de Madrid in Spain enabled the TeraFET testing in hyperspectral imaging setup based on a dual-frequency comb. Both collaborations led to publications of the results in various scientific conferences and journals. The topics are also presented in this work.

The following figure shows the map (left) with all the locations of the partner institutions for the group work of ITN CELTA, the arrows show the two secondments which were presented in this work. At the right of the figure, the imaging demonstrator is presented. All the students were working on a specific part of the demonstrator, containing the THz source and various THz receiver systems.

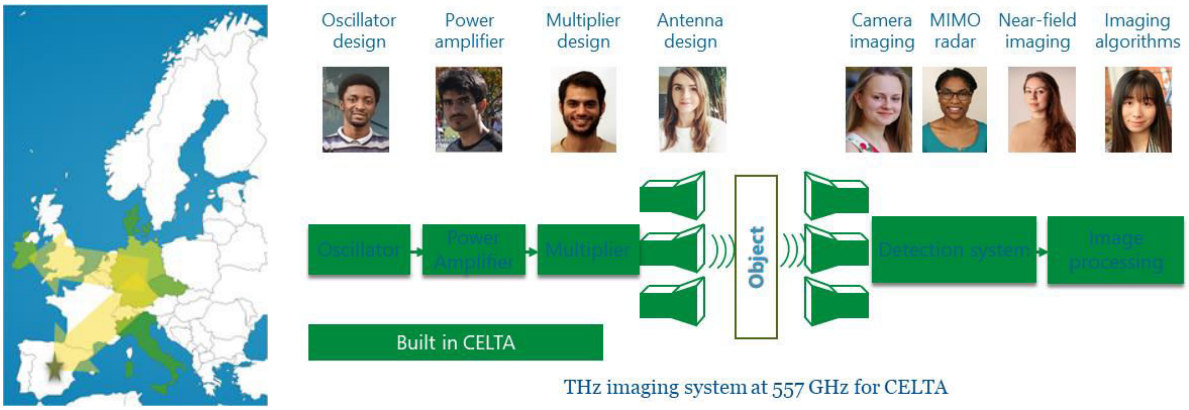

Fig. A.1. Map of secondment and group work partners' locations (left). Group work on the THz imaging system at 557 GHz for the ITN CELTA project (right).

Habeeb Bello, Abdul Ali, and Arsen Turhaner were working on the THz source part: local oscillator, power amplifier, and frequency multiplier, respectively. Dominika Warmowska

was developing planar antennas. Dovilė Čibiraitė-Lukenskienė, Marie Mbeutcha, and Aleksandra Baskakova were developing there different imaging systems for 557 GHz frequency and its subharmonics. Min Wan researched optical THz imaging systems and imaging algorithms. The whole project led to the successful development of each part resulting in the doctoral thesis. Collaborative work led to the improvement of the common THz language skill, as the same word in electronics and photonics might have slightly different definitions. During the group work, the system development skill was improved, and the packaging problem of the single devices has been seen as the most important to be solved for the further development of this system.

Eidesstattliche Erklärung

Hiermit erkläre ich gemäß §7 Abs. 2 der Promotionsordnung, dass ich die vorliegende Arbeit selbständig verfasst und nur die angegebenen Hilfsmittel, unter Beachtung der Grundsätze der guten wissenschaftlichen Praxis, verwendet habe. Ich versichere weiterhin, dass ich bisher noch keinen Versuch zur Promotion unternommen habe.

Frankfurt am Main, den 4. Dezember, 2020

Dovilė Čibiraitė-Lukenskienė